Centrifugal Instability of Wake Dominated Curved Compressible Mixing Layers

by

LI LIN

A thesis submitted to

The University of Birmingham

for the degree of

Doctor of Philosophy

School of Mathematics

The University of Birmingham

January 2008

Abstract

This investigation is concerned with the linear development of Görtler vortices in the high-Reynolds-number laminar compressible wake behind a flat plate which is aligned with the centreline of a curved mixing layer system. The Görtler modes were previously found to exist within the curved compressible mixing layers by Owen et al. (1997). This study extends the work of Owen et al. (1997) and attempts to demonstrate the effect a wake has on the growth rate and location of such modes. The investigations were made by examining the growth rate and the location of the Görtler modes in the limit of large Görtler number and high wave number within the wake-dominated curved compressible mixing-layer systems based on three wake flow models. An analytical Gaussian wake profile is first used to model the behaviour of the basic flow within the mixing layer at the trailing edge of the splitter plate. It is found that the wake has an amplification effect on the growth of the Görtler instability within the concavely curved, or 'unstably' curved compressible mixing layers. It is also found that within the convexly curved, or 'stably' curved compressible mixing layers the wake modes can occur that would behave differently to the 'thermal modes', which were previously found within the plain curved compressible system by Owen et al. (1997). Another analytic composite model which had some practical applications is then used to predict the behaviour of the modes within the systems. A numerical wake flow model has also been derived to compare with the predictions based on the analytic wake flow models.

Acknowledgements

I would like to deeply thank my supervisor Dr Sharon Stephen who offered me lots of encouragement throughout the whole research process. There would be no thesis without her help. I would also like to thank the school for giving me the chance to study my interests. I would especially like to thank my family and all my friends for their support and encouragement.

Contents

List of Figures

Chapter 1

Introduction

Mixing within fluid systems has both desirable and undesirable consequences. As such, an understanding of the processes which affect mixing within fluid systems would be extremely valuable. With the increasing use of high-powered engines nowadays, there have been increased interests in supersonic combustion (scramjets) and noise reduction for the high speed civil transport (HSCT), which prompted renewed research in supersonic mixing processes and means to control them. The technological challenge of mixing enhancement in compressible flows stems from the inherently low growth rates of supersonic mixing layers. Many mixing augmentation methods employed efficiently in subsonic flows failed to work at elevated Mach numbers, and some of the methods were inefficient because they were utilized outside their effective range. Nevertheless, studies of compressible mixing flows have built on the knowledge accumulated in subsonic flow research.

By its nature, the physics of compressible flows implies that there are fluctuations in the density as well as the velocity and pressure. The density of the fluid varies by the change in the pressure forces and the temperature. As a result, the laws of thermodynamics must be considered along with the equations for the conservation of mass and momentum. The study of compressible fluid flows generally concentrates on gas flows. In particular, the study of aerodynamics generates considerable interest in 'high speed' gas flows.

A particular physical application of the compressible mixing is within the scramjet engine system during the mixing between fuel and oxidizer for the propulsion of hypersonic aircraft. The scramjets belong to a family known as the air-breathing jet engines that rely on variations of a basic thrust-generating principle to operate at different ranges of speeds and altitudes. Most commonly used by commercial airline companies are gas turbine engines, which contain five basic components: an air inlet; a compressor (a wheel of airfoils on a rotating shaft) that sucks in air and raises its pressure; a combustion chamber of which fuel is injected and burned within; a turbine wheel that spins when hot combustion gases rush past its airfoils to drive the compressor wheel shaft; and a nozzle through which the high-temperature exhaust expands to generate thrust. In general, the scramjet engines generate thrust by combining compressed atmospheric air with fuel, burning the mixture and then expanding the combustion products out the back of the aircraft (see Figure (1.1)). The mixing process within the scramjet is very important as an incomplete mixing could result in partial burning and a loss in the combustion efficiency. As such, an understanding of the processes which affect mixing within such a system would be extremely valuable.

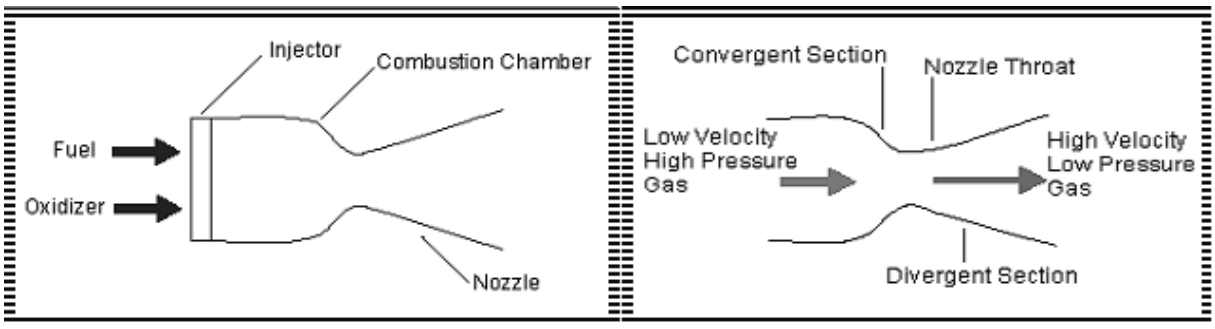

Figure 1.1: Illustration of the mixing process between the fuel and the oxydiser within the scramjet engine system.

Since mixing is generally enhanced within turbulent environments, hydrodynamic stability theory offers one possible route to increasing this understanding. Linear stability theory is concerned with the effect which extremely small perturbations have on a fluid system. The initial stages of the growth of these instabilities can be modelled using linear theory where the disturbances are considered to be infinitesimally small. This assumption allows nonlinear terms in the equations governing the fluid motion to be neglected; this greatly simplifies the resulting analysis. One consequence of using the linear theory is that any predicted growth is exponential, thus the disturbance can no longer be neglected. This is the point where non-linear effects begin to influence the growth of the instability. The non-linear effects play an important role in either stabilizing or destabilizing the flow. Within many fluid systems, the growth of an instability may cause the underlying flow field to become unstable to another instability mechanism. The first instability is classified as a primary instability. The appearance of the new instability is based on the effects of the primary instability, and therefore classified as a secondary instability. The fully formed primary instability causes the flow to be non-planar. This is due to the extra structure imparted into the system. Therefore the linear stability theory is not able to fully describe the structure and the evolution of the flow, thus it is necessary to generate a non-linear formulation for the primary instability in order to fully describe the resulting flow.

An example of this kind of instability occurs in the flow over a concave wall. This type of flow was first studied by Görtler (1940). Görtler found that the flow could develop longitudinal vortical structures with a 'swiss roll' like shape. These vortices became known as Görtler vortices (see Figures (1.2) and (1.3)).

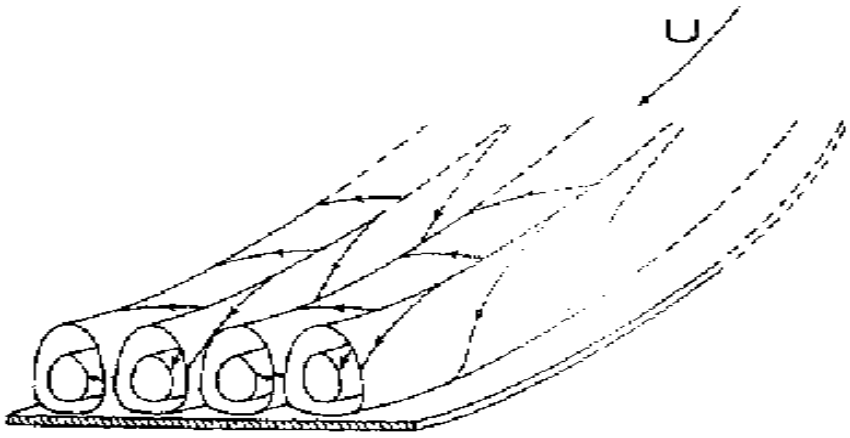

Figure 1.2: Illustration of centrifugal instability occurring within a flow over a concave solid surface, taken from Görtler (1940).

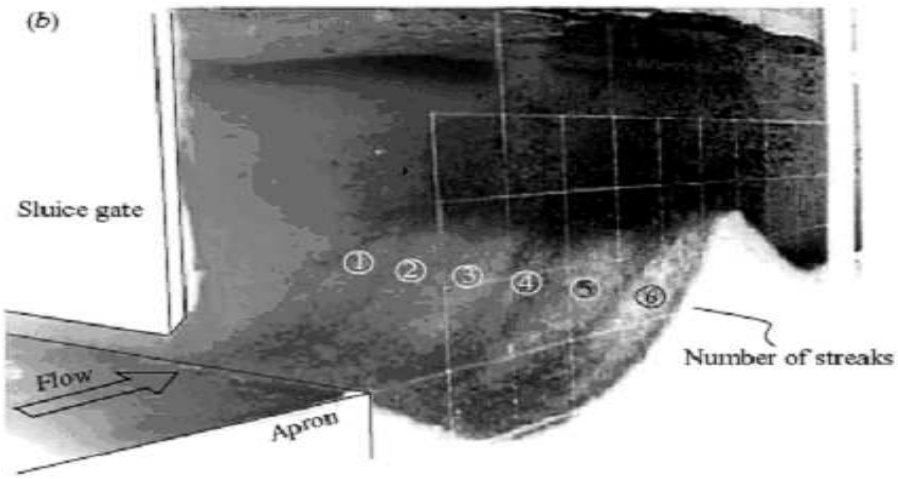

Figure 1.3: Picture taken from Hopfinger et al. (2004) demonstrating the development of the Görtler instability within the boundary layer of the water flowing over a solid concave surface.

There are many practical flow situations where Görtler vortices could potentially occur. A particular situation where Görtler vortices are thought to be the cause of transition to turbulence is the flow over the concave section of a laminar flow wing (Hall (1990)). The vortex develops due to the presence of a centrifugal instability which draws its energy from the innate curvature of the system. It then grows as the flow moves along the surface until it becomes a physically realizable structure in the form described previously. As the vortex becomes larger it can render the flow susceptible to a new rapidly growing instability that is known as the Rayleigh instability. The new instability will quickly grow within a very short period of time and is very destructive to the underlying flow field. This often leads to the flow becoming turbulent which can have a negative effect on the behaviour of the aircraft wing. The study of the secondary instability of this system was done by Hall and Horseman (1991) and Li and Malik (1995) which allows more understanding into the potential control of such instabilities.

It is possible for these instabilities to occur along the curved streamlines of the flow, and thus they are not restricted only to flows over solid surfaces. It is known for these instabilities to occur in situations where the solid boundary is replaced by another fluid. Such type of system is referred to as a mixing layer as the interfacial region between the two fluids quickly begins to entrain fluid from both sides of the surface and thus gives rise to mixing. Previous experiments have shown that the mixing layer system could become unstable to similar centrifugal instabilities. Having mentioned one, there are two further types of instability that could occur in a curved mixing layer:

The Kelvin-Helmholtz instability: This instability is associated with the free mixing layer and produces spanwise vortical structures (see Figure (1.4)).

The Rayleigh-Taylor instability: This instability is associated with the effect of body force opposed to the density gradient and produces three-dimensional mushroom like structures (see Figure (1.5)).

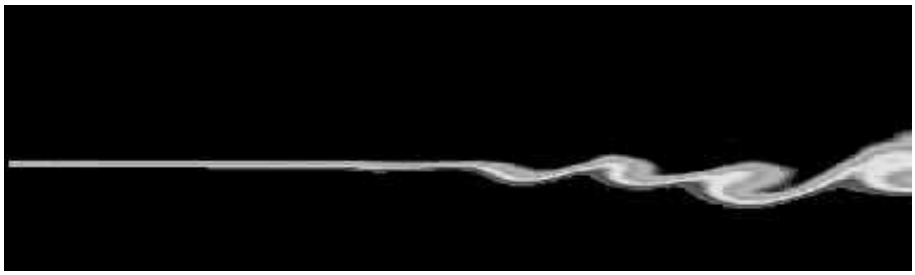

Figure 1.4: A numerical simulation demonstrates the Kelvin instability wherein two stably stratified fluids are flowing from left to right with the uppermost low density fluid travelling 3.5 times faster than the lower heavy fluid. (Movie clip taken from efluid gallery)

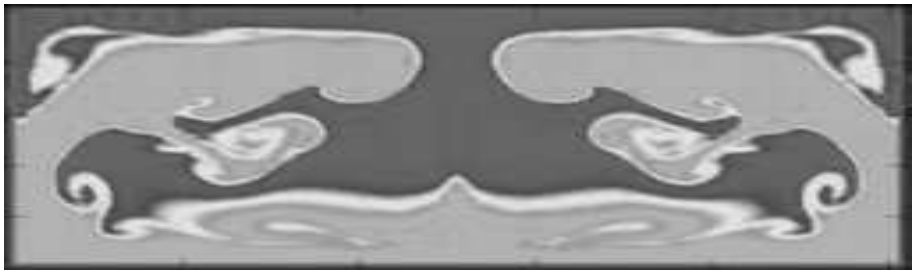

Figure 1.5: A numerical simulation of the Rayleigh-Taylor instability within the shear layer system. When a high density fluid is placed over a low density fluid an unstable condition exists, which causes the two fluids to exchange places. (Movie clip taken from efluid gallery)

The formation of coherent structures in a straight mixing layer is initiated by Kelvin-Helmholtz instability, governed by Rayleigh's equation for inviscid flows. The exponential growth of the velocity perturbations leads to a nonlinear process that eventually causes the roll-up of the mixing layer into vortices. The initial vortex shedding frequency which is also known as the most amplified frequency is determined by various characteristics of the existing velocity profile. The initial vortices grow in the mixing-layer and coalesce as they are convected downstream in a 'pairing' process. Due to merging and entrainment, the mixing-layer spreads, and the frequency associated with the large vortices decreases.

The irrotational entrainment by the large-scale structures leaves the entrained fluids essentially unmixed during the lifetime of vortices. Nonetheless, intense mixing occurs during pairing or other amalgamation process. An early experiment which was done by Bernal and Roshko (1986) had shown that a secondary spanwise instability could appear at some distance downstream of the splitter plate trailing edge, which then lead to the development of streamwise vortices that would enhance the mixing process. This process is referred to as the 'mixing transition'. The streamwise vorticity, which is organized in 'ribs', interacts with the spanwise structures. With increasing downstream distance, the interaction increases the three-dimensional structure in the mixing layer, leading to high-order instabilities and transition to small-scaled dominated flow.

There have been many investigations in the past that were concerned with the spatial and temporal instability of the straight mixing layer. These investigations followed the pioneering work of Rayleigh (1916), Reynolds (1883), Kelvin (1871) and Helmholtz (1890), who were the first to study and categorise the processes of transition from steady flow. For the last decade, there have been increasing interest in the stability of the curved mixing layer, where the curvature could be caused by the drop of the pressure across the two fluids. Investigations of the curved mixing layer case have been primarily concerned with the development of the Görtler instability. The aim of this thesis is to study how the inclusion of non-planar effects into a basic flow alters the stability of the curved compressible mixing layer system. The major findings concerning the straight and curved compressible mixing layers are summarized in the next section as a background for the more detailed review of the compressible mixing flows.

1.1 Background Work

Early studies on the stabilities of compressible mixing layers were done by Lin and Lees (1946), who provided the basic formulation of the theory for the stability of compressible mixing flows, both free and bounded. They were also the first to show the importance of

three-dimensional disturbances for the stability of these flows. Another major contribution comes from Gropengiesser (1969), who carried out inviscid spatial stability calculations for the mixing layer using a generalized hyperbolic tangent profile for temperature ratios of 0.6, 1.0 and 2.0 and for Mach numbers between 0 and 3. Gropengiesser discovered that, for low and moderate Mach numbers, the flow becomes less unstable as the stationary gas becomes hotter. Gropengiesser also showed that spatial growth rates decrease with increasing Mach numbers. Little was done until the late 1980s when scientists began a number of theoretical studies on the stability of compressible free shear layers. In particular, Jackson and Grosch (1991) examined the inviscid stability of the mixing layer to two- and three-dimensional disturbances. They used the hyperbolic tangent profile as an approximation for the basic flow velocity and determined the temperature using Crocco's relation. As a result of their work, the classification of neutral and unstable modes over the Mach number range of 0 to 10 was determined. Their work has effectively extended and completed the results of Gropengiesser.

In 1974, Brown and Roshko (1974) started their investigation on the structure of planar mixing layers. Their work triggered extensive research for the next two decades that substantiated the idea that large-scale coherent structures control the dynamics of all free shear flows including plane mixing layers, jets of different geometries (axisymmetric, plane, elliptic, rectangular, etc.), and wakes. The discovery of large-scale coherent structures in the mixing-layer and their relation to the flow instability make it possible to control the development of the mixing-layer and thus affect its mixing characteristics. This then led to the development of numerous mixing control techniques. In general, large-scale structures are beneficial for the enhancement of bulk mixing, but they hinder fine-scale or molecule mixing, which are necessary in reacting flow applications. Enhancement of both large- and small-scale mixing can be achieved by exciting a combination of unstable modes. A particular type of approach to apply control is known as the passive control, which uses geometrical modifications of the element from which flow separation occurs to

change the mixing-layer stability characteristics. Some examples of these modifications are : convoluted splitter plates (Lasheras, Cho, and Maxworthy (1986)) and splitter plates positioned behind a cylinder for drag reduction (Brown and Roshko (1974)). In addition, Schadow and Gutmark (1989) also reviewed a number of additional passive techniques in non-reacting and reacting flows in their work.

When a thin splitter plate is inserted into the centreline of the mixing layer, the drag force that comes from the surfaces of the splitter plate, which causes rapid variation in the fluid velocity near to the solid boundaries, is very much equivalent to a thin wake. It was Prandtl (1904) who introduced the theory of boundary layers that provided explanation of the thin region of rapid variation in fluid velocity which occurs near solid boundaries at high Reynolds number. The boundary layer theory was then used by Blasius (1908) to describe the flow along a flat plate parallel to a uniform stream. The work of Blasius revealed that for a finite plate the same system of boundary layer equations also governs the flow in the wake downstream of the trailing edge. The solution in the far wake region (as the streamwise coordinate $x^* \longrightarrow \infty$) was studied by both Goldstein (1933) and Stewartson (1957). Goldstein (1930) also provided the solution in the near wake region (as $x^* \longrightarrow 0^+$) by using the method of matched asymptotic expansions. The basic profile at $x^* = 0$ is taken as the Blasius profile. The work of Goldstein was then extended by Daniels (1976) to study the incompressible flow in the wake of a finite flat plate. The complete wake flow was then numerically derived by Daniel using a finite difference procedure. A similar investigation was made by Veldman (1975) around the same period and both results from Daniel and Veldman appeared to be in good agreement. A numerical solution of the two-dimensional compressible Navier Stokes equations for the symmetric wake behind a splitter plate was provided by Ragab (1988). Continuing investigations were later made by Sandham and Reynolds (1990), who investigated the three-dimensional instabilities. A similar investigation was made by Papageorgiou (1991) who studied the inviscid instability of a two-dimensional compressible wake at high Reynolds number and Mach

number both numerically and analytically. Papageorgiou emphasises the use of proper wake profiles that satisfy the equations of motion at high Reynolds numbers. The work of Papageorgiou also showed that the stability characteristics could be affected significantly as the wake developed along the trailing edge of a splitter plate as the Mach number varies from the supersonic through the hypersonic regions. Zhuang and Dimotakis (1995) also studied the instability of wake dominated compressible mixing layers. They used the hyperbolic tangent profile plus a wake component to represent the basic parallel velocity profile. Such profiles are encountered in the initial region of experimental supersonic shear-layer flows, as well as in envisaged hypersonic propulsion systems in which ingested boundary layers generate substantial wake components. They found that the existence of a wake component in the velocity profile renders the mixing layer more unstable at all free-stream Mach numbers. They also found that for convective Mach number exceeding unity, the shear-layer mode splits into two supersonic modes, and the mixing layer becomes more unstable with increasing wake deficit. A joint theoretical and experimental investigation was presented by Liang, Reshotko, and Demetriades (1996) to study the stability of two bounded and semi-bounded compressible wake flows at Mach number 8 and Mach number 3 respectively. The work of Liang, Reshotko, and Demetriades (1996) also presented an analytical analysis of the streamwise evolution of the basic wake flow which formed the basis for the stability calculations. The study of the basic wake flow was conducted analytically using a modified form of the Demetriades (1990) composite method. This analytical basic wake flow calculation was designed by Demetriades to correspond to an experiment performed at hypersonic speeds and to provide a means of interpreting stability observations made in the experiment. The more detailed analysis of such method will be presented in Chapter Four of this project.

1.2 Centrifugal instabilities within curved mixing flows

The centrifugal instabilities within the curved compressible mixing layer system were studied experimentally by Plesniak, Mehta, and Johnson (1994) and analytically by Owen, Seddougui, and Otto (1997). Plesniak et al. (1994) have noted that curved two-stream mixing layers are susceptible to centrifugal instabilities under the condition that the slower stream curves towards the faster stream. However, Owen et al. (1997) showed that in a compressible mixing layer, the centrifugal instabilities can also be observed for certain parameter regimes when the faster stream curves into a cooler slower stream. The type of centrifugal instability which we will be considering is the Görtler instability. As mentioned earlier, the essential properties of the Görtler problem is that the system must be curved; the resulting centrifugal forces then provide an energy source for the instabilities. Görtler instability is initially concerned with the centrifugal instability of a boundary layer on a concave wall. The same problem was investigated experimentally approximately twenty years earlier by Taylor (1923). Taylor's investigation was concerned with the instability of flow between concentric cylinders, and his experimental work showed that the initial instabilities of the flow are axisymmetric. This discovery confirmed Rayleigh's assumption which was made almost five years earlier. The original investigation into the stability of rotating fluids was performed by Rayleigh (1916). As a result, Rayleigh generated a sufficient condition for the flow that is inviscid to be stable to a particular disturbance; this is known as 'Rayleigh's circulation criterion'. Rayleigh's criterion states that if the square of the circulation of the flow does not decrease in the direction of increasing radial distance anywhere within the flow, then the flow is stable to axisymmetric instabilities. Other than proving Rayleigh's criterion, Taylor also studied the instabilities of a viscous fluid within rotating Couette flow, and he showed that the initial instability takes the form of toroidal vortices structured in the streamwise direction. These instabilities have become what we know today as Taylor vortices.

In the Taylor problem, viscous effects in a rotating fluid are usually characterized by a dimensionless Taylor number, T, the precise definition of which may vary. If a basic swirling flow of an inviscid fluid which moves with angular velocity $\Omega(r)$, an arbitrary function of the distance r from the axis of rotation, and if Ω = constant, then one usually takes

$$T = 4\Omega^2 L^4/\nu^2,$$

where L is a convenient length scale and ν is the viscosity of the fluid. According to Rayleigh's criterion for stability of the basic flow, mathematically represented as $\Phi(r) \geqslant 0$ with Φ defined as

$$\Phi(r) = \frac{1}{r^3}\frac{d}{dr}(r^2\Omega)^2,$$

it would be expected to remain stable when viscous effects are considered. However, if the flow is unstable according to Rayleigh's criterion, then we would still expect viscosity to have a stabilizing effect, in the sense that the flow is stable provided the Taylor number is less than a certain critical value, say, T_c.

In the Taylor problem, the flow is bounded at the radial extremities of the region. Görtler (1940) later extended the Taylor problem by studying the flow which is bounded at only one extremity. Görtler found that the resulting flow was to become unstable to centrifugal modes of instability.

Görtler's theory is based on three approximations. First Görtler assumed that the boundary layer thickness δ is much smaller than the radius of the curvature of the wall R_0. Görtler's second assumption is that the basic flow is nearly parallel to the wall so that the centrifugal effects are neglected in the basic flow. Finally, Görtler considered a local stability analysis for which the basic flow is assumed to be independent of streamwise and spanwise variable. In Görtler's theory, the downstream growth of the boundary layer and the normal velocity component associated with that flow was ignored.

Practically all theoretical work on Görtler vortices for the next few decades followed the assumption that the streamwise lengthscale of the vortex is small compared to the

lengthscale over which the boundary layer develops. Many of the results obtained using Görtler's theory proved to be difficult to interpret physically, such as predicted instability growth at zero spanwise wave number (infinite wavelength). The situation was rectified by Hall (1982), who investigated the Görtler problem and showed that without the growth of the basic flow within the governing equations the resulting solution does not behave correctly towards the boundaries of the region except where the vortex wave number is very large. The high wave number analysis was found by Hall to apply to far downstream regions of the flow where the natural boundary layer growth of the system renders the apparent wave number of any vortex large. This allows the far downstream behaviour of the system to be studied with this analysis and the eventual fate of the instability determined. Hall went on to solve the problem numerically for a non-linear vortex with O(1) wave number using a marching scheme in the streamwise coordinate.

Both Taylor and Görtler instability are caused by the same centrifugal mechanism. However, there is a significant distinction between them, that is the dominant flow within the Görtler problem develops spatially in the streamwise direction; whereas in the Taylor problem it is fully developed.

1.3 The Current Project

Our aim is to investigate the Görtler instability mechanism as a mixing enhancement within the system of two non-parallel finite compressible streams with different temperatures travelling at different velocities down the trailing edge of a splitter plate in a curved channel. For the mixing enhancement purpose, the initial growth and the location of the modes are important as these factors determine the role of the Görtler instability during the process of mixing. Hence the linear two-dimensional instability theory seems a reasonable starting point for describing the initial development of the Görtler instability in a wake-dominated curved compressible mixing layer system. In order to understand such system we must derive a set of equations which govern the behaviour of the system.

The governing equations must be transformed into a coordinate system which curves with the centreline of the mixing layer. The detailed process of such transforming will be presented in Section (2.1) of the next chapter. Once we have obtained the governing equations for the system, a set of basic mixing layer equations which governs the behaviour of the basic flow will then be derived and the process of derivation will be presented in Section (2.2). We will use the same formulation method as provided in Hall (1982) on the wake-dominated mixing layer rather than a boundary layer; thus the boundary conditions will be changed for the problem. To investigate the initial development of the Görtler disturbance within the system, linear stability theory is used to perturb the system to obtain a set of equations governing the disturbance. After simplification, an eigenvalue equation which governs the behaviour of the so called inviscid Görtler modes with the Görtler number, $G \gg 1$, can be found. The derivation process will be presented in Section (2.3). For the high wave number limit of the inviscid problem, we are going to employ an asymptotic analysis that was previously derived by Hall (1982). With this analysis, the leading-order behaviour of the growth rate and the location of the modes can be obtained analytically. In this project, we are going to refer to this analysis as the high wave number analysis. Such analysis is very useful towards predicting the behaviour of the modes based on the range of free-stream temperature and velocity ratios within the system. A detailed formulation process using the high wave number analysis based on our problem is going to presented in Section (2.4).

In order to characterize the overall stability of a flow it is necessary to describe the shape of the neutral curve as this determines when a mode will be unstable (Figure (1.6)). The eigenvalue relation effectively describes the behaviour of the inviscid Görtler modes at the left-hand branch of the neutral curve. Within this region it was demonstrated by Owen et al. (1997) that for the plain mixing-layer system the growth rate would increase monotonically with wave number from zero. It was shown that as the wave number increases the growth rates would asymptote to a finite value which can be derived using the

high wave number analysis. Eventually for large enough wave numbers that corresponds to the right-hand branch region of the neutral curve the viscosity effect would play an important role in stabilizing the modes.

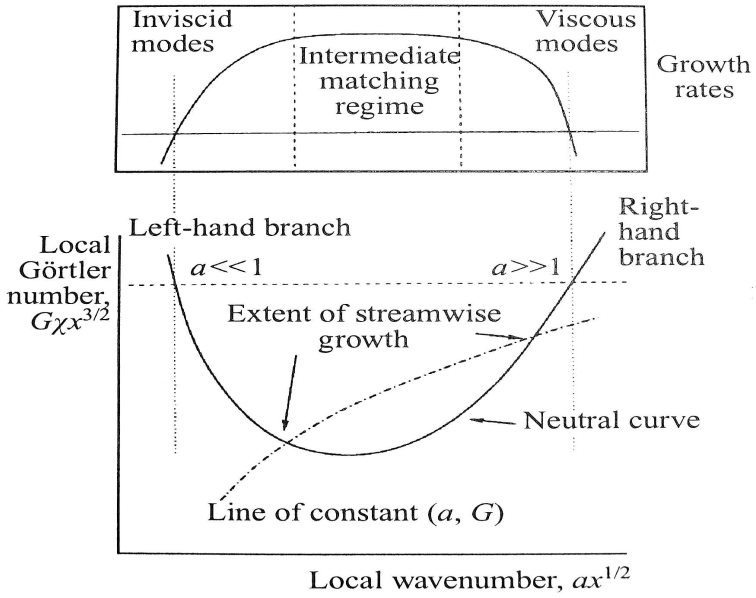

Figure 1.6: Schematic of the neutral curve and growth rate for the mixing flow that is unstable to a wide range of wave numbers, Sarkies and Otto (2000).

Within the right-hand branch region, Hall (1982) also derived an asymptotic analysis, which could be applied to the system to determine the location of the right-hand branch of the neutral curve. It is known that within the right-hand branch region, the Görtler number remains large and the wave number of the modes, a, is relate to the Görtler number by $a \sim G^{1/4}$. The process of formulation within the right-hand branch region for our problem will be presented in Section (2.5).

In Chapter Three, we are going to investigate the behaviour of the modes within the system that is far-down stream from the trailing edge of the splitter plate. Within such a system, the wake effect can be neglected and the modes will lead a similar behaviour to those within the plain curved compressible mixing-layer system. Such a system was

previously investigated by Owen et al. (1997), and for the basic flow problem they have employed a Lock profile (Lock (1951))and a Ting profile (Ting (1959)), which both would need to be solved numerically. For our work, we will be reviewing some of the results in Owen et al. (1997) by employing a different numerical scheme, which will be discussed in Section (3.3). We are also going to extend their investigation by considering an analytic hyperbolic tangent profile, which appearers to be a popular choice by many to approximate the basic flow within the mixing-layer system due to its simplicity. The three basic flow models for the curved mixing-layers will be discussed in detail in Section (3.1).

The major part of this project is concerned with the investigation of the mixing of two steady, laminar streams downstream of the trailing edge of a thin partition. Previous work of Owen et al. (1997) within the curved compressible mixing-layer system had demonstrated that the different basic flow model would offer a different prediction of the behaviour of the Görtler modes within the same system. To investigate the Görtler modes as a mixing enhancement within the wake-dominated system, it is important to employ a basic flow model that is able to accurately describe the behaviour of the flow downstream of the trailing edge of the splitter plate in order to offer correct predictions of the growth rate and the location of the modes. Since for large growth rate and with location near to the centreline of the mixing-layer system, the Görtler modes are more beneficial towards the mixing between the two fluids.

We shall start by investigating the effect of including a Gaussian wake component in the basic hyperbolic tangent profile of the mixing layer as considered by Zhuang and Dimotakis (1995). For our convenience, we are going to refer this model as the Gaussian wake flow profile in the project. Earlier work of Zhuang (1999) also employed such a profile during the investigation of the effect of curvature on the wake-dominated incompressible mixing layers. Their work showed that in a curved incompressible shear layer with a wake component, the growth rate of the wake mode increases with increasing mixing layer curvature and an oblique wake mode can become dominant in the three-dimensional

mixing layers. For our problem, we are going to be investigating the wake-dominated compressible mixing-layer system based on two types of curvature. The first case will be referred as the 'stably curved' case, which corresponds to the centreline of the system curving towards the slower stream direction. The second case will be referred as the 'unstably curved' case, which corresponds to the centreline of the system curving towards the faster stream direction. Previous work of Owen et al. (1997) demonstrated that within the stably curved compressible mixing layers, only the 'thermal modes' could exist and which are restricted to the slower stream being significantly cooler than the faster stream. These thermal modes have no counterpart in the corresponding incompressible curved mixing layer investigation by Otto et al. (1996). For our problem, we are going to look into the stably curved case, and investigate the effect of wake on the behaviour of the modes within the system.

The second basic wake flow model we are going to consider for our problem is referred by us as the analytic composite model. The composite model was previously derived by Brower and Demetriades (1990) to correspond to an experiment performed on the parallel mixing flow travelling at hypersonic speeds. Since such a model has had some relevant practical applications, therefore we are going to apply this model to our problem in order to compare the predictions of the linear Görtler instability within the system. The investigation based on the composite model will be discussed in Section (4.2).

Despite the convenience of using the analytic wake flow models, these models only approximate the behaviour of the basic wake flow within the system, which roughly correspond to the physical flow. It was emphasised by Papageorgiou (1991) that in order to satisfy the physical properties the wake profiles should be obtained numerically from solving the boundary-layer equations for the increasing distance down the trailing edge. Therefore we are going to consider solving the basic flow equations to obtain a more physical numerical wake flow model for our prediction of the Görtler instability. For the initial profiles that are required to solve the basic flow equations in the near wake region, we are

going to employ method of asymptotic expansion from Goldstein (1930). The complete solution to the basic asymmetric wake flow is going to be derived numerically based on the analytical initial profiles. The process of derivation of the numerical wake flow model and its prediction of the Görtler instability within the system will be presented in Chapter Five.

The predictions of the instability based on the three models will be investigated and compared. Finally, a summary and ideas for potential future work are given in the last chapter.

Chapter 2

Formulation of the wake-dominated curved compressible mixing flow system

In order to investigate the stability of a curved compressible mixing layer system we must have a great understanding of the physics of the system. One route to increase this understanding is to offer an estimation of the relative influence of the dominant forces and their components on the system's behaviour. The laws of fluid dynamics are well established and can be deduced from the observation that the behaviour of a physical system is completely determined by conservation laws. These laws state that during the evolution of a fluid a certain number of properties such as mass, generalized momentum and energy are 'conserved' within the system. The conservation of mass can be simplified to a continuity equation. The conservation of momentum is represented by the set of Navier-Stokes equations which were first derived for incompressible flow by Navier in 1882 (the detailed process of such simplifications is discussed in Rogers (1992)). The principle of conservation of energy describes how the total energy in the control volume changes due to transport, heat addition and work done on the volume and can be simplified to the energy equation. A more detailed simplification process of the energy conservation

law is presented in Section (2.1.1).

2.1 Derivation of the equations for curved compressible flow

We start with the continuity equation and Navier-Stokes equations for compressible flow with a cartesian coordinate system (x^*, y^*, z^*), where x^* is the coordinate along the streamwise direction, y^* is in the normal direction, z^* is in the spanwise direction ($*$ indicates dimensional variables). The flow has density ρ^*, velocity $\mathbf{u}^* = (u^*, v^*, w^*)$, where u^* is the velocity in the streamwise direction, v^* is the velocity in the normal direction and w^* is the velocity in the spanwise direction. Assume there are no body forces on the flow. The time of the flow is t^*.

The continuity equation is:

$$\frac{\partial \rho^*}{\partial t^*} + \nabla.(\rho^* \mathbf{u}^*) = 0. \tag{2.1}$$

The Navier-Stokes equations in the vector form are presented as:

$$\rho^* \left(\frac{\partial \mathbf{u}^*}{\partial t^*} + \mathbf{u}^*.\nabla \mathbf{u}^* \right) = -\nabla p^* - \nabla \wedge [\mu^* (\nabla \wedge \mathbf{u}^*)] + \nabla \left[(\lambda^* + 2\mu^*) \nabla.\mathbf{u}^* \right], \tag{2.2}$$

with p^* the pressure of the flow and μ^* and λ^* the first and the second coefficients of viscosity. (We can assume $3\lambda^* + 2\mu^* = 0$ by using the friction law of Newton.)

To convert the governing equations to a curved coordinate system it is necessary to work out the 'stretching functions' h_i associated with the differential operators. These can be calculated by studying how the distance PN varies as δx changes along the centreline of the curved flow. (See Figure (2.1).)

First we assume that the distance δx is sufficiently small such that the radius of curvature R does not change significantly ($R = \frac{1}{\kappa}$ where κ is the curvature of the centreline of the flow). We then work out $\delta x = R \times \delta\theta$ and $PN = (R+y)\delta\theta$ using standard geometry.

We substitute the first expression into the second one to get

$$PN = (R+y)\frac{\delta x}{R} = \left(\frac{1}{\kappa} + y\right)\frac{\delta x}{\frac{1}{\kappa}} = (1+\kappa y)\delta x.$$

Thus we get the required stretching function $h_1 = 1 + \kappa y$.

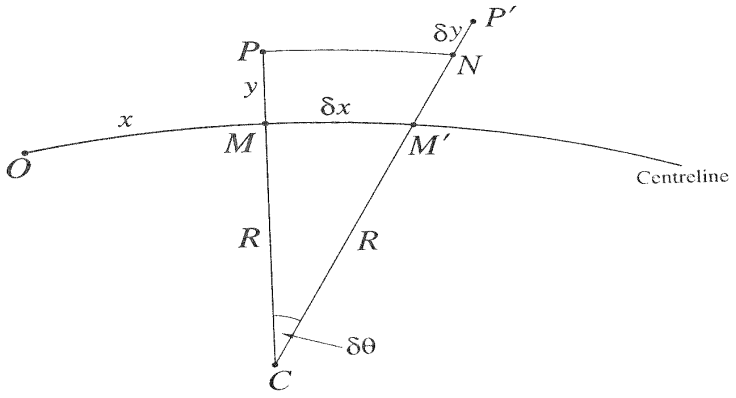

Figure 2.1: Curved coordinates.

Since there are little changes in the normal coordinate y and the spanwise coordinate z, we can take stretching functions h_2 and h_3 to be 1. We then use the formula of divergence of a vector field $\mathbf{F} = (f_1, f_2, f_3)$ in an orthogonal curvilinear coordinate system with length scales h_1, h_2 and h_3 in the direction of u_1, u_2 and u_3 respectively:

$$\nabla.\mathbf{F} = \frac{1}{h_1 h_2 h_3}\left(\frac{\partial}{\partial u_1}(h_2 h_3 f_1) + \frac{\partial}{\partial u_2}(h_1 h_3 f_2) + \frac{\partial}{\partial u_3}(h_1 h_2 f_3)\right). \tag{2.3}$$

We can now apply formula (2.3) on the continuity equation (2.1) to get the continuity equation for curved compressible flow:

$$\frac{\partial \rho}{\partial t^*} + \frac{1}{1+\kappa y^*}\left(\frac{\partial}{\partial x^*}(\rho^* u^*) + \kappa v^* \rho^* + (1+\kappa y^*)\frac{\partial}{\partial y^*}(\rho^* v^*)\right) + \frac{\partial}{\partial z^*}(\rho^* w^*) = 0. \tag{2.4}$$

To derive the Navier-Stokes equations for curved compressible flow, we will also need the formula of gradient and curl in orthogonal curvilinear coordinates:

$$\nabla f = \left(\frac{1}{h_1}\frac{\partial f}{\partial u_1}, \frac{1}{h_2}\frac{\partial f}{\partial u_2}, \frac{1}{h_3}\frac{\partial f}{\partial u_3} \right), \tag{2.5}$$

and

$$\nabla \wedge \mathbf{F} = \frac{1}{h_1 h_2 h_3} \begin{vmatrix} h_1\mathbf{e}_{u_1} & h_2\mathbf{e}_{u_2} & h_3\mathbf{e}_{u_3} \\ \dfrac{\partial}{\partial u_1} & \dfrac{\partial}{\partial u_2} & \dfrac{\partial}{\partial u_3} \\ h_1 f_1 & h_2 f_2 & h_3 f_3 \end{vmatrix}. \tag{2.6}$$

We can now apply formulas (2.5) and (2.6) on the Navier-Stokes equations to suit the curved compressible flow.

For the streamwise component x^*, we get:

$$\begin{aligned} \rho^* \left[\frac{\partial u^*}{\partial t^*} + \frac{u^*}{1+\kappa y^*}\frac{\partial u^*}{\partial x^*} + v^*\frac{\partial u^*}{\partial y^*} + \frac{\kappa u^* v^*}{1+\kappa y^*} + w^*\frac{\partial u^*}{\partial z^*} \right] = \\ -\frac{1}{1+\kappa y^*}\frac{\partial p^*}{\partial x^*} - \left[\frac{-\kappa\mu^*}{(1+\kappa y^*)^2}\frac{\partial v^*}{\partial x^*} + \frac{1}{1+\kappa y^*}\frac{\partial}{\partial y^*}\left(\mu^*\frac{\partial v^*}{\partial x^*}\right) \right. \\ -\frac{\partial}{\partial y^*}\left(\mu^*\frac{\partial u^*}{\partial y^*}\right) + \frac{\kappa^2\mu^* u^*}{(1+\kappa y^*)^2} - \frac{\kappa}{1+\kappa y^*}\frac{\partial}{\partial y^*}\left(\mu^* u^*\right) \\ \left. -\frac{\partial}{\partial z^*}\left(\mu^*\frac{\partial u^*}{\partial z^*}\right) + \frac{1}{1+\kappa y^*}\frac{\partial}{\partial z^*}\left(\mu^*\frac{\partial w^*}{\partial x^*}\right) \right] \\ +\frac{1}{1+\kappa y^*}\frac{\partial}{\partial x^*}\left[\frac{\lambda^*+2\mu^*}{1+\kappa y^*}\left(\frac{\partial u^*}{\partial x^*} + \kappa v^* + (1+\kappa y^*)\frac{\partial v^*}{\partial y^*} + (1+\kappa y^*)\frac{\partial w^*}{\partial z^*} \right) \right]. \end{aligned} \tag{2.7}$$

For the normal component y^*, we get:

$$\begin{aligned}
\rho^*\left[\frac{\partial v^*}{\partial t^*}+\frac{u^*}{1+\kappa y^*}\frac{\partial v^*}{\partial x^*}+v^*\frac{\partial v^*}{\partial y^*}-\frac{\kappa u^* u^*}{1+\kappa y^*}+w^*\frac{\partial v^*}{\partial z^*}\right]= \\
-\frac{\partial p^*}{\partial y^*}-\frac{1}{1+\kappa y^*}\left[\frac{-\kappa' y^*\mu^*}{(1+\kappa y^*)^2}\frac{\partial v^*}{\partial x^*}+\frac{1}{1+\kappa y^*}\frac{\partial}{\partial x^*}\left(\mu^*\frac{\partial v^*}{\partial x^*}\right)\right. \\
-\frac{\partial}{\partial x^*}\left(\mu^*\frac{\partial u^*}{\partial y^*}\right)-\frac{\kappa'\mu^* u^*}{1+\kappa y^*}+\frac{\kappa\kappa^* y^*\mu^* u^*}{(1+\kappa y^*)^2}-\frac{\kappa}{1+\kappa y^*}\frac{\partial}{\partial x^*}(\mu^* u^*) \\
\left.+(1+\kappa y^*)\frac{\partial}{\partial z^*}\left(\mu^*\frac{\partial v^*}{\partial z^*}\right)-(1+\kappa y^*)\frac{\partial}{\partial z^*}\left(\mu^*\frac{\partial w^*}{\partial y^*}\right)\right] \\
+\frac{\partial}{\partial y^*}\left[\frac{\lambda^*+2\mu^*}{1+\kappa y^*}\left(\frac{\partial u^*}{\partial x^*}+\kappa v^*+(1+\kappa y^*)\frac{\partial v^*}{\partial y^*}+(1+\kappa y^*)\frac{\partial w^*}{\partial z^*}\right)\right]. \qquad (2.8)
\end{aligned}$$

For the spanwise component z^*, we get:

$$\begin{aligned}
\rho^*\left[\frac{\partial w^*}{\partial t^*}+\frac{u^*}{1+\kappa y^*}\frac{\partial w^*}{\partial x^*}+v^*\frac{\partial w^*}{\partial y^*}+w^*\frac{\partial w^*}{\partial z^*}\right]=-\frac{\partial p^*}{\partial z^*} \\
-\frac{1}{1+\kappa y^*}\left[\frac{\kappa' y^*\mu^*}{(1+\kappa y^*)^2}\frac{\partial w^*}{\partial x^*}\frac{\partial}{\partial x^*}\left(\mu^*\frac{\partial u^*}{\partial z^*}\right)-\frac{\partial}{\partial x^*}\left(\mu^*\frac{\partial w^*}{\partial x^*}\right)\right. \\
-\kappa\mu^*\frac{\partial w^*}{\partial y^*}+\kappa\mu^*\frac{\partial v^*}{\partial z^*} \\
\left.-(1+\kappa y^*)\frac{\partial}{\partial y^*}\left(\mu^*\frac{\partial w^*}{\partial y^*}\right)+(1+\kappa y^*)\frac{\partial}{\partial y^*}\left(\mu^*\frac{\partial v^*}{\partial z^*}\right)\right] \\
-\frac{\partial}{\partial z^*}\left[\frac{\lambda^*+2\mu^*}{1+\kappa y^*}\left(\frac{\partial u^*}{\partial x^*}+\kappa v^*+(1+\kappa y^*)\frac{\partial v^*}{\partial y^*}+(1+\kappa y^*)\frac{\partial w^*}{\partial z^*}\right)\right]. \qquad (2.9)
\end{aligned}$$

We may set κ to zero on the right-hand side of equations (2.7)-(2.9), since the changes which were made by the effect of the curvature occur much more rapidly in the normal direction than in any other orthogonal direction. Therefore it can only be seen in the substantial derivatives (left-hand side of the equation). This assumption was provided by Stewartson (1964). A detailed mathematical argument for two-dimensional incompressible flow can be found in Lin (1945) and Goldstein (1953). Both of their works demonstrate that the only important curvature term in the substantial derivatives of equations (2.7)-(2.9) is the term

$$-\frac{\rho^*\kappa(u^*)^2}{1+\kappa y^*}$$

in the normal momentum equation (2.8) and the curvature factor is ignored in the continuity equation (2.4). By making use of this assumption, we may now rewrite the continuity and Navier-Stokes equations as:

$$\frac{\partial \rho}{\partial t^*} + \frac{\partial}{\partial x^*}(\rho^* u^*) + \frac{\partial}{\partial y^*}(\rho^* v^*) + \frac{\partial}{\partial z^*}(\rho^* w^*) = 0, \tag{2.10}$$

streamwise momentum equation:

$$\rho^* \frac{Du^*}{Dt^*} = -\frac{\partial p^*}{\partial x^*} + \frac{\partial}{\partial x^*}\left[2\mu^* \frac{\partial u^*}{\partial x^*} + \lambda^* \nabla . \mathbf{u}^*\right] + \frac{\partial}{\partial y^*}\left[\mu^* \frac{\partial u^*}{\partial y^*} + \mu^* \frac{\partial v^*}{\partial x^*}\right] + \frac{\partial}{\partial z^*}\left[\mu^* \frac{\partial w^*}{\partial x^*} + \mu^* \frac{\partial u^*}{\partial z^*}\right], \tag{2.11}$$

normal momentum equation:

$$\rho^* \left[\frac{Dv^*}{Dt^*} - \frac{\kappa (u^*)^2}{1 + \kappa y^*}\right] = -\frac{\partial p^*}{\partial y^*} + \frac{\partial}{\partial y^*}\left[2\mu^* \frac{\partial v^*}{\partial y^*} + \lambda^* \nabla . \mathbf{u}^*\right] + \frac{\partial}{\partial x^*}\left[\mu^* \frac{\partial v^*}{\partial x^*} + \mu^* \frac{\partial u^*}{\partial y^*}\right] + \frac{\partial}{\partial z^*}\left[\mu^* \frac{\partial w^*}{\partial y^*} + \mu^* \frac{\partial v^*}{\partial z^*}\right], \tag{2.12}$$

spanwise momentum equation:

$$\rho^* \frac{Dw^*}{Dt^*} = -\frac{\partial p^*}{\partial z^*} + \frac{\partial}{\partial z^*}\left[2\mu^* \frac{\partial w^*}{\partial x^*} + \lambda^* \nabla . \mathbf{u}^*\right] + \frac{\partial}{\partial y^*}\left[\mu^* \frac{\partial w^*}{\partial y^*} + \mu^* \frac{\partial v^*}{\partial z^*}\right] + \frac{\partial}{\partial x^*}\left[\mu^* \frac{\partial w^*}{\partial x^*} + \mu^* \frac{\partial u^*}{\partial z^*}\right]. \tag{2.13}$$

Equations (2.10)-(2.13) are the continuity and momentum equations for curved compressible flow. The governing equations are completed with the aid of the laws of thermodynamics. We now introduce the equation of state and the energy equation.

2.1.1 The equation of state and the energy equation

Classical thermodynamics considers general systems in equilibrium. A fluid particle in equilibrium possesses three properties describing its state: the temperature T^*, the thermodynamic pressure p^*, and the density ρ^*. These three quantities are functionally related by the equation of state for the fluid, i.e. $f(p^*, \rho^*, T^*) = 0$ for some function f.

It was Robert Boyle who first experimentally studied the relationship between pressure p^* and density ρ^* at fixed mass and temperature for a gas in the seventeenth century. His result showed that for an ideal gas:

$$\frac{p^*}{\rho^*} = \text{constant}.$$

(This relation is also known as Boyle's Law.)

In the eighteenth century, Jacques Charles investigated experimentally the relationship between pressure and temperature in a gas at fixed mass and volume. He concluded that for an ideal gas:

$$\frac{p^*}{T^*} = \text{constant}.$$

(This relation is known as Charles' Law.)

Combining both Boyle's and Charles' results, we get the equation of state for an ideal gas:

$$p^* = \Re \rho^* T^*,$$

where $\Re = R/m$, R is an absolute constant and m is the molecular weight of the ideal gas.

For the energy equation, the first law of thermodynamics states that the sources for the variation of the total energy are the work of the forces acting on the system plus the heat transmitted to the system. The energy conservation law states that the variation of the total energy is equal to the sum of the rate of increase of the kinetic energy and the rate of increase of the internal energy of the system. With simplification the energy equation for the system can be written as

$$\rho^* \frac{(Dc_p T^*)}{Dt^*} = \Phi + \frac{Dp^*}{Dt^*} + \nabla(k \nabla T^*), \tag{2.14}$$

where c_p is the specific heat at constant pressure which is practically constant for air, k is the thermal conductivity and Φ is the viscous dissipation function given by

$$\Phi = \rho_{ij} \frac{\partial u_j^*}{\partial x_i^*} + p^* \rho^* \frac{D}{Dt^*} \left(\frac{1}{\rho^*} \right).$$

Note that the viscous dissipation is always positive and hence any viscous flow is dissipative, i.e., entropy increases. A detailed simplification process of the energy equation can be found in Stewartson (1964).

2.2 Derivation of the mixing layer equations

The curved compressible mixing layer system which we are interested in is dynamically similar in scale and structure to the classical boundary-layer system. We therefore used the method developed for the classical system to progress further. The problem which we are interested in is concerned with the linear stability of the wake-dominated mixing-layer system, which is formed between two finite compressible streams that are travelling at different velocities and posses different temperatures. Within such a system, a thin splitter plate is inserted along the centreline of the layer which separates the two streams, so when the fluid leaves the trailing edge of the splitter plate, the laminar boundary layers from either side of the plate merge and are accelerated to form a thin wake. The upper stream is travelling at velocity $\beta_u U_{-\infty}$ ($0 < \beta_u < 1$), and has temperature $\beta_t T_{-\infty}$. The lower stream is travelling at velocity $U_{-\infty}$, and has temperature $T_{-\infty}$. The lower stream also has fixed density and kinematic viscosity, $\rho_{-\infty}$ and $\nu_{-\infty}$ respectively. The system is enclosed in a curved channel of width L. The mixing layer system which is currently demonstrated within Figure (2.2) has its centreline currently curved towards the lower, faster stream and has curvature

$$\kappa = \frac{\chi(\frac{x^*}{L})}{R},$$

with R the radius of the curvature of the channel and χ determines the direction of the curve. The Reynolds number of the system measures the inertial effects with the viscous effects of the flow and it is defined as usual by

$$Re = \frac{U_{-\infty} L}{\nu_{-\infty}},$$

where

$$\nu_{-\infty} = \frac{\mu_{-\infty}}{\rho_{-\infty}}$$

is the kinematic viscosity of the lower stream at $-\infty$. We are interested in the Görtler instability. The Görtler number, a parameter representing the level of centrifugal effects on the system, is defined as

$$G = 2\delta Re^{1/2},$$

where δ is a measure of the curvature of the flow given by $\delta = L/R$. δ is sufficiently small so that as $\delta \to 0$, and as the Reynolds number increases, the Görtler number remains fixed and is of order 1 (see Figure (2.2)).

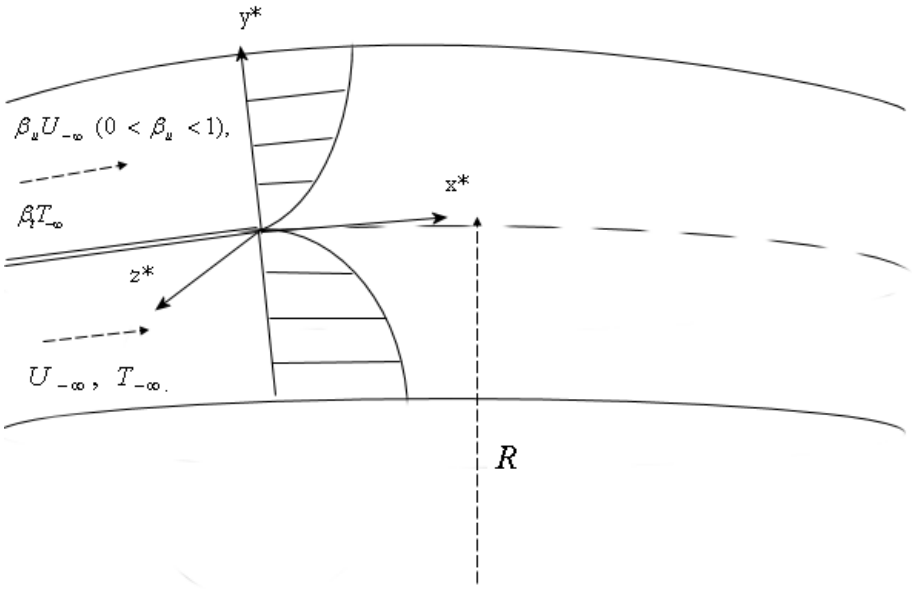

Figure 2.2: Schematic of the flow.

We will first separate the fluid system into basic flow terms and perturbation terms where the basic flow is considered to be steady and planar in the spanwise coordinate. Since the Görtler vortices are known to evolve predominantly in a spatial rather than a temporal sense, the perturbations are also considered to be steady.

2.2.1 Mixing layer scaling

The classical concept of a boundary layer is due to Prandtl (1904). Prandtl divided the flow past a body into two regions: a region far from the surface of the body, in which the effects of viscosity and thermal conductivity are negligible, and a region close to the surface where these effects are not negligible. Prandtl had taken the boundary layer thickness to be $Re^{-\frac{1}{2}}$ for his steady two-dimensional problem. It is known that the mixing layer is confined to a region of size $Re^{-\frac{1}{2}}$ about the centreline, we therefore scale the length scales and velocities in the normal direction by $Re^{-\frac{1}{2}}$. We have learned previously that the Görtler vortices have spanwise variations on the scale of the mixing layer, so we scale the length scales in the spanwise direction by $Re^{-\frac{1}{2}}$.

We first need to put all the equations which were deduced previously for this system into a non-dimensional form and this is done by expressing all variables in terms of L. The velocity and the state of the fluid must also be expressed at some standard place. Since we are only concerned with the mixing-layer system that is confined to a region of size $Re^{-\frac{1}{2}}$ about the centreline, $y^* = 0$, the viscous effect from the wall at $y^* = \pm L/2$ is not going to be considered. Within the mixing-layer system we have taken the standard place to be an infinite distance normal to the plate, $(-\infty)$.

With the previous scalings, we may now transform the dimensional variables to

$$(x^*, y^*, z^*) = L(X, Re^{-\frac{1}{2}}Y, Re^{-\frac{1}{2}}Z).$$

Since the flow is considered to be steady we may also neglect the derivatives with respect to t^*.

The basic flow velocities in a three-dimensional mixing layer are given by

$$\overline{\mathbf{u}} = U_{-\infty}[\overline{u}(X,Y,Z), Re^{-1/2}\overline{v}(X,Y,Z), Re^{-1/2}\overline{w}(X,Y,Z)][1+O(Re^{-1/2})].$$

Here X, Y and Z represent non-dimensional distance along, normal and spanwise to a centreline of variable curvature $\chi(X)/R$. Re is the Reynolds number based on the length L and the lower stream velocity $U_{-\infty}$.

The relative scales for the perturbation velocity components of a Görtler vortex can be written as

$$\mathbf{U} = U_{-\infty}[U(X,Y,Z), Re^{-1/2}V(X,Y,Z), Re^{-1/2}W(X,Y,Z)][1+O(Re^{-1/2})].$$

We may therefore perturb the basic flow velocities by writing

$$(u^*, v^*, w^*) = \overline{\mathbf{u}} + \mathbf{U} = U_{-\infty}[\overline{u}+U, Re^{-\frac{1}{2}}(\overline{v}+V), Re^{-\frac{1}{2}}(\overline{w}+W)].$$

We also perturb the basic density, viscosities, temperature and pressure by adding the vortex density, viscosities, temperature and pressure

$$\rho^* = \rho_{-\infty}(\overline{\rho}+\rho_1),$$

$$\mu^* = \mu_{-\infty}(\overline{\mu}+\mu_1),$$

$$\lambda^* = \mu_{-\infty}(\overline{\lambda}+\lambda_1),$$

$$T^* = T_{-\infty}(\overline{T}+T),$$

$$p^* = \rho_{-\infty}U_{\infty}^2(\overline{p}+P/Re),$$

respectively. Note the different scalings applicable for the basic flow pressure, $\overline{p}$, and the vortex pressure P, are to ensure they appear at the correct order within the associated equations.

2.2.2 Equations for the basic flow

To deduce the basic flow equations, the governing equations for the curved compressible flow system need to non-dimensionalised and this is done by substituting all the scalings into equations (2.10)-(2.13) and taking leading order of the transformed equations.

The leading order equation for the basic flow (unperturbed state) in the three-dimensional mixing layer can be obtained by setting vortex velocities U, V, W and vortex pressure, density, viscosities, P, ρ_1, μ_1, λ_1 to zero respectively.

Note that for our case of steady basic flow in the two dimensional mixing layer, the basic velocity profile becomes

$$\overline{\mathbf{u}} = U_{-\infty}[\overline{u}(X,Y), Re^{-1/2}\overline{v}(X,Y), 0][1 + O(Re^{-1/2})],$$

where we have the spanwise basic velocity $\overline{w} = 0$. Also since the flow is steady and two-dimensional, we ignore time derivatives $\frac{\partial}{\partial t}$ and Z derivatives $\frac{\partial}{\partial Z}$ in our basic flow equations by setting them to zero. Thus our basic flow equations are:

$$\frac{\partial}{\partial X}(\overline{\rho u}) + \frac{\partial}{\partial Y}(\overline{\rho v}) = 0, \tag{2.15}$$

$$\overline{\rho}\left(\overline{u}\frac{\partial \overline{u}}{\partial X} + \overline{v}\frac{\partial \overline{u}}{\partial Y}\right) = -\frac{\partial \overline{p}}{\partial X} + \frac{\partial}{\partial Y}\left(\overline{\mu}\frac{\partial \overline{u}}{\partial Y}\right), \tag{2.16}$$

$$\frac{\partial \overline{p}}{\partial Y} = 0. \tag{2.17}$$

It is not difficult to see that the basic pressure $\overline{p}$ is also independent of X. The reason being that the basic pressure $\overline{p}$ in the layer needs to match with the pressure in the external flow as $Y \to \pm\infty$. Since $\overline{p}$ is independent of both X and Y in the layer, we may therefore conclude that the basic pressure is constant within the layer.

The equation of state for an ideal gas can be written as

$$\overline{\rho}\overline{T} = 1.$$

We may deduce this equation by substituting the scalings of p^*, ρ^* and T^* into the equation of state

$$p^* = \Re \rho^* T^*.$$

Now we have

$$\rho_{-\infty} U_{-\infty}^2 \overline{p} = \Re \rho_{-\infty} \overline{\rho} T_{-\infty} \overline{T}.$$

Writing $\overline{\rho}$ and $\overline{T}$ in terms of the basic pressure $\overline{p}$, we obtain

$$\overline{p} = \frac{\Re T_{-\infty}}{U_{-\infty}^2} \overline{\rho T}. \tag{2.18}$$

Define the free stream Mach number of the lower stream, $M_{-\infty}$ by

$$M_{-\infty} = \frac{U_{-\infty} \sqrt{c_v}}{\sqrt{c_p \Re T_{-\infty}}} \tag{2.19}$$

where c_v, c_p and $\Re$ are the specific heats and gas constant. We then substitute equation (2.19) back into the basic pressure formula, (2.18), to get

$$\overline{p} = \frac{1}{\gamma M_{-\infty}^2} \overline{\rho T},$$

where $\gamma = \frac{c_p}{c_v}$ is defined to be the ratio of specific heats. The boundary condition has provided that

$$\overline{\rho}, \overline{T} \to 1 \quad \text{as} \quad Y \to -\infty.$$

Since the basic pressure $\overline{p}$ is constant within the layer, so we have

$$\overline{p} = \overline{p}_{-\infty} = \frac{1}{\gamma M_{-\infty}^2}.$$

By using the fact that $\overline{p}$ is constant, we may therefore conclude that

$$\overline{\rho T} = 1. \tag{2.20}$$

To non-dimensionalize the energy equation (2.14), for a steady basic flow in the two-dimensional mixing layer, we may take the Prandtl number, Γ, to be unity to simplify the analysis without changing the qualitative results. We also ignore the derivatives with

respect to t, $\frac{\partial}{\partial t}$, and the disturbance quantities in the equation. By using the fact that the basic pressure, $\overline{p}$, is constant within the layer, we now have the energy equation for the basic flow

$$\frac{1}{(\gamma-1)M_{-\infty}^2}\overline{\rho}\left[\overline{u}\frac{\partial\overline{T}}{\partial X}+\overline{v}\frac{\partial\overline{T}}{\partial Y}\right]=\overline{\mu}\left(\frac{\partial\overline{u}}{\partial Y}\right)^2+\frac{1}{(\gamma-1)M_{-\infty}^2}\frac{\partial}{\partial Y}\left(\overline{\mu}\frac{\partial\overline{T}}{\partial Y}\right). \tag{2.21}$$

Equations (2.15)-(2.20) and (2.21) are the governing equations for the two-dimensional basic flow in the curved compressible mixing-layer system. These equations were produced by using the same technique on the standard boundary layer problem. The solution to these equations can be found by using the relevant boundary conditions.

The first set of boundary conditions comes from matching the velocities far from the mixing region. We assume that the stream velocities are normalized on the lower stream velocity; hence the lower stream velocity is taken to be unity. The upper stream velocity is set to be

$$\beta_u=\frac{\text{upper stream velocity}}{\text{lower stream velocity}}.$$

So the required boundary conditions are

$$\overline{u}\to\beta_u \quad \text{as} \quad Y\to\infty, \tag{2.22}$$

and

$$\overline{u}\to 1 \quad \text{as} \quad Y\to-\infty. \tag{2.23}$$

The second set of boundary conditions come from matching the temperatures far from the mixing region. We also assume that the stream temperatures are normalised on the lower stream temperature. Therefore the boundary conditions on the basic temperature are

$$\overline{T}\to\beta_t \quad \text{as} \quad Y\to\infty, \tag{2.24}$$

and

$$\overline{T}\to 1 \quad \text{as} \quad Y\to-\infty. \tag{2.25}$$

However, conditions (2.22) and (2.23) on their own are insufficient for solving for the form of the basic streamwise velocity and a third boundary condition is needed. The detailed investigation of the third boundary condition for solving for the form of the basic streamwise veloctiy far downstream from the splitter plate edge will be presented in Chapter Three. In the mean time it is necessary to perform a coordinate transformation on the compressible mixing layer equations due to the complexity of these equations and their associated boundary conditions.

2.2.3 Transformation of the mixing layer equations

There are two types of transformations in general. The first type uses the stream function: ψ or one of its derivatives, such as the basic velocity, $\overline{u}$, as an independent variable. The second type uses similarity transformations. Two frequently used transformations of the first type are the von Mises transformation and the Crocco transformation.

The von Mises transformation (VM) was originally derived for incompressible boundary layers. It was subsequently extended to compressible flow by von Kármán (1938). The stream function ψ is used as an independent variable in the VM transformation. Von Kármán's reasons being the changes to the flow occur along a streamline and the use of the stream function automatically satisfies the continuity equation.

The Crocco transformation uses the viscous shearing stress as a dependent variable. This has the effect of reducing the order of the governing differential equations. In the Crocco transformation, the basic coordinate X and the basic velocity component $\overline{u}$ are also used as independent variables. The precise details of the VM and Crocco transformations are provided by Stewartson (1964).

In this project we will be frequently applying the Howarth-Dorodnitsyn (HD) transformation on the mixing layer equations. The HD transformation is a typical example of the second type of transformation. The purpose of this transformation is to remove the density $\overline{\rho}$ from the basic equations by introducing a new independent variable into

the equations. This is the most useful transformation on the compressible mixing layer equations since the equations are simplified to a form equivalent to the incompressible form.

To deduce the HD variable, we begin by introducing the compressible stream function defined by

$$\frac{\partial \psi}{\partial Y} = \overline{\rho u}, \tag{2.26}$$

and

$$\frac{\partial \psi}{\partial X} = -\overline{\rho v}. \tag{2.27}$$

The independent variable transformation is also introduced into the governing equations and boundary conditions for the mixing layer

$$\overline{Y} = \overline{Y}(X, Y), \tag{2.28}$$

subject to the condition

$$\frac{\partial \psi}{\partial \overline{Y}} = \overline{u}. \tag{2.29}$$

The particular functional form (2.28) chosen for the independent variable transformations are based on the equivalent forms for incompressible flow. The condition (2.29) is also based on the incompressible results. The transformation of an incompressible form is provided by Rogers (1992).

By combining (2.26) and (2.29), we see that

$$\frac{\partial \psi}{\partial Y} = \overline{\rho} \frac{\partial \psi}{\partial \overline{Y}}.$$

After rearranging the above equation, we end up with

$$\frac{\partial \overline{Y}}{\partial Y} = \overline{\rho}. \tag{2.30}$$

By integrating (2.30) with respect to $\overline{Y}$, we obtain the independent variable transformation for $\overline{Y}$

$$\overline{Y} = \int_0^Y \overline{\rho} dY. \tag{2.31}$$

By using the above definition, the transformation equations are

$$\frac{\partial}{\partial Y} = \frac{\partial}{\partial \overline{Y}}\frac{\partial \overline{Y}}{\partial Y} = \overline{\rho}\frac{\partial}{\partial \overline{Y}},$$

and

$$\frac{\partial}{\partial X} = \frac{\partial}{\partial X} + \frac{\partial}{\partial \overline{Y}}\frac{\partial \overline{Y}}{\partial X} = \int_0^Y \frac{\partial \overline{\rho}}{\partial X} dY \frac{\partial}{\partial \overline{Y}} + \frac{\partial}{\partial X}.$$

We are now ready to transform our mixing layer equations, but before we do this, we must first assume that the variation of viscosity in the fluid obeys the Chapman and Rubesin (1949) linear viscosity law

$$\overline{\mu} = C\overline{T},$$

where C is a constant of proportionality in the above equation. For simplicity, we may take C to be unity, so we have the relation

$$\overline{\mu} = \overline{T}. \tag{2.32}$$

Recall our basic streamwise momentum equation (2.16) with constant basic pressure $\overline{p}$

$$\overline{\rho}\left[\overline{u}\frac{\partial \overline{u}}{\partial X} + \overline{v}\frac{\partial \overline{u}}{\partial Y}\right] = \frac{\partial}{\partial Y}\left[\mu\frac{\partial \overline{u}}{\partial Y}\right]. \tag{2.33}$$

We may write $\overline{v}$ in the above equation in terms of the stream function defined in (2.27). Using the transformation function, we can now remove all the derivatives with respect to Y. The compressible stream function implies that the conservation of mass equation is automatically satisfied. The basic streamwise momentum equation is simplified to

$$\overline{u}\frac{\partial \overline{u}}{\partial X} - \frac{\partial \psi}{\partial X}\frac{\partial \overline{u}}{\partial \overline{Y}} = \frac{\partial^2 \overline{u}}{\partial \overline{Y}^2}, \tag{2.34}$$

which has the following boundary conditions

$$\overline{u} \to \beta_u \quad as \quad \overline{Y} \to \infty,$$

and

$$\overline{u} \to 1 \quad as \quad \overline{Y} \to -\infty.$$

By apply the HD transformation onto the basic energy equation, the basic temperature profile could be obtained from solving the simplified energy equation with the associated boundary conditions, and it is given as

$$\overline{T}(X,\overline{Y}) = 1 - \frac{1-\beta_t}{1-\beta_u}(1-\overline{u}(X,\overline{Y})) + \frac{1}{2}(\gamma-1)M_{-\infty}^2(1-\overline{u}(X,\overline{Y}))(\overline{u}(X,\overline{Y})-\beta_u). \quad (2.35)$$

The above temperature profile has boundary conditions

$$\overline{T}_{(\overline{Y}\to\infty)} = \beta_t, \quad \overline{T}_{(\overline{Y}\to-\infty)} = 1.$$

The transformed mixing-layer equations (2.34) and (2.35) will be required for obtaining the correct behaviour of the basic wake flow. One way to model the basic wake flow is to solve the mixing-layer equations for the increasing distance from the trailing edge of a splitter plate (i.e. the increase in X), based on the associated boundary conditions and the correct initial velocity profile. The technique for deriving the initial wake flow profile and the numerical model for the basic wake flow will be presented in Chapter Five.

2.3 Vortex Equations

Now we turn our attention to the equations governing the behaviour of the vortices (perturbations). The perturbations are considered to be steady, so by linearizing the perturbed mixing-layer equations and setting $\frac{\partial}{\partial t} = 0$ yields the following disturbance equations

$$\frac{\partial}{\partial X}(\overline{\rho}U + \rho_1\overline{u}) + \frac{\partial}{\partial Y}(\overline{\rho}V + \rho_1\overline{v}) + \overline{\rho}\frac{\partial W}{\partial Z} = 0, \quad (2.36)$$

$$\overline{\rho}\left(\overline{u}\frac{\partial U}{\partial X} + U\frac{\partial \overline{u}}{\partial X} + \overline{v}\frac{\partial U}{\partial Y} + V\frac{\partial \overline{u}}{\partial Y}\right) + \rho_1\left(\overline{u}\frac{\partial \overline{u}}{\partial X} + \overline{v}\frac{\partial \overline{u}}{\partial Y}\right) = \frac{\partial}{\partial Y}\left(\overline{\mu}\frac{\partial U}{\partial Y} + \mu_1\frac{\partial \overline{u}}{\partial Y}\right) + \overline{\mu}\frac{\partial^2 U}{\partial Z^2}, \quad (2.37)$$

$$\overline{\rho}\left(\overline{u}\frac{\partial V}{\partial X}+U\frac{\partial\overline{v}}{\partial X}+\overline{v}\frac{\partial V}{\partial Y}+V\frac{\partial\overline{v}}{\partial Y}-\chi G\overline{u}U\right)+\rho_1\left(\overline{u}\frac{\partial\overline{v}}{\partial X}\right.$$
$$\left.+\overline{v}\frac{\partial\overline{v}}{\partial Y}-\frac{\chi}{2}G\overline{u}^2\right)=-\frac{\partial P}{\partial Y}+\frac{\partial}{\partial Y}\left[2\overline{\mu}\frac{\partial V}{\partial Y}+2\mu_1\frac{\partial\overline{v}}{\partial Y}\right.$$
$$\left.+\overline{\lambda}\left(\frac{\partial U}{\partial X}+\frac{\partial V}{\partial Y}+\frac{\partial W}{\partial Z}\right)+\lambda_1\left(\frac{\partial\overline{u}}{\partial X}+\frac{\partial\overline{v}}{\partial Y}\right)\right]$$
$$+\frac{\partial}{\partial X}\left(\overline{\mu}\frac{\partial U}{\partial Y}+\mu_1\frac{\partial\overline{u}}{\partial Y}\right)+\overline{\mu}\frac{\partial^2 V}{\partial Z^2}+\overline{\mu}\frac{\partial^2 W}{\partial Z\partial Y},\tag{2.38}$$

$$\overline{\rho}\left(\overline{u}\frac{\partial W}{\partial X}+\overline{v}\frac{\partial W}{\partial Y}\right)=-\frac{\partial P}{\partial Z}+2\overline{\mu}\frac{\partial^2 W}{\partial Z^2}+\overline{\lambda}\frac{\partial}{\partial Z}\left(\frac{\partial U}{\partial X}+\frac{\partial V}{\partial Y}\right.$$
$$\left.+\frac{\partial W}{\partial Z}\right)+\frac{\partial}{\partial Z}\left[\lambda_1\left(\frac{\partial\overline{u}}{\partial X}+\frac{\partial\overline{v}}{\partial Y}\right)\right]+\frac{\partial}{\partial X}\left(\overline{\mu}\frac{\partial U}{\partial Z}\right)$$
$$+\frac{\partial}{\partial Y}\left(\overline{\mu}\frac{\partial W}{\partial Y}\right)+\frac{\partial}{\partial Y}\left(\overline{\mu}\frac{\partial V}{\partial Z}\right).\tag{2.39}$$

Recall our basic pressure formula

$$\overline{p}=\frac{1}{\gamma M_{-\infty}^2}\overline{\rho}\overline{T}.$$

After perturbing the above equation by substituting in the scalings provided in the previous section, we obtain

$$\overline{p}+\frac{P}{Re}=\frac{1}{\gamma M_{-\infty}^2}(\overline{\rho}+\rho_1)(\overline{T}+T).$$

By linearizing above equation, and making use of the basic equation of state, $\overline{\rho}\overline{T}=1$, and $\overline{p}=\frac{1}{\gamma M_{-\infty}^2}$, we are left with

$$\overline{\rho}T+\rho_1\overline{T}=0.$$

Now we may write ρ_1 as

$$\rho_1=-\frac{\overline{\rho}T}{\overline{T}}=-\frac{T}{\overline{T}^2}.$$

We now consider a normal mode analysis and assume that all the perturbations, U, V, W, P, ρ_1, μ, and λ, are proportional to $\triangle\exp(i\widehat{a}Z)$, where $\triangle$ is a vanishingly small parameter, and for a linear analysis, terms proportional to $\triangle^2$ are neglected.

We may write

$$[U,V,W]=\triangle\exp(i\widehat{a}Z)[\check{U},\check{V},\check{W}],$$

and

$$[P, T, \rho_1, \mu_1, \lambda_1] = \triangle \exp(i\widehat{a}Z)[\check{P}, \check{T}, \check{\rho}, \check{\mu}, \check{\lambda}].$$

Substitute these perturbations into equations (2.36)-(2.39), at $O(\triangle)$ we have the following disturbance equations,

from the equation of continuity,

$$\frac{\partial}{\partial X}\left(\frac{\check{U}}{\overline{\overline{T}}}\right) + \frac{\partial}{\partial Y}\left(\frac{\check{V}}{\overline{\overline{T}}}\right) + \frac{i\widehat{a}}{\overline{\overline{T}}}\check{W} - \frac{\partial}{\partial X}\left(\frac{\check{T}\overline{u}}{\overline{T}^2}\right) - \frac{\partial}{\partial Y}\left(\frac{\check{T}\overline{v}}{\overline{T}^2}\right) = 0, \tag{2.40}$$

the streamwise momentum equation,

$$\begin{aligned}\frac{\overline{u}}{\overline{\overline{T}}}\frac{\partial\check{U}}{\partial X} + \frac{\check{U}}{\overline{\overline{T}}}\frac{\partial\overline{u}}{\partial X} + \frac{\overline{v}}{\overline{\overline{T}}}\frac{\partial\check{U}}{\partial Y} + \frac{\check{V}}{\overline{\overline{T}}}\frac{\partial\overline{u}}{\partial Y} - \frac{\check{T}}{\overline{T}^2}\left(\overline{u}\frac{\partial\overline{u}}{\partial X} + \overline{v}\frac{\partial\overline{u}}{\partial Y}\right) = \\ \frac{\partial}{\partial Y}\left(\overline{\mu}\frac{\partial\check{U}}{\partial Y}\right) + \frac{\partial}{\partial Y}\left(\check{\mu}\frac{\partial\overline{u}}{\partial Y}\right) - \widehat{a}^2\overline{\mu}\check{U},\end{aligned} \tag{2.41}$$

the normal momentum equation,

$$\begin{aligned}\frac{\overline{u}}{\overline{\overline{T}}}\frac{\partial\check{V}}{\partial X} + \frac{\check{U}}{\overline{\overline{T}}}\frac{\partial\overline{v}}{\partial X} + \frac{\overline{v}}{\overline{\overline{T}}}\frac{\partial\check{V}}{\partial Y} + \frac{\check{V}}{\overline{\overline{T}}}\frac{\partial\overline{v}}{\partial Y} - \frac{\chi}{\overline{\overline{T}}}G\overline{u}\check{U} - \frac{\check{T}}{\overline{T}^2}\left(\overline{u}\frac{\partial\overline{v}}{\partial X}\right. \\ \left. + \overline{v}\frac{\partial\overline{v}}{\partial Y} - \frac{\chi}{2}G\overline{u}^2\right) = -\frac{\partial\check{P}}{\partial Y} + 2\frac{\partial}{\partial Y}\left(\overline{\mu}\frac{\partial\check{V}}{\partial Y}\right) + 2\frac{\partial}{\partial Y}\left(\check{\mu}\frac{\partial\overline{v}}{\partial Y}\right) \\ + \frac{\partial}{\partial Y}\left[\overline{\lambda}\left(\frac{\partial\check{U}}{\partial X} + \frac{\partial\check{V}}{\partial Y} + i\widehat{a}\check{W}\right)\right] + \frac{\partial}{\partial Y}\left[\check{\lambda}\left(\frac{\partial\overline{u}}{\partial X} + \frac{\partial\overline{v}}{\partial Y}\right)\right] + \frac{\partial}{\partial X}\left(\overline{\mu}\frac{\partial\check{U}}{\partial Y}\right) \\ + \frac{\partial}{\partial X}\left(\check{\mu}\frac{\partial\overline{u}}{\partial Y}\right) - \widehat{a}^2\overline{\lambda}\check{V} + i\widehat{a}\overline{\mu}\frac{\partial\check{W}}{\partial Y},\end{aligned} \tag{2.42}$$

the spanwise momentum equation

$$\begin{aligned}\frac{\overline{u}}{\overline{\overline{T}}}\frac{\partial\check{W}}{\partial X} + \frac{\overline{v}}{\overline{\overline{T}}}\frac{\partial\check{W}}{\partial Y} = -i\widehat{a}\check{P} - 2\widehat{a}^2\overline{\mu}\check{W} + i\widehat{a}\overline{\lambda}\left(\frac{\partial\check{U}}{\partial X} + \frac{\partial\check{V}}{\partial Y}\right) - \widehat{a}^2\overline{\lambda}\check{W} \\ + i\widehat{a}\check{\lambda}\left(\frac{\partial\overline{u}}{\partial X} + \frac{\partial\overline{v}}{\partial Y}\right) + i\widehat{a}\frac{\partial}{\partial X}(\overline{\mu}\check{U}) + \frac{\partial}{\partial Y}\left(\overline{\mu}\frac{\partial\check{W}}{\partial Y}\right) + i\widehat{a}\frac{\partial}{\partial Y}(\overline{\mu}\check{V}).\end{aligned} \tag{2.43}$$

For the perturbed energy equation, after linearizing and substituting in the scalings, we have

$$\frac{1}{(\gamma-1)M_{-\infty}^2}\left[\frac{\check{U}}{\overline{T}}\frac{\partial\overline{T}}{\partial X}+\frac{\overline{u}}{\overline{T}}\frac{\partial\check{T}}{\partial X}+\frac{\check{V}}{\overline{T}}\frac{\partial\overline{T}}{\partial Y}+\frac{\overline{v}}{\overline{T}}\frac{\partial\check{T}}{\partial Y}-\frac{\overline{u}\check{T}}{\overline{T}^2}\frac{\partial\overline{T}}{\partial X}\right.$$
$$\left.-\frac{\overline{v}\check{T}}{\overline{T}^2}\frac{\partial\overline{T}}{\partial Y}\right]=2\overline{u}\frac{\partial\overline{\mu}}{\partial Y}\frac{\partial\check{U}}{\partial Y}+\check{\mu}\left(\frac{\partial\overline{u}}{\partial Y}\right)^2+\frac{1}{(\gamma-1)M_{-\infty}^2}\left[\frac{\partial}{\partial Y}\left(\overline{\mu}\frac{\partial\check{T}}{\partial Y}\right.\right.$$
$$\left.\left.+\check{\mu}\frac{\partial\overline{T}}{\partial Y}\right)-\overline{\mu}\widehat{a}^2\check{T}\right]. \qquad (2.44)$$

Equations (2.40)-(2.44) are the vortex (disturbance) equations for our mixing layer problem. These vortex equations describe the vortex structure of the instability in the linear region where the size of the vortex is assumed to be sufficiently small to allow the non-linear terms in the governing equations to be neglected. The linear problem allows insights into the full non-linear system and also the initial growth of the type of centrifugal instability which we are investigating.

In the next subsection, we shall investigate the inviscid region which corresponds to the Görtler modes in the limit of large Görtler number with the wave number of O(1). The reason for such investigation is that as we progress downstream the local Görtler number increases and we wish to investigate modes with wave number commensurate with the boundary layer thickness.

2.3.1 The Inviscid modes

Previously we derived the vortex equation for our compressible two-dimensional mixing layer problem. Now we would like to investigate the limit of large Görtler number, G, with wave number, $\widehat{a} = O(1)$. Dando and Seddougui (1991) have conducted a similar investigation for a compressible flow over a curved boundary layer. To study the inviscid limit that arises when G is very large, by following Dando and Seddougui (1991), we shall first expand the disturbance quantities $\check{U}$, $\check{V}$, $\check{W}$, $\check{T}$ and $\check{P}$ in terms of a growth rate in the streamwise direction, $G^{1/2}\widehat{\beta}$.

The expansion of the disturbance quantities are

$$\check{U}(X,Y) = (\mathsf{U}(Y) + G^{-1/2}\mathsf{U}_1(Y) + O(G^{-1}))E_1,$$

$$\check{V}(X,Y) = G^{1/2}(\mathsf{V}(Y) + G^{-1/2}\mathsf{V}_1(Y) + O(G^{-1}))E_1,$$

$$\check{W}(X,Y) = G^{1/2}(\mathsf{W}(Y) + G^{-1/2}\mathsf{W}_1(Y) + O(G^{-1}))E_1,$$

$$\check{P}(X,Y) = G(\mathsf{P}(Y) + G^{-1/2}\mathsf{P}_1(Y) + O(G^{-1}))E_1,$$

and

$$\check{T}(X,Y) = (\mathsf{T}(Y) + G^{-1/2}\mathsf{T}_1(Y) + O(G^{-1}))E_1,$$

where

$$E_1 = \exp\left(\int^X G^{1/2}\left[\widehat{\beta}(X) + G^{-1/2}\widehat{\beta}_1(X) + ...\right]dX\right).$$

Substituting these quantities into the vortex equations (2.40)-(2.44), at leading order, we find

$$\frac{\widehat{\beta}}{\overline{T}}\mathsf{U} + \frac{\partial}{\partial Y}\left(\frac{\mathsf{V}}{\overline{T}}\right) + \frac{i\widehat{a}}{\overline{T}}\mathsf{W} - \frac{\widehat{\beta}\overline{u}}{\overline{T}^2}\mathsf{T} = 0, \tag{2.45}$$

$$\overline{u}\widehat{\beta}\mathsf{U} + \mathsf{V}\frac{\partial \overline{u}}{\partial Y} = 0, \tag{2.46}$$

$$\frac{1}{\overline{T}}\left(\overline{u}\widehat{\beta}\mathsf{V} - \chi\overline{u}\mathsf{U}\right) + \frac{\overline{u}^2\chi}{2\overline{T}^2}\mathsf{T} = -\frac{\partial \mathsf{P}}{\partial Y}, \tag{2.47}$$

$$\frac{\overline{u}\widehat{\beta}}{\overline{T}}\mathsf{W} = -i\widehat{a}\mathsf{P}, \tag{2.48}$$

and

$$\overline{u}\widehat{\beta}\mathsf{T} + \mathsf{V}\frac{\partial \overline{T}}{\partial Y} = 0. \tag{2.49}$$

Equations (2.45)-(2.49) are the disturbance equations for the inviscid limit. To derive a differential equation for the normal disturbance velocity, V, for the inviscid limit, the Howarth-Dorodnitsyn transformation is once again used to simplify the governing equations.

We also introduce a new variable, $\tilde{\chi}$, such that

$$\tilde{\chi} = sign(\chi). \tag{2.50}$$

After combining the resulting equations, we may obtain the required differential equation for V

$$\frac{\partial^2 \mathsf{V}}{\partial \overline{Y}^2} - \frac{\partial \mathsf{V}}{\partial \overline{Y}} \left(\frac{2\frac{\partial \overline{T}}{\partial \overline{Y}}}{\overline{T}} \right) + \mathsf{V} \left[-\widehat{a}^2 \overline{T}^2 - \frac{\frac{\partial^2 \overline{u}}{\partial \overline{Y}^2}}{\overline{u}} + 2\frac{\frac{\partial \overline{T}}{\partial \overline{Y}}}{\overline{T}} \frac{\frac{\partial \overline{u}}{\partial \overline{Y}}}{\overline{u}} - \frac{\tilde{\chi}|\chi|\widehat{a}^2}{\widehat{\beta}^2} \left(\overline{T} \frac{\frac{\partial \overline{u}}{\partial \overline{Y}}}{\overline{u}} - \frac{\frac{\partial \overline{T}}{\partial \overline{Y}}}{2} \right) \right] = 0, \tag{2.51}$$

We take $\tilde{\chi} = 1$ to represent a case where the centreline of the system curves towards the lower faster stream which is also referred to as the unstably curved case. $\tilde{\chi} = -1$ represents the case where the centreline of the system curves towards the slower upper stream which is referred to as the stably curved case. Equation (2.51) is an eigenvalue relation with the leading order normal disturbance velocity, V, as the eigenfunction, and $\frac{1}{\widehat{\beta}^2}$ as the associated eigenvalue.

For the disturbance to be confined within the mixing layer for the unstably curved mixing flow, equation (2.51) must satisfy the boundary conditions

$$| \mathsf{V} | \rightarrow 0 \quad \text{as} \quad \overline{Y} \rightarrow \pm\infty.$$

With the chosen basic wake flow profile known either numerically or analytically (with the temperature profile based on the choice of the basic wake flow profile), equation (2.51) can then be solved numerically subject to the boundary conditions

$$\mathsf{V} \sim e^{-\widehat{a}\beta_t \overline{Y}}, \quad \text{as} \quad \overline{Y} \rightarrow \infty,$$

and

$$\mathsf{V} \sim e^{\widehat{a}\overline{Y}}, \quad \text{as} \quad \overline{Y} \rightarrow -\infty.$$

2.4 High wave number analysis

It is well known that the maximum scaled growth rate is given by consideration of the large-wavenumber of the inviscid Görtler problem, see Denier et al. (1991) for boundary layers and Otto et al. (1996) for mixing layers. The location of layer was also previously determined by Owen et al. (1997) in the limit of large wave number. To study the far downstream behaviour of the system in the limit of large-wavenumber, we are going to use the analysis presented in Owen et al. (1997) which describes the solutions of the eigenfunction (2.51) for $\widehat{a} \gg 1$.

It is first assumed that the modes are localized at location, $\overline{Y}_b$, and the solution is then considered in a narrow layer at $\overline{Y}_b$. We introduce a new variable such that

$$\overline{Y} = \overline{Y}_b + \delta\xi,$$

with $\delta = \delta(\varepsilon)$ and we set $\widehat{a} = \varepsilon^{-1}$ and take the limit $\varepsilon \to 0$.

Owen et al. (1997) considered the viscous right-hand branch modes for the case of no wake and showed that

$$\varepsilon = G^{-1/4},$$

and

$$\delta = O(\sqrt{\varepsilon}) = O(\widehat{a}^{-1/2}),$$

in order for the two regions to match. Their method of investigation of the viscous right-hand branch modes is going to be considered for our wake system in the next section. In the meantime, it is necessary to make use of these results in our analysis. Therefore we write $\widehat{a}^{-1/2}$ instead of δ.

The quantities, V, $\widehat{\beta}$, $\overline{T}$ and f are expanded as

$$\mathrm{V} = V_0 + \widehat{a}^{-1/2}V_1 + \widehat{a}^{-1}V_2 + O(\widehat{a}^{-3/2}),$$

$$\widehat{\beta} = \widehat{\beta}_0 + \widehat{a}^{-1/2}\widehat{\beta}_1 + \widehat{a}^{-1}\widehat{\beta}_2 + O(\widehat{a}^{-3/2}),$$

$$\overline{T} = \overline{T} + \widehat{a}^{-1/2}\xi\frac{\partial\overline{T}}{\partial\overline{Y}} + \frac{1}{2}\widehat{a}^{-1}\xi^2\frac{\partial^2\overline{T}}{\partial\overline{Y}^2} + O(\widehat{a}^{-3/2}),$$

and

$$\overline{u} = \overline{u} + \widehat{a}^{-1/2}\xi\frac{\partial\overline{u}}{\partial\overline{Y}} + \frac{1}{2}\widehat{a}^{-1}\xi^2\frac{\partial^2\overline{u}}{\partial\overline{Y}^2} + O(\widehat{a}^{-3/2}),$$

where the basic flow quantities are evaluated at $(X, \overline{Y})$. The expansions of $\overline{T}$ and $\overline{u}$ were obtained by using Taylor series expansions on $\overline{T}$ and $\overline{u}$ about $\overline{Y}_b$ respectively.

For our inviscid problem, equation (2.51), we use the chain rule to change the derivatives, such that

$$\frac{\partial}{\partial\overline{Y}} = \frac{\partial\xi}{\partial\overline{Y}}\frac{\partial}{\partial\xi} = \widehat{a}^{1/2}\frac{\partial}{\partial\xi}.$$

We now substitute all the expansions into equation (2.51), and take the leading order of the equation to get

$$-V_0\overline{T}^2 + \frac{\tilde{\chi}|\chi|}{\widehat{\beta}_0^2\frac{\partial\overline{u}}{\partial\overline{Y}}}\overline{T}V_0 - \frac{1}{2\widehat{\beta}_0^2}\frac{\partial\overline{T}}{\partial\overline{Y}}V_0 = 0.$$

The above equation can be rearranged to give

$$\widehat{\beta}_0 = \left[\tilde{\chi}|\chi|\left(\frac{\frac{\partial\overline{T}}{\partial\overline{Y}}}{2\overline{T}^2} - \frac{\frac{\partial\overline{u}}{\partial\overline{Y}}}{\overline{T}\overline{u}}\right)\right]^{1/2}. \tag{2.52}$$

For $\tilde{\chi} = \pm 1$ we may obtain the leading-order behaviour of the grow rates which is defined completely in terms of the basic flow quantities which are evaluated at $(X, \overline{Y}_b)$, within the unstably and stably curved systems respectively.

Note that equation (2.52) can be rearranged to give

$$\frac{\widehat{\beta}_0^2}{|\chi|\tilde{\chi}} = \frac{\frac{\partial\overline{T}}{\partial\overline{Y}}}{2\overline{T}^2} - \frac{\frac{\partial\overline{u}}{\partial\overline{Y}}}{\overline{T}\overline{u}}. \tag{2.53}$$

It is noted by Sarkies and Otto (2000) that equation (2.53) can be written as the first term of the Taylor series of

$$-\frac{\overline{\rho}^{1/2}}{\overline{u}}\frac{\partial}{\partial\overline{Y}}\left[(\overline{\rho}(\overline{u})^2)^{1/2}\right],$$

about $(X, \overline{Y}_b)$. Thus we see that the condition for instability is given by Rayleigh's circulation criterion. According to this, the location of the modes could then be determined as

being the point at which the rate of change of circulation achieves an extremum. In order for Görtler modes to exist within both stably and unstably curved systems, $h = \widehat{\beta}_0^2(X, \overline{Y})$ must have two turning points with the positive maximum corresponding to the modes within the unstably curved system and the negative minimum corresponding to the stably curved system.

The alternative method for determining the location of the modes, $\overline{Y}_b$ for fixed distance from the trailing edge of the splitter plate, X, is to consider the next order of equation (2.51). At the next order we find that $\widehat{\beta}_1 = 0$ and this shows that as $\widehat{a} \to \infty$, the growth rate tends to a constant value, $\widehat{\beta}_0$, to second order. We also obtain

$$\overline{T}\frac{\partial^2\overline{T}}{\partial\overline{Y}^2}\overline{u}^2 - 2\overline{u}\frac{\partial^2\overline{u}}{\partial\overline{Y}^2}\overline{T}^2 + 2\overline{u}\frac{\partial\overline{u}}{\partial\overline{Y}}\overline{T}\frac{\partial\overline{T}}{\partial\overline{Y}} + 2\frac{\partial\overline{u}}{\partial\overline{Y}}^2\overline{T}^2 - 2\frac{\partial\overline{T}}{\partial\overline{Y}}^2\overline{u}^2 = 0, \tag{2.54}$$

in terms of the basic flow quantities which are evaluated at $(X, \overline{Y}_b)$. We may also use the above equation to determine the location of the mode, $\overline{Y}_b$.

At this stage, we are left with the form of the mode to determine, so we proceed to the third order. The third-order equation is found to be

$$\frac{\partial^2 V_0}{\partial\xi^2} + \left(\xi^2\left[-\left(\overline{T}\frac{\partial^2\overline{T}}{\partial\overline{Y}^2} + \frac{\partial\overline{T}}{\partial\overline{Y}}^2\right) - \frac{1}{2\widehat{\beta}_0^2\overline{u}}\left[\overline{T}\frac{\partial^3\overline{u}}{\partial\overline{Y}^3} + 2\frac{\partial\overline{T}}{\partial\overline{Y}}\frac{\partial^2\overline{u}}{\partial\overline{Y}^2} + \frac{\partial^2\overline{T}}{\partial\overline{Y}^2}\overline{u}\right]\right.\right.$$
$$\left.\left. + \frac{\frac{\partial\overline{u}}{\partial\overline{Y}}}{(\widehat{\beta}_0\overline{u})^2}\left[\frac{\partial\overline{T}}{\partial\overline{Y}}\frac{\partial\overline{u}}{\partial\overline{Y}} + \overline{T}\frac{\partial^2\overline{u}}{\partial\overline{Y}^2}\right] - \frac{\overline{T}\frac{\partial\overline{u}}{\partial\overline{Y}}}{\widehat{\beta}_0^2\overline{u}}\left[\left(\frac{\frac{\partial\overline{u}}{\partial\overline{Y}}}{\overline{u}}\right)^2 - \frac{\frac{\partial^2\overline{u}}{\partial\overline{Y}^2}}{2}\right] + \frac{\frac{\partial^3\overline{T}}{\partial\overline{Y}^3}}{4\widehat{\beta}_0^2}\right] - 2\overline{T}^2\frac{\widehat{\beta}_2}{\widehat{\beta}_0}\right)V_0 = 0. \tag{2.55}$$

Note that Owen et al. (1997) also went up to third order, but their equation was given in a slightly incorrect form.

By using the transformations

$$\overline{\xi} = \left(2Q(X, \overline{Y}_b)\right)^{1/4}\xi,$$

and

$$\lambda = \frac{2^{1/2}\overline{T}^2\widehat{\beta}_2}{\left(Q(X, \overline{Y}_b)\right)^{1/2}\widehat{\beta}_0}, \tag{2.56}$$

where Q_b is the second term of equation (2.55),

$$Q(X,\overline{Y}_b) = -\left(\overline{T}\frac{\partial^2\overline{T}}{\partial\overline{Y}^2} + \frac{\partial\overline{T}}{\partial\overline{Y}}^2\right) - \frac{1}{2\widehat{\beta}_0^2\overline{u}}\left[\overline{T}\frac{\partial^3\overline{u}}{\partial\overline{Y}^3} + 2\frac{\partial\overline{T}}{\partial\overline{Y}}\frac{\partial^2\overline{u}}{\partial\overline{Y}^2} + \frac{\partial^2\overline{T}}{\partial\overline{Y}^2}\overline{u}\right]$$
$$+\frac{\frac{\partial\overline{u}}{\partial\overline{Y}}}{(\widehat{\beta}_0\overline{u})^2}\left[\frac{\partial\overline{T}}{\partial\overline{Y}}\frac{\partial\overline{u}}{\partial\overline{Y}} + \overline{T}\frac{\partial^2\overline{u}}{\partial\overline{Y}^2}\right] - \frac{\overline{T}\frac{\partial\overline{u}}{\partial\overline{Y}}}{\widehat{\beta}_0^2\overline{u}}\left[\left(\frac{\frac{\partial\overline{u}}{\partial\overline{Y}}}{\overline{u}}\right)^2 - \frac{\frac{\partial^2\overline{u}}{\partial\overline{Y}^2}}{2}\right] + \frac{\frac{\partial^3\overline{T}}{\partial\overline{Y}^3}}{4\widehat{\beta}_0^2},$$

where the basic flow quantities are evaluated at $(X,\overline{Y}_b)$. We may solve equation (2.55) in terms of the parabolic cylinder function, $U(\lambda,\overline{\xi})$. The general form of the solution in terms of the parabolic cylinder function in the compressible case was derived by Dando and Seddougui (1991), and for this solution to tend to zero as $\xi \to \pm\infty$, λ must be given by

$$\lambda = -\frac{1}{2}, -\frac{3}{2}, -\frac{5}{2}, \cdots, -\frac{2n-1}{2},$$

where $-\frac{2n-1}{2}$ is the value of λ at the n-th mode.

With this information, we may determine the next-order correction to the growth rates of the invscid modes, $\widehat{\beta}_2$, by using equation (2.56). We could also use this to generate a formula for the growth rate for the n-th mode to second order,

$$\widehat{\beta}_n = \widehat{\beta}_0 - \frac{1}{\widehat{a}}\frac{(2n-1)Q(X,\overline{Y}_b)^{1/2}\widehat{\beta}_0}{2^{3/2}\overline{T}(X,\overline{Y}_b)^2}. \tag{2.57}$$

Equations (2.52), (2.54) and (2.57) provide the analytic solutions of the maximum growth rate, $\widehat{\beta}_0$, the location of the most unstable mode, $\overline{Y}_b$, and the growth rate for the nth inviscid mode, $\widehat{\beta}_n$, respectively in the limit of large wave number, $\widehat{a}$. Note that these solutions are defined completely in terms of the basic flow quantities, therefore the maximum growth rate, $\widehat{\beta}_0$, and the growth rate for the nth mode, $\widehat{\beta}_n$, can be easily determined once the location of the most unstable mode, $\overline{Y}_b$ is found by solving equation (2.54).

2.5 The right-hand branch

To investigate the behaviour of the viscous modes in the region of the right-hand branch we have considered the method in Hall (1982). It is known that within this region the Görtler number, G would become infinitely large and the wave number, $\widehat{a}$ is proportional to $G^{1/4}$ under the condition that $\chi \sim X^{1/2}$. It is also known that the mode will become localized within a layer of thickness $O(\widehat{a}^{-1/2})$ at some location across the mixing-layer. The method of asymptotic expansions was once again employed to derive the associated equations to search for the location of the modes and the scaled growth rate. For this we expand the Görtler number as

$$G = \widehat{a}^4(G_0 + \widehat{a}^{-1/2}G_1 + O(\widehat{a}^{-1})).$$

The modes are localized at location, Y_b, we consider a solution in a narrow layer at Y_b. We introduce a new variable such that

$$Y = Y_b + \widehat{a}^{-1/2}\varphi,$$

The expansion of the disturbance quantities are

$$\check{U}(X,Y) = (\check{U}_0(\varphi) + \widehat{a}^{-1/2}\check{U}_1(\varphi) + O(\widehat{a}^{-1}))E_2,$$

$$\check{V}(X,Y) = \widehat{a}^2(\check{V}_0(\varphi) + \widehat{a}^{-1/2}\check{V}_1(\varphi) + O(\widehat{a}^{-1}))E_2,$$

$$\check{W}(X,Y) = \widehat{a}^{3/2}(\check{W}_0(\varphi) + \widehat{a}^{-1/2}\check{W}_1(\varphi) + O(\widehat{a}^{-1}))E_2,$$

$$\check{P}(X,Y) = \widehat{a}^{5/2}(\check{P}_0(\varphi) + \widehat{a}^{-1/2}\check{P}_1(\varphi) + O(\widehat{a}^{-1}))E_2,$$

and

$$\check{T}(X,Y) = (\check{T}(\varphi) + \widehat{a}^{-1/2}\check{T}_1(\varphi) + O(\widehat{a}^{-1}))E_2,$$

where

$$E_2 = \exp\left(\widehat{a}^2 \int^X \left[\beta_{00} + \widehat{a}^{-1/2}\beta_{01} + O(\widehat{a}^{-1})\right] dX\right).$$

The basic flow quantities are expanded locally by using the Taylor series expansion as

$$\overline{u} = \overline{u}_0(X) + \widehat{a}^{-1/2}\varphi\overline{u}_1(X) + O(\widehat{a}^{-1}),$$

$$\overline{v} = \overline{v}_0(X) + \widehat{a}^{-1/2}\varphi\overline{v}_1(X) + O(\widehat{a}^{-1}),$$

$$\overline{T} = \overline{T}_0(X) + \widehat{a}^{-1/2}\varphi\overline{T}_1(X) + O(\widehat{a}^{-1}),$$

By substituting these expansion into the disturbance equations (2.40)-(2.44), and combining the streamwise, normal, and the energy equations, at leading order, we have

$$\overline{T}_0\left(\overline{u}_0\beta_{00} + \overline{T}_0^2\right)^2 - \frac{1}{2}\overline{T}_1\overline{u}_0^2 G_0\chi + \overline{T}_0\overline{u}_0\overline{u}_1 G_0\chi = 0, \tag{2.58}$$

and

$$\begin{aligned}\overline{T}_1\left(\overline{u}_0\beta_{00} + \overline{T}_0^2\right)^2 + 2\overline{T}_0\left(\overline{u}_0\beta_{00} + \overline{T}_0^2\right)\left(\overline{u}_1\beta_{00} + 2\overline{T}_0\overline{T}_1\right)\\ -\frac{1}{2}\overline{T}_2\overline{u}_0^2 G_0\chi + \overline{T}_0\overline{u}_1^2 G_0\chi + \overline{T}_0\overline{u}_0\overline{u}_2 G_0\chi = 0.\end{aligned} \tag{2.59}$$

The wave number within the right-hand branch is defined as λ_0, such that

$$\lambda_0 = G_0^{-1/4}.$$

After applying Howarth-Dorodnitsyn transformation to equations (2.58) and (2.59), and using equation (2.50), we now have

$$\overline{T}(\overline{u}\tilde{\beta} + \tilde{\lambda}^2\overline{T}^2)^2 - \frac{\partial\overline{T}}{\partial\overline{Y}}\overline{u}^2\tilde{\chi}/(2\overline{T}) + \overline{u}\frac{\partial\overline{u}}{\partial\overline{Y}}\tilde{\chi} = 0, \tag{2.60}$$

and

$$\begin{aligned}&\frac{\partial\overline{T}}{\partial\overline{Y}}(\overline{u}\tilde{\beta} + \tilde{\lambda}^2\overline{T}^2)^2 + 2\overline{T}(\overline{u}\tilde{\beta} + \tilde{\lambda}^2\overline{T}^2)(\frac{\partial\overline{u}}{\partial\overline{Y}}\tilde{\beta} + 2\tilde{\lambda}^2\overline{T}\frac{\partial\overline{T}}{\partial\overline{Y}})\\ &+\tilde{\chi}\left[-\frac{\frac{\partial^2\overline{T}}{\partial\overline{Y}^2}\overline{u}^2}{2\overline{T}} - \frac{\frac{\partial\overline{T}}{\partial\overline{Y}}\frac{\partial\overline{u}}{\partial\overline{Y}}\overline{u}}{\overline{T}} + \frac{\left(\frac{\partial\overline{T}}{\partial\overline{Y}}\right)^2\overline{u}^2}{2\overline{T}^2} + \left(\frac{\partial\overline{u}}{\partial\overline{Y}}\right)^2 + \overline{u}\frac{\partial^2\overline{u}}{\partial\overline{Y}^2}\right] = 0,\end{aligned} \tag{2.61}$$

where $\tilde{\beta}$ and $\tilde{\lambda}$ are the new scales of the leading-order growth rate and wave number, such that

$$\beta_{00} = \tilde{\beta}\sqrt{G_0}|\chi|^{1/2}, \quad \text{and} \quad \lambda_0 = \tilde{\lambda}|\chi|^{1/4}. \tag{2.62}$$

From solving equations (2.60) and (2.61), and taking $\tilde{\chi} = \pm 1$ for the unstably and stably curved systems separately, we may obtain the location of the modes, $\overline{Y}_v$, and the associated growth rate, $\tilde{\beta}$, with the increasing wave number, $\tilde{\lambda}$, respectively.

2.6 Chapter summary

We started our work by deriving the governing equations of fluid mechanics for a wake-dominated curved compressible mixing-layer system; the equations were then reformed in the relevant curved geometry. We proceeded to formulate the mixing layer problem and derived the basic flow equations for the compressible mixing flow system. Within the set up of the basic flow problem, we also discussed the necessity of the Howarth Dorodnitsyn transformation on the compressible basic flow equations and demonstrated the process of transforming these equations.

For investigating the behaviour of the inviscid Görtler modes with wave lengths comparable with the boundary-layer thickness with $G \gg 1$, an eigenvalue relation was derived which is in terms of the leading-order normal disturbance velocity, V, as the eigenfunction, and $\frac{1}{\tilde{\beta}^2}$ as the associated eigenvalue.

By using the the asymptotic analysis from Hall (1982), we have obtained formulas for analytically determining the maximum scaled growth rate and location of the modes in the limit of high-wavenumber of the inviscid problem, which would help us to gain some useful information pertaining to the ranges of basic flow parameter ratios for which these modes persist.

In order to characterize the overall stability of a flow it is necessary to describe the shape of the neutral curve as this determines when a mode will be unstable, therefore a right-hand branch formulation was conducted from which an asymptotic analysis was used to determine the location of the right-hand branch of the neutral curve, which would help us to increase the understanding of the stability of the situation.

Chapter 3

Linear development of Görtler instability far-down stream

This part of investigation is concerned with the behaviour of the Görtler modes within the system that is far-down stream from the trailing edge of the splitter plate. It is known that as we progress downstream of the wake-dominated system and get further away from the trailing edge of the splitter plate, the effect of wake will be reduced and eventually the system is going to lead a similar behaviour towards the plain curved compressible mixing-layer. The linear development of the Görtler instability within the the curved compressible mixing-layer system has been previously investigated by Owen et al. (1997). The behaviour of the modes within this type of system (without the wake) will be re-investigated and the predictions will be compared with the later results within the near-wake region.

Recall our basic flow equations (2.15)-(2.21) in the previous chapter

$$\frac{\partial}{\partial X}(\overline{\rho u}) + \frac{\partial}{\partial Y}(\overline{\rho v}) = 0, \tag{3.1}$$

$$\overline{\rho}\left[\overline{u}\frac{\partial \overline{u}}{\partial X} + \overline{v}\frac{\partial \overline{u}}{\partial Y}\right] = \frac{\partial}{\partial Y}\left[\mu\frac{\partial \overline{u}}{\partial Y}\right]. \tag{3.2}$$

$$\overline{\rho}\overline{T} = 1. \tag{3.3}$$

$$\frac{1}{(\gamma-1)M_{-\infty}^2}\overline{\rho}\left[\overline{u}\frac{\partial\overline{T}}{\partial X}+\overline{v}\frac{\partial\overline{T}}{\partial Y}\right]=\overline{\mu}\left(\frac{\partial\overline{u}}{\partial Y}\right)^2+\frac{1}{(\gamma-1)M_{-\infty}^2}\frac{\partial}{\partial Y}\left(\overline{\mu}\frac{\partial\overline{T}}{\partial Y}\right). \tag{3.4}$$

It is first assumed that the variation of viscosity in the fluid obeys the Chapman and Rubesin (1949) linear viscosity law

$$\overline{\mu}=C\overline{T},$$

where C is a constant of proportionality in the above equation. For simplicity, we may take C to be unity, so we have the relation

$$\overline{\mu}=\overline{T}. \tag{3.5}$$

For the far down stream behaviour of the basic streamwise and normal velocities, in addition to the Howarth-Dorodnitsyn transformation, we seek self-similar solutions and accordingly define the similarity variable

$$\eta=\frac{\overline{Y}}{\sqrt{X}}, \tag{3.6}$$

such that the spreading of the mixing layer is accounted for. The stream function is taken to be

$$\psi=\sqrt{X}f(\eta).$$

With the similarity variable transformation, the basic temperature profile can be obtained from solving the transformed basic energy equation and is given as

$$\overline{T}(\eta)=1-\frac{1-\beta_t}{1-\beta_u}(1-f')\frac{1}{2}(\gamma-1)M_{-\infty}^2(1-f')(f'-\beta_u), \tag{3.7}$$

with $'$ now denoting the derivative with respect to η.

The velocity components are now of the form

$$\overline{u}=f'(\eta), \tag{3.8}$$

and

$$\overline{v}=-\overline{T}\left[\frac{1}{2\sqrt{X}}(f-\eta f')+\frac{f'}{2\sqrt{X\overline{T}}}\int_0^\eta\overline{T}'\eta d\eta\right], \tag{3.9}$$

with f satisfying the equation

$$f''' + \frac{1}{2} f f'' = 0. \tag{3.10}$$

Thus the solution of the leading order basic momentum equations for the compressible variable property mixing layer for constant pressure is reduced to the solution of an equivalent incompressible constant property equation, i.e., the Blasius equation.

Equation (3.10) is solved in the region $(-\infty, \infty)$ and requires three boundary conditions. Two of the boundary conditions arises from prescribing the stremwise velocity at $\pm\infty$:

$$f'(\eta) \to \beta_u \quad as \quad \eta \to \infty, \tag{3.11}$$

and

$$f'(\eta) \to 1 \quad as \quad \eta \to -\infty. \tag{3.12}$$

In order to solve the governing equation to find a form for the basic flow. The third boundary condition distinguishes between some of the models for the flow.

3.1 Basic flow models

The first model for the basic flow problem is taken from Lock (1951). Lock had taken the normal velocity component, $\overline{v}$, to be zero at the centreline, which is situated at $Y = 0$. Hence by evaluating (3.9) at $\eta = 0$, we arrive at the third boundary condition

$$f(0) = 0. \tag{3.13}$$

We shall refer this condition as Lock's condition in this project.

Another basic flow model comes from Ting (1959). Ting proposed a different third boundary condition from Lock. The Ting condition was derived by matching the pressure terms of the governing basic flow equations at higher order across the mixing layer.

Ting investigated the cases of two incompressible streams, two supersonic streams and two subsonic streams and a supersonic/subsonic mixing layer. Ting's boundary conditions for the different flow situations are presented in the table below: $M_{-\infty}$ is the free stream

Stream type	Boundary condition
Both streams incompressible	$\overline{\rho}_\infty \overline{u}_\infty \overline{v}_\infty + \overline{\rho}_{-\infty} \overline{u}_{-\infty} \overline{v}_{-\infty} = 0.$
Both stream subsonic	$\frac{\overline{\rho}_\infty \overline{u}_\infty \overline{v}_\infty}{\sqrt{1-M_\infty^2}} + \frac{\overline{\rho}_{-\infty} \overline{u}_{-\infty} \overline{v}_{-\infty}}{\sqrt{1-M_{-\infty}^2}} = 0.$
Lower stream subsonic, upper stream supersonic	$\frac{\overline{\rho}_\infty \overline{u}_\infty \overline{v}_\infty}{\sqrt{M_\infty^2-1}} + \frac{\overline{\rho}_{-\infty} \overline{u}_{-\infty} \overline{v}_{-\infty}}{\sqrt{M_{-\infty}^2-1}} = 0.$
Both streams supersonic	$\overline{v}_{-\infty} = 0.$

Table 3.1: The third boundary condition proposed by Ting

Mach numbers of the lower stream, which was defined previously in this project. The free stream Mach number, M_∞ of the slower, upper stream is defined as

$$M_\infty = M_{-\infty} \frac{\beta_u}{\sqrt{\beta_t}}. \tag{3.14}$$

The formulation of the Mach numbers was provided in Criminale et al. (2003). We shall also mention the definition of the convective Mach number,

$$M_c = M_{-\infty} \frac{1-\beta_u}{1+\sqrt{\beta_t}},$$

which was initially defined by Bogdanoff (1983). As discussed in Criminale et al. (2003), the convective Mach number is considered to be a measure of the compressibility of the flow. Therefore if we fix the value of β_u and β_t, we can expect that the increase in the lower stream Mach number, $M_{-\infty}$ results to an increase in the compressibility of the flow.

To classify the different types of the flow we need to trace to the sonic Mach number. The sonic Mach number is defined to be $M = 1$. Whether the flow region is classified as subsonic or supersonic is depending on the variation between the upper or lower stream Mach number M_∞ or $M_{-\infty}$ and the critical Mach number $M_* = \frac{1+\sqrt{\beta_t}}{1-\beta_u}$. I.e. for the regime $M_\infty < M_* < M$, the upper stream is everywhere subsonic with no sonic lines or shocks, and for the region $M_\infty > 1$, with M_∞ not too close to 1 and not too large, the upper stream becomes almost everywhere supersonic. A detailed investigation on the flow regions can be found in Chapman (2000).

Another interesting interpretation of the convective Mach number is given in Jackson and Grosch (1991). They performed extensive spatial stability calculations for the compressible mixing layer and suggested a way to rigorously derive from linear stability theory a single convective Mach number for both a single species gas and a multi-species gas. In particular, the definition is based on the free-stream Mach number in the laboratory frame and is independent of the speed of the large scale structures and the speed of the most unstable wave. They defined the convective Mach number as

$$M_c = \frac{M_{-\infty}}{M_*} = M_{-\infty}\frac{1-\beta_u}{1+\sqrt{\beta_t}}.$$

As we can see from this definition that it is identical to the definition given by Bogdanoff (1983). Therefore with this scaling, we may conclude that subsonic modes exist for $M_c < 1$, and supersonic modes exist for $M_c > 1$.

With the third boundary condition provided by both Lock (1951) and Ting (1959) the basic flow problem now becomes a two-point boundary value problem which can be solved numerically using a shooting technique. The numerical scheme for solving for the Lock and Ting profile will be discussed in section (3.3).

Many studies of the instability of the mixing layer have used a particular simple profile as an approximation for the basic flow. This profile is known as the hyperbolic tangent profile. The formulae for the hyperbolic tangent profile is given as

$$\overline{u} = \frac{1}{2}(1+\beta_u) + \frac{1}{2}(\beta_u - 1)\tanh(\eta), \quad \text{and} \quad \overline{v} = 0. \tag{3.15}$$

With $\overline{T}$ evaluated from equation (3.7). In this way, the entire mixing layer is known analytically. For our convenience, we shall refer to the hyperbolic tangent profile as the Tanh profile from now on. The most obvious difference between the Tanh profile and the other two profiles is that the Tanh profile only describes the correct behaviour of the basic streamwise velocity and it does not offer a solution to the governing basic flow equations.

A comparison of the three basic velocity profiles for $\beta_u = 0.5$ is given in Figure (3.1). It can be observed from the figure that the Lock and Ting profiles are very similar.

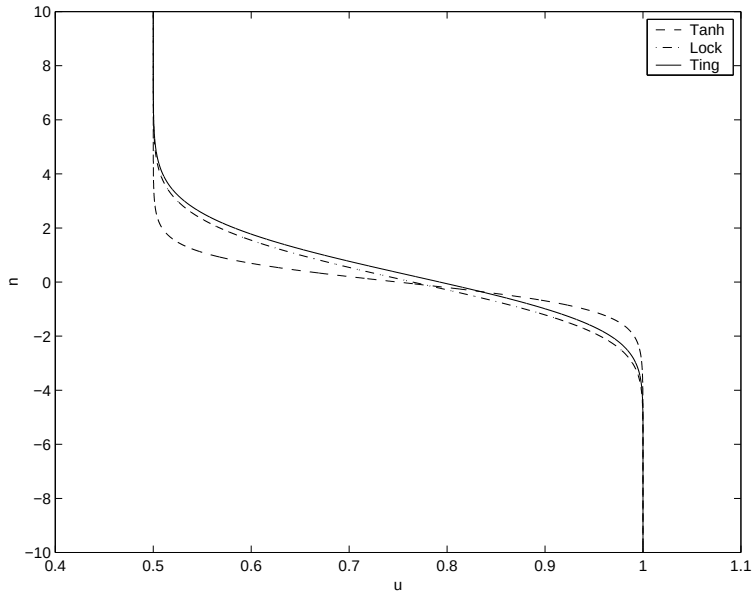

Figure 3.1: A comparison between the Tanh, Lock and Ting profiles for for $\overline{u}(\eta)$, for $\beta_u = 0.5$.

In comparison, the Ting condition comes from matching variable expansions across the mixing layer and represents a more physically accurate situation than the Lock condition : $f(0) = 0$. However, it is noted in Klemp and Acrivos (1972) that the Ting condition becomes invalid when the system is infinite in extent with subsonic stream velocities. Thus, for our analysis to hold we implicitly assume the system is bounded in at least one direction but sufficiently far away such that it has no effect on our region of interest. Previous investigations from Owen et al. (1997) showed that the most significant difference between the Lock and Ting profile is the prediction of the vortex position within the layer rather than its stability characteristics. A comparison of the predictions for the Görtler instability from the three basic velocity profiles will be presented in the following sections.

3.2 Inviscid modes within the unstably curved compressible mixing-layer system

Our aim is to investigate the variation of the scaled growth rate and the location of the Görtler mode by the change of the basic flow parameters and the basic flow profiles.

To derive the equation governing the behaviour of the inviscid modes in the case of a layer curving toward the lower faster stream (i.e. unstably curved case), we start by applying the similarity transformation onto the vortex equation for V, that is equation (2.51), in Section (2.3.1). The growth rate and wave number are scaled as

$$\widehat{\beta} = \frac{|\chi|^{1/2}\beta}{X^{1/4}}, \quad \text{and} \quad \widehat{a} = \frac{a}{X^{1/2}}. \tag{3.16}$$

The reason for these new scalings above is to eliminate χ and X from the equation. The resulting equation governing the behaviour of the inviscid modes is found to be

$$\frac{d^2\mathsf{V}}{d\eta^2} - \frac{d\mathsf{V}}{d\eta}\left(\frac{2\frac{d\overline{T}}{d\eta}}{\overline{T}}\right) + \mathsf{V}\left[-a^2\overline{T}^2 - \frac{\frac{d^3f}{d\eta^3}}{\frac{df}{d\eta}} + \frac{2\frac{d\overline{T}}{d\eta}}{\overline{T}}\frac{\frac{d^2f}{d\eta^2}}{\frac{df}{d\eta}} - \frac{\tilde{\chi}a^2}{\beta^2}\left(\overline{T}\frac{\frac{d^2f}{d\eta^2}}{\frac{df}{d\eta}} - \frac{\frac{d\overline{T}}{d\eta}}{2}\right)\right] = 0, \tag{3.17}$$

with boundary conditions given as

$$\mathsf{V} \sim e^{-a\beta_t\eta}, \quad \text{as} \quad \eta \to \infty, \tag{3.18}$$

and

$$\mathsf{V} \sim e^{a\eta}, \quad \text{as} \quad \eta \to -\infty. \tag{3.19}$$

For the unstably curved system, we take $\tilde{\chi} = 1$.

We are now going to review some of the results from Owen et al. (1997) and extend their investigation by including the prediction of the inviscid Görtler modes based on the Tanh profile, for later comparison with our wake models.

First, we would like to investigate the variation of scaled growth rate, β with scaled wave number, a, based on the chosen profiles. We demonstrate in Figure (3.2) the plots of the spatial growth rate for the first four modes against the wave number for the Tanh,

Lock and Ting velocity profile for a lower free-stream Mach number of 0.2. The relative upper stream velocity and temperature are fixed to be $\beta_u = 0.5$ and $\beta_t = 0.75$.

The growth rate that corresponds to each of the four unstable modes with the increasing wave number were obtained numerically by solving equation (3.17) subject to boundary conditions (3.18) and (3.19), for an increase in a. The numerical techniques that were used to solve the eigenvalue relation will be discussed in the next section.

Within Figure (3.2), the dashed line and the dotted lines are used to represent the asymptotic prediction for the maximum growth rate, β_0, and for the growth rate in terms of the wave number for the first four modes respectively. Note that the asymptotic predictions have used the analytic results from the high wave number analysis which will be discussed in the next section, and they represent the system's general behaviour for larger wave number, a. It is also expected that the numerical results would agree with the analytic results.

Results from Figure (3.2) indicate that for large wave number, a, the scaled growth rate β tends to a constant value, β_0, which is the predicted maximum growth rate. In general, the predictions from both the Lock and the Ting profile are in good agreement. Both profiles predicted that the maximum scaled growth rate β_0 to be 0.3938, which also agrees with the result from Owen et al. (1997). However, the Tanh profile predicted a set of higher scaled growth rates which corresponds to the first four modes, and a maximum scaled growth rate, $\beta_0 = 0.567$.

For the same compressible case with fixed basic flow parameters, plotted in Figure (3.3) are the variation of the eigenfunction, V, for the first inviscid mode with increasing wave number based on different basic flow profiles. In order to compare the predictions, we have normalised the leading order disturbance velocity, V. All three plots show that as the wave number, a, increases, the structure shrinks to a thin layer and the modes become increasingly localized within a certain region. The location of the mode, η_b, was determined using the asymptotic method from the high wave number analysis. For the

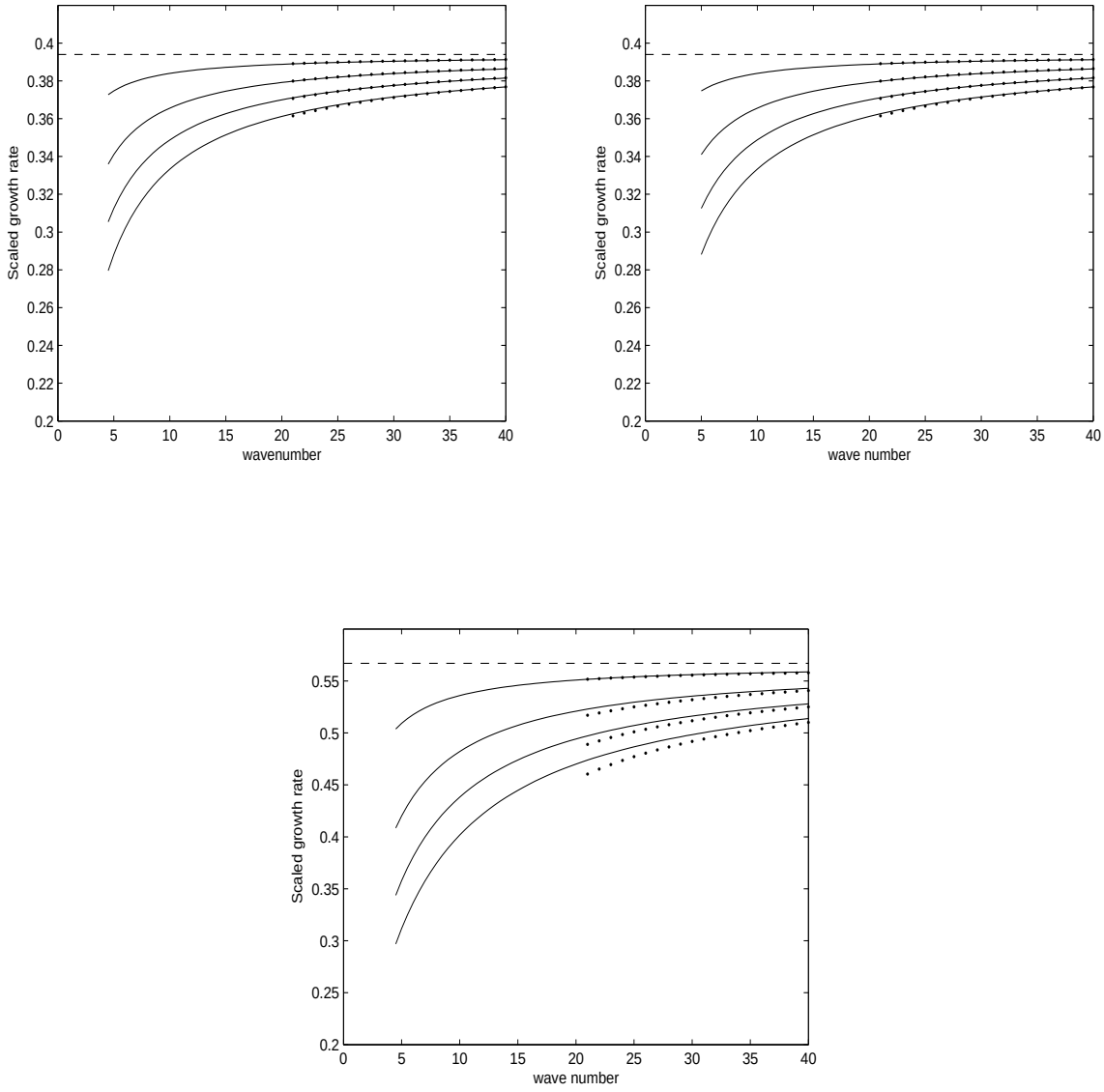

Figure 3.2: The variation of scaled growth rate, β, with scaled wave number, a, for the Lock (top left), Ting (top right) and Tanh profile with $\beta_u = 0.5$, $\beta_t = 0.75$ and $M_{-\infty} = 0.2$. The upper curve represents the first mode. Numerical solution: solid line. Asymptotic solution: dotted line.

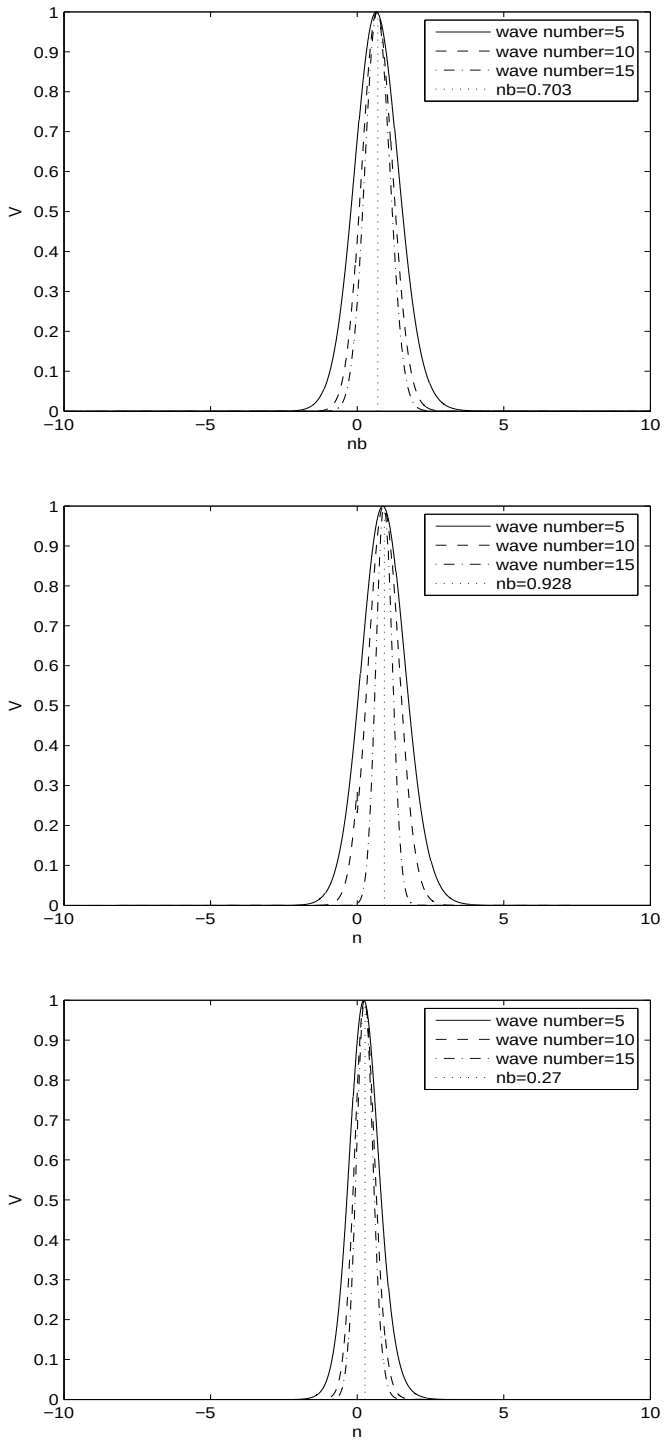

Figure 3.3: The variation of the first inviscid mode, $\mathsf{V}(\eta)$, for $a = 5, 10, 15$ with $\beta_u = 0.5$, $\beta_t = 0.75$ and $M_{-\infty} = 0.2$ for the Lock (top), Ting (middle) and Tanh (bottom) profile.

Lock profile, the location of the most unstable mode is found to be at $\eta = 0.703$. A higher location of the most unstable mode, $\eta = 0.928$, is predicted by the Ting profile, which is in good agreement with the investigation of Owen et al. (1997). For the Tanh profile, the location of the most unstable mode is predicted to be $\eta = 0.27$, which is more towards the centreline of the mixing-layer system.

The overall differences in the results predicted by the Tanh, Lock and Ting profile suggest that the analysis on the compressible flow can be very sensitive to the basic flow approximation. It is important to choose a basic flow profile that is able to accurately predict the correct behaviour of the Görtler modes. Since for large growth rate and with location of the mode near to the centreline of the layer, the disturbance can be more beneficial towards the mixing between the fluids.

3.3 Numerical methods and solutions

In this section the numerical techniques for solving the Lock profile, the Ting profile and the eigenvalue problem (2.51) will be discussed and presented.

We will start by solving for the basic flow problem (3.10) that is associated with boundary conditions (3.11) and (3.12) and using the third boundary condition proposed by Lock (1951), which is equation (3.13). For our basic flow problem using the Lock profile, we have a third order system

$$f'''(\eta) + \frac{1}{2} f(\eta) f''(\eta) = 0,$$

with boundary conditions

$$f(0) = 0,$$

$$f'(\eta) \longrightarrow \beta_u \quad \text{as} \quad \eta \longrightarrow \infty,$$

and

$$f'(\eta) \longrightarrow 1 \quad \text{as} \quad \eta \longrightarrow -\infty.$$

Our problem involves finding the solutions of simultaneous equations of the form

$$l(a,b) = f'(\infty) - \beta_u = 0,$$

and

$$g(a,b) = f'(-\infty) - 1 = 0,$$

where $a = f'(0)$ and $b = f''(0)$. The solution to the above problem can be found by using a particular type of method which is known as the shooting technique. To integrate the system from 0 to $\pm\infty$ a fourth-order Runge-Kutta method is used. The same scheme is also used to solve for the Ting profile and the eigenvalue problem (2.51). The more detailed illustration of the shooting technique is provided next.

3.3.1 The shooting method

The validity of the shooting method depends on the existence of the unique solution to the problem. Assuming a unique solution exists, the problem can be converted to a search for the missing initial conditions. When the conditions are obtained, the problem becomes a simpler initial value problem.

For the Lock profile, the missing initial conditions are a and b respectively. To search for the initial conditions, we have employed a two-dimensional Newton-Raphson method.

3.3.2 Two-dimensional Newton-Raphson method

We start by guessing a value of $f'(0)$ and $f''(0)$ say, a_0 and b_0, respectively. We now expand both functions $l(a,b)$ and $g(a,b)$ in a Taylor series about the point (a_0, b_0),

$$l(a,b) = l(a_0 + \triangle a, b_0 + \triangle b) = l(a_0, b_0) + \triangle a \frac{\partial l}{\partial a}\bigg|_{a_0,b_0} + \triangle b \frac{\partial l}{\partial b}\bigg|_{a_0,b_0} + ... = 0,$$

$$g(a,b) = g(a_0 + \triangle a, b_0 + \triangle b) = g(a_0, b_0) + \triangle a \frac{\partial g}{\partial a}\bigg|_{a_0,b_0} + \triangle b \frac{\partial g}{\partial b}\bigg|_{a_0,b_0} + ... = 0,$$

where $(\triangle a, \triangle b)$ are the step which is likely to take us towards the root.

The above equations can be expressed in matrix form,

$$\begin{pmatrix} \triangle a \\ \triangle b \end{pmatrix} = - \begin{pmatrix} \frac{\partial l}{\partial a} \mid_{a_0,b_0} & \frac{\partial l}{\partial b} \mid_{a_0,b_0} \\ \frac{\partial g}{\partial a} \mid_{a_0,b_0} & \frac{\partial g}{\partial b} \mid_{a_0,b_0} \end{pmatrix}^{-1} \begin{pmatrix} l(a_0, b_0) \\ g(a_0, b_0) \end{pmatrix},$$

where the partial derivatives can be approximated as

$$\left.\frac{\partial l}{\partial a}\right|_{a_0,b_0} \approx \frac{l(a_0 + \triangle a, b_0) - l(a_0, b_0)}{\triangle a},$$

and

$$\left.\frac{\partial l}{\partial b}\right|_{a_0,b_0} \approx \frac{l(a_0, b_0 + \triangle b) - l(a_0, b_0)}{\triangle b}.$$

We then iterate upon the step-sizes $(\triangle a, \triangle b)$, until we reach root a and b of our simultaneous equations. To match the boundary conditions for f' as $\eta \longrightarrow \pm\infty$, the equation needs to be integrated from 0 to $\pm\infty$ and this is performed using a fourth-order Runge-Kutta method.

3.3.3 Fourth-order Runge-Kutta method

The Runge-Kutta method is an extension of the basic idea of Euler's Method using approximations which agree with more terms of the Taylor series. The fourth-order scheme uses a four-stage formula:

$$\mathsf{F}_{n+1} = \mathsf{F}_n + \frac{1}{6}(K_1 + 2K_2 + 2K_3 + K_4),$$

where

$$\begin{aligned} K_1 &= \triangle\eta f(\eta_n, \mathsf{V}_n), \\ K_2 &= \triangle\eta f(\eta_n + \frac{\triangle\eta}{2}, \mathsf{V}_n + \frac{K_1}{2}), \\ K_3 &= \triangle\eta f(\eta_n + \frac{\triangle\eta}{2}, \mathsf{V}_n + \frac{K_2}{2}), \\ K_4 &= \triangle\eta f(\eta_n + \triangle\eta, \mathsf{V}_n + K_3). \end{aligned}$$

The derivation of these formulas is provided in Turner (1994).

The Runge-Kutta scheme is used for solving first order differential equations. For higher-order system such as our third order boundary value problem (3.10), we shall rewrite our equation as coupled first-order systems. This is done by introducing

$$f_1(\eta) = f(\eta), \quad f_2(\eta) = \frac{df}{d\eta}, \quad \text{and} \quad f_3(\eta) = \frac{d^2 f}{d\eta^2}.$$

Hence the basic flow equation can be written as

$$\frac{df_1}{d\eta} = f_2, \quad \frac{df_2}{d\eta} = f_3, \quad \text{and} \quad \frac{df_3}{d\eta} = -\frac{1}{2} f_1 f_3.$$

The solution to the eigenvalue problem (2.51) can also be obtained numerically using a combination of two-dimensional Newton-Raphson and fourth-order Runge-Kutta method. For the eigenvalue problem, there are infinite number of eigenvalues, $\frac{1}{\beta}$, exist for the eigenvalue relation (2.51). The eigenfunction, V, is the associated non-trivial solution for each of the eigenvalues. We refer the first eigenfunction (the one associated with the smallest eigenvalue,) as the first mode. The first mode corresponds to the largest scaled growth rate, β. Our aim is to find the eigenvalues, hence β, and the associated eigenfunctions, V, by numerically solving the eigenvalue relation (2.51), subject to the boundary conditions (3.18) and (3.19). Equation (2.51) has exponentially decaying boundary conditions as $\eta \longrightarrow \pm\infty$. We first assume that V and $\frac{d\mathsf{V}}{d\eta}$ are continuous at $\eta = 0$. By fixing $\mathsf{V} = 1$ and $\frac{d\mathsf{V}}{d\eta} = -a\beta_t$ at $+\infty$; and guessing V at $-\infty$, and β, the equation is then integrated from $\pm\infty$ to zero by using the standard fourth-order Runge-Kutta technique, and the results of V and $\frac{d\mathsf{V}}{d\eta}$ are matched at zero by using a two-dimensional Newton-Raphson technique, based on the condition that they are continuous at $\eta = 0$. The two unknowns are β and V at $-\infty$. The domain $\eta \in (-\infty, +\infty)$ is separated into two regions where

$$\eta_p \in [0, +\infty),$$

and

$$\eta_n \in (-\infty, 0].$$

Since we only need to check the boundary conditions for free stream velocities V at a suitably large positive and negative value of η instead of $\eta = \pm\infty$, we may represent the values of η at $\pm\infty$ by ± 10 respectively. We shall start from $\eta = -10$ with a guess for β and $\mathsf{V}_{-\infty}$, and take

$$\mathsf{V}_{\infty} = 1,$$

and

$$\frac{d\mathsf{V}_{\infty}}{d\eta} = -a\beta_t.$$

The reason for taking $\mathsf{V}_{\infty} = 1$ is to normalize the solution. Also by setting $\frac{d\mathsf{V}}{d\eta} = -a\beta_t$, V will satisfy the provided boundary conditions at $+\infty$ such that V will have the exponential decay. We shall integrate the equation from $\eta = \pm\infty$ to $\eta = 0$ using a backward and forward marching scheme respectively. Such schemes solve the system by using velocity information at two points $\eta = 10$, and $\eta = -10$, to calculate the velocity field at a point $\eta - \triangle\eta$ further down stream, and at $\eta + \triangle\eta$ further upper stream, respectively. The quantity $\triangle\eta$ is the step size. The process is repeated downstream and upstream effectively allowing the velocity field at any downstream and upstream point to be found. We then need to match our solutions for V and $\frac{d\mathsf{V}}{d\eta}$ at $\eta = 0$. The results are validated by choosing a different step size for $\triangle\eta$, and taking a larger value for η at $\pm\infty$ during the calculation process.

However, for the Ting profile, we need to guess all of the three initial conditions for equation (3.10) that are $f(0)$, $f'(0)$ and $f''(0)$, respectively, the equation is then integrated from zero to $\pm\infty$ to match the three boundary conditions which are equations (3.11), (3.12), and (3.1), respectively, thus a three-dimensional Newton-Raphson method combined with Runge-Kutta method is necessary for this procedure.

This shooting technique is different from the finite difference technique used in Owen et al. (1997). The finite difference technique starts by guessing a set of values at a sequence of intermediate mesh points that fit the boundary conditions and then iteratively improve the guess by using the differential equation. The shooting technique involves a

fourth-order Runge-Kutta method which has global truncation error, $O(\triangle\eta^4)$. This is equivalent to a fourth-order finite difference technique which is also accurate in $O(\triangle\eta^4)$. In comparison, the shooting technique is the easiest to understand and also has been broadly used for solving all sorts of nonlinear ordinary differential equations.

3.4 High-wavenumber limit solution within the unstably curved mixing-layer system

We are going to exploit the high-wavenumber limit of the inviscid problem by using the analysis from Hall (1982). Such analysis offers some very useful information pertaining to the ranges of free-stream temperature and velocity ratios for which the modes persist. To investigate the effect of varying the basic flow parameters on the general behaviour of the inviscid Görtler modes in the limit of high wave number, we must turn our attention onto the maximum scaled growth rate, β_0, and the location of the most unstable modes, η_b. These information could be obtained by performing the high wave number analysis on the curved mixing layer system which is similar to that demonstrated in Section (2.4), but based on the similarity variable, η, which was used here to simplify this system.

Therefore we consider solution in a narrow layer at η_b, which is where the modes are expected to be localized at. The basic flow quantities, $\overline{T}$ and f are expanded about η_b by using the conventional Taylor series expansion. The normal disturbance velocity, V, and the scaled growth rate of the system are expanded as

$$\mathrm{V} = V_0 + a^{-1/2}V_1 + a^{-1}V_2 + O(a^{-3/2}),$$

$$\beta = \beta_0 + a^{-1/2}\beta_1 + a^{-1}\beta_2 + O(a^{-3/2}),$$

respectively. By substituting the expansion into the associated eigenvalue relation, (3.17), at leading order we may obtain the equation for determining the maximum scaled growth

rate, β_0

$$\beta_0 = \left[\tilde{\chi}\left(\frac{\overline{T}_b'}{2\overline{T}_b^2} - \frac{f_b''}{\overline{T}_b f_b'}\right)\right]^{1/2}, \quad [\overline{T}_b = \overline{T}(\eta_b) \text{ etc.}], \tag{3.20}$$

where $'$ denotes the derivative with respect to η. We fix $\tilde{\chi} = 1$ for the unstably curved compressible mixing-layer system:

At the next order, we find that $\beta_1 = 0$ and the equation for determining the location of the most unstable modes, η_b, is

$$\overline{T}_b\overline{T}_b''f_b'^2 - 2f_b'f_b'''\overline{T}_b^2 + 2f_b'f_b''\overline{T}_b\overline{T}_b' + 2f_b''^2\overline{T}_b{}^2 - 2(\overline{T}_b')^2f_b'^2 = 0. \tag{3.21}$$

The alternative method for finding η_b, which was suggested by Sarkies and Otto (2000) is by searching for the location of the maximum of the leading-order eigenvalue equation, that is

$$h = \frac{1}{\overline{T}^2}\left(\frac{\overline{T}'}{2} - \frac{\overline{T}f''}{f'}\right). \tag{3.22}$$

The growth rate for the n-th mode to second order could be obtained from the following equation:

$$\beta_n = \beta_0 - \frac{1}{a}\frac{(2n-1)Q_b^{1/2}\beta_0}{2^{3/2}\overline{T}_b^2}, \tag{3.23}$$

with Q_b given as

$$\begin{aligned} Q_b = &-\left(\overline{T}_b\overline{T}_b{}'' + (\overline{T}_b')^2\right) - \frac{1}{2\beta_0^2 f_b'}\left[\overline{T}_b f_b'''' + 2\overline{T}_b' f_b''' + \overline{T}_b'' f_b'\right] \\ &+ \frac{f_b''}{(\beta_0 f_b')^2}\left[\overline{T}_b' f_b'' + \overline{T}_b f_b'''\right] - \frac{\overline{T}_b f_b''}{\beta_0^2 f_b'}\left[\left(\frac{f_b''}{f_b'}\right)^2 - \frac{f_b'''}{2}\right] + \frac{\overline{T}_b'''}{4\beta_0^2}. \end{aligned}$$

Plotted in Figures (3.4) and (3.5) are the effect of increasing relative upper stream speed, β_u, on the maximum scaled growth rate, β_0, and the location of the most unstable modes, η_b, respectively, predicted based on different basic velocity profiles. The rest of the basic flow parameters are fixed to be $\beta_t = 0.75$ and $M_{-\infty} = 0.2$.

It can be seen from Figure (3.4) that the maximum scaled growth rate decreases with an increase in β_u based on the predictions from all three profiles. Note that the increase in β_u also corresponds to the decrease in the disparity of the streams. We may also observe

that the predictions of the maximum scaled growth rates by the Lock and Ting profile are indistinguishable from one another. The only discrepancy being the Tanh results where a higher set of maximum scaled growth rates were predicted in comparison with the Ting and Lock results.

From observing Figure (3.5) on the variation of the location of the most unstable modes with increasing β_u, we see that all three profiles predict that the modes will move from above the centreline towards the lower, faster stream as β_u increases. A slightly higher location of the modes is predicted by the Ting profile in comparison with the Lock results. The lowest location of the modes is being predicted by the Tanh profile.

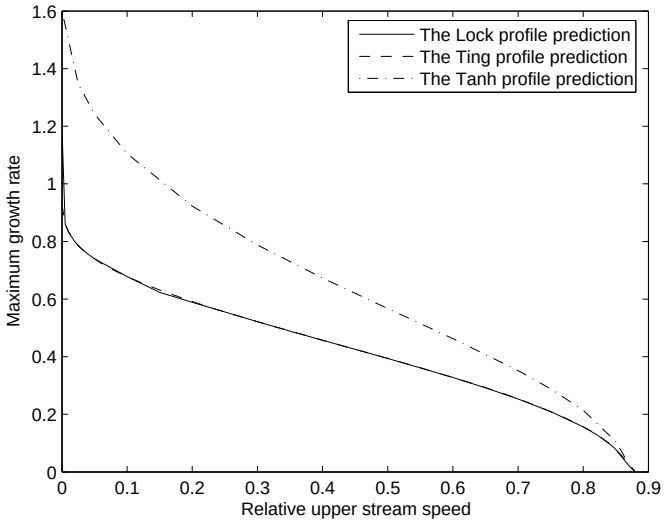

Figure 3.4: The variation of the maximum scaled growth rate, β_0, with the relative upper stream speed, β_u, with $\beta_t = 0.75$ and $M_{-\infty} = 0.2$ for the Lock, Ting and Tanh profile.

Demonstrated in Figures (3.6) and (3.7) is the effect of increasing the relative upper stream temperature, β_t, on the maximum scaled growth rate and the location of the most unstable mode, respectively, predicted using the different basic velocity profiles. The rest of the basic flow parameters are fixed to be $\beta_u = 0.5$ and $M_{-\infty} = 0.2$.

From observing Figure (3.6) we see a good agreement between the Lock and Ting

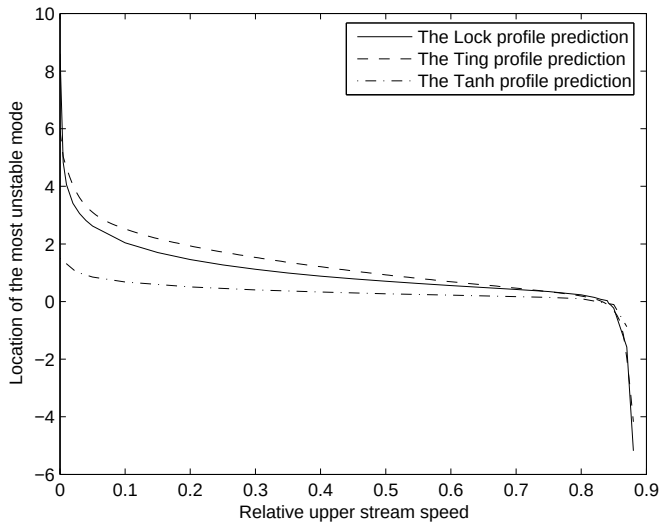

Figure 3.5: The variation of the most unstable mode, η_b, with the relative upper stream speed, β_u, with $\beta_t = 0.75$ and $M_{-\infty} = 0.2$ for the Lock, Ting and Tanh profile.

profile prediction for the maximum scaled growth rate, β_0. The Tanh profile once again predicts a higher set of the maximum scaled growth rate for increasing value of β_t in comparison with the Lock and Ting results. In general, all three profiles predicted an initial sharp increase of the maximum scaled growth rate for $\beta_t < 1$ when the upper stream is cooler than the lower faster stream. For the Lock and Ting results, as β_t continued to increase the maximum scaled growth rate tends to a constant value whereas for the Tanh results, a slight decrease in β_0 is predicted as β_t continues to increase from the value of 1.5.

From Figure (3.7), we see that for all three profiles, the location of the most unstable modes, η_b, initially resides in the faster lower stream, moves up into the slower upper stream as β_t increases to the value of 0.5, then moves back down towards the lower stream as β_t continues to increase. For larger values of β_t, the location predicted by the Lock, Ting and Tanh profile differs greatly, with the Lock profile predicting that the most unstable mode resides well into the lower stream.

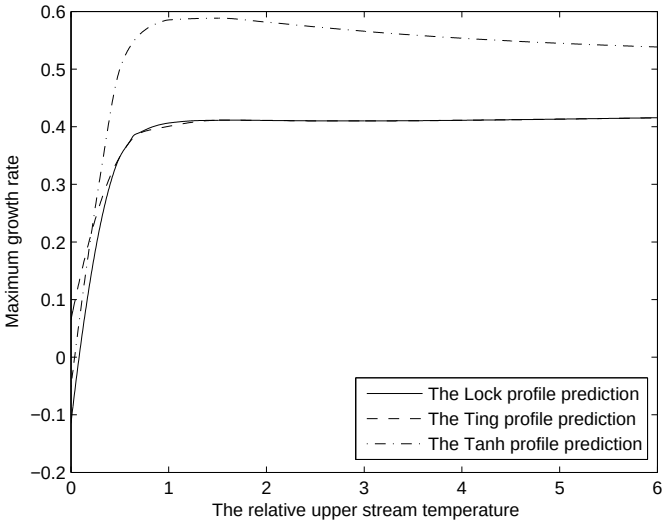

Figure 3.6: The variation of the maximum scaled growth rate, β_0, with the relative upper stream temperature, β_t, with $\beta_u = 0.5$ and $M_{-\infty} = 0.2$ for the Lock, Ting and Tanh profile.

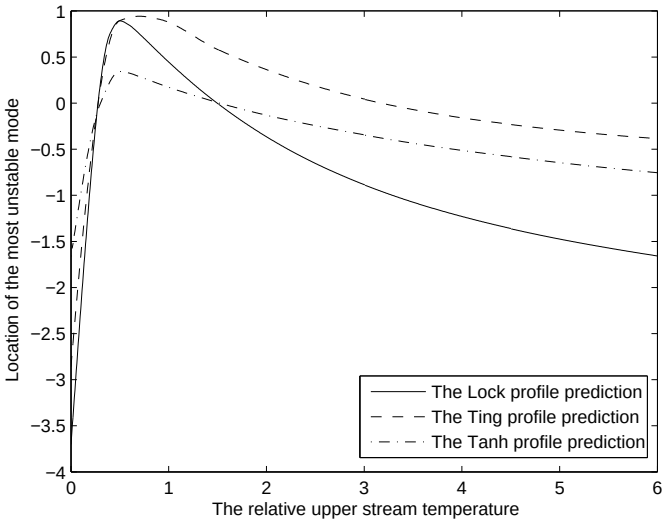

Figure 3.7: The variation of the most unstable mode, η_b, with the relative upper stream temperature, β_t, with $\beta_u = 0.5$ and $M_{-\infty} = 0.2$ for the Lock, Ting and Tanh profile.

To investigate the effect of compressibility on the general behaviour of the Görtler modes it is necessary to investigate the effect of varying the lower stream Mach number, $M_{-\infty}$, of the system. As we mentioned earlier, the compressibility for the mixing layer can be measured by a convective Mach number, M_c, which is in terms of the Mach number of the lower stream. Therefore, the effect of increasing the lower stream Mach number of the system is equivalent to the effect of increasing the compressibility of the system.

Plotted in Figures (3.8) and (3.9) are the effect of increasing lower stream Mach number, $M_{-\infty}$, on the maximum scaled growth rate, β_0 and the location of the most unstable modes, η_b, respectively, based on different basic velocity profiles. The rest of the basic flow parameters are fixed to be $\beta_t = 0.75$ and $\beta_u = 0.5$.

In Figure (3.8), we observe that for the Tanh profile, the maximum growth rate initially decreases for an increase in $M_{-\infty}$ and then tends to a roughly constant value after $M_{-\infty}$ exceeds 5. This behaviour of β_0 differs from the Lock and Ting results. Both Lock and Ting profiles predicted that as Mach number of the lower stream increases, the maximum of the growth rate will decrease for a range of $M_{-\infty}$, but will then increase as $M_{-\infty}$ increases. Once again the Lock result is indistinguishable from the Ting result.

From Figure (3.9), we see that for all three profiles, the location of the most unstable mode will move from above the centreline towards the lower stream as $M_{-\infty}$ increases. In the Ting results, there is a discontinuity for the variation of the location of the mode between $M_{-\infty} = 1$ and $M_{-\infty} = 2$. This is due to the switches in the boundary condition for $f(0)$, which was used in the Ting profile. Since as $M_{-\infty}$ exceeds unity, the lower stream is no longer subsonic but supersonic and as $M_{-\infty}$ approaches 2, the upper stream also becomes supersonic. This leads to a discontinuity in $f(0)$, hence the discontinuity for the variation of the location of the mode with $M_{-\infty}$. Once again the location predicted by the Lock, Ting and Tanh profiles differs from one another.

Previously we have shown that the growth rate, β would increase monotonically with increasing wave number, a, and eventually asymptotes to a finite value which is the

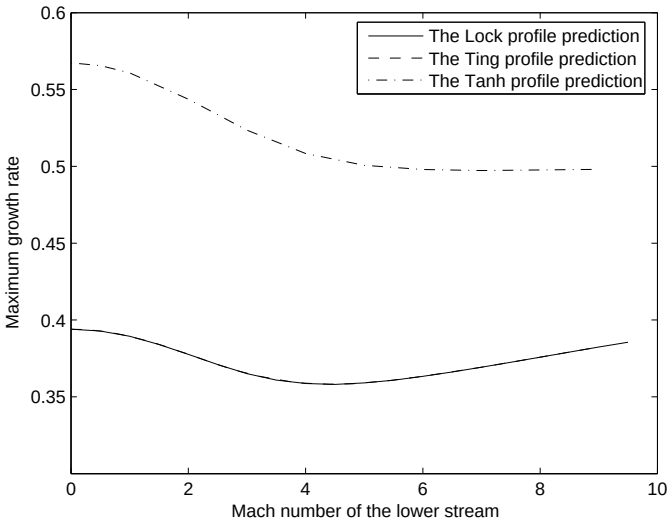

Figure 3.8: The variation of the maximum scaled growth rate, β_0, with the lower stream Mach number, $M_{-\infty}$, with $\beta_u = 0.5$ and $\beta_t = 0.75$ for the Lock, Ting and Tanh profile.

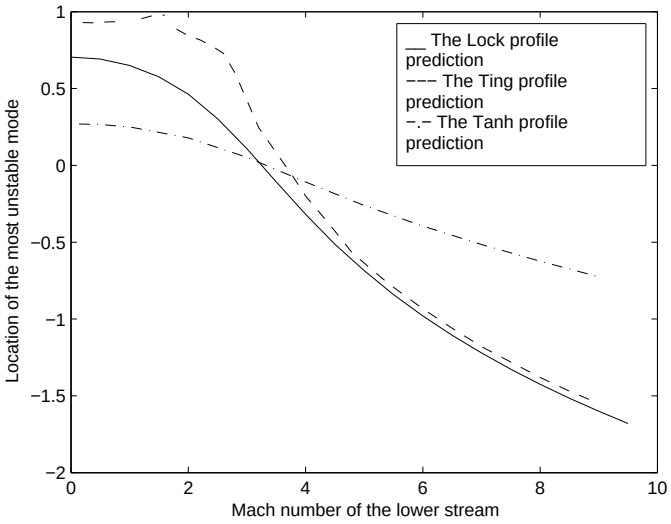

Figure 3.9: The variation of the most unstable mode, η_b, with the lower stream Mach number, $M_{-\infty}$, with $\beta_u = 0.5$ and $\beta_t = 0.75$ for the Lock, Ting and Tanh profile.

maximum scaled growth rate, β_0, Figure (3.2). However for the similar boundary-layer investigation (at which the underlying streamwise velocity is zero) the growth rate would tend to infinity with increasing a, Hall (1982). Within the boundary-layer problems the vortex wavelength is small in comparison with the boundary layer thickness and the vortex are driven to the proximity of the solid boundary and is therefore able to develop in a quasi-parallel manner. Hall (1982) then showed that it is possible to define a unique right-hand branch of the neutral curve which, at zeroth order, has the Görtler number proportional to the fourth power of the vortex wavenumber. The modes were found to be eventually stabilized by the viscosity effect for sufficiently high wavenumbers, Denier et al. (1991).

In the following section, we are going to turn our attention to the behaviour of the modes in the viscous right-hand branch for the mixing-layer system. The previous investigation of Owen et al. (1997) has shown that the modes would be stabilized by the viscosity effect within the system. It is also expected that the high-wavenumber limit of the inviscid modes and the low-wavenumber limit of the viscous modes would be matched directly as those did in Owen et al. (1997).

3.5 Predictions for the right-hand branch modes within the unstably curved mixing-layer system

For the viscous modes in the region of the right-hand branch of the unstably curved compressible mixing-layer system, the associated maximum scaled growth rate and the location of the most unstable mode within such system are going to be referred to as β_{00} and η_v respectively. It is known by Hall (1982) that within this region the Görtler number, G would become infinitely large and the wave number, λ_0 is proportional to a quarter of the power of G. For this we expand the Görtler number as

$$G = \widehat{a}^4(G_0 + \widehat{a}^{-1/2}G_1 + O(\widehat{a}^{-1})).$$

The derivation technique for β_{00} and η_v is similar to those demonstrated in Section (2.5), but based on the similarity variable, η, which now represents the distance across the curved mixing layer system.

We define the scale wave number for the right-hand branch as λ, such that

$$\lambda_0 = G_0^{-1/4}.$$

The wave number, λ_0, and the maximum scaled growth rate, β_{00}, are scaled as

$$\beta_{00} = \frac{\tilde{\beta}\sqrt{G_0}|\chi|^{1/2}}{X^{1/4}} \quad \text{and} \quad \lambda_0 = \frac{\tilde{\lambda}|\chi|^{1/4}}{X^{1/8}}, \tag{3.24}$$

where the different scalings to those from equation (2.62) is to eliminate X from the transformed governing equations.

By applying the similarity transformation ($\eta = \frac{\overline{Y}}{X^{1/2}}$) onto equations (2.58) and (2.59), introducing new scalings (3.24) and fixing $\tilde{\chi} = 1$ for the unstably curved system, we now have

$$\overline{T}\left(f'\tilde{\beta} + \tilde{\lambda}^2\overline{T}^2\right)^2 - \overline{T}'f'^2/(2\overline{T}) + f'f'' = 0, \tag{3.25}$$

and

$$\begin{aligned}\overline{T}'\left(f'\tilde{\beta} + \tilde{\lambda}^2\overline{T}^2\right)^2 + 2\overline{T}\left(f'\tilde{\beta} + \tilde{\lambda}^2\overline{T}^2\right)\left(f''\tilde{\beta} + 2\tilde{\lambda}^2\overline{T}\overline{T}'\right)\\ -\overline{T}''f'^2/(2\overline{T}) - \overline{T}'f'f''/\overline{T} + \overline{T}'^2f'^2/\left(2\overline{T}^2\right) + f''^2 + f'f''' = 0,\end{aligned} \tag{3.26}$$

where $'$ denotes the derivative with respect to η within the above equations. With the choice of basic flow profiles, we may obtain the variation of the location of the modes, η_v, and the maximum growth rate, $\tilde{\beta}$, with the scaled wave number, $\tilde{\lambda}$, respectively, within the unstably curved system from solving the above equations.

Demonstrated in Figure (3.10) is the variation of the scaled growth rate, $\tilde{\beta}$, with the scaled wave number, $\tilde{\lambda}$, based on the different basic velocity profiles within the right-hand viscous region of the unstably curved system. The basic flow parameters are fixed to be $\beta_u = 0.5$, $\beta_t = 0.75$ and $M_{-\infty} = 0.2$ respectively.

The numerical results based on the Lock and Ting profile are once again indistinguishable from one another. Note that as the wave number tends to zero from the viscous right-hand region, the mode is moving towards the inviscid region. Both Lock and Ting profiles predict that for zero wave number in the viscous region, the scaled growth rate is $\tilde{\beta} = 0.3938$, which matches directly on to the inviscid modes (see Figure (3.2)). For the Tanh profile, the scaled growth rate based on zero wave number is predicted to be $\tilde{\beta} = 0.567$, which also matches directly on to the inviscid modes. As the wave number increases all three profiles predicted that the growth rate would decrease to zero which shows that the mode is stabilized by the viscosity effect within the system.

Demonstrated in Figure (3.11) is the variation of the location of the mode, η_v, with the scaled wave number, $\tilde{\lambda}$, based on the different basic velocity profiles within the right-hand viscous region.

For zero wave number in the viscous region, the locations of the mode predicted by the Lock, Ting and Tanh profile are $\eta_v = 0.7027$, $\eta_v = 0.9281$ and $\eta_v = 0.2708$ respectively. These predictions once again match directly with those predicted for the inviscid modes (see Figure (3.3)). The results also indicate that all three profiles predicted that the modes would move towards the centreline for an increase in the wave number with a slight difference in the exact location of the mode.

3.6 Investigation of the thermal modes within the stably curved mixing-layer system

So far we have looked at the behaviour of Görtler modes within the unstably curved compressible mixing-layer system. For the stably curved compressible mixing-layer system, a theoretical investigation that was carried out by Owen et al. (1997) demonstrated that for certain parameter regimes, modes could occur within this case. These modes were labeled as the 'thermal modes' and have no counterpart within incompressible mixing

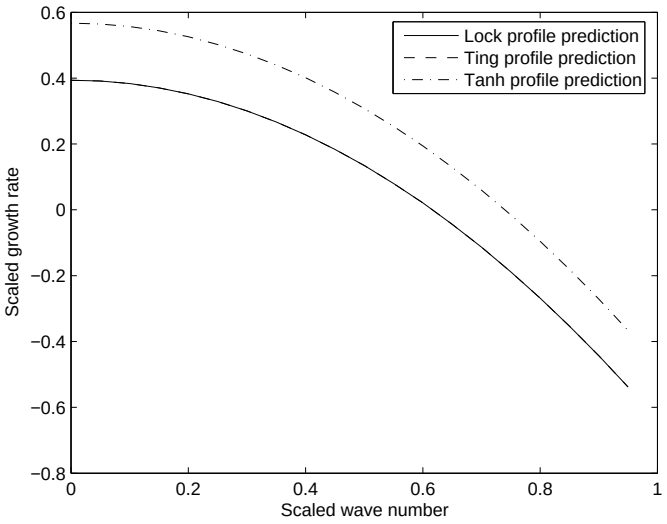

Figure 3.10: The variation of the scaled growth rate, $\tilde{\beta}$, with scaled wave number with fixed basic flow parameters $M_{-\infty} = 0.2$, $\beta_u = 0.5$ and $\beta_t = 0.75$ for the Lock, Ting and Tanh profile.

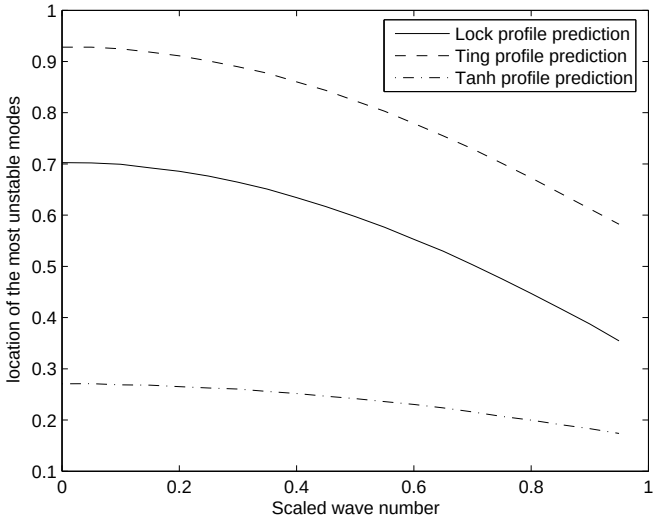

Figure 3.11: The variation of the most unstable mode, η_v, with scaled wave number with fixed basic flow parameters $M_{-\infty} = 0.2$, $\beta_u = 0.5$ and $\beta_t = 0.75$ for the Lock, Ting and Tanh profile.

layers. Recent work of Sarkies and Otto (2000) furthers the analysis of Owen et al. (1997) with regards to these thermal modes. They derived a simple condition which yields information about the parameter ranges for which thermal modes are likely to occur. In this chapter, we will follow the work of Owen et al. (1997) by demonstrating such behaviour.

To obtain the equation governing the behaviour of the inviscid modes in the case of a stably curved mixing layer, we simply reverse the sign of χ in equation (3.17). By fixing $\tilde{\chi} = -1$ for the stably curved system, the resulting equation governing the behaviour of the inviscid modes is found to be

$$\mathsf{V}''(\eta) - \mathsf{V}'(\eta)\left(\frac{2\overline{T}'(\eta)}{\overline{T}}\right) + \mathsf{V}\left[-a^2\overline{T}^2 - \frac{f'''(\eta)}{f'(\eta)} + \frac{2\overline{T}'(\eta)}{\overline{T}}\frac{f''(\eta)}{f'(\eta)}) + \frac{a^2}{\beta^2}\left(\overline{T}\frac{f''(\eta)}{f'(\eta)} - \frac{\overline{T}'(\eta)}{2}\right)\right] = 0. \tag{3.27}$$

Again by fixing $\tilde{\chi} = -1$ in equation (3.20), we may obtain the equation for the maximum scaled growth rate, β_0

$$\beta_0^2 = -\frac{1}{\overline{T}_b^2}\left(\frac{\overline{T}_b'}{2} - \frac{\overline{T}_b f_b''}{f_b'}\right), \tag{3.28}$$

within the stably curved system.

3.6.1 Condition for the thermal modes within the curved compressible mixing-layer system

In order for the flow to be prone to the thermal modes, Sarkies and Otto (2000) derived an upper limit for the relative upper stream temperature for which the thermal mode would exist. Sarkies and Otto (2000) had pointed out that for flow to be prone to both thermal and usual modes, $h = \beta_0^2(\eta_b)$ must have two turning points with the positive maximum corresponding to the usual modes and the negative minimum corresponding to the thermal modes. Since the function is zero at $\eta_0 = \pm\infty$, there must be a further zero if the function is to have two turning points.

By using this condition, we now have

$$h = \frac{1}{\overline{T}^2}\left[\frac{\overline{T}f''}{f'} - \frac{\overline{T}'}{2}\right] = 0.$$

After rearranging the above equation in terms of f', we obtain

$$f' = 2\frac{\overline{T}f''}{\overline{T}'}. \tag{3.29}$$

Now the basic streamwise velocity within the curved compressible mixing-layer system, f', is restricted to the boundary conditions, such that

$$f' \to \beta_u, \text{ as } \eta \to \infty,$$

and

$$f' \to 1, \text{ as } \eta \to -\infty.$$

Therefore we have

$$\beta_u < f'(\eta) < 1. \tag{3.30}$$

Recall our equation for the basic temperature profile:

$$\overline{T} = 1 - \frac{1-\beta_t}{1-\beta_u}(1-f')\frac{1}{2}(\gamma-1)M_{-\infty}^2(1-f')(f'-\beta_u).$$

We then substitute this equation into the right-hand side of equation (3.29) to eliminate $\overline{T}$ and f''. After we rearrange the resulting equation in terms of f', we see that the zero of h occurs at

$$f' = 2\left[\frac{\beta_u - \beta_t + \frac{1}{2}M_{-\infty}^2(\gamma-1)\beta_u(1-\beta_u)}{1-\beta_t+\frac{1}{2}M_{-\infty}^2(\gamma-1)(1-\beta_u^2)}\right]. \tag{3.31}$$

We then substitute the above equation into inequality (3.30), after some algebra, we find the condition for β_t depending on the other basic flow parameters to be

$$\beta_t < \frac{\beta_u}{2-\beta_u}\left(1 + \frac{1}{2}(\gamma-1)M_{-\infty}^2(1-\beta_u)^2\right), \tag{3.32}$$

for $0 < \beta_u < 1$ in the case of a stably curved compressible mixing layer. This condition produces an upper limit for β_t such that the thermal modes exist. With fixed values of β_u and $M_{-\infty}$, we may then use this condition to determine the critical value of β_t and investigate the region where thermal modes are expected to exist within.

3.6.2 Prediction of the thermal modes

Since the highest growth rate and the location of the most unstable mode are predicted by consideration of the high-wave number limit of the inviscid Görtler problem, therefore to investigate the general behaviour of the thermal modes it is necessary to look at the problem in the limit of high-wavenumber. We now demonstrate in Figures (3.12), (3.13) and (3.14) the effect on the asymptotic prediction for the maximum growth rates, β_0, and the location of the most unstable mode, η_b, of the thermal modes upon variations of β_t based on the Lock, Ting and Tanh velocity profile respectively. The predictions of β_0 were obtained by solving equation (3.28) based on the different basic flow profiles. The location of the modes, η_b, was obtained by solving equation (3.21), and was verified by using equation (3.22). The relative upper steam velocity and the lower stream Mach number are fixed to be $\beta_u = 0.5$ and $M_{-\infty} = 0.2$, respectively. On the same plots the prediction of the behaviour of the usual modes within the unstably curved mixing-layer system is also demonstrated in comparison with the thermal modes.

It may be observed that the growth rates of these thermal modes are significantly larger than the previous results of the usual modes. However, these modes only exist for a small range of the upper stream temperature. The critical value of β_t at which the thermal modes are expected to disappear can be determined using inequality (3.32). The critical value of β_t for the case of $\beta_u = 0.5$ and $M_{-\infty} = 0.2$, is predicted to be 0.334, which agrees with the numerical results.

By comparing the predictions of the location of the most unstable thermal modes based on different velocity profiles, we see that the Ting profile predict that the modes move directly away from the centreline before heading off to ∞ at the critical value of β_t, whereas the predictions from both Lock and Tanh profiles indicate that the location of the modes first move slightly toward the centerline then heading off to ∞. For the maximum scaled growth rate, β_0, the Lock result once again is almost indistinguishable from the

Ting result. The Tanh profile in general offered a much higher set of the maximum scaled growth rate, which is the same case within the unstably curved system. We shall note here that both usual modes and thermal modes owe their existence to the presence of centrifugal force. The difference between these modes is that the usual modes are driven by velocity shear, whereas the thermal modes are sustained by thermal gradient.

Up till now, we have looked at the behaviour of the Görtler mode within the plain curved compressible mixing-layer systems in the limit of large Görtler number; large wave number and within the viscous right-hand branch. The predictions of the Görtler modes are made based on the choice of the three basic velocity profiles which were introduced in Section (3.1). With a different numerical scheme, the results that were generated based on the Lock and Ting profile appear to be in good agreement with the previous investigation which was made by Owen et al. (1997).

3.7 Chapter summary

In this chapter we have investigated linear Görtler instability within a system that is far downstream from the trailing edge of the splitter plate. It is expected that as the system progresses downstream further away from the trailing edge of the splitter plate, the modes within the system would lead to a similar behaviour with the modes within the plain curved compressible mixing-layer system. Such system has been previously investigated by Owen et al. (1997).

For this system, both similarity and Howarth-Dorodnitsyn transformations were applied for simplification. For the basic flow problem, we extended the investigation of Owen et al. (1997) by including a hyperbolic tangent profile in order to compare the later prediction with the Lock and Ting profile prediction.

By using a different numerical scheme to Owen et al. (1997), the associated eigenvalue problem was solved based on the different basic flow models. The results of increasing growth rate of the inviscid modes with wave number based on different basic flow models

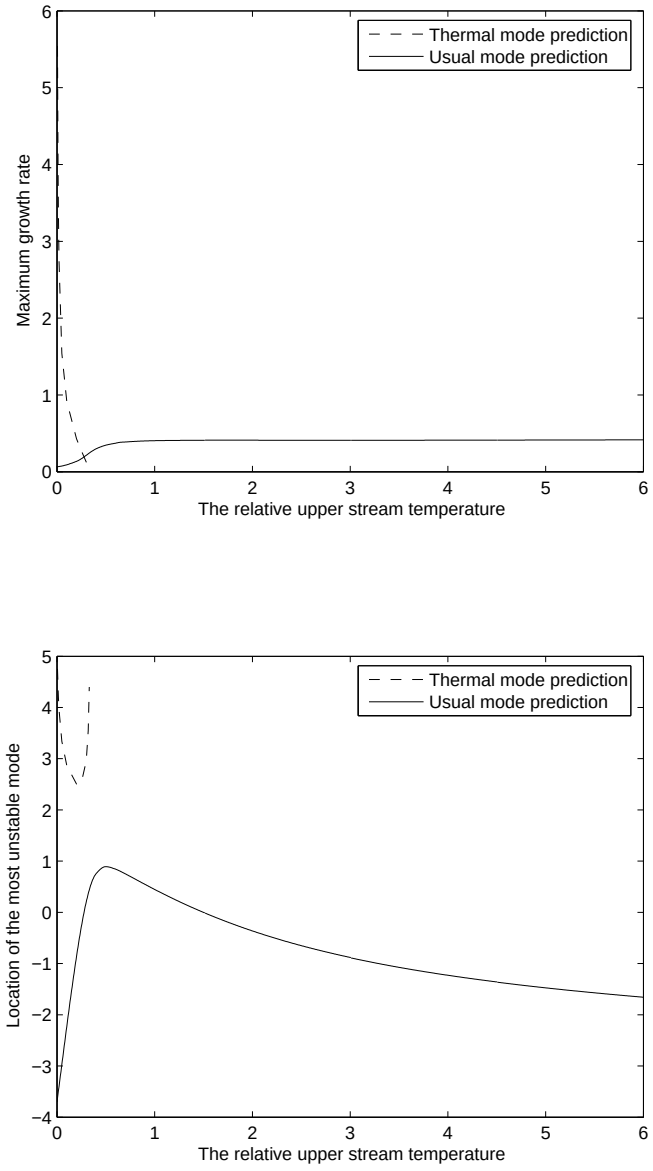

Figure 3.12: The variation of the maximum scaled growth rate (top), β_0, and the location of the most unstable mode (bottom), η_b, with the relative upper stream temperature, β_t, within the stably and unstably curved compressible layer for the Lock profile with $\beta_u = 0.5$ and $M_{-\infty} = 0.2$.

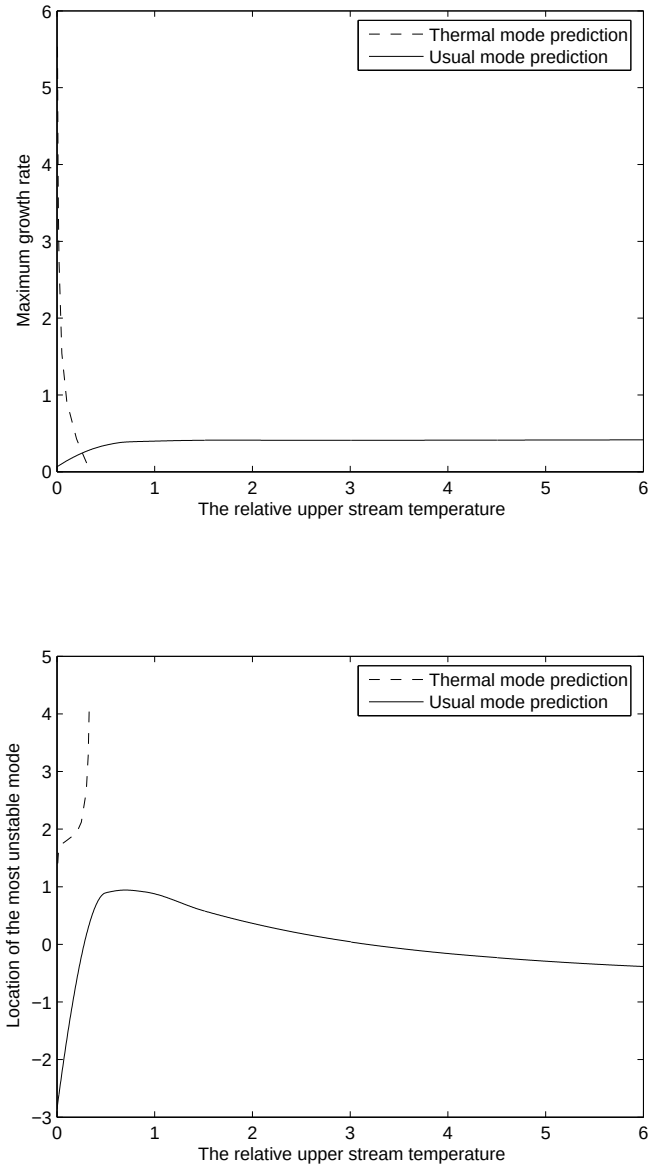

Figure 3.13: The variation of the maximum scaled growth rate (top), β_0, and the location of the most unstable mode (bottom), η_b, with the relative upper stream temperature, β_t, within the stably and unstably curved compressible layer for the Ting profile with $\beta_u = 0.5$ and $M_{-\infty} = 0.2$.

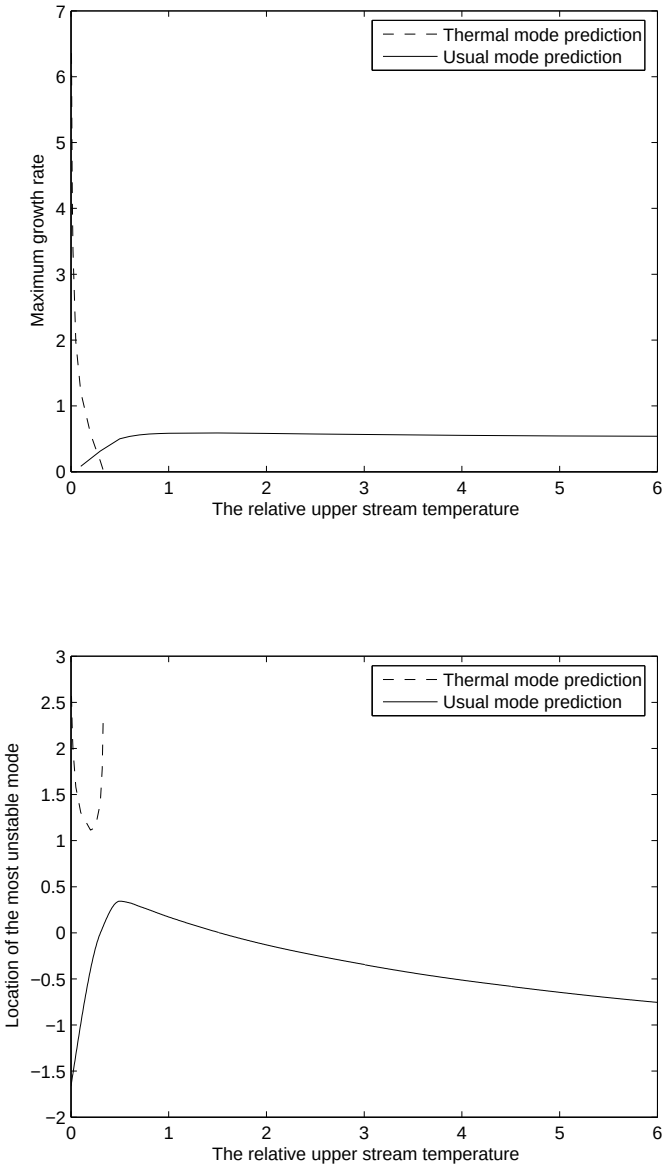

Figure 3.14: The variation of the maximum scaled growth rate (top), β_0, and the location of the most unstable mode (bottom), η_b, with the relative upper stream temperature, β_t, within the stably and unstably curved compressible layer for the Tanh profile with $\beta_u = 0.5$ and $M_{-\infty} = 0.2$.

are reproduced and to show agreement with numerical calculations. Based on the high wave number analysis, we then exploit the high-wavenumber limit of the inviscid problem to gain some useful information pertaining to the ranges of basic flow parameter ratios for which these modes persist. The results within the right-hand branch indicate that the modes would be eventually stabilized by the viscous effect within the system.

Within a stably curved compressible mixing-layer system, the result indicated that only the thermal mode would exist, which were driven by the inflectional basic temperature profile. This result also agrees with the previous result of Owen et al. (1997).

The results also indicate that the different basic flow model would lead to a slightly different prediction for the behaviour of the linear Görtler disturbance within the same mixing-layer system. Based on the Lock and Ting profiles, the differences are at the prediction of the exact location of the modes within the system, with the Lock profile predicted that the modes would generally situate at a lower position than the Ting profile prediction. For the Tanh profile, a slightly higher set of growth rates of the modes were predicted in comparison with the Lock and Ting profiles. For the mixing purpose, it would be desirable for the Görtler mode to situate near to the centreline of the system and posses a larger growth rate. Therefore it is important to choose the most physically realistic basic flow model, so that it will be able to accurately predict the behaviour of the Görtler modes within the system for the mixing enhancement purpose. This will be investigated more precisely in the next two chapters when the effect of the wake is taken into account (based on the three wake flow models) for the near-wake region behind the splitter plate.

Chapter 4

Analytic models for wake-dominated curved compressible mixing layers

A wake can be developed behind a body moving through a viscous fluid, and is not susceptible to even large scale computing since the flow becomes turbulent. However, for a thin wake behind a thin aerofoil we may expect that the boundary layer equations will still hold, but with a difference in the boundary conditions. If a thin splitter plate is inserted into an infinite expanse of the same fluid in such a way as to 'entrain' fluid, the situation is somewhat similar to that of a thin wake. Such a flow is expected to occur in the case of a supersonic engine in which the flow has ingested very thick, turbulent boundary layers that cause a wake-dominated velocity profile. Therefore it is necessary to model such wake-dominated behaviour theoretically for the experimental and industrial purposes. In the experimental studies of the mixing layer problem, a splitter plate is always used to separate the two streams, and on the two sides of the plate. There are the boundary layers which would need to be considered, therefore accurate models for the basic wake flow are required in order to offer correct predictions of the behaviour of the Görtler modes for our problem with curvature.

There have been a number of interests concerning the basic wake flow modelling in the past and most of them are based on the incompressible case. There are also some analytic wake models that are able to describe the correct behaviour of the basic wake flow but do not provide solutions to the basic flow equations. However these analytic wake flow profiles appear to be the most convenient models to apply to the relevant instability analysis, therefore it is worth our interest to start the investigation of the prediction of the behaviour of the Görtler modes based on these analytical wake profiles.

It has been shown experimentally in the past, by Breidenthal (1978), that there is a fundamental difference in the behaviour between mixing layers and wakes formed downstream of a splitter plate. The mixing layer mode was found to dominate in the case where there was uniform density across the mixing layer whereas the wake mode was found to dominate when the layer has non-uniform density and where the faster stream had the lower density. An experiment on the mixing and reaction in the curved mixing-layer system by Karasso and Mungal (1997) had considered the application of the splitter plate insertion technique. It indicated that the inflectionally driven Kelvin Helmholtz modes would occur almost instantaneously downstream of the splitter plate (which was inserted along the centreline of the mixing-layer system) and would cause the two streams to start mixing. It would be interesting to investigate the behaviour of the modes within such system and determine whether centrifugal effects can promote mixing, either directly or via the modification of the inherent inviscid modes.

The linear, spatial Kelvin-Helmholtz instability of inviscid, compressible, parallel supersonic mixing layers, with velocity profiles possessing a wake component has been previously studied by Zhuang and Dimotakis (1995). Their basic velocity profile for the basic flow was represented by the Tanh profile plus a wake component, which we referred to as the Gaussian wake profile. For this situation they found that the existence of a wake component in the velocity profile renders the mixing layer more unstable at all free-stream Mach numbers. They also found that the wake mode becomes less unstable and eventually

stable with increasing compressibility (i.e. increasing convective Mach number).

The second analytic wake flow model we consider was first designed by Liang et al. (1996) to correspond to an experiment performed at hypersonic speeds, and to provide a means of interpreting stability observations made in that experiment. This particular wake flow model is referred to here as the composite wake profile. Such a profile was employed during his investigation of the spatial linear stability of both bounded and semibounded inviscid, parallel mixing layers formed between a laminar Mach 8 stream and Mach 3 stream. It was found that the stability of the developing mixing layer which begins with a wake-like profile with two inflection points differs significantly from that of the related self-similar flow. Their major differences were found to be the magnitude of the growth rates and the character and number of the unstable modes.

4.1 Gaussian wake model and predictions

We are going to start the investigation by considering the effect of including the wake components in the basic flow of the curved compressible mixing layer. The first part of our investigation will be solely concerned with the unstably curved mixing layer. In the second part of the investigation, we will proceed to investigate the effect of including the wake components in the basic flow of the stably curved mixing layer. Similar to our investigation in the previous chapter, the effect of the variations in the upper stream velocity and temperature and the lower stream Mach number, on the location and the growth rates of the unstable modes will be considered for both cases.

For our problem, we are interested in the behaviour of linear inviscid Görtler instability within the curved compressible mixing-layer system. For this situation the flow is non-parallel as the Görtler instability could only exist within the mixing-layer system that is associated with curvature. Previous work of Zhuang and Dimotakis (1995) based the parallel compressible mixing layers had considered a Gaussian wake profile for the mean flow situation. The Gaussian wake profile consists of a hyperbolic tangent profile with

a Gaussian wake parameter which is going to be considered for approximating the basic streamwise velocity for our problem. The Gaussian wake profile is given as

$$\overline{u} = \frac{1}{2}(1+\beta_u) + \frac{1}{2}(\beta_u - 1)\tanh(\eta) + w\exp(-\ln(2)\eta^2), \tag{4.1}$$

where the basic streamwise velocity is in terms of the similarity variable

$$\eta = \frac{\overline{Y}}{\sqrt{X}},$$

which was previously defined in equation (3.6), for the curved compressible system, and $\overline{Y}$ is the Howarth-Dorodnitsyn transformation variable that was previously defined in (2.31). The set up of the basic flow problem remains the same as in the previous chapter. w will be referred to as the wake parameter. In practical situations, $w < 0$ represents the wake that arises from the thickness of the splitter plate and drag of the splitter-plane surfaces in the mixing layer; whereas $w > 0$ represents the jet into the centreline of the system. The general configuration of a curved mixing layer with a wake component in the basic velocity profile from (4.1) is demonstrated in Figure (4.1) where $\overline{u}(\eta)$ is shown for $\beta_u = 0.5$. The basic temperature profile is derived based on the Tanh profile including a wake component and its formula remains unchanged:

$$\overline{T}(\eta) = 1 - \frac{1-\beta_t}{1-\beta_u}(1-\overline{u}(\eta))\frac{1}{2}(\gamma-1)M^2_{-\infty}(1-\overline{u}(\eta))(\overline{u}(\eta)-\beta_u).$$

The variation of the basic temperature, $\overline{T}$, with w is demonstrated in Figure (4.2). The relative upper stream velocity, temperature and lower stream Mach number are fixed to be $\beta_u = 0.5$, $\beta_t = 0.75$ and $M_{-\infty} = 0.2$, respectively.

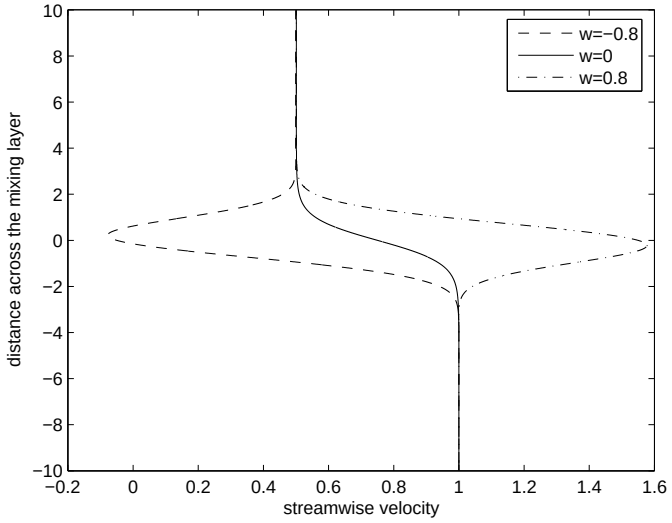

Figure 4.1: The variation of the basic velocity, $\overline{u}(\eta)$, with wake component, w, based on the Gaussian model with $\beta_u = 0.5$.

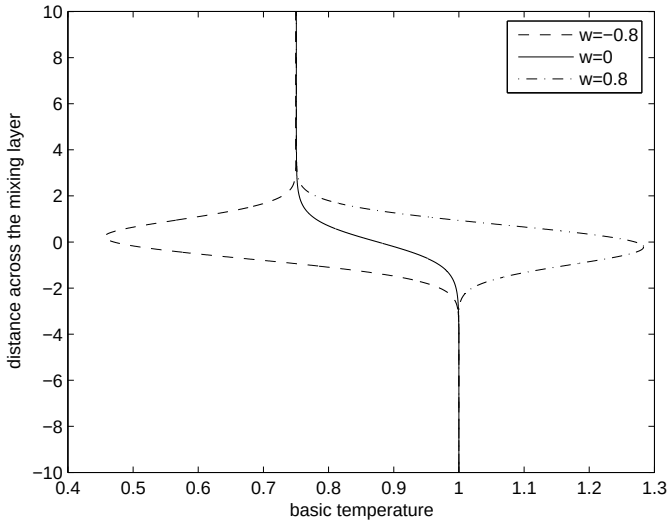

Figure 4.2: The variation of the basic temperature, $\overline{T}(\eta)$, with wake component, w, based on the Gaussian model with $\beta_u = 0.5$, $\beta_t = 0.75$ and $M_{-\infty} = 0.2$.

4.1.1 Investigation of the modes within the unstably curved mixing layer

To investigate the effect of the wake on the inviscid Görtler modes, demonstrated in Figures (4.3) and (4.4) are the effects of both positive and negative variation in the wake parameter, w, on the first inviscid mode, $\mathsf{V}(\eta)$, for a particular case of an unstably curved mixing layer with $a = 5$, $\beta_u = 0.5$, $\beta_t = 0.75$ and $M_{-\infty} = 0.2$. Both figures suggest that as the wake parameter, w increases from being negative to positive, the location of the mode moves from the lower stream towards the slower upper stream. The numerical solution of V was obtained from solving the eigenvalue relation

$$\mathsf{V}''(\eta) - \mathsf{V}'(\eta)\left(\frac{2\overline{T}'(\eta)}{\overline{T}}\right) + \mathsf{V}\left[\left(-a^2\overline{T}^2 - \frac{\overline{u}''(\eta)}{\overline{u}(\eta)} + \frac{2\overline{T}'(\eta)}{\overline{T}}\frac{\overline{u}'(\eta)}{\overline{u}(\eta)}\right) - \frac{a^2\tilde{\chi}}{\beta^2}(\overline{T}\frac{\overline{u}'(\eta)}{\overline{u}(\eta)} - \frac{\overline{T}'(\eta)}{2})\right] = 0, \tag{4.2}$$

associated with the following boundary conditions

$$\mathsf{V} \sim e^{-a\beta_t\eta}, \quad \text{as} \quad \eta \to \infty, \tag{4.3}$$

and

$$\mathsf{V} \sim e^{a\eta}, \quad \text{as} \quad \eta \to -\infty, \tag{4.4}$$

and the condition that both V and $\frac{d\mathsf{V}}{d\eta}$ are continuous at $\eta = 0$.

Equation (4.2) remains in the same form as equation (3.17) in the previous chapter, but with $f'(\eta)$ now written as $\overline{u}(\eta)$ as it was found that $f'(\eta) = \overline{u}(\eta)$ under the similarity transformation for the curved compressible mixing layer problem. The variables χ and X have been eliminated by the transformations (3.16). We fix $\tilde{\chi} = \pm 1$ for the unstably and the stably curved systems, respectively.

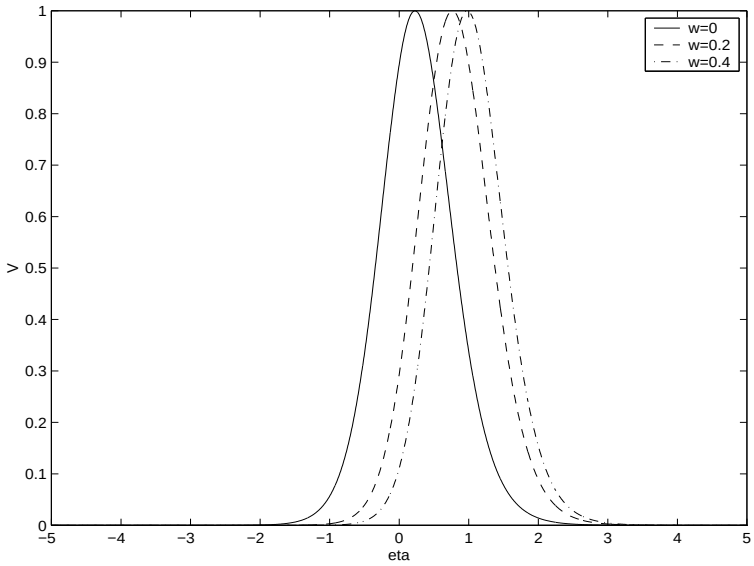

Figure 4.3: The variation of the first inviscid mode, $\mathsf{V}(\eta)$, with positive wake parameter, $(w > 0)$, for $a = 5$, $\beta_u = 0.5$, $\beta_t = 0.75$, $M_{-\infty} = 0.2$, based on the Gaussian model.

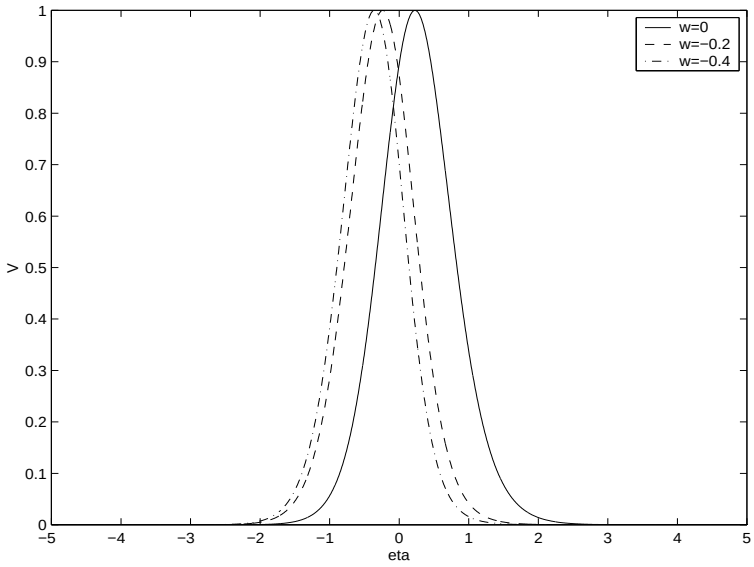

Figure 4.4: The variation of the first inviscid mode, $\mathsf{V}(\eta)$, with wake deficits, $(w < 0)$, for $a = 5$, $\beta_u = 0.5$, $\beta_t = 0.75$, $M_{-\infty} = 0.2$, based on the Gaussian model.

Demonstrated in Figure (4.5) is the variation of $\mathsf{V}(\eta)$ for the first inviscid mode with increasing wave number, a, with the fixed basic flow parameters for $w = -0.4$ with the same unstably curved compressible case. It is observed that the structure of the first inviscid mode based on the Gaussian wake profile shrinks to a thin layer as the wave number, a, increases. For comparison purpose, we normalised V to have maximum 1.

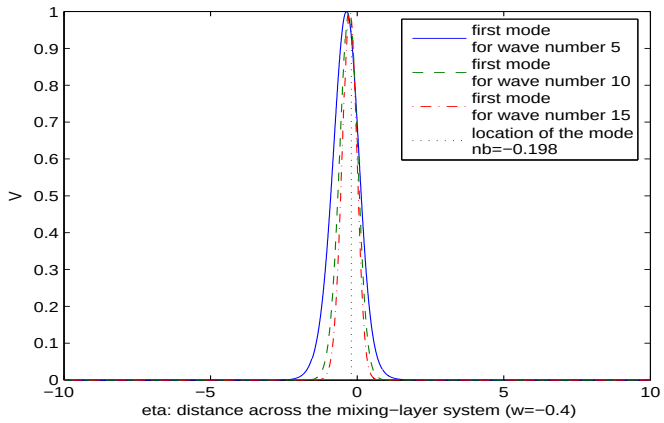

Figure 4.5: The first inviscid mode, $\mathsf{V}(\eta)$, for $a = 5, 10, 15$ with $\beta_u = 0.5$, $\beta_t = 0.75$ and $M_{-\infty} = 0.2$, based on the Gaussian model for $w = -0.4$.

The location of the most unstable modes, η_b, is determined from solving

$$\overline{T}_b\overline{T}''_b{\overline{u}_b}^2 - 2\overline{u}_b\overline{u}''_b\overline{T}_b^2 + 2\overline{u}_b\overline{u}'_b\overline{T}_b\overline{T}'_b + 2{\overline{u}'_b}^2{\overline{T}_b}^2 - 2(\overline{T}'_b)^2{\overline{u}_b}^2 = 0, \quad [\overline{T}_b = \overline{T}(\eta_b) \text{ etc.}], \quad (4.5)$$

which was derived previously for the curved compressible mixing-layer system by using the high wave number analysis (i.e. equation (3.21)). For this wake-dominated system shown in Figure (4.5), the location of the most unstable mode is found to be $\eta_b = -0.198$. This was verified by the alternative method of searching for the location of the maximum of the leading-order eigenvalue function, which is given as

$$h = \frac{1}{\overline{T}^2}\left(\frac{\overline{T}'}{2} - \frac{\overline{T}\overline{u}'}{\overline{u}}\right). \quad (4.6)$$

The above equation was derived previously for the curved compressible mixing-layer system based on the high wave number analysis (i.e. equation (3.22)).

Demonstrated in Figure (4.6) are the numerical solutions for the first four unstable modes at the particular wave number, $a = 5$, with the fixed basic flow parameters for $w = -0.4$ with the same unstably curved compressible case. The normal disturbance velocity, V, was normalised to 1 for these cases. The growth rate which is associated with each of these modes was derived numerically from solving the associated eigenvalue relation (equation (4.2)) and is provided in Table (4.1).

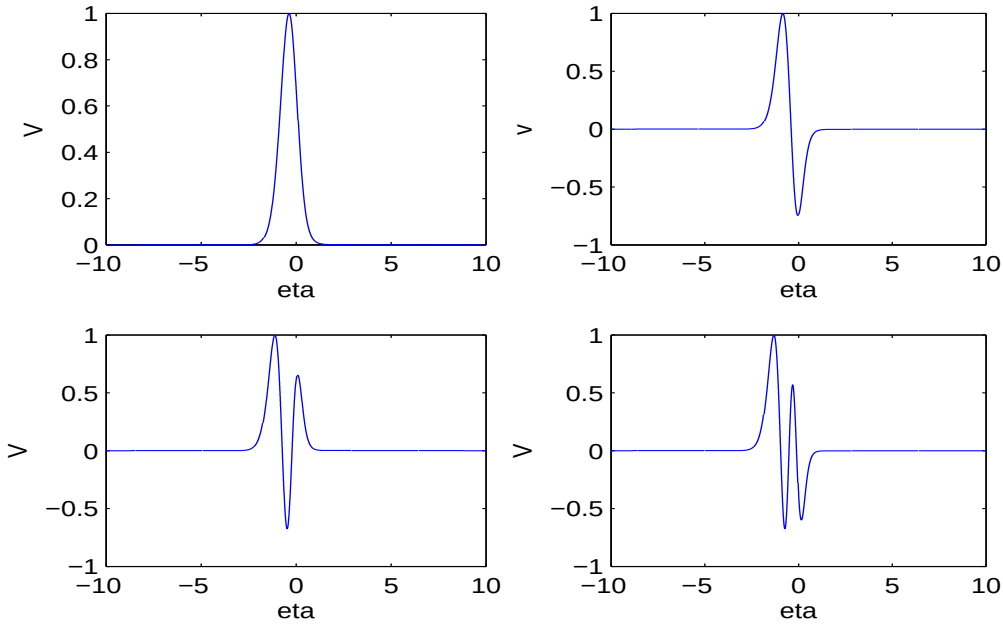

Figure 4.6: The first four inviscid modes, $\mathsf{V}(\eta)$, for $a = 5$ with $w = -0.4$, for $\beta_u = 0.5$, $\beta_t = 0.75$ and $M_{-\infty} = 0.2$, based the Gaussian model for $w = -0.4$.

First unstable mode	Second unstable mode	Third unstable mode	Fourth unstable mode
$\beta_1 = 0.835$	$\beta_2 = 0.6267$	$\beta_3 = 0.5023$	$\beta_4 = 0.4188$

Table 4.1: Growth rates, β, for the first four modes for $a = 5, w = -0.4, \beta_u = 0.5, \beta_t = 0.75$ and $M_{-\infty} = 0.2$, based on the Gaussian model.

Based on the result for the growth rate of the first four modes for $w = -0.4$ in Table (4.1), the effect of increasing wave number, a, on the growth rate of the modes, β, could then be obtained from solving the the associated eigenvalue relation (equation (4.2)). The results are then demonstrated in Figure (4.7).

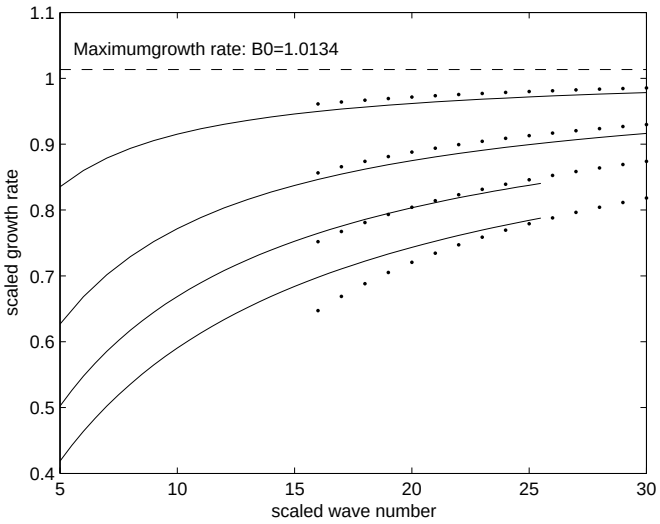

Figure 4.7: The variation of the growth rate of the first four modes, β, with the wave number, a, for $\beta_u = 0.5$, $\beta_t = 0.75$ and $M_{-\infty} = 0.2$, based the Gaussian model for $w = -0.4$. Numerical solution: solid line. Asymptotic solution: dotted line.

It is observed from Figure (4.7) that the growth rates of the first four modes would tend to a constant, which is the asymptotic prediction of the maximum scaled growth rate, β_0, as the wave number increases. The numerical predictions indicate a good agreement with the corresponding asymptotic predictions.

The corresponding asymptotic prediction (for $a >> 1$) for the associated scaled growth rate of the first four modes with increasing wave number was derived from solving

$$\beta_n = \beta_0 - \frac{1}{a}\frac{(2n-1)Q_b^{1/2}\beta_0}{2^{3/2}\overline{T}_b^2}, \tag{4.7}$$

based on the Gaussian wake model. β_0 denotes the maximum scaled growth rate for the

system and was obtained from solving the following equation

$$\beta_0 = \left[\tilde{\chi}\left(\frac{\overline{T}_b'}{2\overline{T}_b^2} - \frac{\overline{u}_b'}{\overline{T}_b\overline{u}_b}\right)\right]^{1/2}, \tag{4.8}$$

For the unstably curved system, we fix $\tilde{\chi} = 1$.

$$\begin{aligned} Q_b = &-\left(\overline{T}_b\overline{T}_b{}'' + (\overline{T}_b')^2\right) - \frac{1}{2\beta_0^2\overline{u}_b}\left[\overline{T}_b\overline{u}_b''' + 2\overline{T}_b'\overline{u}_b'' + \overline{T}_b''\overline{u}_b\right] \\ &+\frac{\overline{u}_b'}{(\beta_0\overline{u}_b)^2}\left[\overline{T}_b'\overline{u}_b' + \overline{T}_b\overline{u}_b''\right] - \frac{\overline{T}_b\overline{u}_b'}{\beta_0^2\overline{u}_b}\left[\left(\frac{\overline{u}_b'}{\overline{u}_b}\right)^2 - \frac{\overline{u}_b''}{2}\right] + \frac{\overline{T}_b'''}{4\beta_0^2}. \end{aligned} \tag{4.9}$$

The equations (4.7), (4.8) and (4.9) were derived previously by using the high wave number analysis for the curved compressible mixing-layer system (i.e. equations (3.23) and (3.20)).

Demonstrated in Figure (4.8) are the numerical and asymptotic predictions of the growth rate of the first mode, β_1, with wake parameter, w, for a particular wave number, $a = 5$, with the same compressible case. The basic flow parameters for the system remain fixed to be $\beta_u = 0.5$, $\beta_t = 0.75$ and $M_{-\infty} = 0.2$.

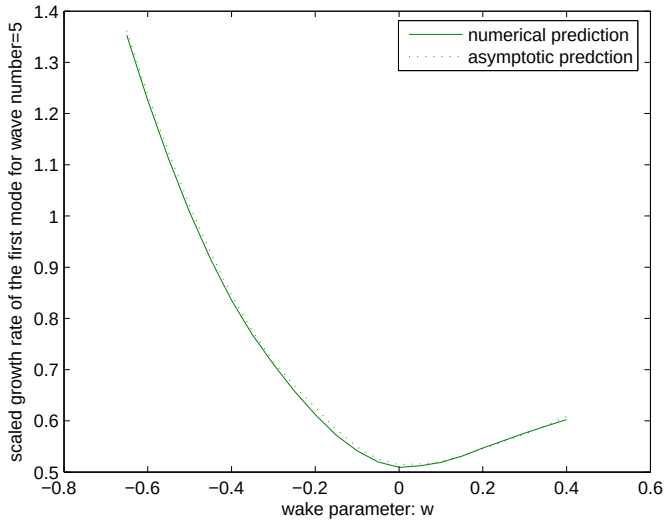

Figure 4.8: The variation of the growth rate of the first mode, β_1, for $a = 5$ with the wake parameter, for $\beta_u = 0.5$, $\beta_t = 0.75$ and $M_{-\infty} = 0.2$, based the Gaussian model.

It is observed from Figure (4.8) that an increase of the wake effect (w becoming more negative) corresponds to an increase in the growth rate of the first mode. The result also indicates that the numerical and asymptotic results agree very well with one another, although a is not particularly large.

To investigate the prediction of the general behaviour of the Görtler mode with the increase in the wake parameter for the corresponding compressible case with $\beta_u = 0.5$, $\beta_t = 0.75$ and $M_{-\infty} = 0.2$, we plot in Figures (4.9) and (4.10), the effect of varying w on the maximum growth rate, β_0, and the location of the most unstable, η_b, in the limit of large wave number.

Figure (4.9) indicates that the increase of the wake effect (w becoming more negative) would lead to an increase in the maximum growth rate, β_0, at a faster rate than the growth in β_0 for the increase in the jet effect($w > 0$). Therefore the mixing layer is more unstable under the effect of the wake for this particular case.

Figure (4.10) indicates that for an initial increase of the wake effect (w becoming more negative from $w = 0$), the most unstable mode would move towards the lower faster stream and as the wake effect gets larger the mode would move back towards the centreline of the system for this particular case.

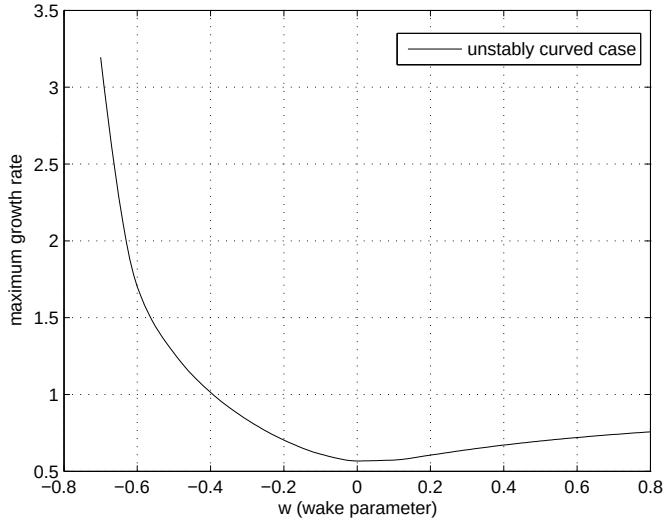

Figure 4.9: The variation of the maximum scaled growth rate, β_0, with wake parameter, w, within the unstably curved mixing layer for $\beta_u = 0.5$, $\beta_t = 0.75$, $M_{-\infty} = 0.2$, based on the Gaussian model.

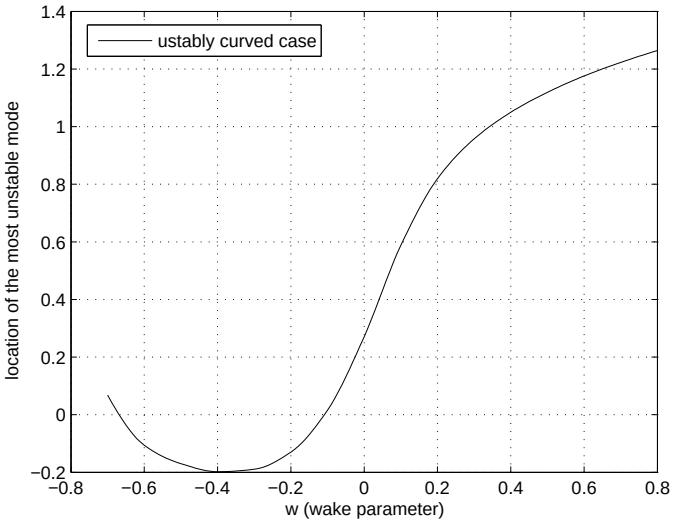

Figure 4.10: The variation of the location of the most unstable mode, η_b, with wake parameter, w, within the unstably curved mixing layer for $\beta_u = 0.5$, $\beta_t = 0.75$, $M_{-\infty} = 0.2$, based on the Gaussian model.

Demonstrated in Figures (4.11) and (4.12) is the effect of the relative upper stream velocity, β_u, on the maximum scaled growth rate, β_0, and the location of the most unstable mode, η_b, for the unstably curved system under increasing wake effect ($w < 0$). To produce these figures we have fixed the other basic flow parameters at $\beta_t = 0.75$ and $M_{-\infty} = 0.2$.

It is observed from Figure (4.11) that the maximum growth rate, β_0, for the cases of $w = -0.4, -0.2, 0$, all decrease to 0 as $\beta_u \to 1$. This result is expected as the instability would no longer exist under the uniform velocities. We also observe from Figures (4.11) and (4.12) that the maximum growth rate, β_0, within the wake-dominated system of $w = -0.4$ is greater than the maximum growth rate within the jet-dominated system of $w = 0.4$ for all values of $\beta_u < 1$. This result is consistent with the previous prediction in Figure (4.9). As the upper and lower stream velocity difference become greater, the flow is expected to become more unstable.

The results from Figure (4.12) indicate that as the relative upper stream velocity increases, modes within the systems would move from the upper stream into the lower stream.

Demonstrated in Figures (4.13) and (4.14) is the effect of the relative upper stream velocity, β_u, on the maximum scaled growth rate, β_0, and the location of the most unstable mode, η_b, for the unstably curved system under increasing jet effect ($w > 0$). To produce these figures we have fixed the other basic flow parameters at $\beta_t = 0.75$ and $M_{-\infty} = 0.2$.

It is again observed from Figure (4.13) that the maximum growth rate, β_0, for the cases of $w = 0.4, 0.2, 0$, all decrease to 0 as $\beta_u \to 1$, which indicates that the instability would no longer exist under the uniform velocities.

The result from Figure (4.14) indicates that as the relative upper stream velocity increases, modes within these jet-dominated systems would slightly move from the upper stream towards the centreline of the system.

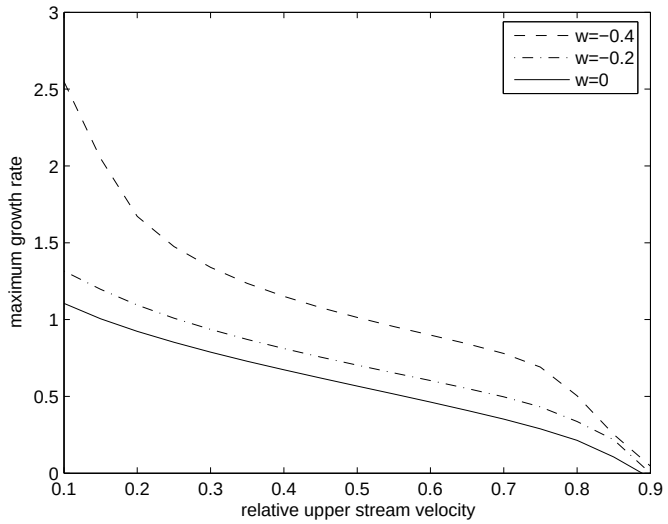

Figure 4.11: The variation of the maximum scaled growth rate, β_0, with β_u, for $w = -0.4, -0.2, 0$, $\beta_t = 0.75$, $M_{-\infty} = 0.2$, based on the Gaussian model within the unstably curved systems.

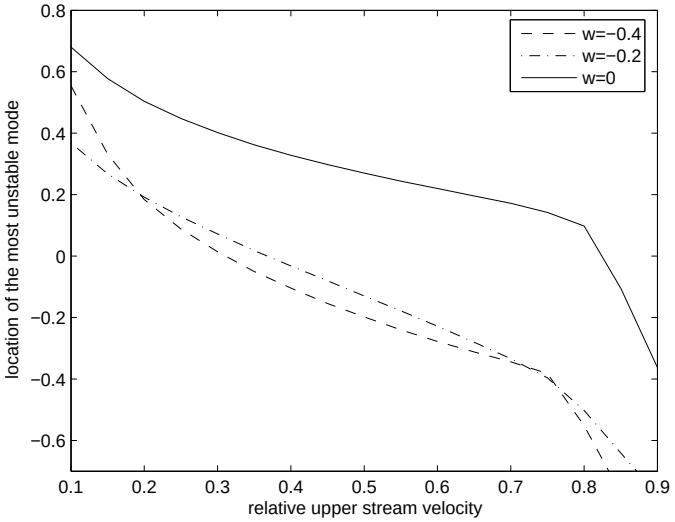

Figure 4.12: The variation of the location of the most unstable mode, η_b, with β_u, for $w = -0.4, -0.2, 0$, $\beta_t = 0.75$, $M_{-\infty} = 0.2$, based on the Gaussian model within the unstably curved systems.

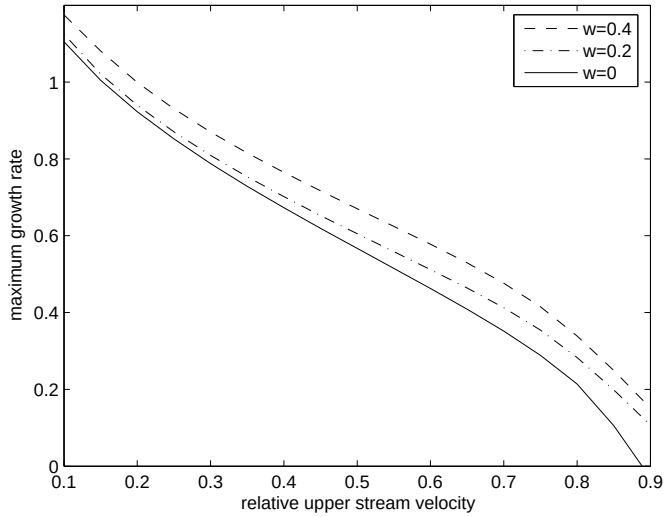

Figure 4.13: The variation of the maximum scaled growth rate, β_0, with β_u, for $w = 0.4, 0.2, 0$, $\beta_t = 0.75$, $M_{-\infty} = 0.2$, based on the Gaussian model within the unstably curved systems.

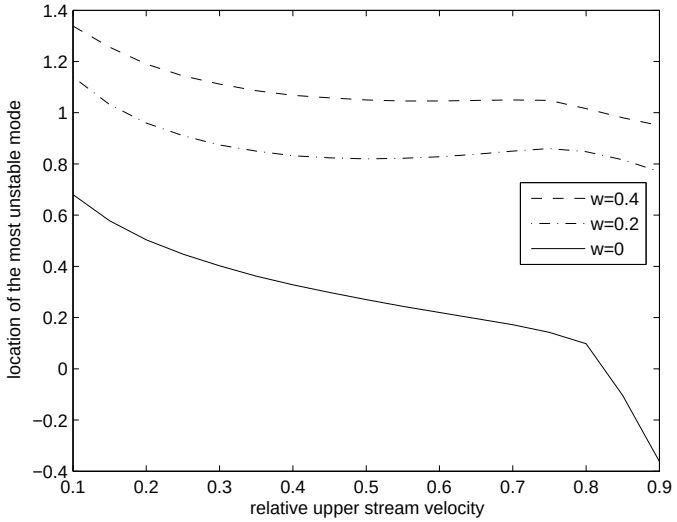

Figure 4.14: The variation of the location of the most unstable mode, η_b, with β_u, for $w = 0.4, 0.2, 0$, $\beta_t = 0.75$, $M_{-\infty} = 0.2$, based on the Gaussian model within the unstably curved systems.

The effect of increasing the relative upper stream temperature, β_t, on the maximum scaled growth rate, β_0, and the location of the most unstable mode, η_b, for the unstably curved system under increasing wake effect ($w < 0$), is demonstrated in Figure (4.15) and (4.16), respectively. The other basic flow parameters are fixed to be $\beta_u = 0.5$ and $M_{-\infty} = 0.2$.

The results from Figure (4.15) indicate that the maximum growth rate, β_0, varies slowly with increasing β_t within the wake-dominated systems for $w = -0.4$ and $w = -0.5$. For $\beta_t < 0.5$, the growth rate of the mode associated with the system of $w = -0.65$ would increase dramatically whereas for systems of $w = -0.5$ and $w = -0.4$, the decrease in β_t would lead to a small decrease in the growth rates.

The results from Figure (4.16) indicates that an increase of β_t would have a larger effect on the location of the mode that corresponds to systems for $w = -0.4$ and $w = -0.5$ in comparison with the mode that is associated with the system for $w = -0.65$.

The effect of increasing the relative upper stream temperature, β_t, on the maximum scaled growth rate, β_0, and the location of the most unstable mode, η_b, for the unstably curved system under increasing jet effect ($w > 0$), is demonstrated in Figures (4.17) and (4.18), respectively. The other basic flow parameters are fixed to be $\beta_u = 0.5$ and $M_{-\infty} = 0.2$.

The results from Figure (4.17) indicate that the maximum growth rate, β_0, increases with increasing β_t within the wake-dominated systems under increasing jet effect ($w > 0$).

The results from Figure (4.18) indicate that an increase of β_t would have a larger effect on the location of the mode that corresponds to systems under increasing jet effect ($w > 0$), rather than for the case $w = 0$.

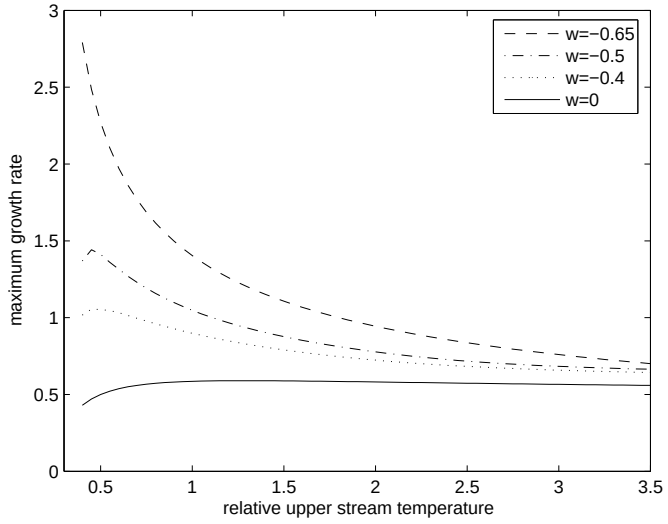

Figure 4.15: The variation of the maximum scaled growth rate, β_0, with the relative upper stream temperature, β_t, for $\beta_u = 0.5$, $M_{-\infty} = 0.2$, for $w = -0.65, -0.5, -0.4, 0$, based the Gaussian model.

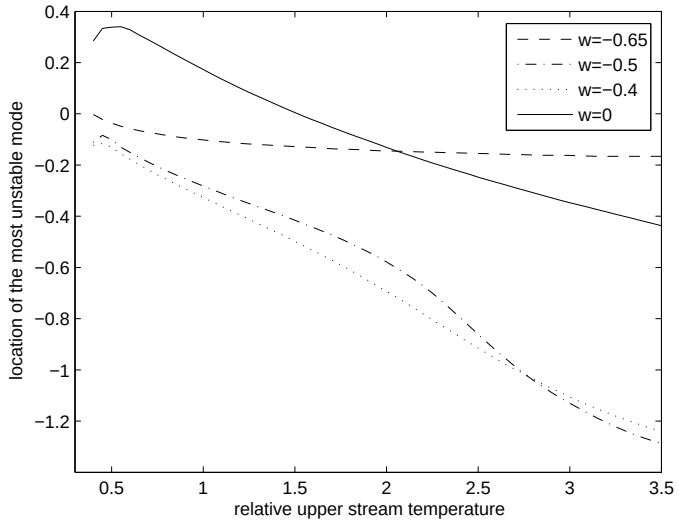

Figure 4.16: The variation of the location of the most unstable mode, η_b, with the relative upper stream temperature, β_t, for $\beta_u = 0.5$, $M_{-\infty} = 0.2$, for $w = -0.65, -0.5, -0.4, 0$, based the Gaussian model.

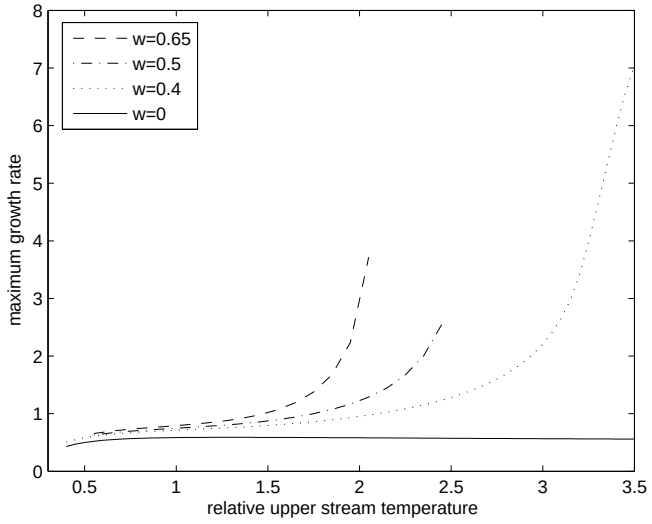

Figure 4.17: The variation of the maximum scaled growth rate, β_0, with the relative upper stream temperature, β_t, for $\beta_u = 0.5$, $M_{-\infty} = 0.2$, for $w = 0.65, 0.5, 0.4, 0$, based the Gaussian model.

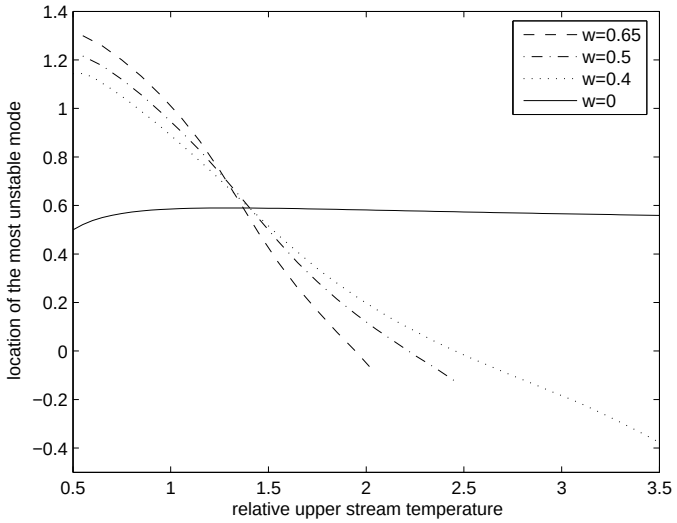

Figure 4.18: The variation of the location of the most unstable mode, η_b, with the relative upper stream temperature, β_t, for $\beta_u = 0.5$, $M_{-\infty} = 0.2$, for $w = 0.65, 0.5, 0.4, 0$, based the Gaussian model.

We now proceed to investigate the effect of increasing the compressibility (i.e. lower stream Mach number) on the general behaviour of the system for large wave number, based on the Gaussian wake profile for the wake-dominated and jet-dominated, unstably curved compressible mixing layers. The basic flow parameters are fixed to be $\beta_u = 0.5$ and $\beta_t = 0.75$.

Figures (4.19) and (4.20) demonstrate the effect of increasing the lower stream Mach number on the maximum growth rate, β_0, and the location of the most unstable mode, η_b, respectively within the unstably curved systems under increasing wake effect ($w < 0$). It is observed from Figure (4.19) that within the wake-dominated system for $w = -0.4$, the maximum growth rate decreases slowly with increasing $M_{-\infty}$. As the compressibility increases, the maximum growth rate decreases and behaves similarly to the mode within the plain curved system ($w = 0$). It is also observed from Figure (4.19) that the maximum growth rate which is associated with the systems of $w = -0.5$ and $w = -0.65$ would increase dramatically as $M_{-\infty}$ continues to increase past some critical value dependent on w, which corresponds to a decrease in the stability of the system.

The results from Figure (4.20) indicate that an increase of $M_{-\infty}$ would lead to the mode which corresponds to $w = -0.4$ moving downwards into a lower position in the faster stream. However for the mode that is associated with $w = -0.5$, as $M_{-\infty}$ continues to increase past some critical value dependent on w, the modes would move towards the slower upper stream instead. For $w = -0.65$, we see that an increase of $M_{-\infty}$ would only lead to the mode moving towards the slower upper stream.

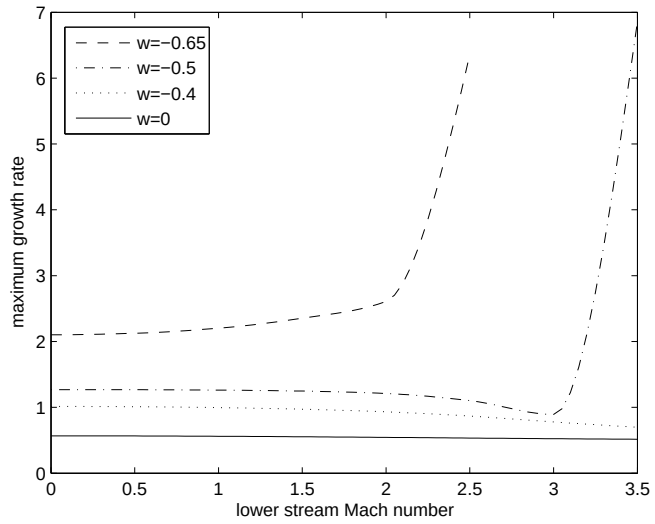

Figure 4.19: The variation of the maximum scaled growth rate, β_0, with the lower stream Mach number, $M_{-\infty}$, for $\beta_u = 0.5$, $\beta_t = 0.75$, for $w = -0.65, -0.5, -0.4, 0$, using the gaussian wake profile.

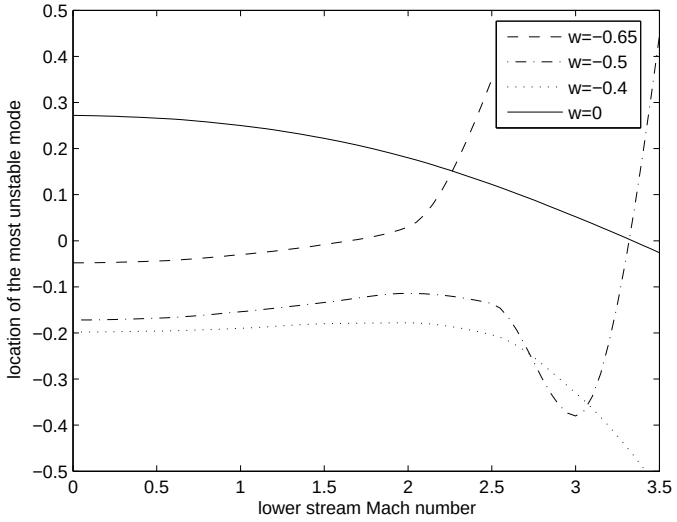

Figure 4.20: The variation of the location of the most unstable mode, η_b, with the lower stream Mach number, $M_{-\infty}$, for $\beta_u = 0.5$, $\beta_t = 0.75$, for $w = -0.65, -0.5, -0.4, 0$, using the gaussian wake profile.

Figures (4.21) and (4.22) demonstrate the effect of increasing the lower stream Mach number on the maximum growth rate, β_0, and the location of the most unstable mode, η_b, respectively, within the unstably curved systems under increasing jet effect ($w > 0$).

From Figure (4.21) we see that the growth rate within the jet-dominated system would increase for an increase in $M_{-\infty}$, which corresponds to a decrease in the stability of the system. As the compressibility increases, the maximum growth rate increases and behaves differently to the mode within the plain curved system ($w = 0$).

From Figure (4.22) we see that the mode within the jet-dominated system would gradually move from the upper stream towards the centreline of the system for an increase in $M_{-\infty}$.

This part of the investigation is concerned with the behaviour of the system within an unstably curved mixing layer based on the Gaussian wake model. The influences of both adding and subtracting the Gaussian wake parameter from the basic velocity profile on the instability behaviour of a unstably curved mixing layer have been investigated. It is found that the jet-dominated and wake-dominated system has an unstable side and a stable side. An increase of the relative upper stream temperature β_t, decreases the maximum growth rate, β_0, within the wake-dominated systems, but has the opposite effect on the maximum scaled growth rate within the jet-dominated systems. The results indicate that the amplification rate of the wake mode for the negative wake parameters is larger than that of the corresponding mixing layer mode for the Tanh profile in the previous chapter.

For the next part of the investigation we are going to turn our attention onto the behaviour of the Görtler modes within a wake-dominated stably curved system.

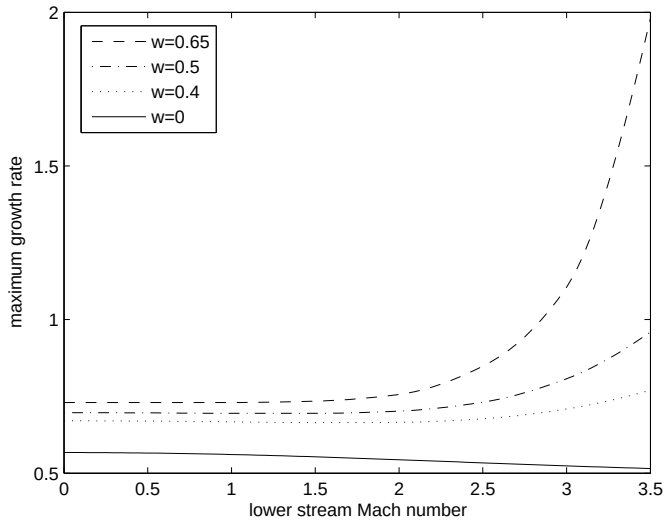

Figure 4.21: The variation of the maximum scaled growth rate, β_0, with the lower stream Mach number, $M_{-\infty}$, for $\beta_u = 0.5$, $\beta_t = 0.75$, for $w = 0.65, 0.5, 0.4, 0$, using the Gaussian wake profile.

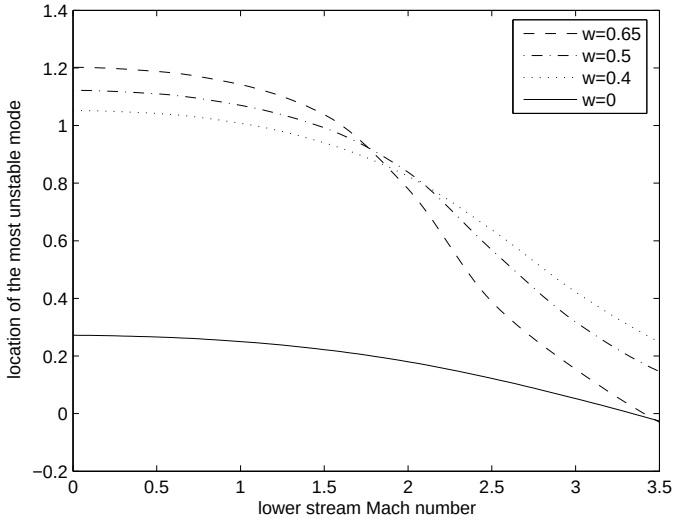

Figure 4.22: The variation of the location of the most unstable mode, η_b, with the lower stream Mach number, $M_{-\infty}$, for $\beta_u = 0.5$, $\beta_t = 0.75$, for $w = 0.65, 0.5, 0.4, 0$, using the Gaussian wake profile.

4.1.2 Investigation of the wake modes within the stably curved mixing layer

Previously, we have seen that the Görtler vortices also exist in the type of compressible mixing layer with the centreline curving towards the slower upper stream (stably curved case) under the condition that the slower stream is significantly cooler than the faster lower stream. These unstable modes were labelled by Owen et al. (1997) as the thermal modes due to the fact that they are driven by the inflectional curved temperature profile and possess significantly higher growth rates than the usual modes. To investigate the effect of the wake on the thermal modes, we begin by demonstrating in Figures (4.23) and (4.24), the variation with the wake parameter, w, of the maximum growth rate, β_0, and of the location of the most unstable, η_b, respectively, for the stably curved system. These results were obtained from solving equations (3.20) and (3.21), by fixing $\tilde{\chi} = -1$ for the stably curved system. The relative upper stream velocity and temperature and the lower stream Mach number are taken to be $\beta_u = 0.5$, $\beta_t = 0.01$, and $M_{-\infty} = 0.2$ for this system. The maximum growth rate that corresponds to the wake deficit was not demonstrated for $w < -0.1$ as the results indicated that the increase of the wake effect would lead to a dramatic increase in the maximum growth rate, which would exceed 10^3 and therefore would become incomparable with the results that correspond to the jet case.

From Figure (4.23), it is observed that both increases in the wake and jet effect would lead to an increase in the instability of the system. Figure (4.24) indicates that the increase in the jet effect would lead to the movement of the location of the most unstable mode towards a higher position in the slower upper stream, whereas the increase of the wake effect would lead to the mode moving towards a lower position in the lower faster stream. Previously we have mentioned that thermal modes exist under the condition

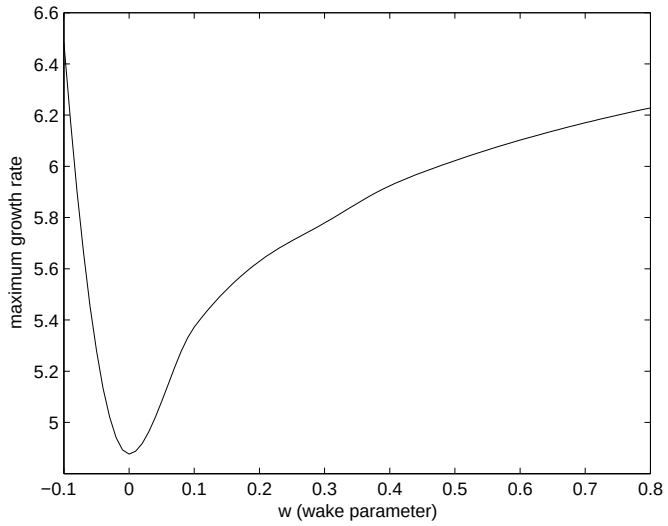

Figure 4.23: The variation of the maximum scaled growth rate, β_0 with the wake parameter, $w > 0$, for $\beta_u = 0.5$, $\beta_t = 0.01$, $M_{-\infty} = 0.2$, in the stably curved mixing layer.

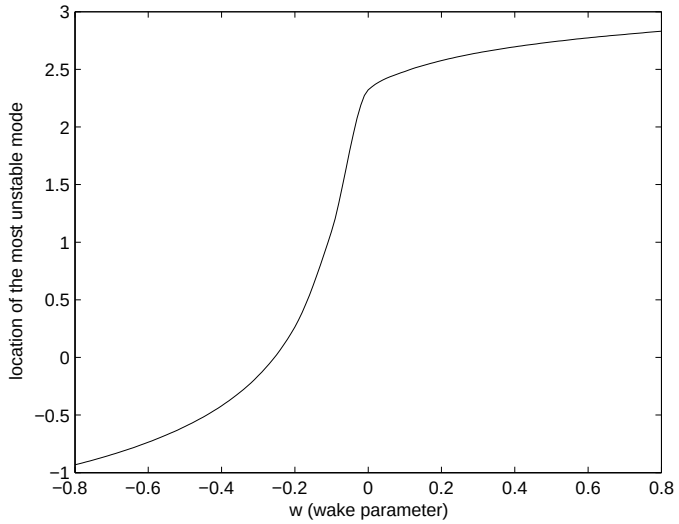

Figure 4.24: The variation of the location of the most unstable mode, η_b, with the wake parameter, $w > 0$, for $\beta_u = 0.5$, $\beta_t = 0.01$, $M_{-\infty} = 0.2$, in the stably curved mixing layer.

that β_t is below a critical value. With the fixed upper stream velocity and the lower stream Mach number, we could then analytically determine the critical value of β_t by using inequality (3.32). For the system with $\beta_t = 0.5$ and $M_{-\infty} = 0.2$, the critical value of β_t is predicted to be 0.334. Demonstrated in Figures (4.25) and (4.26), are the effect of increasing the upper stream temperature, β_t, on the maximum growth rates, β_0, and the locations of the most unstable mode, η_b, respectively, for different strengths of the positive wake component. β_u and $M_{-\infty}$ are fixed at the values stated previously for this system. It is observed from Figure (4.25) that the positive increase of the wake component leads to a slight increase in the maximum growth rate of the system which is consistent with the results demonstrated in Figure (4.23). Figure (4.26) indicates that the positive increase of the wake parameter leads to the slow upward movement of the location of the most unstable mode. This result also agrees with the previous result demonstrated in Figure (4.24).

So far we have investigated the effect of the jet on the thermal modes which were found previously within the stably curved mixing layers in the limit of large wave number. Based on the Gaussian wake profile prediction, we have seen that these modes which are found within the jet-dominated stably curved mixing layer have maintained similar characteristics of the thermal modes. We also observed that the positive increase of the wake parameter would destabilize the system.

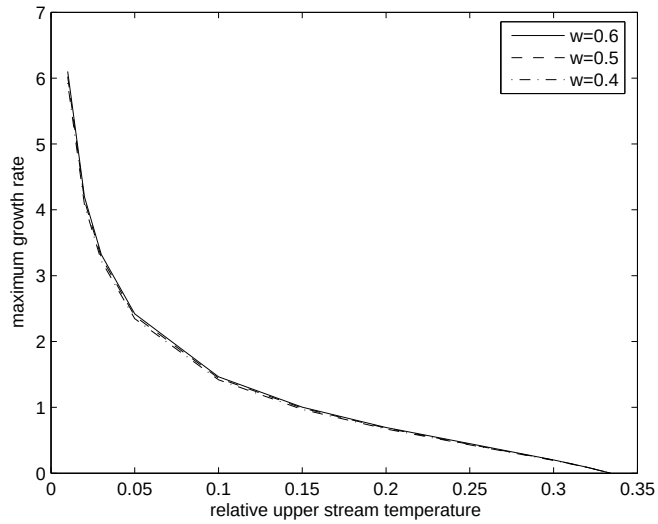

Figure 4.25: The variation of the maximum scaled growth rate, β_0, with the upper stream temperature, β_t, for $\beta_u = 0.5$, $M_{-\infty} = 0.2$, for $w = 0.4, 0.5, 0.6$, in the stably curved mixing layer.

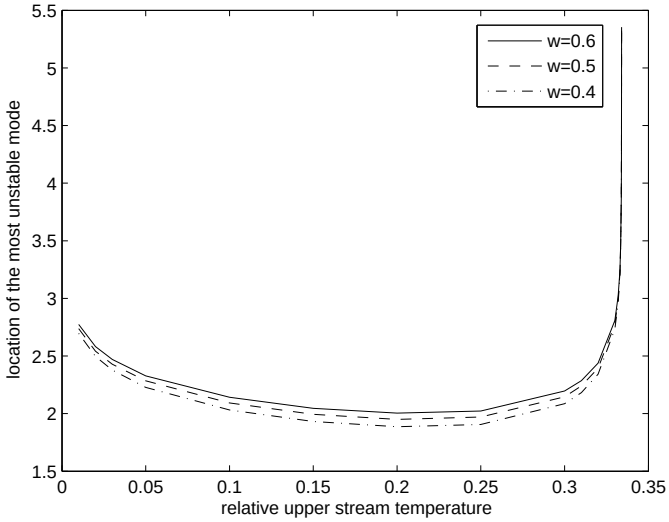

Figure 4.26: The variation of the location of the most unstable mode, η_b, with the upper stream temperature, β_t, for $\beta_u = 0.5$, $M_{-\infty} = 0.2$, for $w = 0.4, 0.5, 0.6$, in the stably curved mixing layer.

Recall that the previous investigation of Sarkies and Otto (2000) had produced an upper limit for β_t based on the fixed values of β_u and $M_{-\infty}$, such that the thermal modes could exist within the stably curved compressible mixing layers (inequality (3.32)). This condition for β_t was derived based on the fact that the basic streamwise velocity, $\overline{u}$, is restricted to the boundary conditions (i.e. inequality (3.30)) within the simple curved compressible mixing-layer system. However for the curved compressible mixing layers that are dominated by the wake ($w < 0$), the effect of the wake would cause rapid variation of the basic streamwise velocity near to the centreline of the layer. In this case the streamwise velocity is no longer restricted to the boundary conditions, so there will not be an upper limit for β_t such that the modes could exist within the system. The remaining question is: Will it be possible for the modes to exist within the stably curved case that are not restricted to the relative upper stream temperature being small? Previously in Chapter Two it was stated that the condition for the instability to exist within the system would depend on the leading-order eigenvalue $h = \beta_0^2(\eta)$ (equation (4.6)). Since the sign of the curvature $\tilde{\chi} = \pm 1$ corresponds to the unstably and stably curved systems, respectively, therefore the positive extremity of h would correspond to the location of the mode within the system that curves towards the lower faster stream (unstably curved case), whereas the negative extremity of h would correspond to the location of the mode within the system that curves towards the upper slower stream (stably curved case).

Demonstrated in Figures (4.27) and (4.28) is the effect of increasing the relative upper stream temperature ratio, β_t on the leading-order eigenvalue, h, for the simple curved compressible system ($w = 0$), and the curved compressible system which is dominated by the wake effect ($w < 0$), respectively. The basic flow parameters are fixed to be $\beta_u = 0.5$ and $M_{-\infty} = 0.2$ for these systems. It is observed from Figure (4.27) that a mode for $w = 0$ would appear within the concavely curved compressible system (centreline curving towards the slower upper stream) only for a short range of the relative upper stream temperature ratio and as β_t exceeds the upper limit bound for the thermal mode (for

this case the upper limit is $\beta_t = 0.334$), the mode would only appear within the convexly curved system. However within the wake-dominated curved compressible system, the results from Figure (4.28) for $w = -0.15$ indicates that the mode would appear within both convexly and concavely curved compressible systems which is not restricted to the relative upper stream temperature ratio being small.

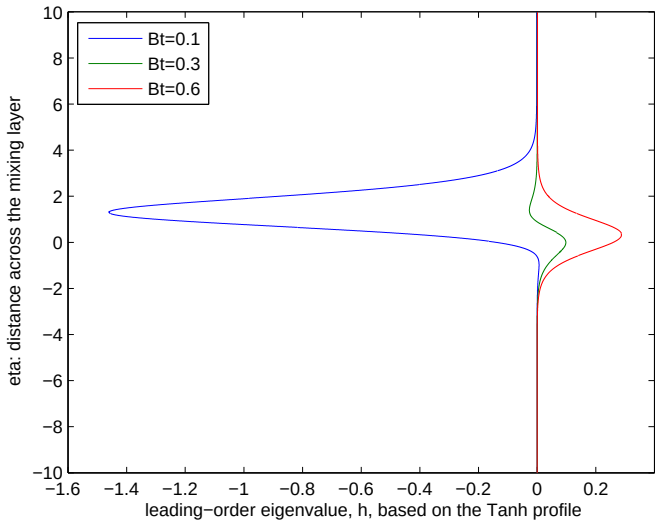

Figure 4.27: The variation of the leading-order eigenvalue function, $h(\eta)$, for a range of β_t, based on the Tanh profile within the curved compressible system, for $\beta_u = 0.5$, $M_{-\infty} = 0.2$.

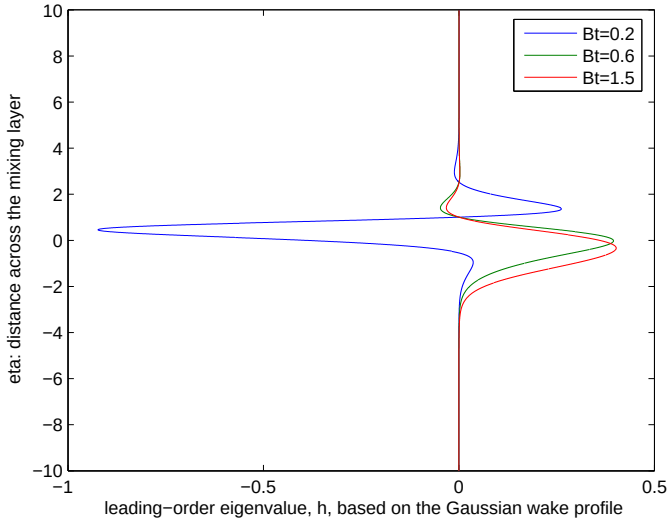

Figure 4.28: The variation of the leading-order eigenvalue function, $h(\eta)$, for a range of β_t, based on the Gaussian model with $w = -0.15$, within the wake-dominated curved compressible system, for $\beta_u = 0.5$, $M_{-\infty} = 0.2$.

Demonstrated in Figure (4.29) is the variation of the growth rate of the first mode, β_1, for a particular wave number, $a = 5$, for the stably curved compressible mixing-layer system under increasing wake effect. The basic flow parameters are fixed at $\beta_u = 0.5$, $\beta_t = 0.75$ and $M_{-\infty} = 0.2$. For comparison purposes, demonstrated within the same figure is the corresponding predictions for β_1 for the unstably curved case, which was previously demonstrated in Figure (4.8). The numerical solutions for β_1 were obtained from numerically solving the eigenvalue relation (4.2) based on the Gaussian model, by fixing the wave number $a = 5$ and $\tilde{\chi} = \pm 1$, respectively, for the unstably and the stably curved cases. The corresponding asymptotic predictions for β_1 were obtained from equation (4.7) by fixing $n = 1$ and $\tilde{\chi} = -1$ for the systems.

The results from Figure (4.29) indicate that the wake modes can exist within the stably wake-dominated curved compressible system, for β_t exceeding the upper limit for the thermal mode case within the plane curved compressible system, which obtain a different characteristic to the thermal mode. As the wake parameter increases, the growth rate of these modes behave in a similar way to the usual modes that are found within the corresponding unstably curved case. By comparing the growth rates of the modes within the unstably curved system to those of the stably curved system within the same figure, we see that the growth rates of the unstably curved wake modes are larger than the other case. Both numerical predictions agree well with the asymptotic results for $a >> 1$.

Demonstrated in Figure (4.30) are the corresponding asymptotic predictions of the variation of the location of the most unstable mode, η_b, and the maximum growth rate, β_0, with the wake parameter, w. The maximum scaled growth rates, β_0, for both the unstably and stably curved cases were obtained by solving equation (4.8) for $\tilde{\chi} = \pm 1$, respectively. The location of the modes, η_b, were obtained from equation (4.5) and verified using equation (4.6). The results indicate that as both the stably and unstably curved systems become more dominated by the wake, the location of the mode would shift towards the centreline of the layer with the mode for the unstably curved case situated closer to the

centreline of the system. The asymptotic predictions for the behaviour of the maximum growth rate within both systems also agree with the corresponding numerical predictions in Figure (4.29).

Demonstrated in Tables (4.2) and (4.3) are some of the exact predictions of the maximum scaled growth rate and the location of the unstable modes (taken from results in Figure (4.30)), which correspond to the increasing value of the wake deficit ($w < 0$), within the associated unstably and stably curved systems, respectively.

w within the unstably curved system	-0.65	-0.4	-0.2	-0.1	0
Scaled growth rate, β_0	2.1051	1.0134	0.7034	0.6116	0.5670
Location of the mode, η_b	-0.048	-0.1980	-0.13	0.0154	0.2703

Table 4.2: The maximum scaled growth rate, β_0, and the location of the mode, η_b, with w, within the unstably curved system.

w within the stably curved system	-0.65	-0.4	-0.3	-0.2	-0.1
Scaled growth rate, β_0	1.9617	0.7866	0.5555	0.3386	0.036
Location of the mode, η_b	0.574	0.93	1.068	1.258	1.744

Table 4.3: The maximum scaled growth rate, β_0, and the location of the mode, η_b, with w, within the stably curved system.

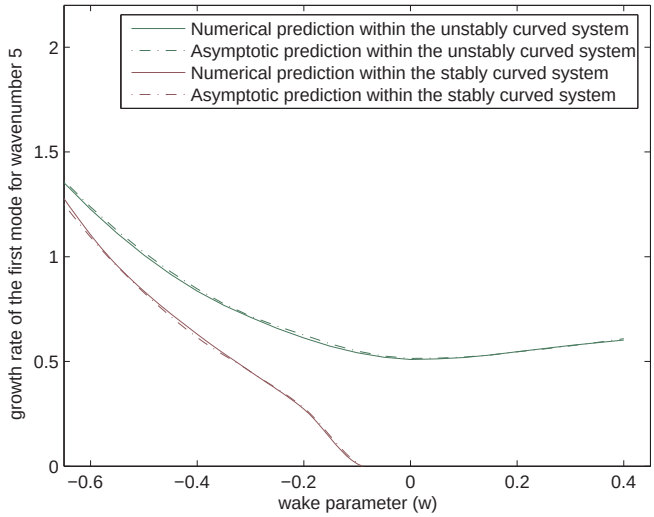

Figure 4.29: The variation of the growth rate of the first mode, β_1, for $a = 5$ with the wake parameter, for $\beta_u = 0.5$, $\beta_t = 0.75$ and $M_{-\infty} = 0.2$, based on the Gaussian model within the stably and unstably curved system.

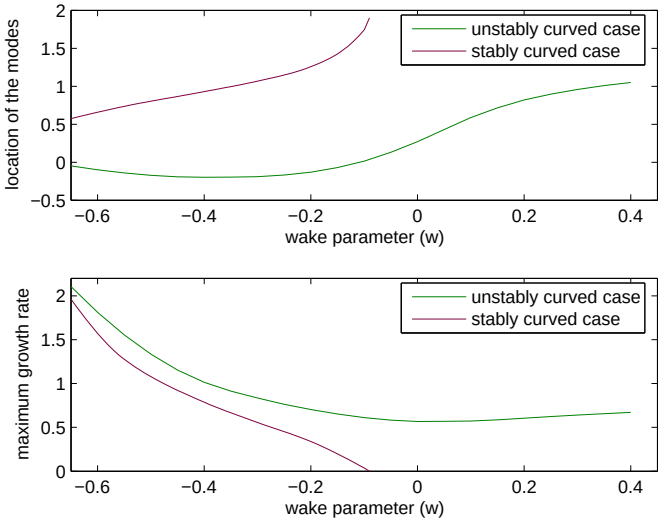

Figure 4.30: The variation of the location of the most unstable mode, η_b, and the maximum growth rate, β_0, with the wake parameter, for $\beta_u = 0.5$, $\beta_t = 0.75$ and $M_{-\infty} = 0.2$, based on the Gaussian model within the stably and unstably curved system.

Demonstrated in Figure (4.31) are the numerical solutions for first four unstable modes at a particular wave number, $a = 5$, with the fixed basic flow parameters for $w = -0.4$ within the same stably curved compressible mixing-layer system. The basic flow parameters are fixed at $\beta_u = 0.5$, $\beta_t = 0.75$ and $M_{-\infty} = 0.2$. The normal disturbance velocity, V, was normalised to have maximum 1 for these cases.

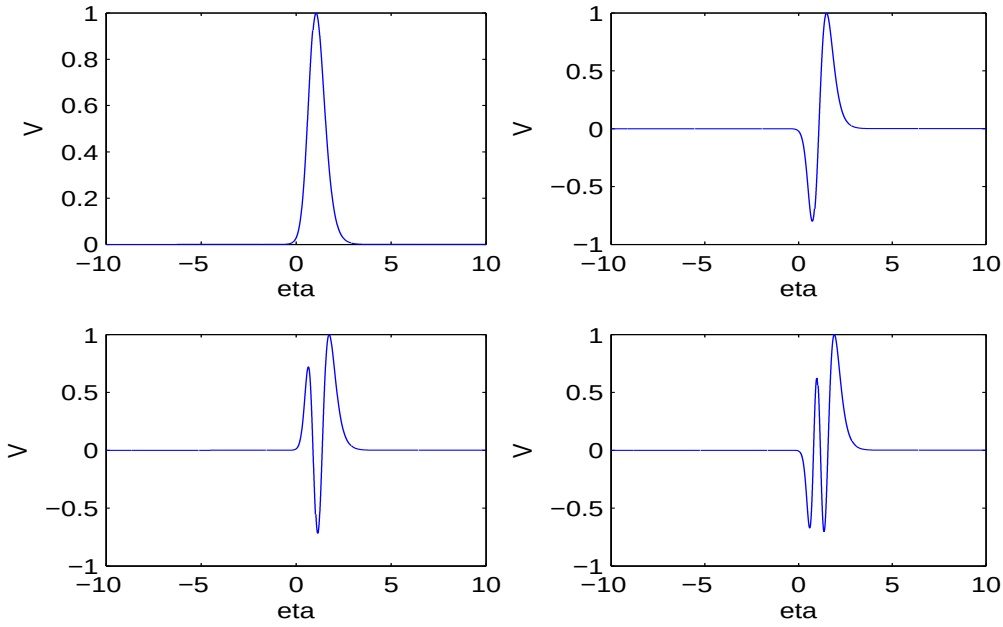

Figure 4.31: The first four inviscid modes, $\mathsf{V}(\eta)$, for $a = 5$ with $w = -0.4$, for $\beta_u = 0.5$, $\beta_t = 0.75$ and $M_{-\infty} = 0.2$, based the Gaussian model for $w = -0.4$, within the stably curved system. Numerical solution: solid line. Asymptotic solution: dotted line.

First unstable mode	Second unstable mode	Third unstable mode	Fourth unstable mode
$\beta_1 = 0.6297$	$\beta_2 = 0.4428$	$\beta_3 = 0.3381$	$\beta_4 = 0.2720$

Table 4.4: The growth rate of first four modes, β, for $a = 5$, $w = -0.4$, and $\beta_u = 0.5, \beta_t = 0.75, M_{-\infty} = 0.2$, within the stably curved system.

The growth rate which is associated with each of these modes was derived numerically

from solving the eigenvalue relation (4.2) based on $\tilde{\chi} = -1$, and is provided in the Table (4.4).

Based on the results for the growth rate of first four modes for $w = -0.4$, the effect of increasing wave number on the growth rate of the modes within the stably curved system was obtained from solving the the associated eigenvalue relation (4.2). The results are then demonstrated in Figure (4.32). The asymptotic predictions for $a >> 1$ are plotted within the same figure for comparison purposes, and they are represented by the dotted lines. It is observed from Figure (4.32) that as the wave number, a, increases the growth rates of the first four modes would tend to a constant, which is the asymptotic prediction of the maximum scaled growth, β_0. The numerical predictions are in good agreement with the corresponding asymptotic predictions.

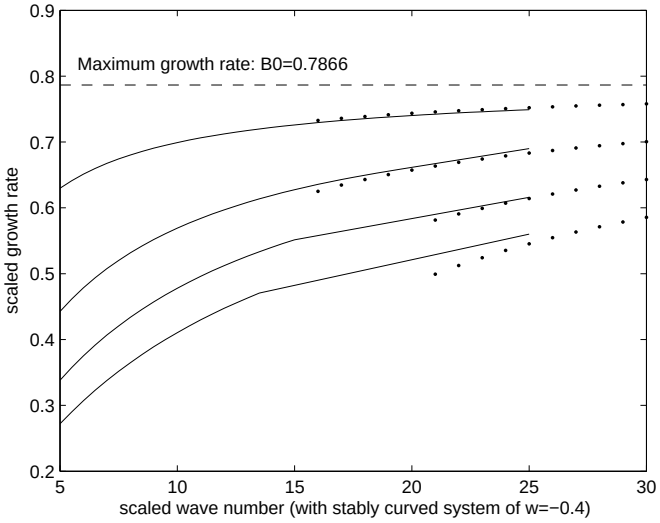

Figure 4.32: The variation of the growth rate of the first four modes, β, with the wave number, a, for $\beta_u = 0.5$, $\beta_t = 0.75$ and $M_{-\infty} = 0.2$, based the Gaussian model for $w = -0.4$, within the stably curved system. Numerical solution: solid line. Asymptotic solution: dotted line.

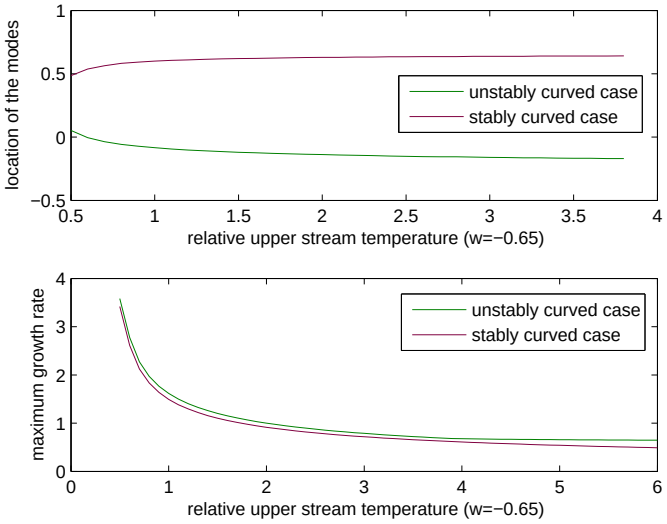

Figure 4.33: The variation of the location of the most unstable mode, η_b, and the maximum growth rate, β_0, with the relative upper stream temperature, β_t, for $\beta_u = 0.5$ and $M_{-\infty} = 0.2$, based on the Gaussian model for $w = -0.65$, within the stably and unstably curved system.

Demonstrated in Figure (4.33) are the asymptotic predictions ($a >> 1$) of the variation of the location of the most unstable mode, η_b, and the maximum growth rate, β_0, with the relative upper stream temperature, β_t, within both the stably and unstably curved wake-dominated systems of $w = -0.65$. The basic flow parameters for both systems are fixed to be $\beta_u = 0.5$ and $M_{-\infty} = 0.2$. The results indicate that the increase of the relative upper stream temperature has little effect on the location of the most unstable mode within both systems. By comparing the predictions within the stably and unstably curved cases, we see that the maximum growth rate would considerably increase for a decrease in β_t within both systems; and with the most unstable mode within the unstably curved system situated closer to the centreline of the system. It is also observed from Figure (4.33) that the maximum growth rate within the stably curved system are quite comparable with that of the unstably curved case.

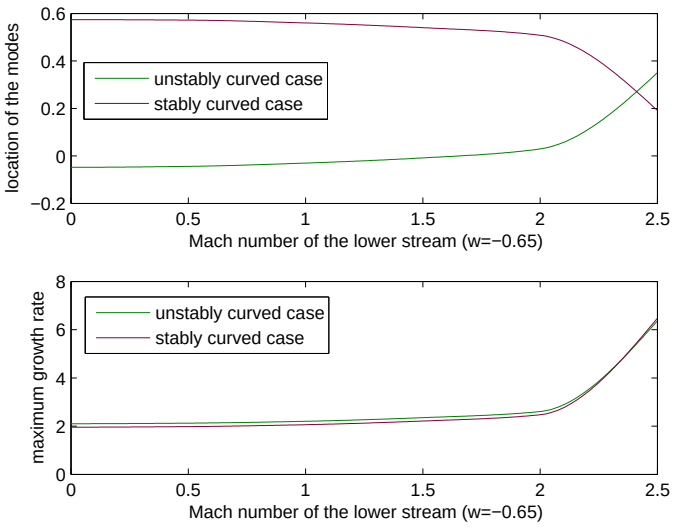

Figure 4.34: The variation of the location of the most unstable mode, η_b, and the maximum growth rate, β_0, with the lower stream Mach number, $M_{-\infty}$, for $\beta_u = 0.5$, $\beta_t = 0.75$, based on the Gaussian model for $w = -0.65$, within the stably and unstably curved system.

Demonstrated in Figure (4.34) is the asymptotic predictions of the variation of the location of the most unstable mode, η_b, and the maximum growth rate, β_0, with the lower stream Mach number, $M_{-\infty}$, within both stably and unstably curved wake-dominated systems of $w = -0.65$. The basic flow parameters for both systems are fixed to be $\beta_u = 0.5$ and $\beta_t = 0.75$. The result indicates that as the compressibility of both systems increases, the most unstable mode that is associated with the unstably curved system would move towards the upper stream direction whereas the mode within the stably curved system would move towards the lower stream direction. The maximum scaled growth rates that are associated with both systems behave similarly and are comparable, with both increasing considerably for the increased compressibility of the system.

4.1.3 The viscous right-hand branch modes based on the Gaussian model

In the previous chapter, we investigated the viscous right-hand branch modes within the plain curved compressible mixing-layer system, and discussed the importance for investigating the modes within such region. We now turn our attention onto the viscous right-hand branch for the wake-dominated unstably curved system to investigate the shape of the neutral curve and the effect of the wake on the behaviour of modes within this region.

The equations that would be used to determine the asymptotic predictions of the location and the growth rate of the right-hand branch modes would be in a slightly different form to the previous equations (3.25) and (3.26), which were obtained for the right-hand branch region within the plain curved mixing-layer system. The maximum growth rate, β_{00}, and the wave number, λ_0, are scaled as

$$\beta_{00} = \frac{\tilde{\beta}\sqrt{G_0}|\chi|^{1/2}}{X^{1/4}} \quad \text{and} \quad \lambda_0 = \frac{|\chi|^{1/4}\tilde{\lambda}}{X^{1/8}}.$$

The technique for obtaining β_{00} and η_v is similar to those demonstrated in Section (2.5), but based on the similarity variable, η, which represents the distance across the curved mixing layer system.

With the choice of basic flow profiles, we may obtain the variation of the scaled wave number, $\tilde{\lambda}$, with the location of the modes, η_v, and the maximum growth rate, $\tilde{\beta}$, respectively, from solving the following equations.

$$\overline{T}(\overline{u}\tilde{\beta} + \tilde{\lambda}^2\overline{T}^2)^2 - \tilde{\chi}\overline{T}'\overline{u}^2/(2\overline{T}) + \tilde{\chi}\overline{uu}' = 0, \tag{4.10}$$

and

$$\begin{aligned}\overline{T}'\left(\overline{u}\tilde{\beta} + \tilde{\lambda}^2\overline{T}^2\right)^2 + 2\overline{T}\left(\overline{u}\tilde{\beta} + \tilde{\lambda}^2\overline{T}^2\right)\left(\overline{u}'\tilde{\beta} + 2\tilde{\lambda}^2\overline{TT}'\right)\\ +\tilde{\chi}\left[-\overline{T}''\overline{u}^2/(2\overline{T}) - \overline{T}'\overline{uu}'/\overline{T} + \overline{T}'^2\overline{u}^2/(2\overline{T}^2) + \overline{u}'^2 + \overline{uu}''\right] = 0,\end{aligned} \tag{4.11}$$

where $'$ denotes the derivative with respect to η, $\frac{d}{d\eta}$, within the above equations. $\tilde{\chi}$ is the sign of χ, and $\tilde{\chi} = \pm 1$ corresponds to the unstably and unstably curved systems, respectively.

Demonstrated in Figures (4.35) and (4.36) are the variation with the scaled wave number, $\tilde{\lambda}$, of the scaled growth rate, $\tilde{\beta}$, and location of the modes, η_v, respectively, based on the Gaussian wake flow model within the right-hand viscous region for the unstably curved systems under the increasing wake effect. The basic flow parameters are fixed at $\beta_u = 0.5$, $\beta_t = 0.75$ and $M_{-\infty} = 0.2$, respectively.

The result from Figure (4.35) indicates an increase in the growth rate of the modes for the increased wake effect within the systems, which agrees with the previous prediction in the limit of high wave number within the intermediate region in Figure (4.9). The results also indicate that the growth rate, $\tilde{\beta}$, would decrease for an increase in the wave number, $\tilde{\lambda}$, which shows that the modes are stabilized by the viscosity effect within the unstably curved systems.

Figure (4.36) indicates that as the wave number increases the modes would move towards the lower faster stream. By comparing the results that correspond to the different wake effect within the systems, we see that the initial increase in the wake effect (w becoming more negative) would lead to the mode moving towards the lower stream direction and for larger effect of wake, $w = -0.65$, the mode would move back to be situated near to the centreline of the system.

As the wave number tends to zero from the viscous right-hand region, the mode is moving towards the inviscid region. The Gaussian model predictions for zero wave number in the viscous region of the scaled growth rate, $\tilde{\beta}$, and the location of the mode, η_v, that corresponds the each of the unstably curved systems are demonstrated in Table (4.5), which matches very well on to the inviscid modes (compare with Table (4.2)) within the corresponding unstably curved systems).

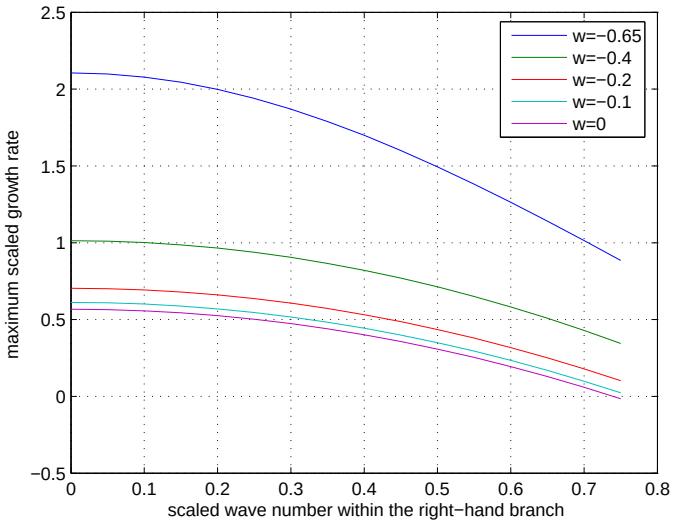

Figure 4.35: The variation of the scaled growth rate, $\tilde{\beta}$, with scaled wave number, $\tilde{\lambda}$, with fixed basic flow parameters $M_{-\infty} = 0.2$, $\beta_u = 0.5$ and $\beta_t = 0.75$ based on the Gaussian model for different wake parameter, w, within the unstably curved systems.

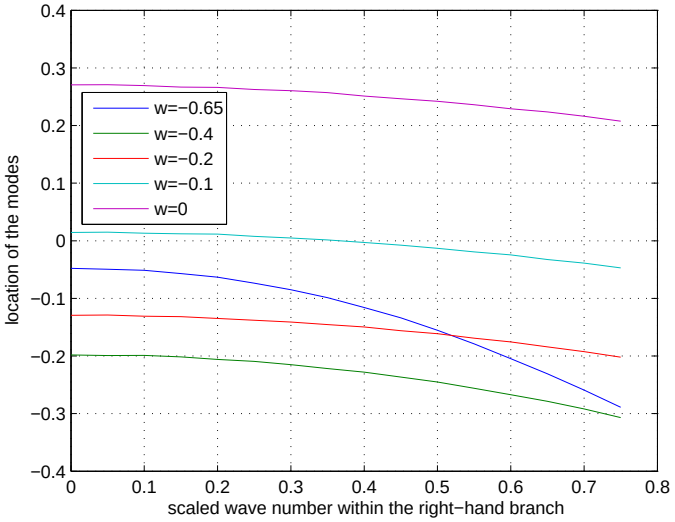

Figure 4.36: The variation of the most unstable mode, η_v, with scaled wave number, $\tilde{\lambda}$, with fixed basic flow parameters $M_{-\infty} = 0.2$, $\beta_u = 0.5$ and $\beta_t = 0.75$ based on the Gaussian model for different wake parameter, w, within the unstably curved systems.

Value of w within the system	-0.65	-0.4	-0.2	-0.1	0
$\tilde{\beta}$ for $\tilde{\lambda} = 0$	2.1051	1.0134	0.7034	0.6116	0.567
η_v for $\tilde{\lambda} = 0$	-0.0478	-0.1981	-0.1294	0.0145	0.2707

Table 4.5: The maximum scaled growth rate, $\tilde{\beta}$, and the location of the unstable mode, η_v, for $\tilde{\lambda} = 0$, with w, within the unstably curved systems.

Demonstrated in Figures (4.37) and (4.38) are the variation of the scaled wave number, $\tilde{\lambda}$, with the scaled growth rate, $\tilde{\beta}$, and location of the modes, η_v, respectively, based on the Gaussian wake flow model within the right-hand viscous region for the stably curved systems under the increasing wake effect. For these systems, the basic flow parameters remained fixed at $\beta_u = 0.5$, $\beta_t = 0.75$ and $M_{-\infty} = 0.2$, respectively.

The results from Figure (4.37) indicate an increase in the maximum growth rate, $\tilde{\beta}$, of the modes for the increased wake effect ($w < 0$) within the stably curved systems.

Figure (4.38) indicates that as the wave number, $\tilde{\lambda}$, increases the modes would move towards the slower upper stream. By comparing the results that correspond to the different wake effect within the systems, we see that the increase in the wake effect would lead to the mode moving towards the centreline of the system.

For zero wave number in the viscous region, the scaled growth rates and the location of the modes that correspond to these stably curved systems are demonstrated in Table (4.6). These results show an excellent agreement with the previous predictions of the inviscid modes (compare with Table (4.3)) within the corresponding stably curved systems).

Value of w within the system	-0.65	-0.4	-0.3	-0.2	-0.1
$\tilde{\beta}$ for $\tilde{\lambda} = 0$	1.9617	0.7866	0.5555	0.3386	0.036
η_v for $\tilde{\lambda} = 0$	0.574	0.9303	1.0688	1.2588	1.7436

Table 4.6: The maximum scaled growth rate, $\tilde{\beta}$, and the location of the unstable mode, η_v, for $\tilde{\lambda} = 0$, with w, within the stably curved systems.

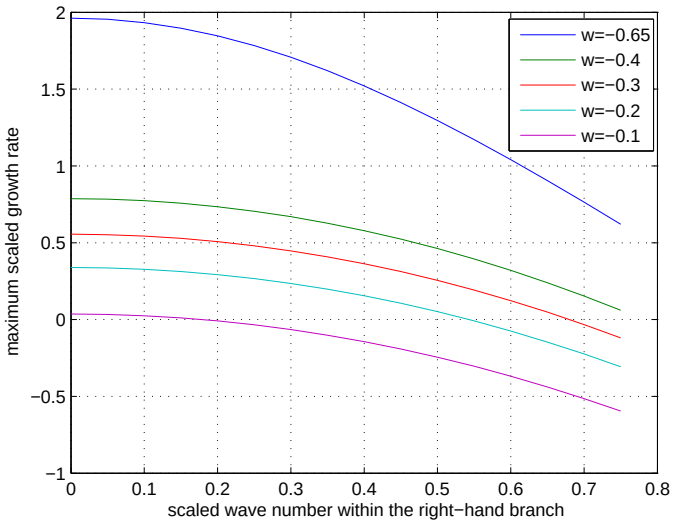

Figure 4.37: The variation of the scaled growth rate, $\tilde{\beta}$, with scaled wave number, $\tilde{\lambda}$, with fixed basic flow parameters $M_{-\infty} = 0.2$, $\beta_u = 0.5$ and $\beta_t = 0.75$ within the stably curved systems under the increasing wake effect.

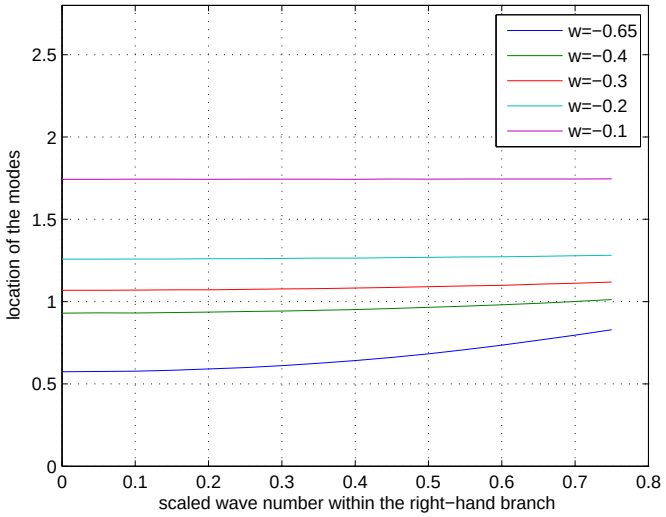

Figure 4.38: The variation of the most unstable mode, η_v, with scaled wave number, $\tilde{\lambda}$, with fixed basic flow parameters $M_{-\infty} = 0.2$, $\beta_u = 0.5$ and $\beta_t = 0.75$ within the stably curved systems under the increasing wake effect

4.2 Composite wake flow model and predictions

The composite model was initially designed by Liang et al. (1996) to correspond to an experiment performed at hypersonic speeds. This particular model was used to offer some theoretical predictions of the inviscid linear instability within the parallel mixing layer which was formed between two streams that are travelling at hypersonic speeds. The predictions were used to provide a means of instability observation made in the corresponding experiment. In the experiment, a sharp-lipped, long flat plate was placed parallel to the continuous air flow of Mach 8. The model was set up based on the faster stream travelling on the top of the lower stream. The prediction of the amplification rate of the instability within the system based on this model appeared to have some agreement with the corresponding experimental data. It was found that the stability characteristics of the developing portion of such a mixing layer differs significantly from that of the related self-similar flow. The difference lies not only in the magnitude of the growth rates but also in the character and number of the unstable modes, Liang, Reshotko, and Demetriades (1996).

Since this model had some practical applications, therefore it would be interesting to apply this model to our problem and to investigate its prediction of the linear Görtler instability within the non-parallel wake-dominated compressible mixing-layer system.

Similar to the construction of the Gaussian wake profile, the composite wake profile consists of the combination of a wake component on a self-similar free mixing layer with a Gropengiesser profile that was derived by Gropengiesser (1969) to model the variation of the basic streamwise velocity and the temperature across the free mixing-layer system.

The composite streamwise velocity and the temperature profile are given as

$$\overline{u} = U_{\text{wake}} U_{\text{fsl}} \quad \text{and} \quad \overline{T} = T_{\text{wake}} T_{\text{fsl}}, \tag{4.12}$$

respectively, with $(\,)_{\text{wake}}$ and $(\,)_{\text{fsl}}$ denoting the wake-like profile and the free shear layer profile respectively.

The Gropengiesser profile for the free mixing-layer system is given as

$$U_{\text{fsl}} = (1-\beta_u)\left[1-\left(\frac{1-\tanh(a(\eta-\eta_0))}{2}\right)^b\right]+\beta_u, \tag{4.13}$$

$$T_{\text{fsl}} = 1+\frac{\gamma-1}{2}M_{-\infty}^2\left(1-U_{\text{fsl}}^2\right)+\left(U_{\text{fsl}}-1\right)\left[\frac{1-\beta_t}{1-\beta_u}+\frac{\gamma-1}{2}M_{-\infty}^2\left(1+\beta_u\right)\right], \tag{4.14}$$

where $a = 0.307257$, $b = 3.69564$, and $\eta_0 = 2.127137$.

The wake-like profile is given by

$$U_{\text{wake}} = 1-\frac{1}{2}\exp\left(-Y^{''2}/\left(4X^{'}\right)\right)\left[\exp\left(a^{'2}\right)\text{erfc}\left(a^{'}\right)+\exp\left(b^{'2}\right)\text{erfc}\left(b^{'}\right)\right], \tag{4.15}$$

$$T_{\text{wake}} = 1+B\left(1-U_{\text{wake}}\right)+\frac{C}{2}\exp\left(-Y^{''2}/\left(4X^{'}\right)\right)\left[\exp\left(c^{'2}\right)\text{erfc}\left(c^{'}\right)+\exp\left(d^{'2}\right)\text{erfc}\left(d^{'}\right)\right], \tag{4.16}$$

where

$$a^{'} = (\widehat{P}^{'}+1)\sqrt{X^{'}}+Y^{''}/2\sqrt{X^{'}}, \qquad b^{'} = \tfrac{\widehat{P}^{'}+1}{\widehat{P}^{'}}\sqrt{X^{'}}-Y^{''}/2\sqrt{X^{'}},$$
$$c^{'} = 2(\widehat{P}^{'}+1)\sqrt{X^{'}}+Y^{''}/2\sqrt{X^{'}}, \qquad d^{'} = 2\tfrac{\widehat{P}^{'}+1}{\widehat{P}^{'}}\sqrt{X^{'}}-Y^{''}/2\sqrt{X^{'}},$$
$$B = \tfrac{\gamma-1}{2}M_{-\infty}^2U_{\text{fsl}}T_{\text{fsl}}^{-1/2}+T_w/T_{\text{fsl}}-1, \qquad C = -\tfrac{\gamma-1}{2}M_{-\infty}^2U_{\text{fsl}}T_{\text{fsl}}^{-1/2},$$

and

$$\widehat{P}^{'} = \frac{\theta_1}{\theta_2}\beta_t,$$

that is defined as the asymmetric parameter with θ_1 and θ_2 denoting the momentum thickness of the lower and the upper layer, respectively.

For the experiment, $\widehat{P}^{'}$ was measured to be 2.41. The system that was set up by Liang, Reshotko, and Demetriades (1996) consists of faster stream above the slower stream therefore for our problem the system needs to be reflected in y^* (refer to Figure (2.2)). For this case the basic flow parameters are fixed to be

$$\beta_u = 0.585, \quad \beta_t = 2.46, \quad M_{-\infty} = 8, \quad \gamma = 1.4.$$

T_w denotes the partition temperature and is fixed to be $T_w = 10$. The asymmetric parameter is fixed to be $\widehat{P}^{'} = 2.41$.

$X^{'}$ and $Y^{'}$ represent the non-dimensional distance beyond the trailing edge and the non-dimensional lateral distance, respectively. $X^{'}$ and $Y^{'}$ are scaled as

$$X^{'} = \frac{x^*}{\theta}\frac{1}{\theta Re_1}, \tag{4.17}$$

and

$$Y^{'} = \frac{1}{\theta}\int_0^{y^*} \overline{\rho} dy^*, \tag{4.18}$$

where $Re_1 = Re/L$ is the unit Reynolds number of the faster lower stream and θ is the total momentum thickness of the two streams at the partition trailing edge, such that $\theta = \theta_1 + \theta_2$. x^* and y^* represent the dimensional distance beyond the trailing edge and the lateral distances, respectively. It could be seen that the Howarth-Dorodnitsyn transformation was also involved in non-dimensionalising y^*.

η denotes the non-dimensional variable in the free mixing-layer analysis and is expressed as

$$\eta = \frac{Y^{'} - Y^{'}_m}{\sqrt{X^{'}}},$$

where $Y^{'}_m$ denotes the location of the minimum wake velocity along $Y^{'}$, which is the value of $Y^{'}$ by zeroing the $Y^{'}$ derivative of equation (4.15).

Demonstrated in Figure (4.39) is the variation of the location of the wake minimum, $Y^{'}_m$, with increasing distance from the trailing edge, $X^{'}$.

$Y^{''}$ also represents the non-dimensional lateral distance and is in terms of

$$Y^{''} = \frac{Y' + (S-1)Y^{'}_m}{S},$$

where S denotes the stretching factor which is an input parameter. Previously Brower and Demetriades (1990) had obtained a laminar boundary-layer velocity profile for the accelerating flow of a supersonic nozzle and found that the profile would fit quite well with the experiment by taking $S = 1.8$. Demetriades' reason for defining a new variable, $Y^{''}$ is that if $Y^{'}$ was directly stretched by S, the profile would then be stretched about the zero

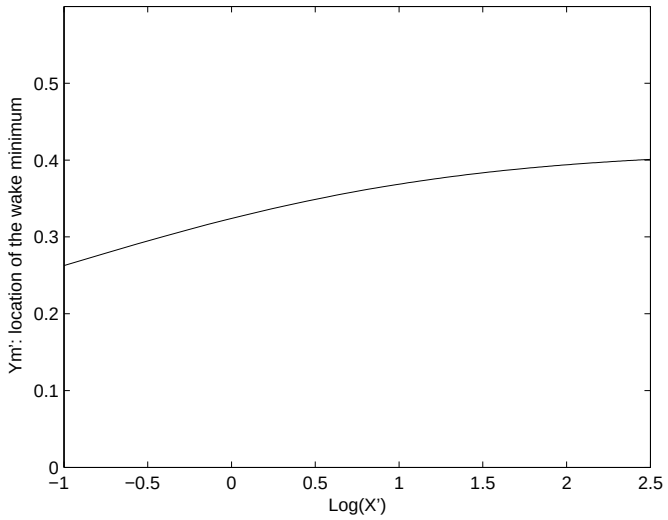

Figure 4.39: The variation of the location of the wake minimum, $Y_m^{'}$, with the distance from the trailing edge, $X^{'}$, based on the composite model with $\beta_u = 0.585$.

streamline $y^* = Y^{'} = 0$, therefore it would be more reasonable to apply the stretching about the wake minimum at $Y_m^{'}$.

Demonstrated in Figures (4.40) and (4.41) are the variation of the basic streamwise velocity and temperature across the mixing-layer system with the increasing distance from the trailing edge, $X^{'}$, respectively, evaluated from (4.12).

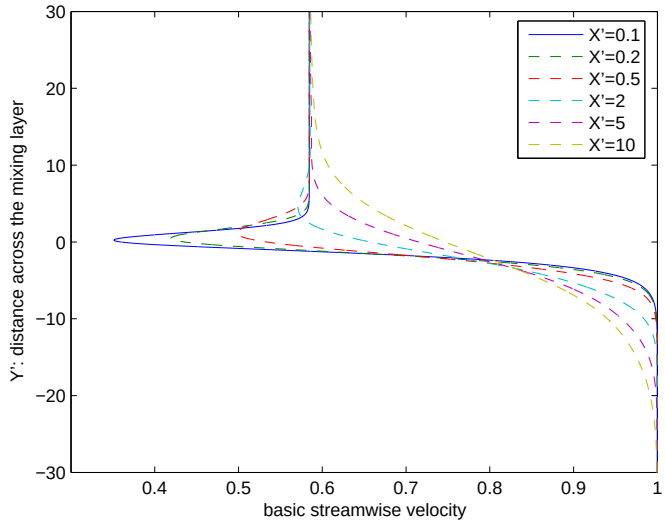

Figure 4.40: The variation of the basic streamwise velocity, $\overline{u}(Y')$, with distance downstream from the trailing edge, X', based on the composite model with $\beta_u = 0.585$.

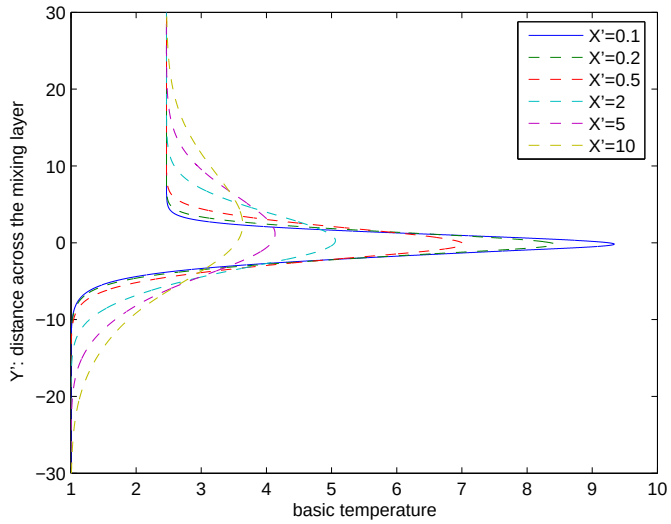

Figure 4.41: The variation of the basic temperature, $\overline{T}(Y')$, with distance downstream from the trailing edge, X', based on the composite model with $\beta_u = 0.585$, $\beta_t = 2.46$ and $M_{-\infty} = 8$.

4.2.1 Inviscid mode analysis based on the composite model

To investigate the behaviour of the inviscid Görtler mode based on the composite model, recall our eigenvalue relation, equation (2.51), which was set up previously for the curved compressible wake-dominated system in Chapter Two

$$\frac{\partial^2 \mathsf{V}}{\partial \overline{Y}^2} - \frac{\partial \mathsf{V}}{\partial \overline{Y}} \left(\frac{2\frac{\partial \overline{T}}{\partial \overline{Y}}}{\overline{T}} \right) + \mathsf{V} \left[-\widehat{a}^2 \overline{T}^2 - \frac{\frac{\partial^2 \overline{u}}{\partial \overline{Y}^2}}{\overline{u}} + \frac{2\frac{\partial \overline{T}}{\partial \overline{Y}}}{\overline{T}} \frac{\frac{\partial \overline{u}}{\partial \overline{Y}}}{\overline{u}} - \frac{\tilde{\chi}|\chi|\widehat{a}^2}{\widehat{\beta}^2} \left(\overline{T} \frac{\frac{\partial \overline{u}}{\partial \overline{Y}}}{\overline{u}} - \frac{\frac{\partial \overline{T}}{\partial \overline{Y}}}{2} \right) \right] = 0, \quad (4.19)$$

with the associated boundary conditions given as

$$\mathsf{V} \sim e^{-\widehat{a}\beta_t \overline{Y}}, \quad \text{as} \quad \overline{Y} \to \infty,$$

and

$$\mathsf{V} \sim e^{\widehat{a}\overline{Y}}, \quad \text{as} \quad \overline{Y} \to -\infty,$$

with $\tilde{\chi} = \pm 1$ denoting the unstably and stably curved cases, respectively. Previously the system was set up based on $\overline{Y}$ denoting the non-dimensionalised normal or lateral distance, which was the Howarth-Dorodnitsyn transformation variable. We notice that within the formulation of the composite model, the non-dimensionalised distance from the trailing edge and the normal distance were taken to be $X^{'}$ and $Y^{'}$, respectively (see equations (4.17) and (4.18)), and they are scaled based on the momentum of thickness term, θ, such that

$$\theta = \theta_1 + \theta_2, \quad (4.20)$$

where θ_1 and θ_2 are defined as the momentum thickness of the lower and the upper layer, respectively. Based on the previous mixing-layer scalings for the system in Section (2.2), the momentum of thicknesses for the lower and the upper layer are obtained as

$$\theta_1 = \int_0^\infty \frac{\rho^* u^*}{\rho_{-\infty} U_{-\infty}} \left(1 - \frac{u^*}{U_{-\infty}} \right) dy^*, \quad (4.21)$$

and

$$\theta_2 = \int_0^\infty \frac{\beta_t \rho^* u^*}{\rho_{-\infty} \beta_u U_{-\infty}} \left(1 - \frac{u^*}{\beta_u U_{-\infty}} \right) dy^*. \quad (4.22)$$

By non-dimensionalising and transforming the above equations (4.21) and (4.22), based on the Howarth-Dorodnitsyn transformation variable (2.31), we now have

$$\theta_1 = LRe^{-1/2}\int_0^\infty \overline{u}\,(1-\overline{u})\,d\overline{Y} \quad \text{and} \quad \theta_2 = LRe^{-1/2}\beta_t\int_0^\infty \overline{u}\,(1-\overline{u})\,d\overline{Y}. \tag{4.23}$$

By substituting the above expressions into equation (4.20), the total momentum of thickness, θ, becomes

$$\theta = LRe^{-1/2}\,(1+\beta_t)\int_0^\infty \overline{u}\,(1-\overline{u})\,d\overline{Y} = LRe^{-1/2}\widehat{\theta}, \tag{4.24}$$

where $\widehat{\theta}$ is the newly defined variable, such that

$$\widehat{\theta} = (1+\beta_t)\int_0^\infty \overline{u}\,(1-\overline{u})\,d\overline{Y}. \tag{4.25}$$

Recall the scales of $Y^{'}$ and $X^{'}$ in equations (4.17) and (4.18), respectively, by non-dimensionalising and applying the Howarth-Dorodnitsyn transformation onto the right-hand side of these equations, we may obtain

$$Y^{'} = \frac{1}{\theta}\int_0^{y^*} \overline{\rho}dy^* = \frac{\overline{Y}}{\widehat{\theta}}, \tag{4.26}$$

and

$$X^{'} = \frac{x^*}{\theta}\frac{1}{\theta Re_1} = \frac{X}{\widehat{\theta}^2} \tag{4.27}$$

The existence of θ would complicate the eigenvalue relation (2.51) for our system. A convenient way to avoid θ within our problem is to re-scale the growth rate, $\widehat{\beta}$, and the wave number, $\widehat{a}$, as

$$\widehat{\beta} = \frac{1}{\sqrt{\widehat{\theta}}}\beta^{'}|\chi|^{1/2}, \quad \text{and} \quad \widehat{a} = \frac{1}{\widehat{\theta}}a^{'}, \tag{4.28}$$

respectively, so that after the transformation the eigenvalue relation is

$$\frac{\partial^2 \mathsf{V}}{\partial Y^{'2}} - \frac{\partial \mathsf{V}}{\partial Y^{'}}\left(\frac{2\frac{\partial \overline{T}}{\partial Y^{'}}}{\overline{T}}\right) + \mathsf{V}\left[-a^{'2}\overline{T}^2 - \frac{\frac{\partial^2 \overline{u}}{\partial Y^{'2}}}{\overline{u}} + 2\frac{\frac{\partial \overline{T}}{\partial Y^{'}}}{\overline{T}}\frac{\frac{\partial \overline{u}}{\partial Y^{'}}}{\overline{u}} - \frac{\tilde{\chi}a^{'2}}{\beta^{'2}}\left(\overline{T}\frac{\frac{\partial \overline{u}}{\partial Y^{'}}}{\overline{u}} - \frac{\frac{\partial \overline{T}}{\partial Y^{'}}}{2}\right)\right] = 0, \tag{4.29}$$

with the boundary conditions given as

$$\mathsf{V} \sim e^{-a^{'}\beta_t Y^{'}}, \quad \text{as} \quad Y^{'} \to \infty,$$

and

$$\mathsf{V} \sim e^{a^{'}Y^{'}}, \quad \text{as} \quad Y^{'} \to -\infty,$$

which would remain in the same form as the original eigenvalue relation, with $\tilde{\chi} = \pm 1$ correspond to the behaviour of the inviscid Görtler modes within the unstably and stably curved systems, respectively.

The equations for determining the location and maximum scaled growth rate of the mode could be obtained by using the method of asymptotic expansion from the high wave number analysis, which was demonstrated in Section (2.4). We now assume that the mode will be localized at some location, $Y_b^{'}$ and consider the solution in a narrow layer there. By using the technique of asymptotic expansion, at leading-order we may obtain the equation for deriving the maximum scaled growth rate, β_0, and it is given as

$$\beta_0 = \left[\tilde{\chi} \left(\frac{\frac{\partial \overline{T}}{\partial Y^{'}}}{2\overline{T}^2} - \frac{\frac{\partial \overline{u}}{\partial Y^{'}}}{\overline{T}\overline{u}} \right) \right]^{1/2}, \tag{4.30}$$

where the basic flow quantities are evaluated at $(X, Y_b^{'})$.

The location of the mode within the unstably and stably curved systems can be obtained by searching for the maximum and minimum, respectively, of the leading-order eigenvalue

$$h = \beta_0^2(X, Y^{'}). \tag{4.31}$$

At the next order of the associated eigenvalue relation (4.29), we then obtained $\beta_1 = 0$, which shows that as $a^{'} \to \infty$, the growth rate would tend to a constant value, β_0, to second order. We also obtain

$$\overline{T}\frac{\partial^2 \overline{T}}{\partial Y^{'2}}\overline{u}^2 - 2\overline{u}\frac{\partial^2 \overline{u}}{\partial Y^{'2}}\overline{T}^2 + 2\overline{u}\frac{\partial \overline{u}}{\partial Y^{'}}\overline{T}\frac{\partial \overline{T}}{\partial Y^{'}} + 2\frac{\partial \overline{u}}{\partial Y^{'}}^2\overline{T}^2 - 2\frac{\partial \overline{T}}{\partial Y^{'}}^2\overline{u}^2 = 0, \tag{4.32}$$

where the basic flow quantities are evaluated at $(X, Y_b^{'})$. Equation (4.32) is the alternative equation for determining the location of the mode, $Y_b^{'}$.

Demonstrated in Figure (4.42) are the first four inviscid modes, $\mathsf{V}(0.5, Y^{'})$, within the unstably curved ($\tilde{\chi} = 1$) wake-dominated system for $X^{'} = 0.5$, based on a particular wave number, $a^{'} = 0.5$, which was obtained by numerically solving the associated eigenvalue relation (4.29). The basic flow parameters are set to be $\beta_u = 0.585$, $\beta_t = 2.46$ and $M_{-\infty} = 8$ for this system.

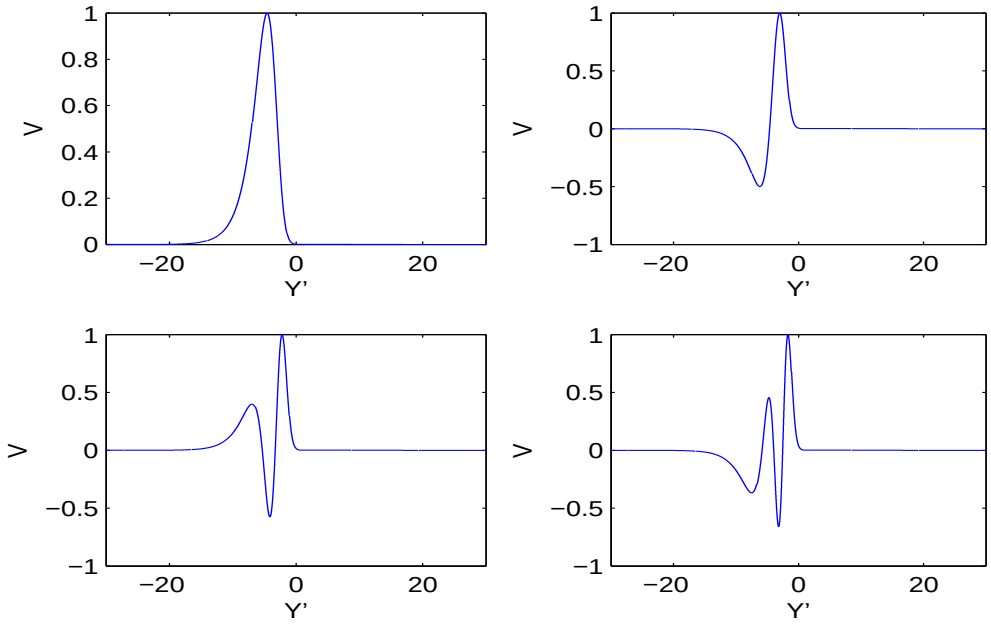

Figure 4.42: The first four inviscid modes, $\mathsf{V}(0.5, Y^{'})$, for $a^{'} = 0.5$, $\beta_u = 0.585$, $\beta_t = 2.46$, $M_{-\infty} = 8$, within the unstably curved system for $X^{'} = 0.5$.

The corresponding growth rate of the first four modes (demonstrated in Figure (4.42)) are demonstrated in Table (4.7).

The derivatives of $\overline{u}$ and $\overline{T}$ that were required to solve the eigenvalue relation were obtained from calculating the exact derivatives with respect to $Y^{'}$ from the associated equations. Due to the length of the equations for the derivatives, they are not going to be presented in this project.

First unstable mode	Second unstable mode	Third unstable mode	Fourth unstable mode
$\beta_1 = 0.2598$	$\beta_2 = 0.2145$	$\beta_3 = 0.1847$	$\beta_4 = 0.1624$

Table 4.7: The growth rate of first four modes, β, for $a^{'} = 0.5$, and $\beta_u = 0.585, \beta_t = 2.46, M_{-\infty} = 8$, based on the composite model with $X^{'} = 0.5$, within the unstably curved system.

We also plot in Figure (4.43) the first four inviscid modes, $\mathsf{V}(0.5, Y^{'})$, within the stably curved ($\tilde{\chi} = -1$) wake-dominated system for $X^{'} = 0.5$, based on a particular wave number, $a^{'} = 0.5$. These results were obtained by numerically solving the associated eigenvalue relation (4.29), based on $\tilde{\chi} = -1$ for the stably curved system. The basic flow parameters are set to be $\beta_u = 0.585$, $\beta_t = 2.46$ and $M_{-\infty} = 8$ for this system.

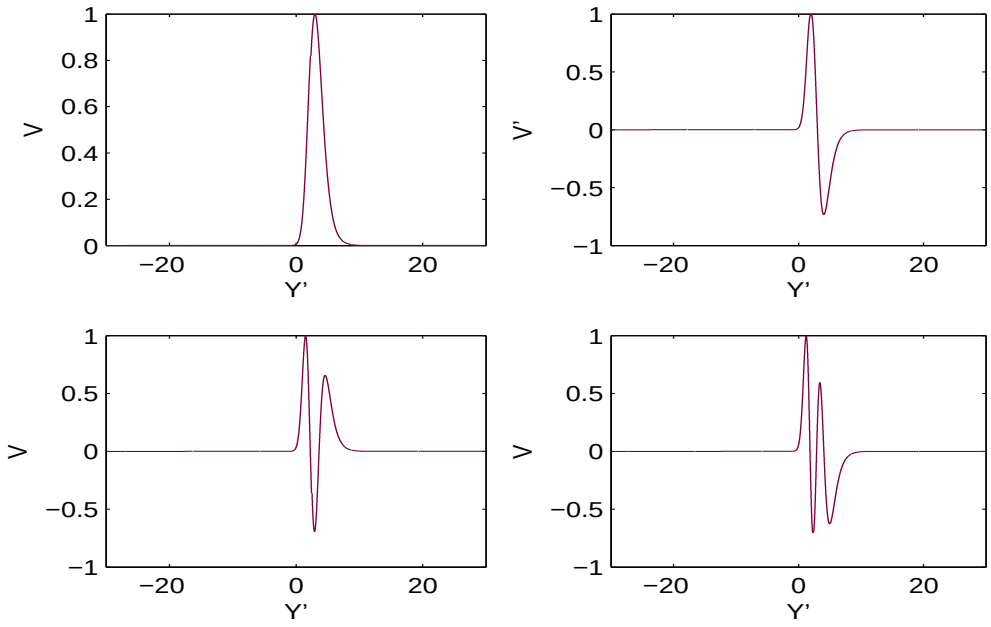

Figure 4.43: The first four inviscid modes, $\mathsf{V}(0.5, Y^{'})$, for $a^{'} = 0.5$, $\beta_u = 0.585$, $\beta_t = 2.46$, $M_{-\infty} = 8$, within the stably curved system for $X^{'} = 0.5$.

The growth rate of the first four modes (demonstrated in Figure (4.43)) within the associated stably curved system are demonstrated in Table (4.8).

First unstable mode	Second unstable mode	Third unstable mode	Fourth unstable mode
$\beta_1 = 0.1929$	$\beta_2 = 0.1611$	$\beta_3 = 0.1372$	$\beta_4 = 0.1187$

Table 4.8: The growth rate of first four modes, β, for $a^{'} = 0.5$, and $\beta_u = 0.585, \beta_t = 2.46, M_{-\infty} = 8$, based on the composite model with $X^{'} = 0.5$, within the stably curved system.

We had several attempts to use our numerical scheme to calculate the variation of the increasing wave number, $a^{'}$, on the scaled growth rate of the first four modes within both the stably and the unstably curved systems based on the results from Table (4.7) and (4.8), but were unable to progress further. Based on the large Mach number of the lower stream, $M_{-\infty} = 8$, which was fixed for the composite model, the variation of the scaled growth rate for the first four modes could only be obtained corresponding to a very small step size in the wave number, $a^{'}$. Another difficulty we have encountered is that the composite model was set up on a domain between $Y^{'} = \pm 30$, therefore within each iteration the system would have to be integrated from $Y^{'} = \pm 30$ to 0, based on a relatively small step size, which was found to be time-consuming.

The effect of increasing the distance from the trailing edge, $X^{'}$, on the first mode, $\mathsf{V}(X^{'}, Y^{'})$, for a particular wave number, $a^{'} = 0.5$, within the stably curved system is demonstrated in Figure (4.44). It is observed that as the wake effect gets larger (i.e. decrease in $X^{'}$), the mode would move towards the centreline of the stably curved system.

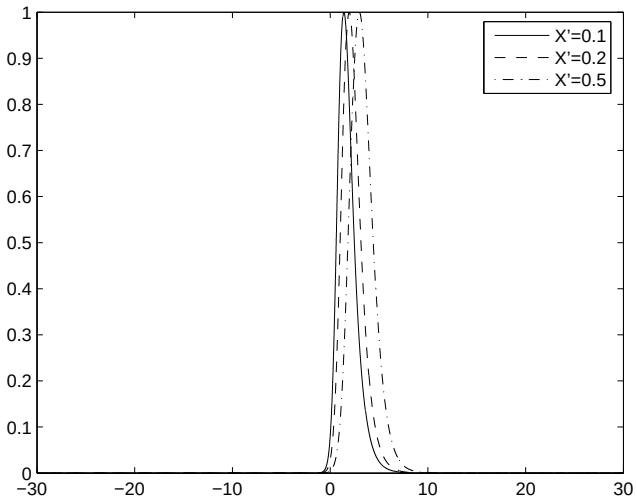

Figure 4.44: The first inviscid modes, $\mathsf{V}(X, Y^{'})$, for $a^{'} = 0.5$, $\beta_u = 0.585$, $\beta_t = 2.46$, $M_{-\infty} = 8$, based on the composite model with the increase in $X^{'}$.

The effect of increasing the wake on the general behaviour of the Görtler modes within both the stably curved and the unstably curved systems are demonstrated in Figures (4.45) and (4.46), respectively, which are the corresponding asymptotic predictions ($a^{'} >> 1$) of the maximum growth rate, β_0, and the variation of the location of the most unstable mode, Y'_b, with $X^{'}$, respectively. These results were obtained from solving equations (4.30) and (4.32), respectively. The predictions of the location of the modes, η_b, was also verified by the leading-order eigenvalue function (4.31). The basic flow parameters are fixed at $\beta_u = 0.585$, $\beta_t = 2.46$, and $M_{-\infty} = 8$.

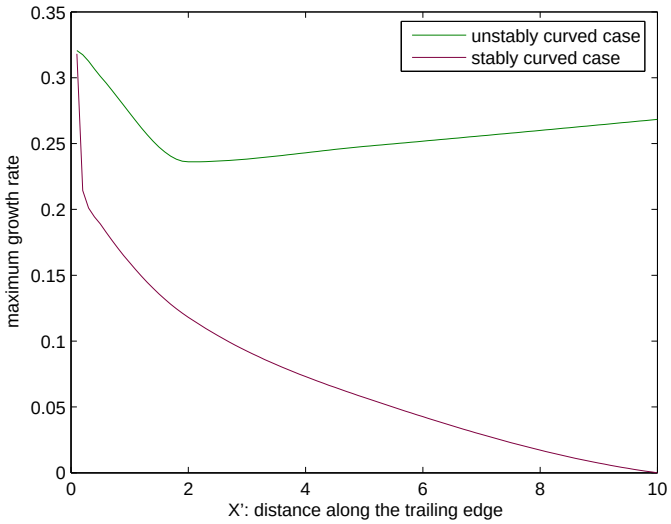

Figure 4.45: The variation of the maximum growth rate, β_0, with distance downstream from the trailing edge, $X^{'}$, based on the composite model with $\beta_u = 0.585$, $\beta_t = 2.46$ and $M_{-\infty} = 8$.

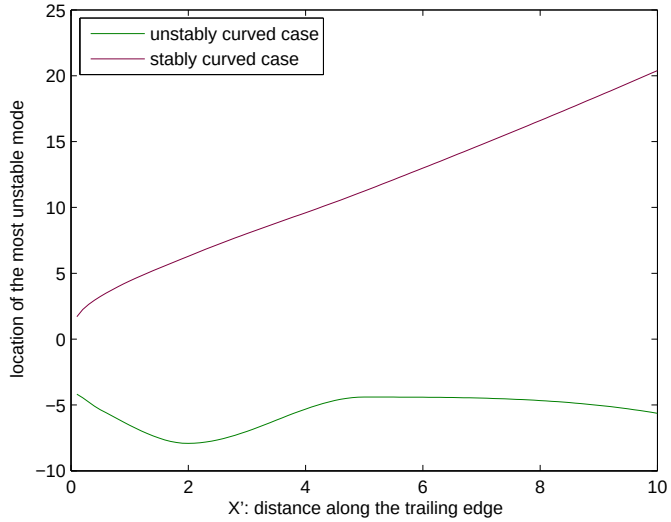

Figure 4.46: The variation of the location of the most unstable mode, $Y_b^{'}$, with distance downstream from the trailing edge, $X^{'}$, based on the composite model with $\beta_u = 0.585$, $\beta_t = 2.46$ and $M_{-\infty} = 8$.

It is observed from Figure (4.45) that the initial decrease of the wake effect (i.e. increase in X') would generally decrease the growth rate of the Görtler disturbance within both stably and unstably curved systems. However as the wake effect continues to decrease the growth rate of the disturbances would slightly increase within the unstably curved system, whereas within the stably curved system, the growth rate continues to decrease. This prediction differs slightly from the previous Gaussian wake profile prediction in Figure (4.30), for the parameters that have been considered for this case, with the previous profile predicting that the increase of the wake effect would render both systems more unstable.

Results from Figure (4.45) indicate that as the wake effect gets larger, the most unstable modes within both systems would move towards the centreline of the systems. A slight different prediction within the unstably curved system was offered by the composite profile in comparison the Gaussian wake profile prediction in Figure (4.30), based on the different basic flow parameters. The composite model predicted a slight downward movement of the modes for X' between 2 and 5, whereas for the Gaussian model this behaviour was not predicted.

Demonstrated in Tables (4.9) and (4.10) are some of the exact predictions of the maximum scaled growth rate and the location of the unstable modes (taken from results in Figures (4.45) and (4.46)), which correspond to the increasing wake effect (decrease in $X^{'}$), within the associated unstably and stably curved systems, respectively.

Distance along the trailing edge, $X^{'}$	0.2	0.5	2	5	10
Scaled growth rate, β_0	0.3175	0.3011	0.2361	0.2478	0.2684
Location of the mode, $Y_b^{'}$	-4.458	-5.358	-7.918	-4.4	-5.628

Table 4.9: The maximum scaled growth rate, β_0, and the location of the mode, $Y_b^{'}$, with $X^{'}$, within the unstably curved system.

Distance along the trailing edge, $X^{'}$	0.2	0.5	2	5	10
Scaled growth rate, β_0	0.2143	0.1890	0.1181	0.0572	0
Location of the mode, $Y_b^{'}$	2.244	3.2340	6.294	11.24	20.3960

Table 4.10: The maximum scaled growth rate, β_0, and the location of the mode, $Y_b^{'}$, with $X^{'}$, within the stably curved system.

A particular disadvantage of the application of the composite model is that the model was derived based on the fixed basic flow parameters which were previously set for experimental purpose therefore the composite model is less flexible in comparison with the Gaussian wake model when it comes to the general prediction of the behaviour of the system.

4.2.2 The right-hand branch mode based on the composite model

To investigate the behaviour of the viscous modes based on the composite model in the region of the right-hand branch, we are going to use the same method of asymptotic expansion which was demonstrated in Section (2.5).

The Görtler number is expanded as

$$G = \widehat{a}^4(G_0 + \widehat{a}^{-1/2}G_1 + O(\widehat{a}^{-1})).$$

The modes are localized at location, Y_b, we consider a solution in a narrow layer at Y_b. We introduce a new variable such that

$$Y = Y_b + \widehat{a}^{-1/2}\varphi,$$

The expansion of the disturbance quantities are

$$\check{U}(X,Y) = (\check{U}_0(\varphi) + \widehat{a}^{-1/2}\check{U}_1(\varphi) + O(\widehat{a}^{-1}))E_2,$$

$$\check{V}(X,Y) = \widehat{a}^2(\check{V}_0(\varphi) + \widehat{a}^{-1/2}\check{V}_1(\varphi) + O(\widehat{a}^{-1}))E_2,$$

$$\check{W}(X,Y) = \widehat{a}^{3/2}(\check{W}_0(\varphi) + \widehat{a}^{-1/2}\check{W}_1(\varphi) + O(\widehat{a}^{-1}))E_2,$$

$$\check{P}(X,Y) = \widehat{a}^{5/2}(\check{P}_0(\varphi) + \widehat{a}^{-1/2}\check{P}_1(\varphi) + O(\widehat{a}^{-1}))E_2,$$

and

$$\check{T}(X,Y) = (\check{T}(\varphi) + \widehat{a}^{-1/2}\check{T}_1(\varphi) + O(\widehat{a}^{-1}))E_2,$$

where

$$E_2 = \exp\left(\widehat{a}^2 \int^X \left[\widehat{\beta}_{00} + \widehat{a}^{-1/2}\widehat{\beta}_{01} + O(\widehat{a}^{-1})\right] dX\right).$$

The basic flow quantities are expanded locally by using the Taylor series expansion as

$$\overline{u} = \overline{u}_0(X) + \widehat{a}^{-1/2}\varphi\overline{u}_1(X) + O(\widehat{a}^{-1}),$$

$$\overline{v} = \overline{v}_0(X) + \widehat{a}^{-1/2}\varphi\overline{v}_1(X) + O(\widehat{a}^{-1}),$$

$$\overline{T} = \overline{T}_0(X) + \widehat{a}^{-1/2}\varphi\overline{T}_1(X) + O(\widehat{a}^{-1}),$$

By substituting these expansion into the disturbance equations (2.40)-(2.44), and combining the streamwise, normal, and the energy equations, at leading order, we have

$$\overline{T}_0\left(\overline{u}_0\widehat{\beta}_{00} + \overline{T}_0^2\right)^2 - \frac{1}{2}\overline{T}_1\overline{u}_0^2 G_0\chi + \overline{T}_0\overline{u}_0\overline{u}_1 G_0\chi = 0, \tag{4.33}$$

and

$$\begin{aligned}\overline{T}_1\left(\overline{u}_0\widehat{\beta}_{00} + \overline{T}_0^2\right)^2 + 2\overline{T}_0\left(\overline{u}_0\widehat{\beta}_{00} + \overline{T}_0^2\right)\left(\overline{u}_1\widehat{\beta}_{00} + 2\overline{T}_0\overline{T}_1\right)\\ -\frac{1}{2}\overline{T}_2\overline{u}_0^2 G_0\chi + \overline{T}_0\overline{u}_1^2 G_0\chi + \overline{T}_0\overline{u}_0\overline{u}_2 G_0\chi = 0.\end{aligned} \tag{4.34}$$

The wave number within the right-hand branch is defined as λ_0, such that

$$\lambda_0 = G_0^{-1/4}.$$

Since for the composite profile the derivatives of the basic flow quantities are based on $Y^{'}$, therefore we are going to apply this transform onto equations (4.33) and (4.34).

We know that

$$Y^{'} = \frac{\overline{Y}}{\widehat{\theta}},$$

where $\overline{Y}$ is the Howarth-Dorodnitsyn transformation variable defined in (2.31).

Therefore by changing the partial derivatives of $\overline{u}$ and $\overline{T}$ in equations (4.33) and (4.34), from Y to $Y^{'}$, we have

$$\frac{\partial}{\partial Y} = \frac{\partial}{\partial Y'}\frac{\partial Y'}{\partial Y} = \frac{1}{\overline{T}\widehat{\theta}}\frac{\partial}{\partial Y'},$$

and

$$\frac{\partial^2}{\partial Y^2} = \frac{1}{\overline{T}\widehat{\theta}}\left(-\frac{1}{\overline{T}^2\widehat{\theta}}\frac{\partial\overline{T}}{\partial Y'}\frac{\partial}{\partial Y'} + \frac{1}{\overline{T}\widehat{\theta}}\frac{\partial^2}{\partial Y'^2}\right).$$

The maximum grow rate, $\widehat{\beta}_{00}$, and the wave number, λ_0, are scaled as

$$\widehat{\beta}_{00} = \tilde{\beta}\sqrt{G_0}|\chi|^{1/2}\widehat{\theta}^{-1/2}, \quad \text{and} \quad \lambda_0 = \tilde{\lambda}|\chi|^{1/4}\widehat{\theta}^{-1/4},$$

respectively, where $\tilde{\beta}$ and $\tilde{\lambda}$ are the new scales of the leading-order growth rate and wave number, respectively.

After substituting the scales of $\tilde{\beta}$ and $\tilde{\lambda}$ into equations (4.33) and (4.34); and transforming the derivatives to be with respect to $Y^{'}$, we now obtain

$$\overline{T}(\overline{u}\tilde{\beta}+\tilde{\lambda}^2\overline{T}^2)^2-\frac{\partial\overline{T}}{\partial Y^{'}}\overline{u}^2\tilde{\chi}/(2\overline{T})+\overline{u}\frac{\partial\overline{u}}{\partial Y^{'}}\tilde{\chi}=0, \tag{4.35}$$

and

$$\frac{\partial\overline{T}}{\partial Y^{'}}(\overline{u}\tilde{\beta}+\tilde{\lambda}^2\overline{T}^2)^2+2\overline{T}(\overline{u}\tilde{\beta}+\tilde{\lambda}^2\overline{T}^2)(\frac{\partial\overline{u}}{\partial Y^{'}}\tilde{\beta}+2\tilde{\lambda}^2\overline{T}\frac{\partial\overline{T}}{\partial Y^{'}})$$
$$+\tilde{\chi}\left[-\frac{\frac{\partial^2\overline{T}}{\partial Y^{'2}}\overline{u}^2}{2\overline{T}}-\frac{\frac{\partial\overline{T}}{\partial Y^{'}}\frac{\partial\overline{u}}{\partial Y^{'}}\overline{u}}{\overline{T}}+\frac{\left(\frac{\partial\overline{T}}{\partial Y^{'}}\right)^2\overline{u}^2}{2\overline{T}^2}+\left(\frac{\partial\overline{u}}{\partial Y^{'}}\right)^2+\overline{u}\frac{\partial^2\overline{u}}{\partial Y^{'2}}\right]=0, \tag{4.36}$$

From solving equations (4.35) and (4.36), and taking $\tilde{\chi}=\pm1$ for the unstably and stably curved systems separately, we may obtain the location of the modes, ${Y^{'}}_v$, and the associated growth rate, $\tilde{\beta}$, with the increasing wave number, $\tilde{\lambda}$, respectively.

Demonstrated in Figures (4.47) and (4.48) are the variation with the scaled wave number, $\tilde{\lambda}$, of the scaled growth rate, $\tilde{\beta}$, and location of the modes, ${Y^{'}}_v$, respectively, based on the composite model within the right-hand viscous region for the unstably curved systems under the increasing wake effect (decrease in $X^{'}$). The basic flow parameters are fixed at $\beta_u=0.585$, $\beta_t=2.46$ and $M_{-\infty}=8$, respectively.

The result from Figure (4.47) indicates an increase in the growth rate of the modes for the increased wake effect (i.e. decrease in $X^{'}$) within the systems, which agrees with the previous prediction in the limit of high wave number within the intermediate region in Figure (4.45). The results also indicate that the growth rate, $\tilde{\beta}$, would decrease for an increase in the wave number, $\tilde{\lambda}$, which shows that the modes are stabilized by the viscosity effect within the unstably curved systems.

Figure (4.48) indicates that the modes would move further into the lower stream direction for an increase in the wave number. As the wake effect increases within the unstably curved system, we also see that the modes are moving towards the centreline of the layer, which again agrees with the previous prediction in the limit of high wave number within the intermediate region in Figure (4.46).

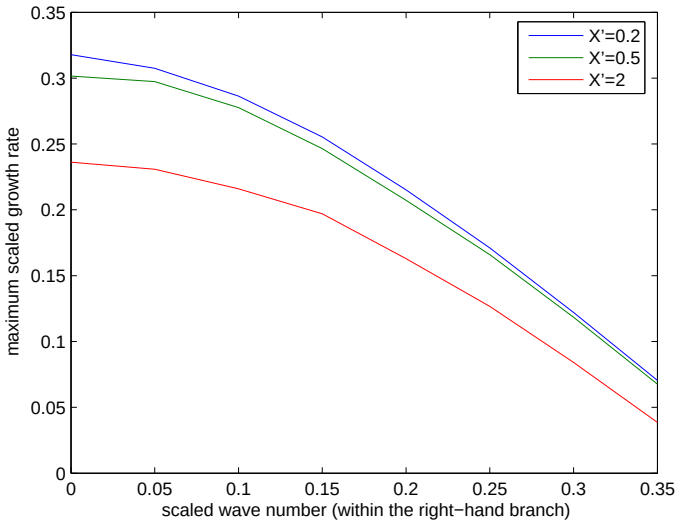

Figure 4.47: The variation of the scaled growth rate, $\tilde{\beta}$, with scaled wave number, $\tilde{\lambda}$, with fixed basic flow parameters $M_{-\infty} = 0.2$, $\beta_u = 0.5$ and $\beta_t = 0.75$, for increasing $X^{'}$, based on the composite model within the unstably curved systems.

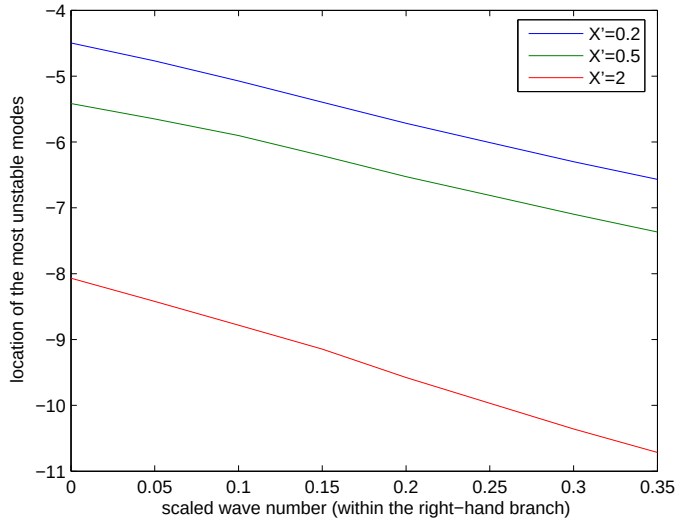

Figure 4.48: The variation of the most unstable mode, $Y_v^{'}$, with scaled wave number, $\tilde{\lambda}$, with fixed basic flow parameters $M_{-\infty} = 0.2$, $\beta_u = 0.5$, for increasing $X^{'}$, based on the composite model within the unstably curved systems.

As the wave number tends to zero from the viscous right-hand region, the mode is moving towards the inviscid region. The composite model predictions for zero wave number in the viscous region, of the scaled growth rate, $\tilde{\beta}$, and the location of the mode, $Y_v^{'}$, that corresponds the each of the unstably curved systems are demonstrated in Table (4.11), which matches very well on to the inviscid modes (compare with Table (4.9) within the corresponding unstably curved systems).

distance from the trailing edge, $X^{'}$,	0.2	0.5	2
$\tilde{\beta}$ for $\tilde{\lambda} = 0$	0.3178	0.3016	0.2361
$Y_v^{'}$ for $\tilde{\lambda} = 0$	-4.4956	-5.4156	-8.0691

Table 4.11: The maximum scaled growth rate, $\tilde{\beta}$, and the location of the unstable mode, $Y_v^{'}$, for $\tilde{\lambda} = 0$, with $X^{'}$, within the unstably curved systems.

Demonstrated in Figures (4.49) and (4.50) are the variation of the scaled growth rate, $\tilde{\beta}$, and location of the modes, $Y^{'}{}_v$, with the scaled wave number, $\tilde{\lambda}$, respectively, based on the numerical wake flow model within the right-hand viscous region for the stably curved systems. To obtain these results, we need to solve equations (4.35) and (4.36) by fixing $\tilde{\chi} = -1$. The basic flow parameters still remain fixed as $\beta_u = 0.585$, $\beta_t = 2.46$ and $M_{-\infty} = 8$, respectively.

The results from Figure (4.49) indicate an increase in the maximum growth rate, $\tilde{\beta}$, of the modes for the increased wake effect (decrease in $X^{'}$) within the stably curved systems.

Figure (4.50) indicates that as the wave number, $\tilde{\lambda}$, increases the modes would slowly move further into the slower upper stream. By comparing the results that correspond to the different wake effect within the systems, we see that the increase in the wake effect would lead to the mode moving towards the centreline of the system.

As the wave number tends to zero from the viscous right-hand region, the mode is moving towards the inviscid region. The numerical model predicts that for zero wave number in the viscous region, the scaled growth rate, $\tilde{\beta}$, and the location of the mode, $Y_v^{'}$,

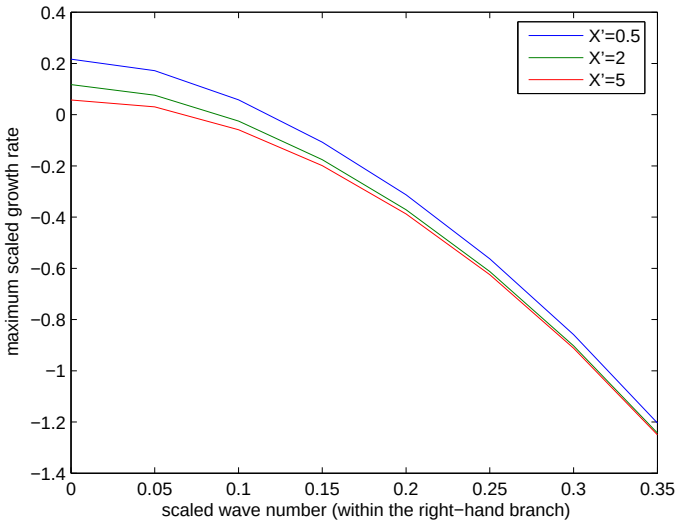

Figure 4.49: The variation of the scaled growth rate, $\tilde{\beta}$, with scaled wave number, $\tilde{\lambda}$, with fixed basic flow parameters $M_{-\infty} = 8$, $\beta_u = 0.585$ and $\beta_t = 2.46$ for increasing $X^{'}$ within the stably curved systems.

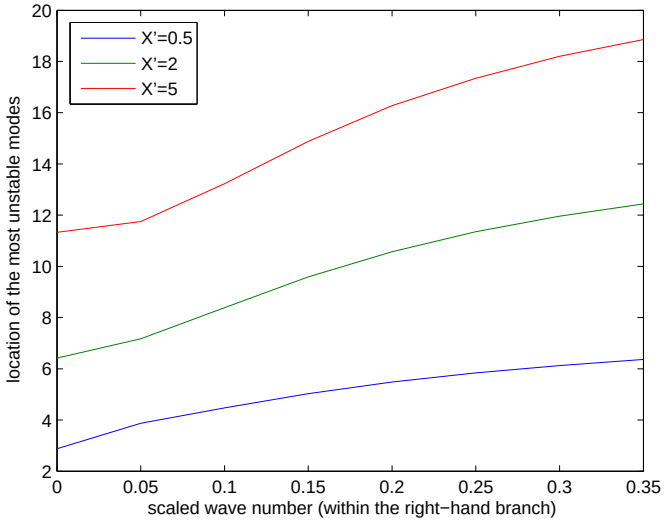

Figure 4.50: The variation of the most unstable mode, $Y_v^{'}$, with scaled wave number, $\tilde{\lambda}$, with fixed basic flow parameters $M_{-\infty} = 8$, $\beta_u = 0.585$ and $\beta_t = 2.46$ for increasing $X^{'}$ within the stably curved systems.

X' within the system	0.5	2	5
$\tilde{\beta}$ for $\tilde{\lambda} = 0$	0.2067	0.1179	0.0572
Y'_v for $\tilde{\lambda} = 0$	3.12	6.417	11.3308

Table 4.12: The maximum scaled growth rate, $\tilde{\beta}$, and the location of the unstable mode, Y'_v, for $\tilde{\lambda} = 0$, with X', within the stably curved systems.

that corresponds the each of the stably curved systems are demonstrated in Table (4.12), which matches quite well on to the inviscid modes (compare with Table (4.10)) within the corresponding stably curved systems).

4.3 Chapter summary

In this chapter, we turned our attention onto the curved compressible mixing layers that are dominated by the wake effect. It had been demonstrated by a number of experiments that the application of the splitter plate insertion technique on the mixing-layer system would increase the mixing between the two streams. Within such a system, the wake could develop behind the trailing edge of the splitter plate which would cause rapid variation of the basic streamwise velocity as well as the temperature within the layer, therefore two basic wake flow models were considered which were previously used to approximate this behaviour within the system.

So far we have investigated the behaviour of the Görtler mode with the wake-dominated system based on both the Gaussian and the composite wake flow models. The Gaussian wake flow model consists of adding a wake parameter onto the analytic hyperbolic tangent profile which was considered in the previous chapter to model the variation of the basic streamwise velocity within the plain curved compressible system. Based on the Gaussian model, the behaviour of the inviscid modes within both stably curved and unstably curved compressible system were investigated and the prediction indicates that modes could exist within both cases. New modes have been found to exist within the stably curved system

that have no counterpart with the previous thermal mode case. These modes are not driven by the inflectional curved temperature profile and behave similarly to the modes that are found within the unstably curved wake-dominated compressible system. Based on our interest, we also conducted an investigation on the effect of jet on the behaviour of the Görtler modes within the unstably curved compressible mixing-layer system. The basic jet flow could be approximated by simply taking the opposite sign of the wake parameter within the Gaussian wake profile. The results demonstrated that the Görtler modes would lead a different behaviour to the modes within the wake-dominated case.

We should mention here that the investigations of the general behaviour of these wake-dominated systems were conducted using the analytic Gaussian and composite models which do not satisfy the governing basic flow equations. The composite model was derived in comparison with the experiment that was performed by Liang et al. (1996) with fixed basic flow parameters, therefore it has more practical application in comparison with the Gaussian model. Both models only approximate the behaviour of the basic wake flow but do not satisfy the basic flow equations for the system, which in physical situations may affect the accuracy in the prediction of the behaviour of the system. Therefore it is necessary to derive a numerical wake flow model which is physically more realistic in comparison with the analytic models to compare the predictions of the development of the Görtler disturbance within the system. The method of derivation of the numerical wake flow model and its predictions of the instability of the system will be demonstrated in the next chapter.

Chapter 5

The numerical wake flow model

Previously we have seen that the different basic flow models would offer a different prediction for the behaviour of the Görtler modes within the system, therefore it is essential to employ a basic wake model that is able to accurately predict the behaviour of the system.

When a splitter plate is inserted along the centreline of a laminar mixing-layer system that consists of non-uniform velocities, as the two fluids travel downstream and leave the trailing edge, the boundary layers from both sides of the plate will merge and will form an asymmetric thin wake at the trailing edge of the plate. One of the earliest attempts to calculate the flow field in the near wake region was made by Goldstein (1930). Goldstein had set up asymptotic expansions valid for $X \to 0$ in the near wake region for the case of an incompressible symmetric flow, where X is defined to be the distance from the trailing edge of the splitter plate. The basic symmetric wake flow is associated with the flow that consists of uniform velocity, and is travelling down the trailing edge of the splitter plate. To obtain the entire wake flow, it is necessary to solve the corresponding boundary layer equations for all X, starting with the correct initial profile. However Goldstein (1930) expansion near $X = 0$ possesses a singularity in the velocity which makes the boundary layer equation not valid for $X = 0$. The correct structure of the flow field upstream of the trailing edge was later determined by Stewartson (1969) and Messiter (1970). Their work suggested a triple-deck structure in a region where $x^* = O(Re^{-3/8})$. This triple-

deck consists of three layers with a viscous sub-layer where $y^* = O(Re^{-5/8})$ and the boundary layer equations with pressure gradient must be used; an inviscid main deck where $y^* = O(Re^{-1/2})$ and the main term in the stream function is the Blasius solution; and a potential upper deck where $y^* = O(Re^{-3/8})$, which smooths out the disturbance of the boundary layer (see Sobey (2000) and Figure (5.1)).

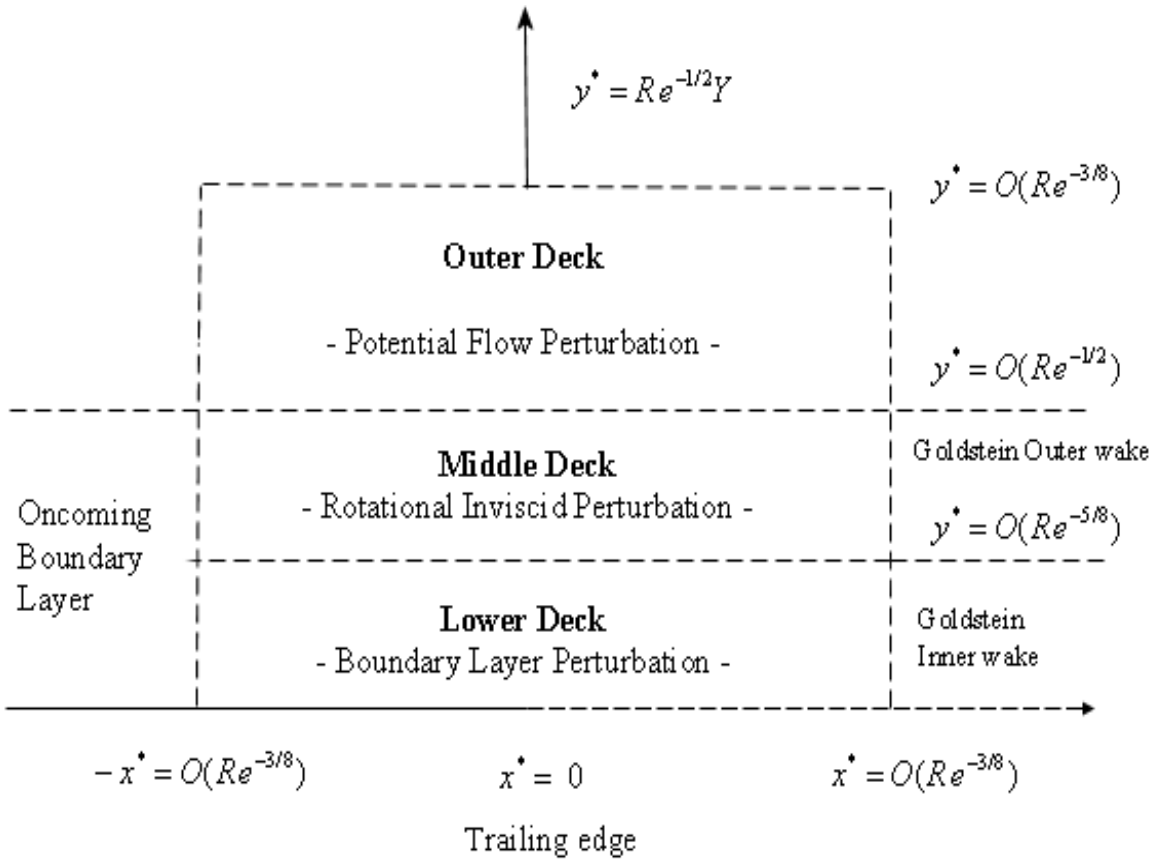

Figure 5.1: Schematic triple deck structure based on heuristic examination of asymptotic expansions in the near wake and upstream of the trailing edge.

Based on Golstein's work, the near wake is split into two regions, with the outer layer region that can be shown to match the inviscid main deck and the inner layer region

matches the sub-layer. The entire symmetric wake flow was later derived numerically by Veldman (1975) based on the initial profile from Goldstein (1930).

Before we consider deriving the basic asymmetric wake profile for our case of a compressible mixing-layer system with non-uniform velocities, we shall first demonstrate the Goldstein (1930) method for calculating the initial symmetric wake profile for an incompressible symmetric flow, and numerically derive the entire symmetric wake flow to compare our results with the previous results from Veldman (1975).

5.1 Goldstein's method for calculating the initial symmetric wake profile

For the incompressible symmetric wake flow, we consider a flat plate of length L, that is inserted into an incompressible stream of density, ρ^*, and viscosity, ν, and has uniform velocity, U, at ∞. The plate is inserted along the streamwise axis, x^*, with $-L \leqslant x^* \leqslant 0$, and at $y^* = 0$. The Reynolds number for the system is defined as

$$Re = \frac{UL}{\nu}.$$

In the limit of $Re \to \infty$, at downstream of the trailing edge where $(x^* \geqslant 0)$, the wake-triggered boundary layer is of thickness $O(Re^{-1/2})$.

By using Prandtl's boundary layer theory, the streamwise and normal velocity components are non-dimensionalised as

$$u^* = \overline{u}U \quad \text{and} \quad v^* = Re^{-1/2}U\overline{v}, \tag{5.1}$$

where $\overline{u}$ and $\overline{v}$ are the basic streamwise and normal velocities, respectively.

The physical streamwise and normal length scales, x^* and y^*, are non-dimensionalised as

$$y^* = Re^{-1/2}LY \quad \text{and} \quad x^* = XL, \tag{5.2}$$

respectively.

By substituting the above scalings into the equations for the incompressible flow, at leading-order, we may obtain the following basic flow equations

$$\frac{\partial \overline{u}}{\partial X} + \frac{\partial \overline{v}}{\partial Y} = 0, \quad (X > 0), \tag{5.3}$$

and

$$\overline{u}\frac{\partial \overline{u}}{\partial X} + \overline{v}\frac{\partial \overline{u}}{\partial Y} = \frac{\partial^2 \overline{u}}{\partial Y^2}, \quad (X > 0). \tag{5.4}$$

with the pressure, $\overline{p}$, found to be constant across the layer. Equations (5.3) and (5.4) have boundary conditions as

$$\overline{v}(X, 0) = \frac{\partial \overline{u}}{\partial \overline{Y}}(X, 0) = 0, \quad \overline{u} \to 1 \quad \text{as} \quad Y \to \infty, \quad (X > 0), \tag{5.5}$$

in the case of a symmetric wake flow.

A stream function $\psi(X, Y)$ is introduced, such that

$$\overline{u} = \frac{\partial \psi}{\partial Y}, \quad \overline{v} = -\frac{\partial \psi}{\partial X}. \tag{5.6}$$

Based on the definition of the incompressible stream function, ψ, in equation (5.6), the incompressible basic flow equations (5.3) and (5.4) can be simplified to

$$\overline{u}\frac{\partial \overline{u}}{\partial X} - \frac{\partial \psi}{\partial X}\frac{\partial \overline{u}}{\partial Y} = \frac{\partial^2 \overline{u}}{\partial Y^2}, \tag{5.7}$$

with the stream function automatically satisfying the basic continuity equation (5.3). The boundary conditions are transformed to

$$\psi(X, 0) = \frac{\partial \overline{u}}{\partial \overline{Y}}(X, 0) = 0, \quad \overline{u} \to 1 \quad \text{as} \quad Y \to \infty, \quad (X > 0), \tag{5.8}$$

To solve the basic flow equation (5.7) which satisfies the boundary condition (5.8), we need to specify the initial profile for $\overline{u}$ at $X = 0$. For this we have the Blasius profile, which offers the solution to the boundary-layer flow at the trailing edge of the plate. Since the basic streamwise velocity tends to 1 at ∞, therefore the initial velocity distribution at $X = 0$ is given by

$$u_0 = \frac{1}{2}\frac{d\zeta}{dY},$$

where

$$\frac{d^3\zeta}{dY^3} + \zeta\frac{d^2\zeta}{dY^2} = 0, \quad \zeta(0) = \frac{d\zeta}{dY}(0) = 0 \quad \text{and} \quad \frac{d\zeta}{dY} \to 2, \quad \text{as} \quad Y \to \infty. \tag{5.9}$$

The numerical solution for $\frac{d\zeta}{dY}(0)$ is $\alpha = 1.32824$.

u_0 maybe expanded in a series in powers of Y, and after substituting the series of u_0 into equation (5.9), the following result is obtained:

$$u_0 = \frac{1}{2}\alpha Y + (-\frac{1}{2}\alpha^2/4!)Y^4 + O(Y^7) \tag{5.10}$$

For the inner layer region as $X \to 0^+$ and $Y \sim X^{1/3}$, the stress is zero along the centreline ($Y = 0$ for $X > 0$), therefore we introduce a new similarity variable,

$$\eta = \frac{Y}{3X^{1/3}}, \tag{5.11}$$

and we have $\eta = O(1)$ within the near wake region.

ψ is now expanded as

$$\psi(X, Y) = X^{2/3} f(X, \eta) = x^{2/3}\left[f_0(\eta) + x f_1(\eta) + O(x^2)\right]. \tag{5.12}$$

We now introduce a new variable, ε, such that $\varepsilon = X^{1/3}$, so we may write the expansion of the stream function (equation (5.12)) as

$$\psi = \varepsilon^2 f(\varepsilon, \eta).$$

Therefore within the inner layer region, we have

$$\overline{u} = \frac{\partial\psi}{\partial Y} = \frac{\partial\psi}{\partial\eta}\frac{\partial\eta}{\partial Y} = \frac{\varepsilon}{3}\frac{\partial f}{\partial\eta}, \tag{5.13}$$

and

$$\overline{v} = -\frac{\partial\psi}{\partial X} = -\left[\frac{\partial\psi}{\partial\eta}\frac{\partial\eta}{\partial X} + \frac{\partial\psi}{\partial\varepsilon}\frac{\partial\varepsilon}{\partial X}\right] = -\left[2f + \varepsilon\frac{\partial f}{\partial\varepsilon} - \eta\frac{\partial f}{\partial\eta}\right]/(3\varepsilon). \tag{5.14}$$

Since $\overline{u} \to u_0$ as $X \to 0^+$, therefore by matching the expansion of $\overline{u}$ in equation (5.13), with that of u_0 in equation (5.10), as $\eta \to \infty$, the following results are obtained:

$$\frac{f_0'(\eta)}{\eta} \to \frac{9\alpha}{2} \approx 5.97708, \quad \text{and} \quad \frac{f_1'(\eta)}{\eta^4} \to \frac{-3^5\alpha^2}{2\cdot 4!} \approx -8.93136. \tag{5.15}$$

By substituting the expansions of $\overline{u}$ and $\overline{v}$ (equations (5.13), (5.14)) into equation (5.3), at leading-order, we may obtain the following equation for f_0:

$$f_0''' + 2f_0 f_0'' - f_0'^2 = 0, \tag{5.16}$$

with the boundary conditions defined as

$$f_0(0) = \frac{df_0}{d\eta}(0) = 0; \quad f_0' \to \frac{9\alpha}{2}\eta \quad \text{as} \quad \eta \to \infty. \tag{5.17}$$

Equation (5.16) is a third-order ordinary differential equation with the missing boundary condition of $\frac{d^2 f_0}{d\eta^2}$ at $\eta = 0$. The system was solved by using a combination of one-dimensional Newton-Raphson and fourth-order Runger-Kutta methods. We started with a guess of $\frac{d^2 f_0}{d\eta^2}$ at $\eta = 0$, then integrated the system towards $+\infty$ (in this case $\eta = 10$). The discrepancy between the value of f_0' at this point and $\frac{9\alpha}{2}\eta$ was used to iterate on the value of $\frac{d^2 f_0}{d\eta^2}$ at $\eta = 0$.

A numerical solution of equation (5.16) satisfying conditions in (5.17) gives the following result:

$$f_0'(\eta) \to 61.807789 \quad \text{as} \quad \eta \to \infty.$$

Therefore

$$f_0(\eta) \to \frac{9\alpha}{4}\eta'^2,$$

where η' is given by

$$\eta' = \eta + \delta_0 \quad \text{with} \quad \delta_0 = 0.3408.$$

At the next order ($O(\varepsilon)$), we obtain

$$f_1''' + 2f_0 f_1'' - 5f_0' f_1' + 5f_0'' f_1 = 0, \tag{5.18}$$

with boundary conditions defined as

$$f_1(0) = \frac{df_1}{d\eta}(0) = 0; \quad f_1' \to \frac{-3^5\alpha^2}{2 \cdot 4!}\eta^4 \quad \text{as} \quad \eta \to \infty. \tag{5.19}$$

The required solution for equation (5.18) is $f_1 = \beta_1 F_1$, where

$$F_1''' + 2f_0 F_1'' - 5f_0' F_1' + 5f_0'' F_1 = 0, \tag{5.20}$$

with the initial and boundary conditions defined as

$$F_1(0) = \frac{dF_1}{d\eta}(0) = 0; \quad F_1' \to 1 \quad \eta \to \infty. \tag{5.21}$$

Equation (5.20) was then solved numerically by using the same method for solving equation (5.16). By numerical solution of equation (5.20) which satisfying the boundary conditions in (5.21), it was found that

$$F_1 \sim 0.50438\eta'^5 + 1.6877\eta'^2 + 0.64504\eta' \quad \text{as} \quad \eta' \to \infty; \quad \eta' = \eta + \delta_0.$$

Therefore we have

$$\frac{F_1'}{\eta^4} \sim 5 \times 0.50438 \quad \text{as} \quad \eta \to \infty.$$

Since

$$f_1' \to \frac{-3^5\alpha^2}{2 \cdot 4!}\eta^4 \quad \text{as} \quad \eta \to \infty \quad \text{and} \quad f_1' = \beta_1 F_1',$$

therefore we may calculate the value for β_1 as

$$\beta_1 = \lim_{\eta\to\infty} \left(\frac{-3^5\alpha^2}{2 \cdot 4!}\right) / \left(\frac{F_1'}{\eta^4}\right) = -3.5415.$$

These results agree well with the results in Goldstein (1933).

For the outer layer region, we have $Y \sim O(1)$. We now expand ψ in the form

$$\psi(X, Y) = \psi_0(Y) + X^{1/3}\psi_1(Y) + X^{2/3}\frac{\psi_2(Y)}{2!} + O(x), \tag{5.22}$$

with

$$\psi_0' = \frac{1}{2}\zeta', \quad \psi_1' = \frac{1}{2}\mathrm{A}\zeta'', \quad \frac{\psi_2'}{2!} = \frac{\mathrm{A}^2}{4}\zeta''',$$

where A is written for brevity instead of $3\delta_0$. ζ, ζ' and ζ'' were obtained by numerically solving the Blasius equation (5.9). Therefore, the velocity distribution for the outer layer is

$$\begin{aligned}\overline{u}(X,Y) = \frac{\partial \psi}{\partial Y} &= \psi_0' + X^{1/3}\psi_1' + X^{2/3}\frac{\psi_2'}{2!} + O(X) \\ &= \frac{1}{2}\zeta' + X^{1/3}\frac{1}{2}\mathrm{A}\zeta'' + X^{2/3}\frac{\mathrm{A}^2}{4}\zeta''' + O(X). \end{aligned} \tag{5.23}$$

The complete initial velocity distribution for the basic symmetric wake flow can be derived by matching the inner layer solution for $\overline{u}$, that is equation (5.13), with its outer layer solution, equation (5.23).

Within Figure (5.2), we have demonstrated the matching between the inner and outer layer solutions for the initial velocity, $\overline{u}(0.05^3, Y)$. The initial X is taken to be 0.05^3, and the matching begins at $Y = 0.21$.

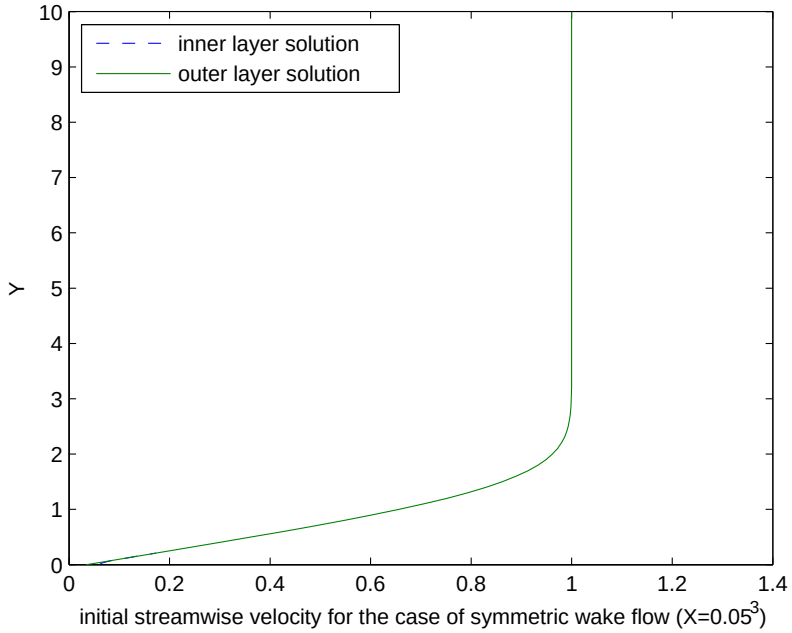

Figure 5.2: Match between the inner and outer layer solutions at $X = 0.05^3$.

Based on the initial profiles for ψ and $\overline{u}$, the boundary layer equation (5.7) with the associated boundary conditions (5.8) can then be solved numerically. The numerical scheme for solving a similar system in the case of an asymmetric wake flow will be discussed in the following section.

We now demonstrate in Figure (5.3), the variation of basic streamwise velocity, $\overline{u}$, with the increasing distance from the trailing edge of the plate, X.

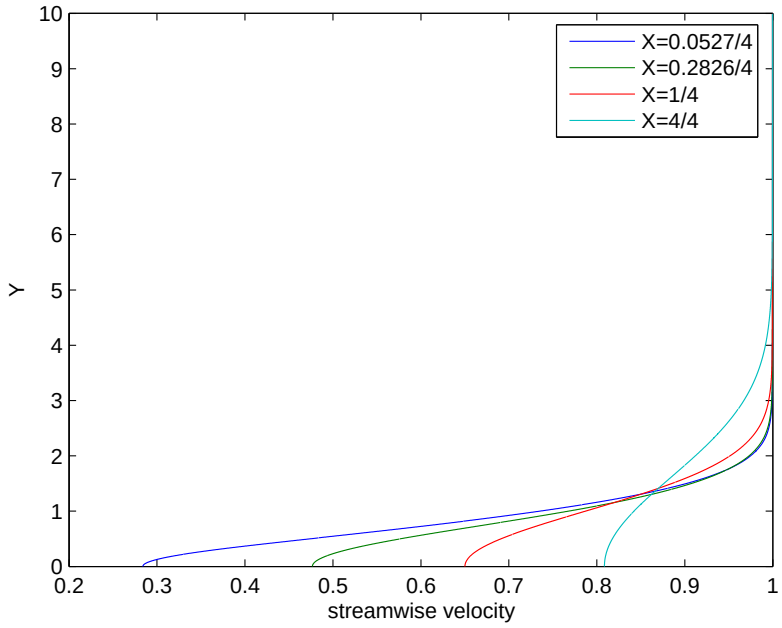

Figure 5.3: The variation of the basic streamwise velocity, $\overline{u}(Y)$, with the distance from the trailing edge, X.

A similar investigation was previously conducted by Veldman (1975), in which Veldman employed a finite difference method to obtain the solution for the boundary layer equation (5.7), based on the initial profiles from Goldstein (1933), and the boundary conditions (5.8), for the case of symmetric wake. In Veldman (1975) a Crank-Nicholson method was employed to discretise the boundary layer equation, and the system was set up based on a different scale of X that is four times greater than our scale. Based on a

different numerical scheme (which will be discussed in the next section), we also obtained solutions to the boundary layer equation for the case of symmetric wake. After comparing our computed results for the centreline streamwise velocity, $u(X, 0)$, to those from Veldman (1975), we have found that the results match up to 10^{-3}.

The investigation of the incompressible symmetric and asymmetric wake flow profiles is given in Daniels (1976), in which the initial symmetric wake flow profiles were also taken from Goldstein (1933), and the solutions to the boundary layer equations were computed using a finite difference downstream marching scheme that is different from Veldman (1975). By comparing with the result from Daniels (1976), we have also found agreement for the form of the symmetric wake flow profiles.

5.2 Calculation of the initial asymmetric wake profile

To derive the initial asymmetric wake profile for our curved compressible mixing-layer system, we recall our previously derived two-dimensional compressible mixing-layer equations (2.15), (2.16), with the basic energy equation (2.21). The pressure was previously found to be constant across the mixing-layer system. We also demonstrated that after we applied the Howarth-Dorodnitsyn transformation (2.31) and the compressible stream functions ((2.26) and (2.27)), onto the governing basic flow equations the compressible basic flow equations could then be simplified to a form that is equivalent to the incompressible case (equation (2.34)):

$$\overline{u}\frac{\partial \overline{u}}{\partial X} - \frac{\partial \psi}{\partial X}\frac{\partial \overline{u}}{\partial \overline{Y}} = \frac{\partial^2 \overline{u}}{\partial \overline{Y}^2}, \tag{5.24}$$

which has the following boundary conditions

$$\overline{u} \to \beta_u \quad as \quad \overline{Y} \to \infty, \quad \text{and} \quad \overline{u} \to 1 \quad as \quad \overline{Y} \to -\infty. \tag{5.25}$$

The basic temperature profile could be obtained from solving the simplified energy equation with the associated boundary conditions, and was previously given in equation (2.35):

$$\overline{T}(X,\overline{Y}) = 1 - \frac{1-\beta_t}{1-\beta_u}(1-\overline{u}(X,\overline{Y})) + \frac{1}{2}(\gamma-1)M_{-\infty}^2(1-\overline{u}(X,\overline{Y}))(\overline{u}(X,\overline{Y})-\beta_u), \tag{5.26}$$

with the boundary conditions

$$\overline{T}_{(\overline{Y}\to\infty)} = \beta_t, \quad \overline{T}_{(\overline{Y}\to-\infty)} = 1. \tag{5.27}$$

In order to solve for the basic streamwise velocity, $\overline{u}$, a third condition is required. We have followed Lock's proposal by setting the normal velocity component to be zero at the centreline of the system, therefore the third boundary condition is

$$\overline{v}(X,0) = 0. \tag{5.28}$$

The initial velocity distribution at $X = 0$ is the Blasius profile. For the slower upper stream, its non-dimensional basic velocity tends to β_u as $Y \to \infty$ within the layer. Therefore, the initial velocity distribution at $X = 0$ is given by

$$u_0 = \frac{1}{2}\frac{d\zeta}{d\overline{Y}},$$

$$\frac{d^3\zeta}{d\overline{Y}^3} + \zeta\frac{d^2\zeta}{d\overline{Y}^2} = 0, \quad \zeta(0) = \zeta'(0) = 0 \quad \text{and} \quad \zeta'(\infty) = 2\beta_u. \tag{5.29}$$

$\zeta''(0) = \alpha_1$ can be calculated numerically by solving above equation. For $\beta_u = 0.5$, α_1 is found to be 0.496900034.

For the lower stream, as the basic velocity tends to 1 so the Blasius equation for the lower stream is

$$\frac{d^3\zeta_1}{d\overline{Y}^3} + \zeta_1\frac{d^2\zeta_1}{d\overline{Y}^2} = 0, \quad \zeta_1(0) = \zeta_1'(0) = 0 \quad \text{and} \quad \zeta'(-\infty) = 2. \tag{5.30}$$

The numerical solution for $\zeta_1''(0)$ is $\alpha_2 = -1.32824$.

For the inner layer region as $X \to 0^+$, the stress is zero along the centreline $Y = 0$, therefore a new similarity variable, $\eta = \frac{\overline{Y}}{3X^{1/3}}$ is introduced, and $\eta = O(1)$ within the near wake region. The stream function $\psi(X, \overline{Y})$ is expanded as

$$\psi(X, \overline{Y}) = X^{2/3} f_0(\eta) + X^{5/3} f_1(\eta) + O(X^{8/3}).$$

Therefore within the inner layer region, we have

$$\overline{u} = \frac{\partial\psi}{\partial\overline{Y}} = \frac{\partial\psi}{\partial\eta}\frac{\partial\eta}{\partial\overline{Y}} = \frac{X^{\frac{1}{3}}}{3}\left(f_0'(\eta) + X f_1'(\eta) + O(X^2)\right). \tag{5.31}$$

After substituting above expansion of $\overline{u}$ in (5.31) into equation (5.24), for the inner layer region we may obtain the following equations for f_0 and f_1 respectively:

$$f_0''' + 2f_0 f_0'' - f_0'^2 = 0, \tag{5.32}$$

with boundary conditions defined as

$$f_0' \to \frac{9\alpha_2}{2}\eta \quad \text{as} \quad \eta \to -\infty; \quad f_0' \to \frac{9\alpha_1}{2}\eta \quad \text{as} \quad \eta \to \infty; \quad f_0(0) = 0. \tag{5.33}$$

At the next order, we have

$$f_1''' + 2f_0 f_1'' - 5f_0' f_1' + 5f_0'' f_1 = 0, \tag{5.34}$$

with boundary conditions defined as

$$f_1' \to \frac{-3^5\alpha_2^2}{2\cdot 4!}\eta^4 \quad \text{as} \quad \eta \to -\infty; \quad f_1' \to \frac{-3^5\alpha_1^2}{2\cdot 4!}\eta^4 \quad \eta \to \infty; \quad f_1(0) = 0. \tag{5.35}$$

Equation (5.32) is a third-order ordinary differential equation with the missing boundary conditions of $\frac{df_0}{d\eta}$ and $\frac{d^2 f_0}{d\eta^2}$ at $\eta = 0$, respectively. The system was solved by using a combination of two-dimensional Newton-Raphson and fourth-order Runger-Kutta methods. We started with a guess of $\frac{df_0}{d\eta}$ and $\frac{d^2 f_0}{d\eta^2}$ at $\eta = 0$, respectively, then integrated the system towards $\pm\infty$ (in this case $\eta = \pm 10$). The discrepancies between the values of f_0' at $\eta = \pm 10$ and $\frac{9\alpha_1}{2}\eta$ with $\frac{9\alpha_2}{2}\eta$; were used to iterate on the values of $\frac{df_0}{d\eta}$ and $\frac{d^2 f_0}{d\eta^2}$ at $\eta = 0$.

A numerical solution of equation (5.32) satisfying the initial and boundary conditions gives the following result:

$$f_0' \to 22.4439 \quad \text{as} \quad \eta \to \infty.$$

Therefore

$$f_0(\eta) \to \frac{9\alpha_1}{4}\eta'^2,$$

where η' is given by

$$\eta' = \eta + \iota_0 \quad \text{with} \quad \iota_0 = 0.62081232.$$

The solution for the second order f_1 is in the form of $\beta_1 F_1$, where

$$F_1''' + 2f_0 F_1'' - 5f_0' F_1' + 5f_0'' F_1 = 0, \tag{5.36}$$

with boundary conditions and initial condition defined as

$$F_1' \to \ 1 \quad \text{as} \quad \eta \to -\infty; \quad F_1' \to \left|\frac{\alpha_1}{\alpha_2}\right| \quad \eta \to \infty; \quad F_1(0) = 0. \tag{5.37}$$

Equation (5.36) was then solved by using the same method for solving equation (5.32). By numerical solution of equation (5.36) satisfying the boundary conditions (5.37), it was

found that

$$F_1 \sim 0.00003305584376\eta'^5 + 0.0006107402\eta'^2 - 0.0026712860272\eta' \quad \text{as} \quad \eta' \to \infty; \quad \eta' = \eta + \iota_0.$$

Therefore we have

$$\frac{F_1'}{\eta^4} \sim 5 \times 0.00003305584376 \quad \text{as} \quad \eta \to \infty.$$

Since

$$f_1' \to \frac{-3^5\alpha_1^2}{2 \cdot 4!}\eta^4 \quad \text{as} \quad \eta \to \infty \quad \text{and} \quad f_1' = \beta_1 F_1',$$

therefore we may calculate the value for β_1 as

$$\beta_1 = \lim_{\eta \to \infty} \left(\frac{-3^5\alpha_1^2}{2 \cdot 4!} \right) / \left(\frac{F_1'}{\eta^4} \right) = -6754.652697.$$

For large values of η, there are two separate solutions for the outer layer region, one corresponds to the slower upper stream, and the other one corresponds to the lower faster stream.

The velocity distribution for the upper stream outer layer is

$$\begin{aligned} \overline{u}(X, \overline{Y}) &= \frac{\partial \psi}{\partial \overline{Y}} = \psi_0' + X^{1/3}\psi_1' + X^{2/3}\frac{\psi_1'}{2!} \\ &= \frac{1}{2}\zeta' + X^{1/3}\frac{1}{2}\mathrm{A}\zeta'' + X^{2/3}\frac{\mathrm{A}^2}{4}\zeta''' + O(X), \end{aligned} \tag{5.38}$$

where A is written for brevity instead of $3\iota_0$. ζ, ζ' and ζ'' were obtained by numerically solving equation (5.29).

For the lower stream outer layer, we have the non-dimensional basic velocity tends to 1, therefore the velocity distribution for the lower stream outer layer is

$$\overline{u}(X, \overline{Y}) = \frac{1}{2}\zeta_1' + X^{1/3}\frac{1}{2}\mathrm{B}\zeta_1'' + X^{2/3}\frac{\mathrm{B}^2}{4}\zeta_1''' + O(X), \tag{5.39}$$

where B is written for brevity instead of $-3\iota_0$. ζ_1, ζ_1' and ζ_1'' were obtained by numerically solving equation (5.30).

The complete initial streamwise velocity distribution for the basic asymmetric wake flow can be derived by matching the inner layer solution for $\overline{u}$, equation (5.31), with its

outer layer solutions, equation (5.38) and (5.39) respectively. The initial value of X is taken to be 0.05^3, and the matching begins at $\overline{Y} = 0.21$ and $\overline{Y} = -0.21$, respectively.

Within Figures (5.4) and (5.5), we have demonstrated the matching between the inner and outer layer solution for the initial velocity, $\overline{u}$, and initial basic temperature, $\overline{T}$.

The same method was also employed to calculate the initial profile for the compressible stream function, ψ, and $\frac{\partial \overline{u}}{\partial \overline{Y}}$, which are needed to solve the boundary layer equation (5.24).

For the initial profile of the compressible stream function, ψ, the outer layer expansions for ψ within the lower and upper streams are given as

$$\psi(X, \overline{Y}) = \frac{1}{2}\zeta_1 + X^{1/3}\frac{1}{2}\mathrm{A}\zeta_1' + X^{2/3}\frac{\mathrm{A}^2}{4}\zeta_1'' + O(X), \tag{5.40}$$

and

$$\psi(X, \overline{Y}) = \frac{1}{2}\zeta + X^{1/3}\frac{1}{2}\mathrm{A}\zeta' + X^{2/3}\frac{\mathrm{A}^2}{4}\zeta'' + O(X), \tag{5.41}$$

respectively, with the inner layer expansion of ψ given as

$$\psi(X, \overline{Y}) = X^{2/3} f_0(\eta) + X^{5/3} f_1(\eta) + O(X^{8/3}). \tag{5.42}$$

For the initial profile of $\frac{\partial \overline{u}}{\partial \overline{Y}}$, the outer layer expansions for $\frac{\partial \overline{u}}{\partial \overline{Y}}$ within the lower and upper streams are given as

$$\frac{\partial \overline{u}}{\partial \overline{Y}}(X, \overline{Y}) = \frac{1}{2}\zeta_1'' + X^{1/3}\frac{1}{2}\mathrm{A}\zeta_1''' + X^{2/3}\frac{\mathrm{A}^2}{4}\zeta_1'''' + O(X), \tag{5.43}$$

and

$$\frac{\partial \overline{u}}{\partial \overline{Y}}(X, \overline{Y}) = \frac{1}{2}\zeta'' + X^{1/3}\frac{1}{2}\mathrm{A}\zeta''' + X^{2/3}\frac{\mathrm{A}^2}{4}\zeta'''' + O(X), \tag{5.44}$$

respectively, with the associated inner layer expansion given as

$$\frac{\partial \overline{u}}{\partial \overline{Y}} = \frac{\partial \overline{u}}{\partial \eta}\frac{\partial \eta}{\partial \overline{Y}} = \frac{1}{9}\left(f_0''(\eta) + X f_1''(\eta) + O(X^2)\right). \tag{5.45}$$

Equation (5.24) is a system of parabolic partial differential equations and with its associated initial profiles and boundary conditions it is solved using a Nag routine: D03PDF in Fortran for increasing values of X.

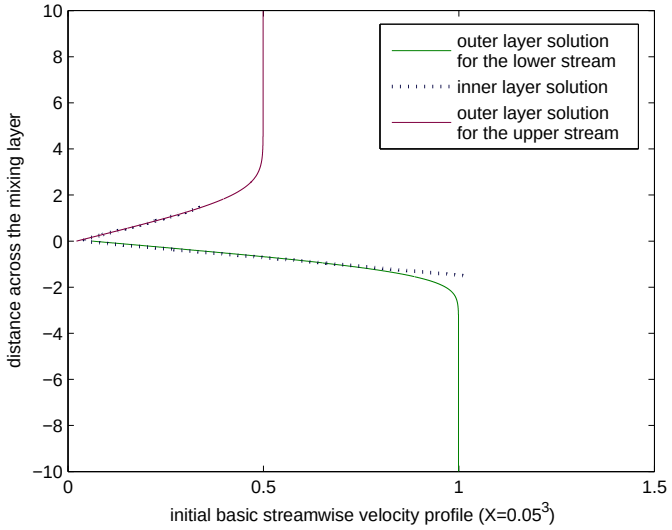

Figure 5.4: Comparison between the inner and outer layer solutions for $\overline{u}(\overline{Y})$, for the asymmetric Blasius profile at $X = 0.05^3$, with $\beta_u = 0.5$.

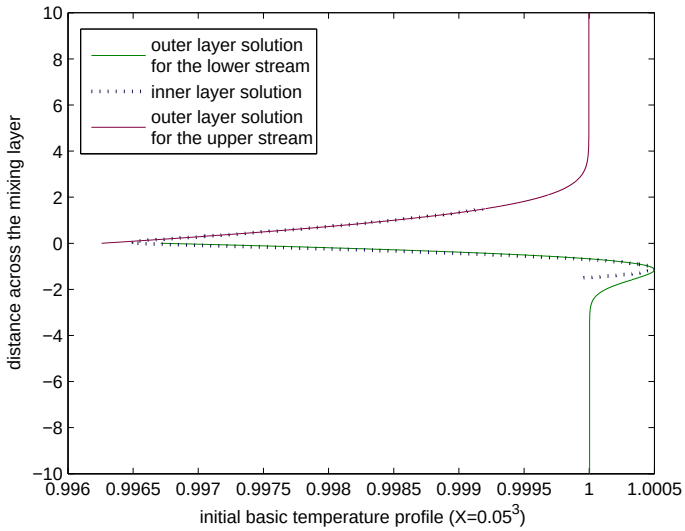

Figure 5.5: Comparison between the inner and outer layer solutions for the initial basic temperature profile, $\overline{T}(\overline{Y})$, at $X = 0.05^3$, with $\beta_u = 0.5$, $\beta_t = 1$, $M_{-\infty} = 0.2$.

5.3 The numerical scheme

The Nag routine D03PEF is suitable for integrating a system of linear or nonlinear, first-order partial differential equations (PDEs). The spatial discretisation is performed using the Keller box scheme and the method of lines is employed to reduce the PDEs to a system of ordinary differential equations (ODEs). The resulting system is then solved using a Backward Differentiation Formula method.

For our problem, we have a second-order parabolic partial differential equation

$$\overline{u}\frac{\partial \overline{u}}{\partial X} - \frac{\partial \psi}{\partial X}\frac{\partial \overline{u}}{\partial \overline{Y}} = \frac{\partial^2 \overline{u}}{\partial \overline{Y}^2},$$

with the previously calculated initial profiles

$$\psi(0.05^3, \overline{Y}), \quad \overline{u}(0.05^3, \overline{Y}), \quad \frac{\partial \overline{u}}{\partial \overline{Y}}(0.05^3, \overline{Y}),$$

and the boundary conditions

$$\overline{u} \to 1 \quad \text{as} \quad \overline{Y} \to -\infty, \quad \text{and} \quad \overline{u} \to \beta_u \quad \text{as} \quad \overline{Y} \to \infty.$$

To make the system suitable for the Nag routine D03PDF, the above equation must be rewritten as the set of first-order PDEs, therefore we introduce new variables such that

$$u_1 = \psi, \quad u_2 = \overline{u} = \frac{\partial \psi}{\partial \overline{Y}}, \quad u_3 = \frac{\partial \overline{u}}{\partial \overline{Y}}.$$

The system is then transformed to a set of first-order PDEs with

$$u_2 = \frac{\partial u_1}{\partial \overline{Y}}, \quad u_3 = \frac{\partial u_2}{\partial \overline{Y}} \tag{5.46}$$

and

$$u_2\frac{\partial u_2}{\partial X} - \frac{\partial u_1}{\partial X}u_3 = \frac{\partial u_3}{\partial \overline{Y}}. \tag{5.47}$$

To solve for the above PDEs, the boundary condition for ψ is required and we have chosen the condition from the Lock profile, that is the normal velocity, $\overline{v}$, is zero at the

centreline, therefore we may specify the value of the compressible stream function as zero on the centreline $\overline{Y} = 0$. The third boundary condition is then given as

$$\psi(X, 0) = 0. \tag{5.48}$$

The more detailed process of deriving the above boundary condition is given in the work of Daniels (1976).

With the provided initial and boundary conditions, the solutions of ψ, $\overline{u}$, and $\frac{\partial \overline{u}}{\partial \overline{Y}}$ that correspond to the increasing values of X could then be obtained numerically by using a combination of the Newton-Raphson technique with the D03PEF routine.

5.4 The predictions based on the numerical model

By numerically solving the compressible basic flow equation (5.24) with the boundary conditions, (5.25), defined for the asymmetric wake flow, based on the scheme that was discussed in the previous section, we now demonstrate in Figures (5.6) and (5.7), the variation of the basic streamwise velocity, $\overline{u}(\overline{Y})$, and the basic temperature, $\overline{T}(\overline{Y})$, with increasing values of X, respectively.

To investigate the behaviour of the inviscid Görtler modes based on the numerical model, we recall the eigenvalue relation, (2.51), which was derived previously in Chapter Two. To eliminate χ from equation (2.51), we scale the growth rate, $\widehat{\beta}$, and the wave number, $\widehat{a}$, as

$$\widehat{\beta} = \beta|\chi|^{1/2}, \quad \text{and} \quad \widehat{a} = a, \tag{5.49}$$

respectively. Note that the new scaled growth rate, β, and wave number, a, are defined differently from equation (3.16) in Chapter Three, where the previous scalings were employed to eliminate X after the similarity transformation.

The resulting equation governing the behaviour of the inviscid modes is found to be

$$\frac{\partial^2 \mathsf{V}}{\partial \overline{Y}^2} - \frac{\partial \mathsf{V}}{\partial \overline{Y}}\left(\frac{2\frac{\partial \overline{T}}{\partial \overline{Y}}}{\overline{T}}\right) + \mathsf{V}\left[-\widehat{a}^2\overline{T}^2 - \frac{\frac{\partial^2 \overline{u}}{\partial \overline{Y}^2}}{\overline{u}} + \frac{2\frac{\partial \overline{T}}{\partial \overline{Y}}}{\overline{T}}\frac{\frac{\partial \overline{u}}{\partial \overline{Y}}}{\overline{u}} - \frac{\tilde{\chi}a^2}{\beta^2}\left(\overline{T}\frac{\frac{\partial \overline{u}}{\partial \overline{Y}}}{\overline{u}} - \frac{\frac{\partial \overline{T}}{\partial \overline{Y}}}{2}\right)\right] = 0, \tag{5.50}$$

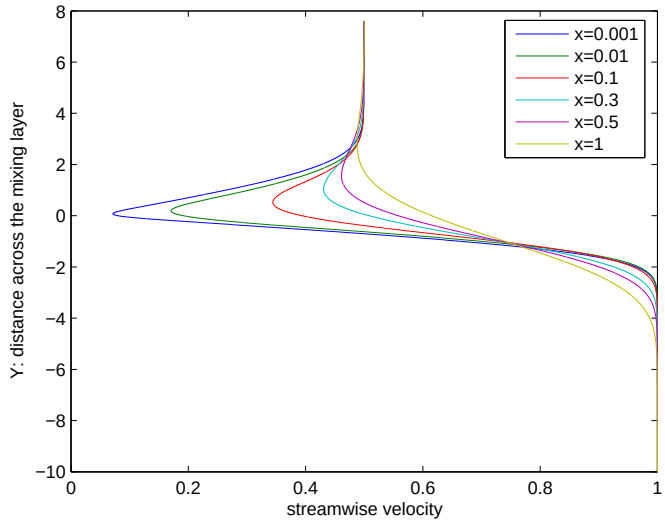

Figure 5.6: The variation of the basic streamwise velocity, $\overline{u}(\overline{Y})$, with distance from the trailing edge, X, based on the numerical model with $\beta_u = 0.5$.

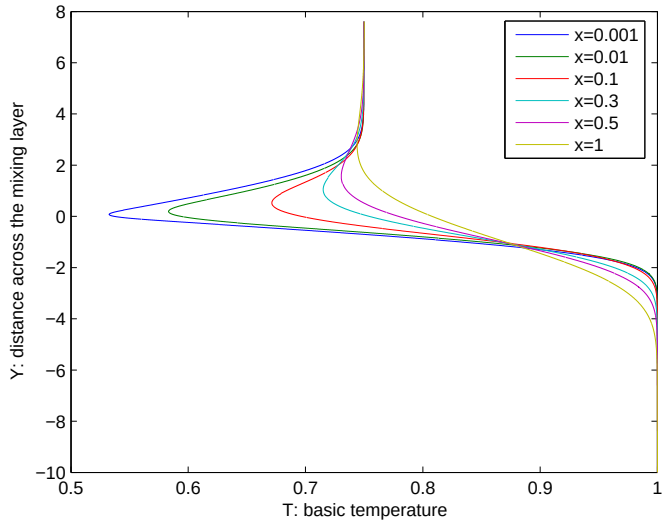

Figure 5.7: The variation of the basic temperature, $\overline{T}(\overline{Y})$, with distance from the trailing edge, X, based on the numerical model with $\beta_u = 0.5$, $\beta_t = 0.75$ and $M_{-\infty} = 0.2$.

with boundary conditions given as

$$\mathsf{V} \sim e^{-a\beta_t \overline{Y}}, \quad \text{as} \quad \overline{Y} \to \infty, \tag{5.51}$$

and

$$\mathsf{V} \sim e^{a\overline{Y}}, \quad \text{as} \quad \overline{Y} \to -\infty. \tag{5.52}$$

We fix $\tilde{\chi} = \pm 1$ for the unstably and the stably curved systems, respectively. With the fixed distance from the trailing edge, X, and the scaled wave number, a, we may obtain the numerical solutions of the inviscid mode, V, and the corresponding scaled growth rate, β, from solving eigenvalue relation (5.50).

With the new scales of the wave number, a, and growth rate, β, the asymptotic solution of the leading-order scaled growth rate, β_0 (for $a \gg 1$), can be obtained by eliminating $|\chi|$ from equation (2.52) , in Section (2.4), such that

$$\beta_0 = \left[\tilde{\chi} \left(\frac{\frac{\partial \overline{T}}{\partial \overline{Y}}}{2\overline{T}^2} - \frac{\frac{\partial \overline{u}}{\partial \overline{Y}}}{\overline{T}\,\overline{u}} \right) \right]^{1/2}, \tag{5.53}$$

where the basic flow quantities are evaluated at $(X, \overline{Y}_b)$.

The location of the most unstable mode, $\overline{Y}$, can be determined from either solving equation (2.54); or using the alternative method of searching for the location of the maximum and the minimum of the leading-order eigenvalue function, $h = \beta_0^2(X, \overline{Y})$, within the unstably curved ($\tilde{\chi} = 1$) and the stably curved ($\tilde{\chi} = -1$) systems, respectively.

Based on the numerical wake flow model with $X = 0.01$, the prediction of the first inviscid mode, $\mathsf{V}(X, \overline{Y})$, with increasing wave number, a, within the unstably curved case ($\tilde{\chi} = 1$), was obtained numerically by solving the eigenvalue relation (5.50), and is demonstrated in Figure (5.8). For this case the basic flow parameters are fixed to be $\beta_u = 0.5$, $\beta_t = 0.75$ and $M_{-\infty} = 0.2$. It is observed that as the wave number increases, the mode would be confined to a thin layer. The location of the most unstable mode was calculated asymptotically by using equation (2.54) in Section (2.4), and is determined to be $\overline{Y}_b = -0.182$. This result was validated by using $h = \beta_0^2(X, \overline{Y})$.

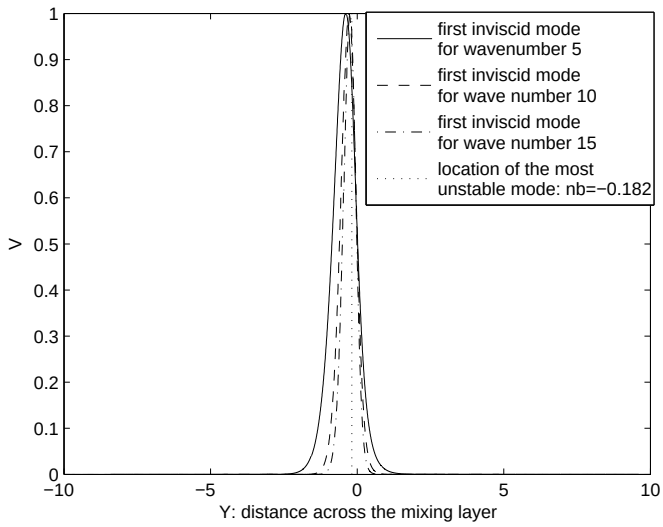

Figure 5.8: The variation of the first inviscid mode, $\mathsf{V}(X, \overline{Y})$, with increasing wave number, a, for $X = 0.01$, within the unstably curved system with $\beta_u = 0.5$, $\beta_t = 0.75$ and $M_{-\infty} = 0.2$.

Demonstrated in Figure (5.9) are the numerical solutions for the first four unstable modes, $\mathsf{V}(X, \overline{Y})$, at the particular wave number, $a = 5$, with the fixed basic flow parameters for $X = 0.01$ within the unstably curved ($\tilde{\chi} = 1$) compressible system. For this case the basic flow parameters are fixed to be $\beta_u = 0.5$, $\beta_t = 0.75$ and $M_{-\infty} = 0.2$. The normal disturbance velocity, $\mathsf{V}(X, \overline{Y})$, was normalised to 1 for these cases.

The corresponding scaled growth rate which is associated with each of these modes in Figure (5.8) was also derived numerically from solving the associated eigenvalue relation (5.50), and is provided in Table (5.1).

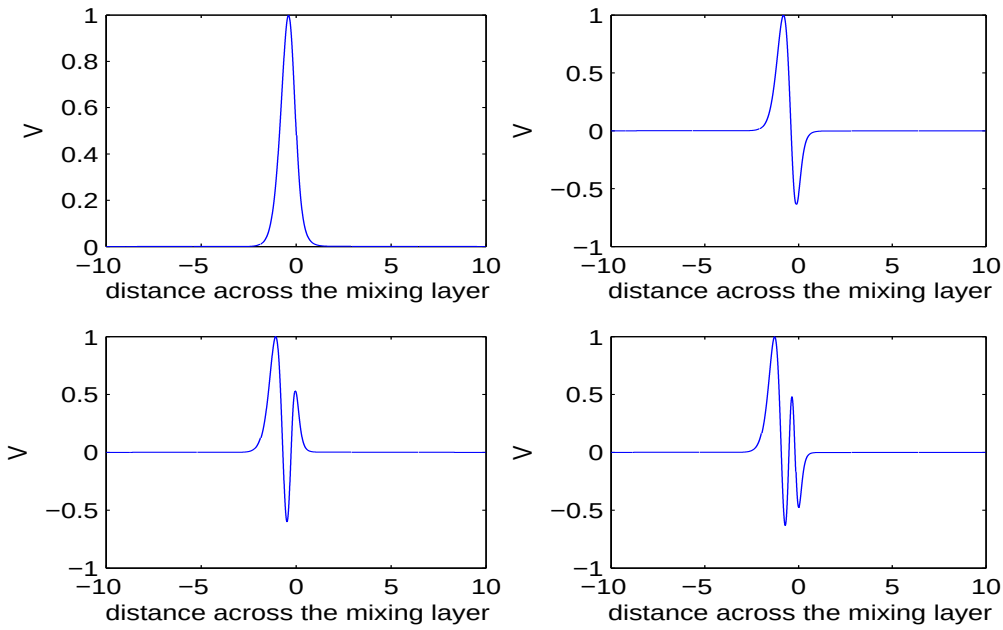

Figure 5.9: The first four inviscid modes, $\mathsf{V}(X, \overline{Y})$, for $a = 5$ with $X = 0.01$, for $\beta_u = 0.5$, $\beta_t = 0.75$ and $M_{-\infty} = 0.2$, within the unstably curved system.

First unstable mode	Second unstable mode	Third unstable mode	Fourth unstable mode
$\beta_1 = 1.1214$	$\beta_2 = 0.7579$	$\beta_3 = 0.5862$	$\beta_4 = 0.4799$

Table 5.1: Growth rates β for the first four modes for $a = 5, X = 0.01, \beta_u = 0.5, \beta_t = 0.75$ and $M_{-\infty} = 0.2$, based on the numerical model.

Based on the result for the growth rate of the first four modes for $X = 0.01$ in Table (5.1), the effect of increasing wave number, a, on the growth rate of the modes, β, within the unstably curved system could then be obtained from solving the the associated eigenvalue relation. The results are then demonstrated in Figure (5.10). Within the figure, the dashed line and the dotted lines are used to represent the asymptotic prediction for the maximum growth rate, β_0, and for the growth rate in terms of the wave number for the first four modes respectively. The maximum growth rate, β_0, was obtained using

equation (5.53); and the asymptotic predictions of the growth rate of the first four modes were obtained from equation (2.57), based on the newly scaled maximum growth rate, β_0, respectively.

It is observed that both the numerical and asymptotic predictions are in good agreement for $a \gg 1$. As the wave number increases, the scaled growth rate of the modes would tend to the maximum growth rate, β_0, which for this case was found to be $\beta_0 = 1.5868$.

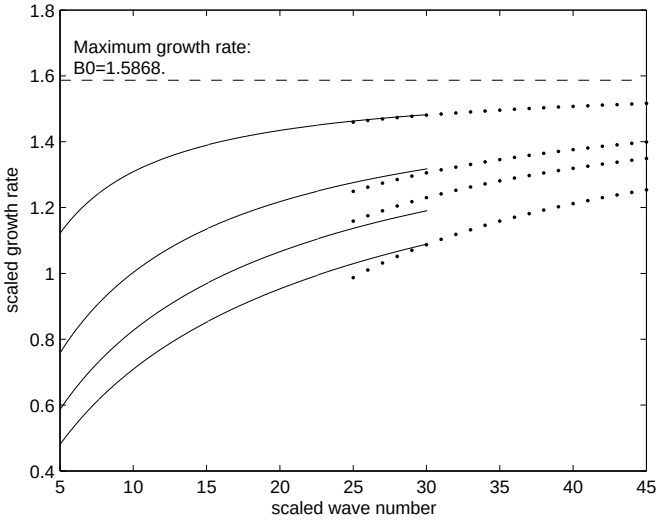

Figure 5.10: The variation of the growth rate, β, for the first four unstable modes, $\mathsf{V}(X, \overline{Y})$, with increasing wave number, a, for $X = 0.01$, $\beta_u = 0.5$, $\beta_t = 0.75$ and $M_{-\infty} = 0.2$, within the unstably curved system. Numerical solution: solid line. Asymptotic solution: dotted line.

Demonstrated in Figure (5.11) is the variation of the growth rate of the first mode, β, for a particular wave number, $a = 5$, with the distance from the trailing edge, X, based on the numerical model for both the stably and the unstably curved compressible mixing-layer systems. The basic flow parameters are fixed at $\beta_u = 0.5$, $\beta_t = 0.75$ and $M_{-\infty} = 0.2$. Similar to the prediction based on the Gaussian model in Figure (4.29), the numerical model also predicts that for β_t exceeding the upper limit for the thermal

mode case, another set of modes can be found within the stably curved compressible system which behave differently to the thermal modes. As the wake increases ($X \to 0^+$), the growth rate of these modes become comparable to those of the usual modes that are found within the corresponding unstably curved case. It is also observed that the numerical predictions agree well with the asymptotic results.

Demonstrated in Figure (5.12) are the corresponding asymptotic predictions of the variation of the location of the most unstable mode, $\overline{Y}_b$, and the maximum growth rate, β_0, with the distance from the trailing edge, X, based on the numerical model. The results indicate that as both stably and unstably curved system become more dominated by the wake, the location of the mode would shift towards the centreline of the layer with the mode for the unstably curved case situated closer to the centreline of the system. By comparing this result with the previous Gaussian model prediction in figure (4.30), we see that both models predicted similar behaviour of the modes within the systems. The asymptotic predictions for the behaviour of the maximum growth rate, β_0, within both systems based on the numerical model agree with the corresponding numerical predictions in Figure (5.11).

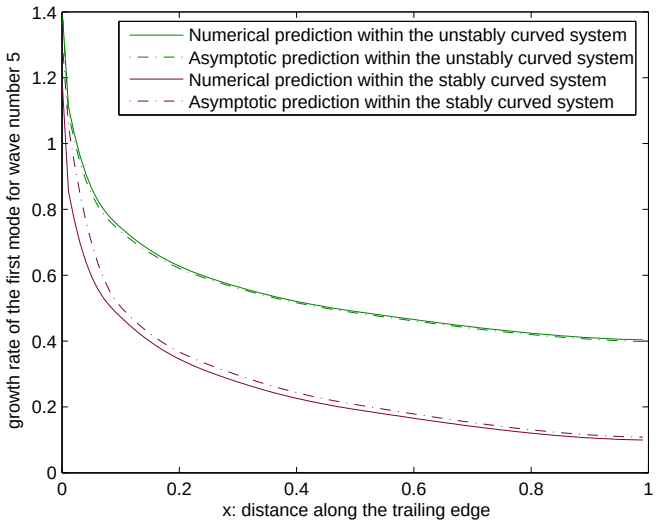

Figure 5.11: The variation of the growth rate of the first mode, β, for $a = 5$ with the distance from the trailing edge, X, for $\beta_u = 0.5$, $\beta_t = 0.75$ and $M_{-\infty} = 0.2$, based on the numerical model within the stably and unstably curved system.

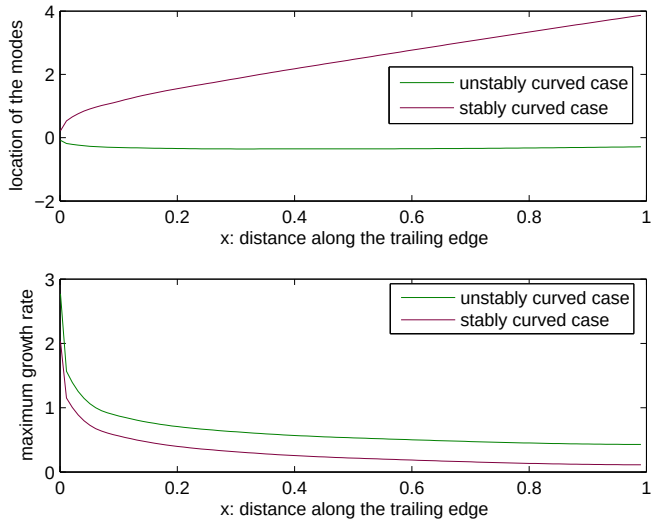

Figure 5.12: The variation of the location of the most unstable mode, $\overline{Y}_b$, and the maximum growth rate, β_0, with the distance from the trailing edge, X, for $\beta_u = 0.5$, $\beta_t = 0.75$ and $M_{-\infty} = 0.2$, based on the numerical model within the stably and unstably curved system.

Demonstrated in Tables (5.2) and (5.3) are some of the exact predictions of the maximum scaled growth rate, β_0, and the location of the unstable modes, $\overline{Y}_b$, (taken from results in Figure (5.12)) which correspond to the increasing distance from the trailing edge of the splitter plate,X, within the associated unstably and stably curved systems, respectively.

X within the unstably curved system	0.001	0.01	0.1	0.3	0.5	1
Scaled growth rate, β_0	2.7676	1.5868	0.8720	0.624	0.5298	0.4259
Location of the mode, $\overline{Y}_b$	-0.082	-0.1820	-0.31	-0.356	-0.3540	-0.286

Table 5.2: The maximum scaled growth rate, β_0, and the location of the mode, $\overline{Y}_b$, with X, within the unstably curved system.

X within the stably curved system	0.001	0.01	0.1	0.3	0.5	1
Scaled growth rate, β_0	2.0313	1.1656	0.5611	0.3137	0.2154	0.1098
Location of the mode, $\overline{Y}_b$	0.216	0.5160	1.146	1.8660	2.472	3.892

Table 5.3: The maximum scaled growth rate, β_0, and the location of the mode, $\overline{Y}_b$, with X, within the stably curved system.

For the stably curved case in Figure (5.11), we have also obtained the numerical solutions for the first four unstable modes, $\mathsf{V}(X,\overline{Y})$, at a particular wave number, $a = 5$, with the fixed basic flow parameters for $X = 0.01$. These results are demonstrated in Figure (5.13). The normal disturbance velocity, $\mathsf{V}(X,\overline{Y})$, was normalised to 1 for these cases.

The growth rate which is associated with each of these modes was derived numerically from solving the associated eigenvalue relation (equation (2.51)) with $\tilde{\chi} = -1$ for the stably curved case. We now provided these results in Table (5.4).

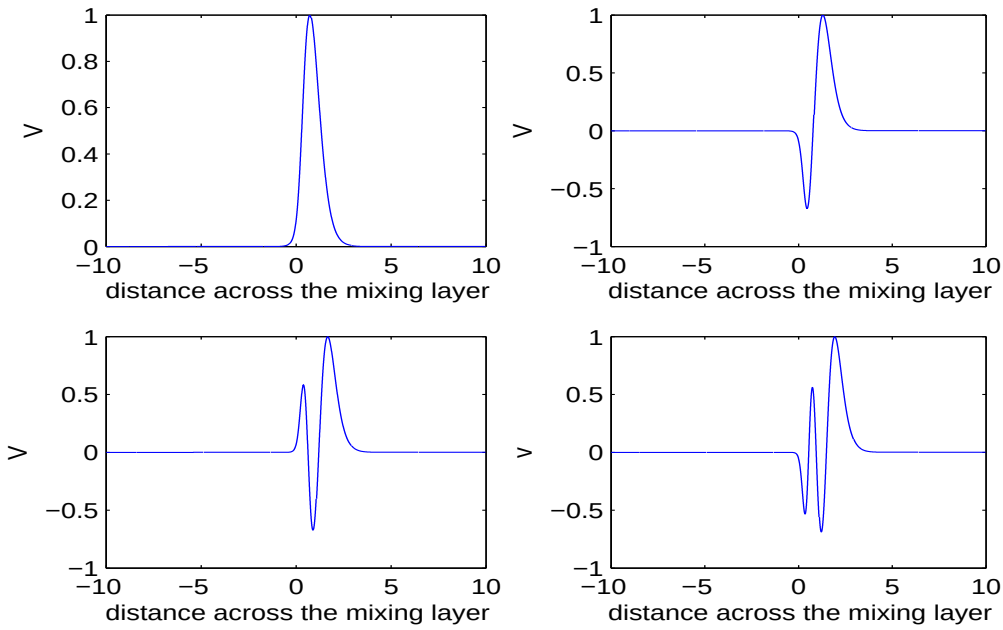

Figure 5.13: The first four inviscid modes, $\mathsf{V}(X, \overline{Y})$, for $a = 5$ with $X = 0.01$, for $\beta_u = 0.5$, $\beta_t = 0.75$ and $M_{-\infty} = 0.2$, within the stably curved system.

First unstable mode	Second unstable mode	Third unstable mode	Fourth unstable mode
$\beta_1 = 0.8644$	$\beta_2 = 0.6109$	$\beta_3 = 0.4791$	$\beta_4 = 0.3947$

Table 5.4: Growth rates β for the first four modes for $a = 5, X = 0.01, \beta_u = 0.5, \beta_t = 0.75$ and $M_{-\infty} = 0.2$, within the stably curved system.

Based on the result for the growth rate of the first four modes for $X = 0.01$ within the stably curved system in Table (5.4), the effect of increasing wave number, a, on the growth rate of the modes, β, was also obtained from solving the the associated eigenvalue relation with $\tilde{\chi} = -1$. The results are demonstrated in Figure (5.14). Within the figure, the dashed line and the dotted lines are again used to represent the asymptotic prediction for the maximum growth rate, β_0, and for the growth rate in terms of the wave number for the first four modes, respectively. The maximum growth rate, β_0, and the asymptotic

predictions of the growth rate of the first four modes were obtained using equations (5.53) and (2.57) (based on β_0), respectively, based on $\tilde{\chi} = -1$.

It is observed from Figure (5.14) that both numerical and asymptotic predictions are in good agreement for $a \gg 1$ within the stably curved system. As the wave number increases, the scaled growth rate of the modes would tend to the maximum growth rate, β_0, which for this stably curved case was found to be $\beta_0 = 1.1656$.

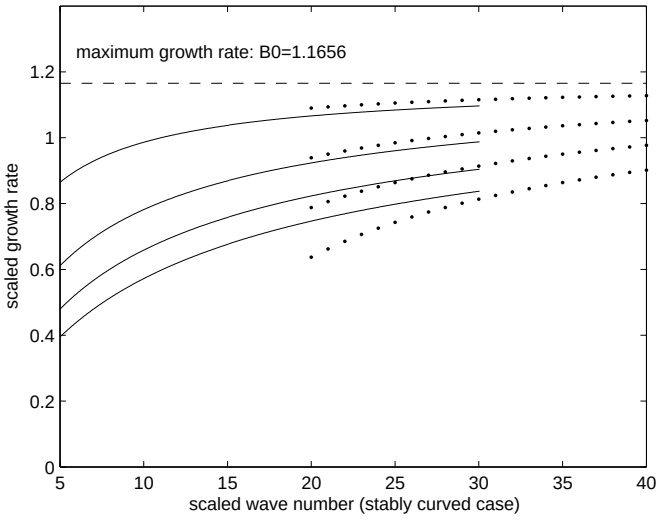

Figure 5.14: The variation of the growth rate, β, for the first four unstable modes, $\mathsf{V}(X, \overline{Y})$, with increasing wave number, a, for $X = 0.01$, $\beta_u = 0.5$, $\beta_t = 0.75$ and $M_{-\infty} = 0.2$, within the stably curved system. Numerical solution: solid line. Asymptotic solution: dotted line.

Demonstrated in Figure (5.15) are the asymptotic predictions of the variation of the location of the most unstable mode, $\overline{Y}_b$, and the maximum growth rate, β_0, with the relative upper stream temperature, β_t, within both the stably and the unstably curved wake-dominated systems based on the numerical model for $X = 0.001$. The basic flow parameters for both systems are fixed to be $\beta_u = 0.5$ and $M_{-\infty} = 0.2$. The results indicate that the increase of the relative upper stream temperature, β_t, has little effect on the

location of the most unstable modes within both systems. As the upper stream temperature becomes significantly cooler, the modes within both systems would move gradually towards the centreline of the systems. The results also indicate that the maximum growth rate, β_0 would considerably increase for a decrease in β_t within both systems.

Since the wake effect, $X = 0.001$, from the numerical model is almost equivalent to the Gaussian model with wake parameter, $w = -0.65$, therefore we could compare the prediction based on the numerical model in Figure (5.15) to the previous prediction based on the gaussian model in Figure (4.33). From comparing the two figures, we see that both models have predicted similar results.

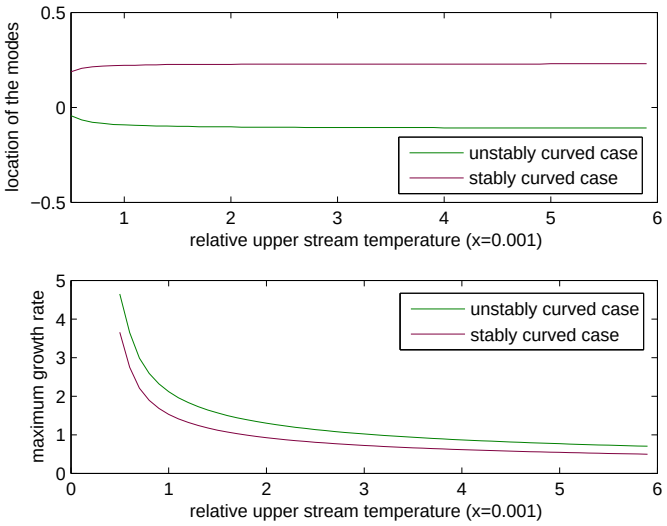

Figure 5.15: The variation of the location of the most unstable mode and the maximum growth rate with the relative upper stream temperature, β_t, for $\beta_u = 0.5$ and $M_{-\infty} = 0.2$, based on the numerical model for $X = 0.001$, within the stably and unstably curved system.

Demonstrated in Figure (5.16) are the asymptotic predictions of the variation of the location of the most unstable mode, $\overline{Y}_b$, and the maximum growth rate, β_0, with the lower stream Mach number, $M_{-\infty}$, within both the stably and the unstably curved wake-dominated systems based on the numerical model with $X = 0.001$. The basic flow parameters for both systems are fixed to be $\beta_u = 0.5$ and $\beta_t = 0.75$. The results are very similar to the previous prediction based on the Gaussian model in Figure (4.34), which indicates that as the compressibility of both systems increases, the most unstable mode that is associated with the unstably curved system would move towards the upper stream direction whereas the mode within the stably curved system would move towards the lower stream direction. The maximum scaled growth rates that are associated with both systems behave similarly with both increasing considerably for the increased compressibility of the system and with the mode that is associated with the stably curved system growing at a slightly faster rate than the unstably curved case.

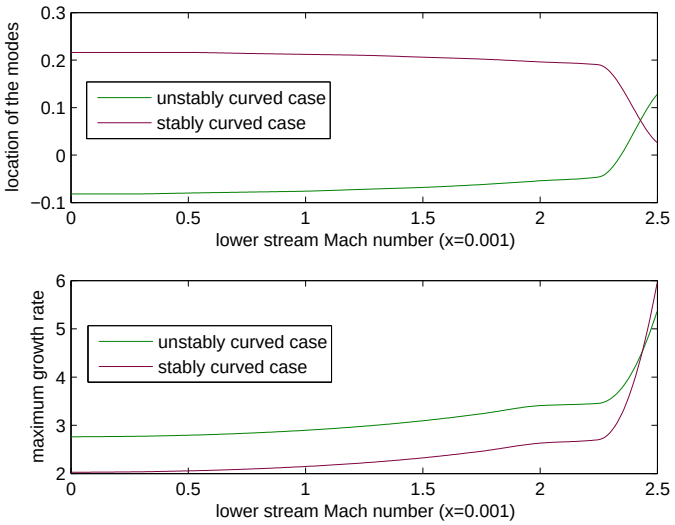

Figure 5.16: The variation of the location of the most unstable mode and the maximum growth rate with the lower stream Mach number, $M_{-\infty}$, for $\beta_u = 0.5$, $\beta_t = 0.75$, based on the numerical model for $X = 0.001$, within the stably and unstably curved system.

To investigate the general effect of increasing relative upper stream temperature on the systems that are dominated by increasing wake effect, demonstrated in Figures (5.17) and (5.18) are the asymptotic predictions of the variation of the location of the most unstable mode, $\overline{Y}_b$, and the maximum growth rate, β_0, with the relative upper stream temperature, β_t, within the unstably curved wake-dominated systems based on the numerical model with increasing wake effect (i.e. decreasing value of X), respectively. The basic flow parameters for all systems are fixed to be $\beta_u = 0.5$ and $M_{-\infty} = 0.2$.

From Figure (5.17), it is observed that the increase of the wake effect within the unstably curved system would lead to the mode moving from the lower stream towards the centreline of the system, which in general agrees with the previous prediction in Figure (5.12). The result also indicates that the increase of the temperature of the slower upper stream would have a larger effect on the location of the mode that is associated with the unstably curved system which is dominated by smaller effect of wake.

The results from Figure (5.18) indicate that the increase of the wake effect would lead to an increase of the growth rate of the mode within the unstably curved system. As the slower upper stream gets much cooler, there is an increasing effect on the growth rate which is associated with the mode that corresponds to the unstably curved system which is dominated by the increasing effect of wake.

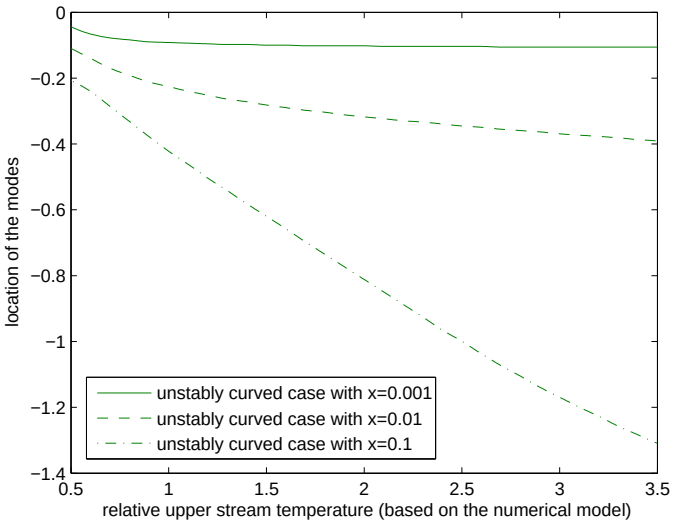

Figure 5.17: The variation of the location of the most unstable mode with the relative upper stream temperature, β_t, for $\beta_u = 0.5$, $M_{-\infty} = 0.2$, based on the numerical model for $X = 0.001, 0.01, 0.1$ respectively, within the unstably curved systems

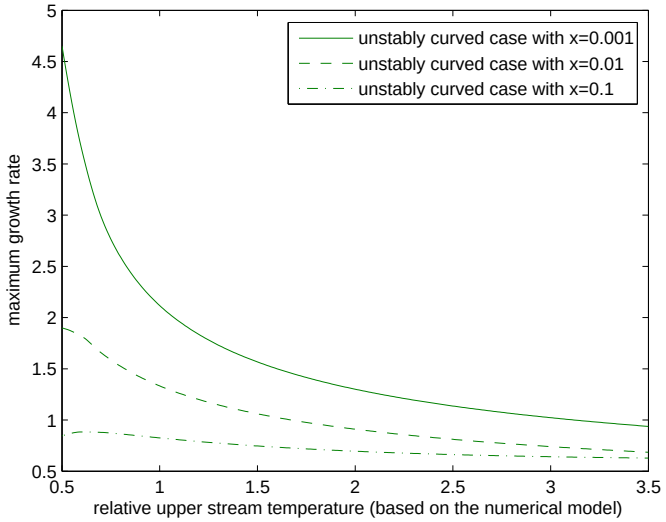

Figure 5.18: The variation of the maximum growth rate with the relative upper stream temperature, β_t, for $\beta_u = 0.5$, $M_{-\infty} = 0.2$, based on the numerical model for $X = 0.001, 0.01, 0.1$ respectively, within the unstably curved systems.

We now turn our attention onto the stably curved systems. Demonstrated in Figures (5.19) and (5.20) are the asymptotic predictions of the variation of the location of the most unstable mode, $\overline{Y}_b$, and the maximum growth rate, β_0, with the relative upper stream temperature, β_t, within the stably curved wake-dominated systems based on the numerical model with increasing wake effect (i.e. decreasing value of X), respectively. The basic flow parameters for all systems remain fixed to be $\beta_u = 0.5$ and $M_{-\infty} = 0.2$.

From Figure (5.19), it is observed that the increase of the wake effect within the stably curved system would lead to the mode moving from the upper stream towards the centreline of the system. The result also indicates that the continuing increase of the slower upper stream temperature has little impact on the systems which are dominated by the different wake effect.

The results from Figure (5.20) indicate that the increase of the wake effect would lead to an increase of the growth rate of the mode within the stably curved system, which lead to a similar behaviour to the growth rate of the mode that is associated with the unstably curved system in Figure (5.18). As the slower upper stream gets significantly cooler, there is an increasing effect on the growth rate of the mode which corresponds to the stably curved system that is dominated by the larger effect of the wake.

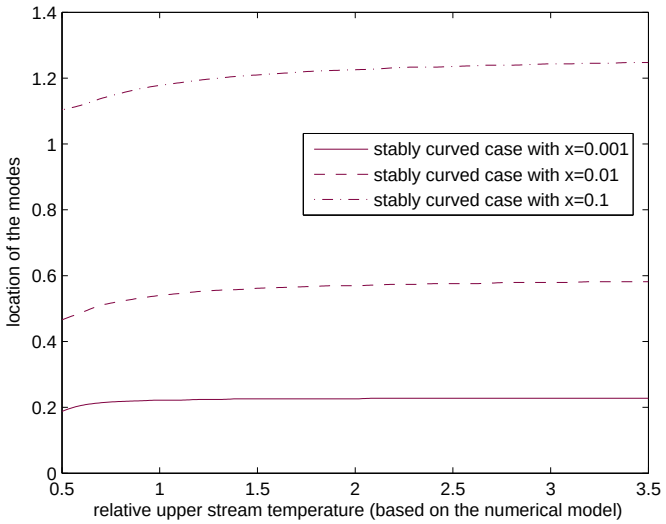

Figure 5.19: The variation of the location of the most unstable mode, $\overline{Y}_b$, with the relative upper stream temperature, β_t, for $\beta_u = 0.5$, $M_{-\infty} = 0.2$, based on the numerical model for $X = 0.001, 0.01, 0.1$ respectively, within the stably curved systems

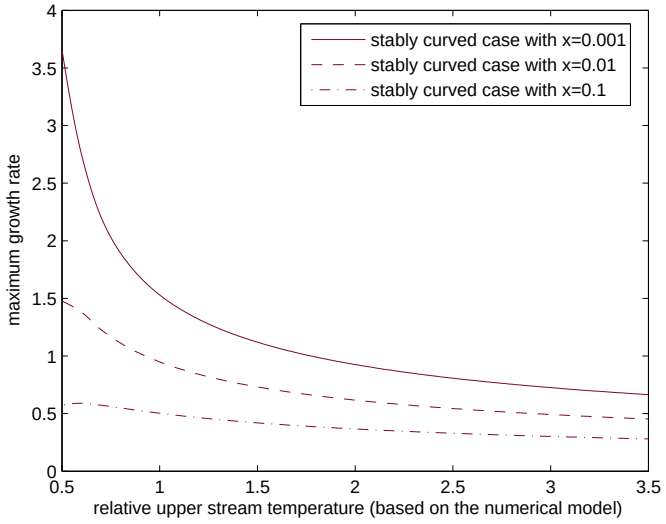

Figure 5.20: The variation of the maximum growth rate, β_0, with the relative upper stream temperature, β_t, for $\beta_u = 0.5$, $M_{-\infty} = 0.2$, based on the numerical model for $X = 0.001, 0.01, 0.1$ respectively, within the stably curved systems.

To investigate the general effect of compressibility on the systems that are dominated by increasing wake effect, demonstrated in Figures (5.21) and (5.22) are the asymptotic predictions of the variation of the location of the most unstable mode, $\overline{Y}_b$, and the maximum growth rate, β_0, with the lower stream Mach number, $M_{-\infty}$, within the unstably curved wake-dominated systems based on the numerical model with increasing wake effect (i.e. decreasing value of X), respectively. The basic flow parameters for all systems are fixed to be $\beta_u = 0.5$ and $\beta_t = 0.75$.

It is observed from Figure (5.21) that for unstably curved systems that are dominated by the smaller effect of wake, the increase of the lower stream Mach number would correspond to a downward movement of the modes towards the faster stream direction. As the wake effect gets larger within the unstably curved system, the increase of the lower stream Mach number would lead to the modes moving towards the opposite direction into the slower upper stream. By comparing the results that are associated with the different wake effect, we see that the increase of the wake would correspond to the mode moving towards the centreline from the lower stream of the system. This prediction is in good agreement with the previous prediction in Figure (5.12).

By comparing the behaviour of the maximum growth rates, β_0, in Figure (5.22), that are associated with the unstably curved systems under different wake effect, we see that the increase of the lower stream Mach number would decrease the growth rate of the modes within the systems that are dominated by the smaller effect of wake. For a system that is dominated by the larger wake effect, the increase of the lower stream Mach number would then increase the growth rate of the system in general. By comparing the maximum growth rates that are associated with the different wake effect, we see that the increase of the wake would correspond to an increase in the growth rate of the modes.

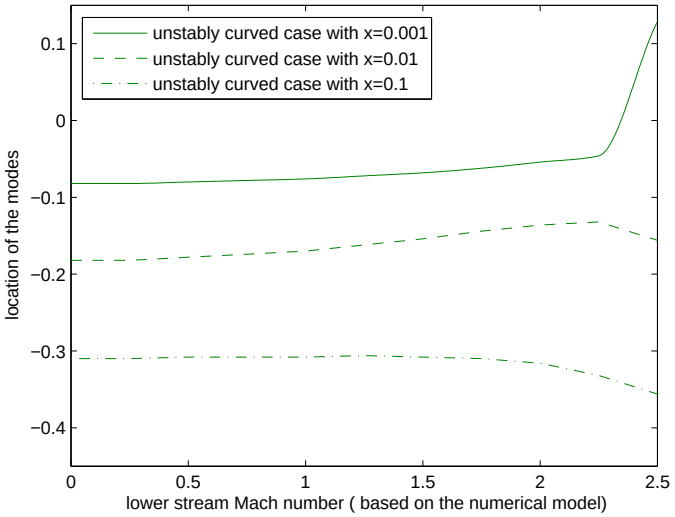

Figure 5.21: The variation of the location of the most unstable mode, $\overline{Y}_b$, with the lower stream Mach number, $M_{-\infty}$, for $\beta_u = 0.5$, $\beta_t = 0.75$, based on the numerical model for $X = 0.001, 0.01, 0.1$ respectively, within the unstably curved systems

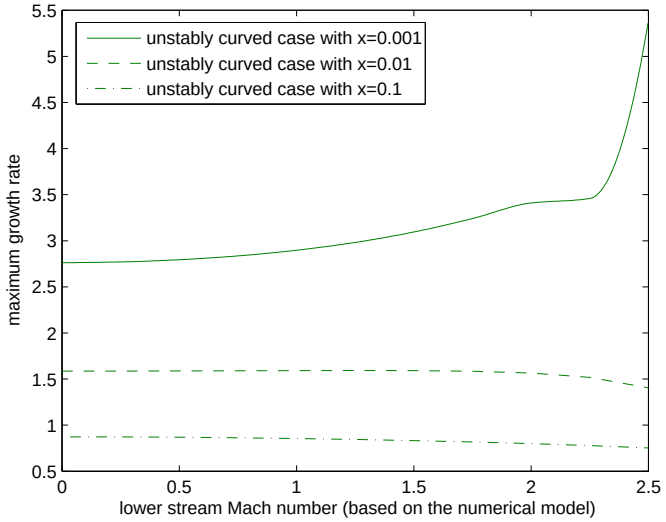

Figure 5.22: The variation of the maximum growth rate, β_0, with the lower stream Mach number, $M_{-\infty}$, for $\beta_u = 0.5$, $\beta_t = 0.75$, based on the numerical model for $X = 0.001, 0.01, 0.1$ respectively, within the unstably curved systems.

We now turn our attention to investigate the general effect of compressibility on the stably curved systems that are dominated by increasing wake effect. Demonstrated in Figures (5.23) and (5.24) are the asymptotic predictions of the variation of the location of the most unstable mode, $\overline{Y}_b$, and the maximum growth rate, β_0, with the lower stream Mach number, $M_{-\infty}$, within the stably curved wake-dominated systems based on the numerical model with the increasing wake effect (i.e. decreasing value of X), respectively. The basic flow parameters for all systems remain fixed to be $\beta_u = 0.5$ and $\beta_t = 0.75$.

The results from Figure (5.23) indicate that for the stably curved systems that are dominated by smaller effect of wakes, the increase of the lower stream Mach number would correspond to a slight upward movement of the modes towards the faster stream direction. As the wake effect gets larger within the stably curved system, the increase of the lower stream Mach number, $M_{-\infty}$, would lead to the modes moving towards the opposite direction into the faster lower stream. By comparing the results that are associated with the different wake effect, we see that the increase of the wake would correspond to the mode moving towards the centreline from the upper stream of the system. This prediction is in good agreement with the previous prediction in Figure (5.12).

The result from Figure (5.24) indicates that the increase of the lower stream Mach number, $M_{-\infty}$, would decrease the growth rate of the modes within the stably curved systems that are dominated by the smaller effect of wakes. For system that is dominated by the larger wake effect, the increase of $M_{-\infty}$ would then increase the growth rate of the system in general. By comparing the growth rates that are associated with the different wake effect, we see that the increase of the wake would correspond to an increase in the maximum growth rate.

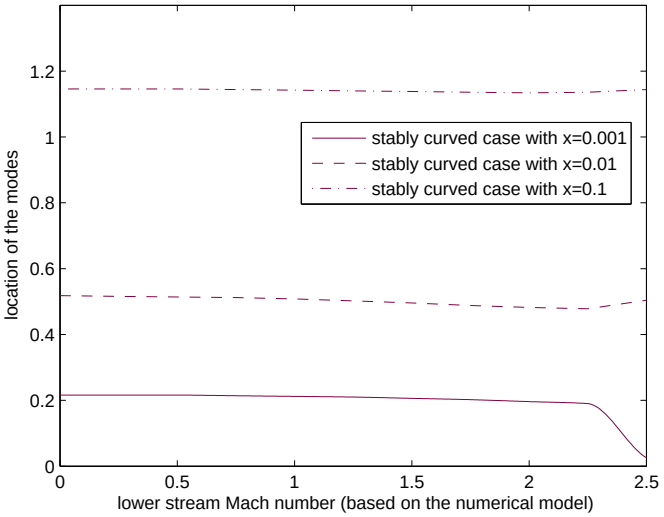

Figure 5.23: The variation of the location of the most unstable mode, $\overline{Y}_b$ with the lower stream Mach number, $M_{-\infty}$, for $\beta_u = 0.5$, $\beta_t = 0.75$, based on the numerical model for $X = 0.001, 0.01, 0.1$ respectively, within the stably curved systems

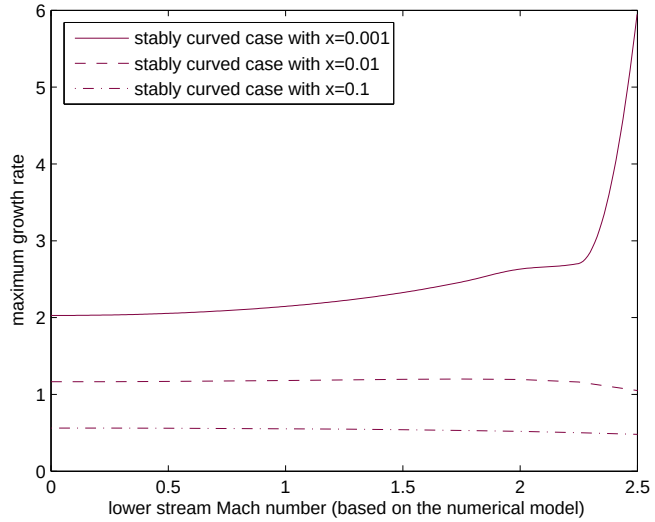

Figure 5.24: The variation of the maximum growth rate, β_0 with the lower stream Mach number, $M_{-\infty}$, for $\beta_u = 0.5$, $\beta_t = 0.75$, based on the numerical model for $X = 0.001, 0.01, 0.1$ respectively, within the stably curved systems.

5.4.1 The viscous right-hand branch modes

We now turn our attention onto the viscous right-hand branch for the curved compressible system to investigate the shape of the neutral curve as this would help us to determine when a mode will be unstable. The asymptotic analysis that is used to determine the location and the growth rate of the right-hand branch modes remains the same as in chapter one.

Demonstrated in Figures (5.25) and (5.26) are the variation of the scaled growth rate, $\tilde{\beta}$, and location of the modes, $\overline{Y}_v$, with the scaled wave number, $\tilde{\lambda}$, respectively, based on the numerical wake flow model within the right-hand viscous region for increasingly wake-dominated unstably curved systems (i.e systems based on the model with decreases in X). The basic flow parameters are fixed to be $\beta_u = 0.5$, $\beta_t = 0.75$ and $M_{-\infty} = 0.2$, respectively. The predictions of the variation of $\tilde{\beta}$ and $\overline{Y}_v$ with $\tilde{\lambda}$ within the unstably curved system can be obtained by solving equations (2.60) and (2.61) with fixed $\tilde{\chi} = 1$ for the unstably curved case.

Figure (5.25) indicates a increase in the growth rate of the modes for the increased wake effect within the systems, which agrees with the previous prediction in the limit of high wave number within the intermediate region in Figure (5.12). Figure (5.25) also indicates that the growth rates would decrease for an increase in the wave numbers which shows that the modes are stabilised by the viscosity effect within the systems.

Figure (5.26) indicates that the modes would move further into the lower stream direction for an increase in the wave number.

As the wave number tends to zero from the viscous right-hand region, the mode is moving towards the inviscid region. The numerical model predictions for zero wave number in the viscous region, for the scaled growth rate, $\tilde{\beta}$, and the location of the mode, $\overline{Y}_v$, that corresponds the unstably curved system are demonstrated in Table (5.5), which matches directly on to the inviscid modes (compare with Table (5.2)).

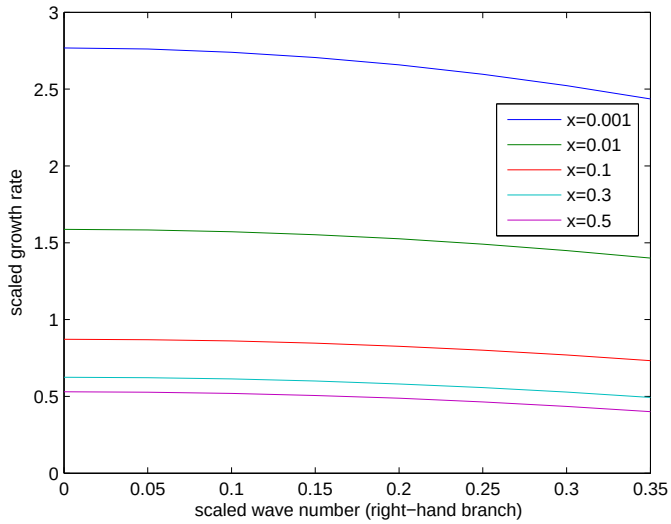

Figure 5.25: The variation of the scaled growth rate, $\tilde{\beta}$, with scaled wave number, $\tilde{\lambda}$, with fixed basic flow parameters $M_{-\infty} = 0.2$, $\beta_u = 0.5$ and $\beta_t = 0.75$ for increasing X, within the unstably curved systems.

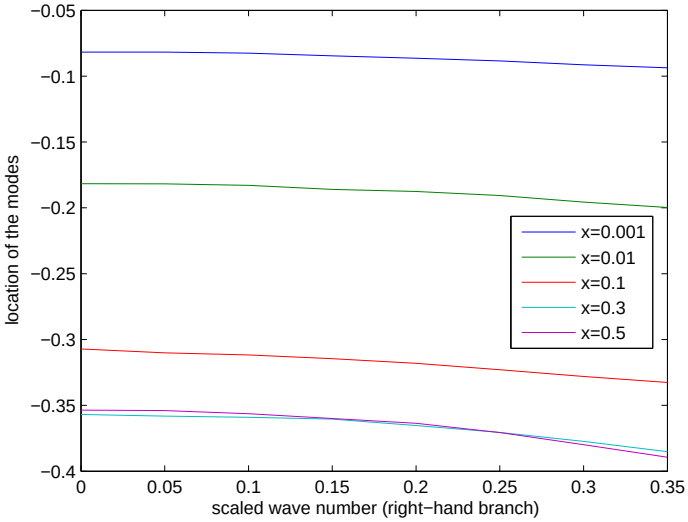

Figure 5.26: The variation of the most unstable mode, $\overline{Y}_v$, with scaled wave number, $\tilde{\lambda}$, with fixed basic flow parameters $M_{-\infty} = 0.2$, $\beta_u = 0.5$ and $\beta_t = 0.75$ for increasing X, within the unstably curved systems.

X within the system	0.001	0.01	0.1	0.3	0.5
$\tilde{\beta}$ for $\tilde{\lambda} = 0$	2.7675	1.5868	0.8720	0.6240	0.5298
$\overline{Y}_v$ for $\tilde{\lambda} = 0$	-0.0818	-0.1817	-0.3072	-0.3569	-0.3537

Table 5.5: The maximum scaled growth rate, $\tilde{\beta}$, and the location of the unstable mode, $\overline{Y}_v$, for $\tilde{\lambda} = 0$, with X, within the unstably curved systems.

Demonstrated in Figures (5.27) and (5.28) are the variation of the scaled growth rate, $\tilde{\beta}$, and location of the modes, $\overline{Y}_v$,with the scaled wave number, $\tilde{\lambda}$, respectively, based on the numerical wake flow model within the right-hand viscous region for the stably curved systems. To obtain these results, we need to solve equations (2.60) and (2.61) by fixing $\tilde{\chi} = -1$. The basic flow parameters still remain fixed as $\beta_u = 0.5$, $\beta_t = 0.75$ and $M_{-\infty} = 0.2$, respectively.

The results from Figure (5.27) indicate an increase in the maximum growth rate, $\tilde{\beta}$, of the modes for the increased wake effect (decrease in X) within the stably curved systems.

Figure (5.28) indicates that as the wave number, $\tilde{\lambda}$, increases the modes would slowly move further into the slower upper stream. By comparing the results that correspond to the different wake effect within the systems, we see that the increase in the wake effect would lead to the mode moving towards the centreline of the system.

As the wave number tends to zero from the viscous right-hand region, the mode is moving towards the inviscid region. The numerical model predicts that for zero wave number in the viscous region, the scaled growth rate, $\tilde{\beta}$, and the location of the mode, $\overline{Y}_v$, that corresponds the each of the stably curved systems are demonstrated in Table (5.6), which matches very well on to the inviscid modes (compare with Table (5.3)) within the corresponding stably curved systems).

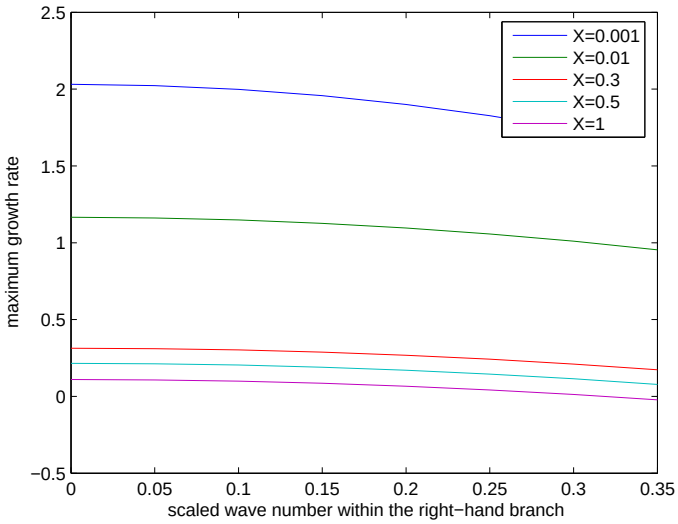

Figure 5.27: The variation of the scaled growth rate, $\tilde{\beta}$, with scaled wave number, $\tilde{\lambda}$, with fixed basic flow parameters $M_{-\infty} = 0.2$, $\beta_u = 0.5$ and $\beta_t = 0.75$ for increasing X within the stably curved systems.

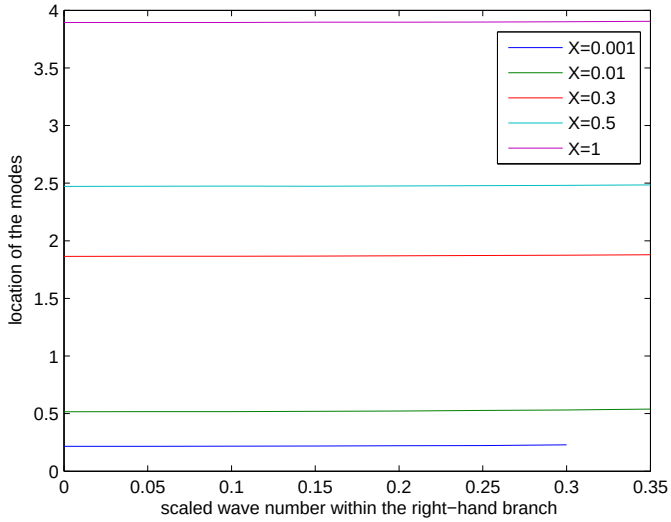

Figure 5.28: The variation of the most unstable mode, $\overline{Y}_v$, with scaled wave number, $\tilde{\lambda}$, with fixed basic flow parameters $M_{-\infty} = 0.2$, $\beta_u = 0.5$ and $\beta_t = 0.75$ for increasing X within the stably curved systems.

X within the system	0.001	0.01	0.3	0.5	1
$\tilde{\beta}$ for $\tilde{\lambda} = 0$	2.0315	1.166	0.3137	0.2154	0.1098
$\overline{Y}_v$ for $\tilde{\lambda} = 0$	0.2160	0.5164	1.8647	2.4723	3.8938

Table 5.6: The maximum scaled growth rate, $\tilde{\beta}$, and the location of the unstable mode, $\overline{Y}_v$, for $\tilde{\lambda} = 0$, with X, within the stably curved systems.

5.5 Chapter summary

The work in this chapter demonstrates the process of deriving the numerical wake flow model from the governing basic flow equations and the investigation of the Görtler disturbance within both stably and unstably wake-dominated curved compressible mixing layers.

The numerical wake flow model offers a solution to the compressible mixing layer equations. For the initial profiles that are required to solve the basic flow equations we have used the techniques of asymptotic expansions which was initially employed by Goldstein (1933) for a solution in the near wake region in the incompressible symmetric boundary layer case. The basic flow equations were then solved numerically by using a Nag routine in Fortran to obtain the numerical wake flow model that describes the variation of the basic streamwise velocity for increasing distance from the trailing edge of the splitter plate within the mixing-layer system with relative upper steamwise velocity fixed at $\beta_u = 0.5$.

A similar investigation to that based on the Gaussian model was conducted using the numerical model. The prediction based on the numerical model confirms the previous Gaussian model prediction of the new modes that could exist within the stably wake-dominated curved compressible system. For a system that is dominated by large a wake the asymptotic prediction based on the numerical model indicates that the increase of the compressibility effect would render the system more unstable which appears to be

the opposite case within the plain curved compressible system. This result also agrees with the previous Gaussian model prediction, which suggests that the wake effect would dominate the system and lead to change of the system's stability characteristics. The difference among the predictions of the growth rate and location of the modes based on the models indicates that the choice of the basic wake flow model has a large effect on the predictions of the system's behaviour.

Chapter 6

Summary

Within this project we have been principally concerned with the study of the linear Görtler instability within the wake-dominated curved compressible mixing layers. The Görtler instability is a type of centrifugal instability that could arise from the fluid system owing to the dynamic effect of flow line curvature. Since the flow is naturally unstable to inviscid modes of instability and therefore any modification of this by the additional flow variation would potentially be of interest to the study of fluid mixing process. The first work on this centrifugal instability was concerned with their growth over curved surfaces, Görtler (1940). Although there have been a number of works that were devoted to the study of this instability, it was not until Hall (1982) that a fully consistent formulation was presented. Since the Görtler modes take the form of pairs of streamwise-orientated counter-rotating vortices which are periodic in the spanwise direction, it is expected that the development of this instability would enhance the mixing between the two fluids. However, little attention has been given to study this instability within the mixing layer system until the experimental work from Plesniak et al. (1994) within the turbulent mixing layers which demonstrated that the Görtler instability could exist within the incompressible curved mixing layers under the condition that the slower of the streams curves towards the faster one. Previous numerical and analytical work of Otto et al. (1996) has also elucidated the structure of the Görtler vortices within the incompressible mixing layers. It was the

later work of Owen et al. (1997) which then extended the investigation by considering the effect of compressibility and heating in determining the streamwise evolution of the Görtler vortices within these systems. As well as finding modes that have counterparts in the incompressible problem which were referred to as the 'conventional modes', the investigation of Owen et al. (1997) also showed that for certain parameter regimes modes could occur within the compressible mixing layer with its centreline curving towards the slower stream, which is referred to as the stably curved case; these thermal modes have no counterpart within the incompressible mixing layers.

The aim of this project is to investigate the linear Görtler disturbance as a mixing enhancement within the wake-dominated curved compressible mixing-layer system. Such a system was known to occur at downstream of the trailing edge of a thin partition. We have set up our system based on two non-parallel compressible streams with the slower stream travelling above the faster stream. Within the system, a splitter plate was inserted into the centreline of the system which initially separates the two streams and as both streams travel down the trailing edge of the plate, the merging of the boundary layers from either side of the plate will form a thin wake like structure. We started the work by demonstrating the process of deriving the governing equations of fluid mechanics for this type of curved compressible mixing layer system, then discussed the requirement for an equation of state and energy equation in compressible flows and reformed the equations in the relevant curved geometry. We then formulated the mixing layer problem and proceeded to derive the basic flow equations. We also discussed the necessity of transformations on the basic flow equations and went through the process of transforming these equations into simpler forms using both the Howarth-Dorodnitsyn transformation and the compressible stream function. During the set up for the instability problem, we introduced a variable, $\tilde{\chi}$, to denote the sign of the curvature, χ, and this would allow us to study the mixing-layer systems with the centreline curving towards the both faster and the slower stream directions. Throughout the project, we referred to the system that curves

towards the direction of the slower upper stream as the 'stably curved' case, whereas the system that curves towards the direction of the lower faster stream was referred to as the 'unstably curved' case. For the investigation of the behaviour of the inviscid Görtler modes with wave lengths comparable with the boundary-layer thickness with $G \gg 1$, we have used the linear stability analysis to derive an eigenvalue relation between the normal disturbance velocity, V, and the scaled growth rate, β, for both the stably and the unstably curved systems. Based on the eigenvalue relation, we then used the asymptotic analysis from Hall (1982), to obtain a set of equations for analytically determining the leading-order behaviour of the scaled growth rate and location of the modes in the limit of high-wavenumber of the inviscid problem, which would help us to gain some useful information pertaining to the ranges of basic flow parameter ratios for which these modes persist. It is known that as the modes progress downstream, the viscosity effect would eventually stabilise the disturbance. Within this right-hand viscous region, Hall (1982) then showed that it is possible to define a unique right-hand branch of the neutral curve which, at zeroth order, has the Görtler number proportional to the fourth power of the vortex wavenumber. By using the method of asymptotic expansion from Hall (1982), we then derived the equations for determining the leading-order scaled growth rate and the location of the modes of the right-hand branch for both the stably and the unstably curved wake-dominated compressible mixing-layer systems. It was shown by Owen et al. (1997) that within the curved mixing-layer systems, there was a direct matching between the inviscid left-hand branch and the viscous right-hand branch regions. This is in contrast to the behaviour of Görtler vortices within the boundary-layer case, which was studied by Denier et al. (1991). Within the boundary-layer problems the vortex wavelength is small in comparison with the boundary layer thickness and the modes are driven to the proximity of the solid boundary and is therefore able to develop in a quasi-parallel manner.

The next chapter consists of the investigation of the linear Görtler instability within a system that is far downstream from the trailing edge of the splitter plate. It is expected

that as the system progresses downstream further away from the trailing edge of the splitter plate, the modes within the system would lead to a similar behaviour with the modes within the plain curved compressible mixing-layer system, which was previously investigated by Owen et al. (1997). For this problem, we re-formulated the problem by including a similarity transformation onto the governing equations for the system. With the similarity transformation, the governing equations were reduced to one-dimensional form. We then reproduced some of the results in Owen et al. (1997) by considering a different numerical scheme. The predictions of the instability based on the Tanh, Lock and Ting basic flow models were investigated and compared. The results indicate that the different basic flow models would lead to a different prediction of the behaviour of the modes within the same system. To enhance the mixing within the system, it is desirable for the Görtler instability to posses a large growth rate and be situated close to the centreline of the system. Therefore it is important to accurately predict the growth rate and location of the mode within the system. Our investigation indicates that the Tanh profile offers a slightly higher set of growth rates of the modes in comparison with the Lock and Ting profiles. The location of the modes were also predicted to be slightly different by the three models. These results were later used to compare with the predictions within the wake-dominated systems.

In Chapter Four, we turned our attention onto the wake-dominated system by considering two analytic models that were previously used to approximate the behaviour of the basic wake flow within the parallel mixing-layer systems. The first model that was considered is the Gaussian wake flow profile. Such profile consists of a Tanh profile with a Gaussian wake component subtracted off. Based on our interest, we also conducted an investigation of the jet-dominated system, which could be approximated by adding the Gaussian wake component onto the Tanh profile instead of subtracting off. The results indicate that the increase of the wake effect would lead to an increase of the growth rate of the modes at a faster rate than the growth rate of the modes within the corresponding

jet-dominated cases. Within the unstably curved wake-dominated compressible systems the Gaussian model predicts that the decrease of the relative upper stream velocity and temperature will considerable increase the growth rate of the modes. As the slower stream becomes significantly cooler than the faster stream, the Gaussian model predicts that the modes would reside close to the centreline of the unstably wake-dominated curved system. However within the corresponding unstably curved jet-dominated systems, the increase of the relative upper stream temperature lead to an increase in the growth rate of the modes and also lead to the modes moving from the slower stream towards the faster stream direction. For an increased compressibility within the unstably curved wake-dominated systems, the Gaussian wake profile predicts that as the lower stream Mach number continues to increase past some critical value dependent on the wake parameter, w, the increase of the compressibility would lead to an increase of the growth rate of the modes. Within the corresponding jet-dominated systems, the results indicate the increase of the compressibility would lead to an increase of the growth rate and the modes will move towards the centreline from the slower upper stream. Therefore within an unstably curved compressible mixing-layer system that is dominated by large a wake and the slower stream is significantly cooler than the faster stream, the Görtler disturbance becomes more effective towards enhancing the mixing under the increase of the compressibility within the system.

Within the wake-dominated stably curved compressible mixing-layer systems, we have found a set of wake triggered modes which behave differently to the previous 'thermal modes' that were found within the plain stably curved compressible mixing layers. Unlike the thermal modes, these wake modes are not driven by the thermal gradient, but in fact the wake effect on the system. The results based on the Gaussian model indicate that as the wake effect increases within the stably curved system the growth rate of the wake modes would be comparable to the modes within the corresponding unstably curved wake-dominated system. In general the Gaussian wake profile predicts that the existence of the wake would render both the stably and the unstably curved systems more unstable.

The results indicate that a decrease in the relative upper stream temperature will lead to the wake mode moving towards the centreline from the slower upper stream of the stably curved system, and the increase of the growth rate of the wake mode, which become comparable to that of the unstably curved system. For an increase of the compressibility of the stably curved system, the wake mode will move towards the centreline from the slower upper stream, and with the growth rate of the mode becomes comparable or even larger than the corresponding unstably curved case. An investigation of the modes within the corresponding right-hand branch region of both the stably and the unstably curved wake-dominated compressible systems was conducted based on the Gaussian model. The results indicate that the modes will eventually be stabilized by the viscous effect within the systems. Within the unstably curved system, the increase of the wave number will lead to the modes moving towards the lower stream, whereas for the stably curved cases, the modes will move towards a higher position in the slower upper stream. For zero wave number within the right-hand branch the location and the growth rate of the modes match directly onto the predictions of the inviscid modes within both the stably curved and the unstably curved cases.

The second analytic model which we have considered is the composite model. This model was initially designed by Liang et al. (1996) to correspond to an experiment performed at hypersonic speeds. The model was set up based on the fixed basic flow parameters for a parallel hypersonic mixing-layer system based on the faster stream travelling above the slower stream. For the non-dimensional normal distance across the mixing layer, Liang et al. (1996) employed a transformation variable, $Y^{'}$, that involves the thickness of momentum term, θ, which is in slightly different form to the Howarth Dorodnitsyn transformation variable, (2.31). Therefore to apply this model to our system, we need to re-scale the growth rate and the location of the most unstable mode in order to remove θ from our equations that governs the behaviour of the linear Görtler disturbance. Based on the composite model, we then generated the growth rate of the first four modes within

both the unstably and the stably curved system for a particular wave number by numerically solving the associated eigenvalue relation. Due to the time constraint of this project we were unable to progress further by using our numerical scheme to demonstrate the increase of the scaled wave number on the growth rate of the modes within the unstably curved system based on composite model. The reason is that the composite model was set up on a domain between $Y^{'} = \pm 30$, therefore within each iteration the system would need to be integrated from $Y^{'} = \pm 30$ to 0, based on a relatively small step size, which proved to be time-consuming. We then proceeded to investigate the effect of increasing distance from the trailing edge of the plate, $X^{'}$, on the scaled growth rate and the location of the modes in the limit of a large wave number within both the stably and the unstably curved systems. The results indicate that as the wake effect continues to decrease within the unstably curved system the growth rate of the disturbances would slightly increase, whereas within the stably curved system, the growth rate continues to decrease. The results also indicate that the increase of the wake effect will lead to an increase of the growth rate of the modes within both systems and the modes will move towards the centreline of the layer, which will make the modes more beneficial towards enhancing the mixing within the systems. We have also conducted an investigation of the modes within the corresponding right-hand branch region of both the stably and the unstably curved wake-dominated compressible systems based on the composite model. Similar to those of the Gaussian wake profile predictions, the results indicate that the modes will eventually be stabilized by the viscous effect within the systems. Within the unstably curved system, the increase of the wave number will lead to the modes moving towards the lower stream, whereas for the stably curved cases, the modes will move towards a higher position in the slower upper stream. For zero wave number within the right-hand branch the location and the growth rate of the modes match quite well onto the predictions of the inviscid modes within both the stably curved and the unstably curved cases.

In Chapter Five, we demonstrated the process of deriving a numerical wake flow model,

which provides the solution in the near wake to the governing basic flow equations for the curved compressible system. To solve the compressible basic flow equations numerically, we required a set of initial profiles for the flow, and we have employed the method of asymptotic expansion from Goldstein (1933). The compressible basic flow equations were first simplified by the Howarth Dorodnitsyn transformation variable, $\overline{Y}$, and the compressible stream function. For the missing third boundary condition for the basic flow equation, we have considered the condition which was proposed by Lock (1951), that is the normal velocity is zero at the centreline of the layer. A set of initial profiles for $\overline{u}$, $\frac{\partial \overline{u}}{\partial \overline{Y}}$ and ψ, in the case of an asymmetric wake flow were derived based on the system with the relative upper stream velocity fixed at $\beta_u = 0.5$. These initial profiles were employed during the numerical calculation of the basic wake flow with the increasing distance from the trailing edge, X, within the system. Similar investigations to those based on the Gaussian model were then conducted using the obtained numerical model. Within the stably curved system the numerical model predicts the similar behaviour of the wake modes to those based on the Gaussian model prediction. As the wake increase ($X \to 0$), the numerical model predicts that the growth rate of the wake modes will become comparable to the modes within the corresponding unstably curved case. The numerical model also predicts that as the wake increases the modes within both the unstably and the stably curved systems will move towards the centreline of the systems from the lower and the upper streams, respectively. In comparison, the mode within the unstably curved system will reside closer to the centreline of the system and posses a slightly larger growth rate, therefore for large wake ($X \to 0$) within the system the Görtler disturbance is more beneficial towards enhancing the mixing when the system is unstably curved. For the effect of the relative upper stream temperature on the behaviour of the modes within the unstably curved systems, the numerical results predict that as the wake effect increases within the system, the increase of the relative temperature will have less effect on the location of the modes; and the decrease of the relative upper stream temperature will

amplify the growth rate of the mode within the unstably curved system that is dominated by large effect of a wake. Therefore the mode is more beneficial towards mixing within the unstably curved case when the upper stream is significantly cooler than the lower stream; and the wake effect is large within the system. Within the corresponding stably curved systems, the numerical model predicts that the growth rate of the mode will increase and the mode will move towards the centreline from the upper slower stream for a decrease in the relative upper stream temperature. Therefore within the stably curved system, the mode is also more beneficial towards mixing when the slower upper stream is significantly cooler than the lower faster stream. For an increase of the compressibility within the unstably curved systems, the numerical model predicts that for systems that are dominated by smaller effect of wakes, the increase of the lower stream Mach number will lead to a slight decrease in the growth rate of the systems, and as the wake effect gets larger and as the lower stream Mach number continues to increase past some critical value dependent on the distance from the trailing edge of the splitter plate, X, the increase of the compressibility would lead to an significant increase of the growth rate of the modes. For the unstably curved systems that are dominated by smaller wake effect (increasing X), the increase of the compressibility of the systems will lead to the mode moving towards a lower position in the faster stream; and as the wake effect gets larger, the increase of the compressibility will lead to the mode moving towards the centreline of the system and into the slower upper stream. Within the corresponding stably curved systems, the numerical model offers similar predictions of the growth rate of the modes to those within the unstably curved cases, in comparison, the growth rate will be comparable to or even larger than that within the unstably curve system that is dominated by large a wake (in this case we have $X = 0.001$ to compare with). For an increased compressibility within the stably curved systems, the numerical model predicts that the increase of the lower stream Mach number has a little effect on the location of the modes that correspond to the system under smaller wake effect ($X > 0.001$), and as the wake effect gets larger

within the system (for $X = 0.001$), the mode will then move from the slower upper stream towards the centreline of the system. In comparison to the mode within the corresponding unstably curved system (for $X = 0.001$), we see that the mode will reside closer to the centreline within the stably curved system. Therefore, under large compressibility effect and large wake effect ($X \leqslant 0.001$), the modes are more beneficial towards mixing within the stably curved system. We then conducted an investigation of the modes within the corresponding right-hand branch region of both the stably and the unstably curved wake-dominated compressible systems based on the numerical model. The results indicate that the modes will eventually be stabilized by the viscous effect within the systems. Similar to the Gaussian model predictions, the numerical model also predicts that the increase of the wave number will lead to the modes moving towards a lower position in the faster stream within the unstably curved systems, whereas for the stably curved cases, the increase of the wave number has little effect on the location of the modes, which all reside in the slower upper stream of the systems. For zero wave number within the right-hand branch the location and the growth rate of the modes match directly onto the predictions of the inviscid modes within both the stably curved and the unstably curved cases.

So far we have demonstrated that Görtler instability can exist within both stably and unstably curved laminar wake-dominated compressible mixing layers. For modes that are associated with the system that curves towards the slower stream direction (i.e. stably curved case), these modes were found to behave differently to the previous thermal mode case. It is found that these modes within the stably curved system are initially triggered by the effect of the wake, therefore we have labelled them as the 'wake modes'. A comparison of the wake modes to those within the corresponding unstably curved systems was made based on both the Gaussian and the numerical model; and the results indicate that that the growth rate of these wake modes can be comparable to or even larger than those within the unstably curved systems.

6.1 Future Work

The study in this project is concerned with the linear evolution of Görtler vortices within a wake-dominated curved compressible mixing layer. The work undertaken within this project could provide the basis for further work within both the inviscid and centrifugal instability areas.

The next obvious step is to study the non-linear evolution of the modes for $O(1)$ wave numbers within the wake-dominated systems. Within this project we have briefly investigated the effect of increasing wave number on the behaviour of the right-branch modes. Perhaps a more detailed investigation in the effect of varying the basic flow parameters on the behaviour of the modes within such region can be conducted in the future. The current numerical wake flow model was derived based on a fixed relative upper stream velocity, $\beta_u = 0.5$, by using the condition that was proposed by Lock (1951). The fixed basic upper stream velocity brings a disadvantage to the numerical model when it comes to predict the effect of varying the full range of basic flow parameters on the system in order to compare with the Gaussian wake model prediction. Perhaps the numerical model can be improved to include more ranges of the relative upper stream velocities for the wake-dominated curved mixing-layer system. The investigations of the wake-dominated mixing layers could also be more generalized by including Ting (1959)'s boundary condition within the derivation of the numerical wake flow model.

Previously we have mentioned that the presence of the vortex within the curved mixing layer causes the system to become unstable to three modes of instability, having studied the behaviour of the Görtler vortex, it would be interesting to conduct a similar investigation on the Kelvin-Helmholtz and Rayleigh-Taylor instabilities within the wake-dominated curved compressible system to study how the modes of these instabilities behave when both stably and unstably curved wake-dominated mixing layers are considered.

Within this project, we have set up the problem to investigate the linear Görtler

instability within the systems based on two types of curving directions (i.e. the unstably curved and the stably curved cases). The problem can be extended to suit a further investigation on the effect of the curvature for both the stably curved and the unstably curved wake-dominated curved compressible mixing layers.

List of References

L. P. Bernal and A. Roshko. Streamwise vortex structure in plane mixing layers. *J. Fluid Mech.*, 170:499–525, 1986.

H. Blasius. Grenzschichten in flüssigkeiten mit kleiner reibung. *Z. Math. Phys.*, 56:1–37, 1908.

D. W. Bogdanoff. Compressibility effects in turbulent shear layers. *AIAA J.*, 21:926, 1983.

R. E. Breidenthal. A chemically reacting turbulent shear layer. *Ph.D.thesis, California Institute of Technology*, 1978.

T. Brower and A. Demetriades. Experiments on the free shear layer between two supersonic streams. *AIAA J.*, 41:90–710, 1990.

G. L. Brown and A. Roshko. On the density effects and large structure in turbulent mixing layers. *J. Fluid Mech.*, 64:775–816, 1974.

C. J. Chapman. *High speed flow.* Cambridge University Press, 2000.

D. R. Chapman and M. W. Rubesin. Temperature and velocity profiles in the compressible laminar boundary layer with arbitrary distribution of surface temperature. *J. Aero. Sci*, 16:547–565, 1949.

W. O. Criminale, T. L. Jackson, and D. Joslin, R. *Theory and Computation of Hydrodynamic stability*. Cambridge University Press, 2003.

A. H. Dando and S. O. Seddougui. The compressible görtler problem in two-dimensional boundary layers. *J. Appl. Maths*, 51:27–67, 1991.

P. G. Daniels. A numerical and asymptotic investigation of boundary-layer wake evolution. *J. Inst. Maths. Applics.*, 17:367–386, 1976.

A. Demetriades. Composite method for the mixing of two steady laminar flows. *AIAA J.*, 29:168–173, 1990.

J. P. Denier, P. Hall, and S. O. Seddougui. On the receptivity problem for görtler vortices: vortex motions induced by wall roughness. *Phil. Trans. Roy. Soc. Ser.*, A335:51–85, 1991.

S. Goldstein. Concerning some solutions of the boundary layer equations in hydrodynamics. *Proc. Cambr. Phil. Soc.*, 26:1–30, 1930.

S. Goldstein. On the two-dimensional steady flow of a viscous fluid behind a solid body. *Proc. R. Soc. Lond.*, A 142:545–562, 1933.

S. Goldstein. *Modern developments in fluid dynamics*. Oxford University Press, 1953.

H. Görtler. übereine dreidimensionale instabilität larmarer grenzschichten an konkaven wänden. *Ges. D. Wiss.*, 1, 1940.

H. Gropengiesser. Study of the stability of boundary layers and compressible fluids. *NASA-TTF-12786*, 1969.

P. Hall. Taylor-görtler vortices in fully developed or growing boundary-layer flows: linear theory. *J. Fluid Mech.*, 24:475–494, 1982.

P. Hall. Görtler vortices in growing boundary-layers: The leading edge receptivity problem, linear growth and the nonlinear breakdown stage. *Mathematika.*, 37:151–189, 1990.

P. Hall and N. J. Horseman. The linear inviscid secondary instability of longitudinal vortex structures in boundary layers. *J. Fluid Mech.*, 232:357–375, 1991.

H. v. Helmholtz. Die energie der wogen und des winders. *Ann. Phys.*, 41:641–662, 1890.

E. J. Hopfinger, A. Kurniawan, W. H. Graf, and U. Lemmin. Sediment erosion by görtler vortices the scour-hole problem. *J. Fluid Mech.*, 520:327–342, 2004.

T. L. Jackson and C. E. Grosch. Inviscid spatial stability of a compressible mixing layer. *J. Fluid Mech.*, 786:609–637, 1991.

P. S. Karasso and M. G. Mungal. Mixing and reaction in curved liquid shear layers. *J. Fluid Mech.*, 334:381–409, 1997.

W. Kelvin. The influence of wind on waves in water suppoused frictionless. *Phil. Mag.*, 42:368–374, 1871.

J. B. Klemp and A. Acrivos. A note on the mixing of two uniform parallel semi-infinite streams. *J. Fluid Mech.*, 55:25–30, 1972.

J. C. Lasheras, J. S. Cho, and T. Maxworthy. On the origin and evolution of streamwise vortical structures in a plane free shear layer. *J. Fluid Mech.*, 172:231–258, 1986.

F. Li and M. R. Malik. Fundamental and subharmonic secondary instabilities of görtler vortices. *J. Fluid Mech.*, 297:77–100, 1995.

F. Liang, E. Reshotko, and A. Demetriades. A stability study of the developing mixing layer formed by supersonic laminar streams. *Phys. Fluids*, 8:3253–3263, 1996.

C. C. Lin. On the stability of two-dimensional parallel flows. *Quart. Appl. Math.*, 3: 117–142, 1945.

C. C. Lin and L. Lees. On the linear stability of a compressible inviscid parallel shear flow. *NASA Techn.*, 1115, 1946.

R. C. Lock. The velocity disturbance in laminar boundary layer between parallel streams. *Quart. J. Mech.*, 4:42–57, 1951.

A. F. Messiter. Boundary layer flow near the trailing edge of a flat plate. *Siam J. Appl. Math.*, 18:241–257, 1970.

S. R. Otto, T. L. Jackson, and F. Q. Hu. On the spatial evolution of centrifugal instabilities within curved incompressible mixing layers. *J. Fluid Mech.*, 315:85–103, 1996.

D. J. Owen, S. O. Seddougui, and S. R. Otto. The linear evolution of centrifugal instabilities in curved, compressible mixing layers. *Phys. Fluids*, 9:2506–2518, 1997.

D. T. Papageorgiou. The stability of two-dimensional wakes and shear layers at high mach numbers. *Phys. Fluids*, 3:793–802, 1991.

M. W. Plesniak, R. D. Mehta, and J. P. Johnson. Curved two-stream turbulent mixing layers: three-dimensional structure and streamwise evolution. *J. Fluid Mech.*, 270:1–50, 1994.

L. Prandtl. Uber flüssigheitbewegung bein sehr kleiner reibung. *Proc 3rd Inter. Math. Congress, Heidelberg*, pages 484–491, 1904.

S. A. Ragab. Instabilities in the wake/mixing-layer region of a splitter plate seperating two supersonic streams. *AIAA Pap.*, 88-3677, 1988.

J. Rayleigh, Lord. On the dynamics of revolving fluids. *Scientific Papers.*, 6:447–453, 1916.

O. Reynolds. An experimental investigation of the circumstances which determine whether the motion of water shall be direct or sinuous, and of the law of resistance in parallel channels. *Phil. Trans. Roy. Soc.*, 174:935–982, 1883.

D. F. Rogers. *Laminar flow analysis.* Cambridge University Press, 1992.

N. D. Sandham and C. Reynolds, W. Compressible mixing layer: linear theory and direct simulation. *AIAA J.*, 28:618–624, 1990.

J. M. Sarkies and S. R. Otto. Görtler vortices in compressible mixing layers. *J. Fluid Mech.*, 427:359–388, 2000.

K. C. Schadow and E. Gutmark. Review of passive shear-flow control research for improved subsonic and supersonic combustion. *AIAA Pap.*, 89-2786, 1989.

I. J. Sobey. *Introduction to Interative Boundary Layer Theory.* Oxford University Press, 2000.

K. Stewartson. On asymptotic expansions in the theory of boundary layers. *J. Math. Phys.*, 36:173–191, 1957.

K. Stewartson. *The theory of laminar boundary layers in compressible fluids.* Oxford University Press, 1964.

K. Stewartson. On the flow near the trailing edge of a flat plate. *Mathematika.*, 16: 106–121, 1969.

G. I. Taylor. Stability of a viscous liquid contained between two rotating cylinders. *Phil. Trans.*, A223:289–343, 1923.

L. Ting. On the mixing of two parallel streams. *J. Math. Phys.*, 28:153–165, 1959.

P. R. Turner. *Numerical Analysis.* The Macmillan Press Ltd, 1994.

A. E. P. Veldman. A new calculation of the wake of a flat plate. *J. Eng. Math.*, 9:65–70, 1975.

T. von Kármán. Boundary layer in compressible fluids. *JAS*, 5:227–232, 1938.

M. Zhuang. The effects of curvature on wake-dominated incompressible free shear layers. *Phys. Fluids*, 11:3106–3115, 1999.

M. Zhuang and P. E. Dimotakis. Instability of wake-dominated compressible mixing layers. *Phys. Fluids*, 7:2489–2495, 1995.